



# Formation of hybrid structures of carbon nanotubes and alumina microparticles by CVD method: mechanisms and chemical kinetics

Delong He

## ► To cite this version:

Delong He. Formation of hybrid structures of carbon nanotubes and alumina microparticles by CVD method: mechanisms and chemical kinetics. Other. Ecole Centrale Paris, 2010. English. NNT: 2010ECAP0021 . tel-00504681

**HAL Id: tel-00504681**

<https://theses.hal.science/tel-00504681>

Submitted on 31 Dec 2012

**HAL** is a multi-disciplinary open access archive for the deposit and dissemination of scientific research documents, whether they are published or not. The documents may come from teaching and research institutions in France or abroad, or from public or private research centers.

L'archive ouverte pluridisciplinaire **HAL**, est destinée au dépôt et à la diffusion de documents scientifiques de niveau recherche, publiés ou non, émanant des établissements d'enseignement et de recherche français ou étrangers, des laboratoires publics ou privés.



**ÉCOLE CENTRALE DES ARTS  
ET MANUFACTURES  
« ÉCOLE CENTRALE PARIS »**

**THÈSE**  
présentée par

**DELONG HE**

pour l'obtention du

**GRADE DE DOCTEUR**

**Spécialité : Science des matériaux**

**Laboratoire d'accueil : Laboratoire de Mécanique des Sols, Structures et Matériaux**

**Formation of hybrid structures of carbon nanotubes and  
alumina microparticles by CVD method: Mechanisms and  
Chemical kinetics**

**Soutenue publiquement le 6 juillet 2010**

**devant le jury composé de :**

<b>M.</b>	<b>Paul-Marie MARQUAIRE</b>	Directeur de Recherche, ENSIC Nancy	<b>Président</b>
<b>Mme</b>	<b>Pascale LAUNOIS</b>	Directeur de Recherche, Paris Sud Orsay	<b>Rapporteur</b>
<b>M.</b>	<b>Jean-Louis VIGNES</b>	Professeur émérite, Paris 12	<b>Rapporteur</b>
<b>Mme</b>	<b>Cathie VIX</b>	Directeur de Recherche, ICSI Mulhouse	<b>Examinateur</b>
<b>M.</b>	<b>Fabien MIOMANDRE</b>	Maître de Conférences HDR, ENS Cachan	<b>Examinateur</b>
<b>M.</b>	<b>Jinbo BAI</b>	Directeur de Recherche, EC Paris	<b>Directeur de thèse</b>



**ÉCOLE CENTRALE DES ARTS  
ET MANUFACTURES  
« ÉCOLE CENTRALE PARIS »**

**THÈSE**  
présentée par

**DELONG HE**

pour l'obtention du

**GRADE DE DOCTEUR**

**Spécialité : Science des matériaux**

**Laboratoire d'accueil : Laboratoire de Mécanique des Sols, Structures et Matériaux**

**Formation de structures hybrides de nanotubes de carbone et  
de microparticules d'alumine par la méthode CVD :  
Mécanismes et Cinétiques chimiques**

**Soutenue publiquement le 6 juillet 2010**

**devant le jury composé de :**

<b>M.</b>	<b>Paul-Marie MARQUAIRE</b>	Directeur de Recherche, ENSIC Nancy	<b>Président</b>
<b>Mme</b>	<b>Pascale LAUNOIS</b>	Directeur de Recherche, Paris Sud Orsay	<b>Rapporteur</b>
<b>M.</b>	<b>Jean-Louis VIGNES</b>	Professeur émérite, Paris 12	<b>Rapporteur</b>
<b>Mme</b>	<b>Cathie VIX</b>	Directeur de Recherche, ICSI Mulhouse	<b>Examinateur</b>
<b>M.</b>	<b>Fabien MIOMANDRE</b>	Maître de Conférences HDR, ENS Cachan	<b>Examinateur</b>
<b>M.</b>	<b>Jinbo BAI</b>	Directeur de Recherche, EC Paris	<b>Directeur de thèse</b>

# Remerciements

Cette thèse a été réalisée de tout mon coeur au sein du laboratoire MSSMAT de l'Ecole Centrale Paris, CNRS UMR8579.

Je voudrais tout d'abord remercier Mr Yongning Liu, mon ancien directeur à XJTU en Chine, pour sa grande personnalité et particulièrement pour cette chance qu'il m'a fournie de faire mes études de doctorat en France. Je tiens également à remercier le CSC (China Scholarship Council) pour son soutien financier pendant trois ans, et le Service de l'Education de l'Ambassade de la République Populaire de Chine en République Française pour ses aides et toutes les activités culturelles et scientifiques organisées.

Je tiens extrêmement à remercier Mr Jinbo Bai, mon directeur de thèse, de m'avoir accueilli au laboratoire et d'avoir accepté de diriger cette thèse. Il m'a apporté ses compétences en nanosciences et nanotechnologies, et m'a témoigné sa confiance lors de ces années.

Je tiens aussi à remercier Mr Paul-Marie Marquaire, Président du jury, d'avoir accepté présider le jury de ma soutenance. Il a une grande connaissance dans le domaine de réactions chimiques organiques. Je lui très reconnaissant de ses remarques, ses suggestions, et les discussions constructives sur la simulation de la procédure CVD.

Je tiens sincèrement à remercier Mme Pascale Launois et Mr Jean-Louis Vignes, Rapporteurs de ma thèse, pour leurs lectures minutieuses du manuscrit et leurs grands intérêts à ces travaux. J'admire beaucoup Mme Pascale Launois de ses grandes compétences et sa grande connaissance des nanotechnologies, et Mr Jean-Louis Vignes de sa connaissance spécifique sur les matériaux céramiques.

Je tiens à remercier Mme Cathie Vix et Mr Fabien Miomandre, Examinateurs de ma thèse, pour leur lecture attentive du manuscrit, leurs remarques précises et leurs suggestions importantes.

Je voudrais exprimer spécialement ma reconnaissance envers Mr Bernard Jouffrey pour

plusieurs discussions sur les mécanismes de formation des structures hybrides en six branches. Sa grande compétence en microscopie électronique en transmission, ses diverses connaissances sur les matériaux et phénomènes physiques m'avaient bénéficié beaucoup. Je voudrais également remercier Mr Pascal Lejay de l'Institut NEEL pour sa grande gentillesse de nous avoir fourni deux échantillons - monocristaux d'alumine.

Je voudrais remercier vivement les techniciens avec qui j'ai fait les diverses caractérisations de mes échantillons, sans lesquelles je n'aurais pas pu finir mes études : Johane Sobotka pour caractérisation AFM, Pascale Gemeiner pour caractérisation Raman, Nicolas Guiblin pour caractérisation XRD, Gilles Boemare pour caractérisation TGA... En particulier, une sincère reconnaissance est pour Mme Fançoise Garnier, avec qui j'ai passé avec plaisir beaucoup de temps, et pris pleins de images impressionnantes de MEB ; Un grand merci est à Mr Paul Haghi-Ashtiani pour sa disponibilité, sa générosité et ses travaux sur MET. D'ailleurs, je suis également très reconnaissant à Farida Djebbari, Sokona Konate, Sylviane Bourgeois, Gilbert Le-Gal, Denis Martin, Nicolas Roubier pour leur disponibilité et leurs aides.

Je tiens également à remercier tous les thésards que j'ai eu l'occasion de connaître, et avec qui j'ai travaillé ensemble : Hao Li, Meijuan Jiang, Jing Chen, Yangzhong Wang, Weilong Li, Maxime Genestoux, Rui Liu, Yang Hu, Youqin Lin, Jinkai Yuan, Shenghong Yao, Jing Zhang, Jing Shen, Jérôme Helary, Anthony Dichiara, John Saba, Hande Yavuz, Maguy Dominiczak... En particulier, je voudrais remercier très chaleureusement mes deux amis Michael Bozlar et Hassan Harris pour vos encouragements, vos aides généreuses et nos amitiés profondes. C'était avec grand plaisir de partager des expériences de la vie et de la recherche, qui seront très précieuses pour ma carrière à l'avenir.

Je remercie également de tout mon coeur l'ensemble de ma famille pour son soutien sans faille depuis toujours, et je suis particulièrement reconnaissant envers mes parents et ma belle-mère pour leurs encouragement, leurs compréhension et leurs confiance en moi.

Enfin, ma dernière pensée est pour ma femme Yingjie qui m'a accompagné de surmonter les moments les plus difficiles lors de ces années. Son amour, son encouragement, son soutien, sa compréhension et sa générosité sont les forces permanentes qui me supportent d'affronter des difficultés pour aller au plus haut niveau. Cette thèse est donc dédiée à elle, Yingjie.

# Table of Contents

ACRONYMS AND SYMBOLS .....	1
GENERAL INTRODUCTION .....	3
<b>CHAPTER I</b>	
CARBON NANOTUBES AND THEIR HYBRID MATERIALS .....	5
1.1 BACKGROUND .....	5
1.2 CARBON NANOTUBE STRUCTURES AND PROPERTIES .....	9
<i>1.2.1 Structures</i> .....	9
<i>1.2.2 Properties</i> .....	10
1.2.2.1 Mechanical properties .....	11
1.2.2.2 Thermal properties .....	13
1.2.2.3 Electronic properties .....	13
<i>1.2.3 Potential and current applications</i> .....	14
1.2.3.1 Carbon nanotube composites .....	15
1.2.3.2 Energy storage .....	16
1.2.3.3 Electronic devices .....	17
1.3 CHEMICAL VAPOR DEPOSITION (CVD) SYNTHESIS OF CNTs .....	18
<i>1.3.1 Introduction to CNT synthesis</i> .....	18
<i>1.3.2 Principle of chemical vapor deposition</i> .....	20
<i>1.3.3 Catalytic CVD synthesis of CNTs</i> .....	21
1.3.3.1 Introduction .....	21
1.3.3.2 Catalysts .....	22
1.3.3.3 Substrates .....	24
1.3.3.4 Carbon sources .....	26
1.3.3.5 Atmosphere .....	28
1.3.3.6 Temperature .....	30
1.4 CNT GROWTH MECHANISMS IN CVD .....	30
<i>1.4.1 General mechanism</i> .....	30
<i>1.4.2 Mechanism in floating catalytic CVD</i> .....	36

---

## Table of contents

1.5 CNT BASED HYBRID MATERIALS.....	38
1.5.1 <i>Introduction</i> .....	38
1.5.2 <i>CNTs-based hybrid materials</i> .....	38
1.5.3 <i>Nano-micro hybrid structures</i> .....	40
1.5.3.1 <i>Introduction</i> .....	40
1.5.3.2 <i>In-situ CVD synthesis</i> .....	41
1.5.3.3 <i>Enhanced properties</i> .....	42
1.6 CONCLUSION .....	43

## CHAPTER II

MULTIFORM NANO-MICROMETER HYBRID STRUCTURES AND THERMAL TRANSPORT .....	45
2.1 INTRODUCTION .....	45
2.2 EXPERIMENTAL.....	46
2.2.1 <i>Materials</i> .....	46
2.2.2 <i>Floating CVD equipment and processes</i> .....	46
2.2.3 <i>Characterization methods</i> .....	48
2.3 MULTIFORM HYBRID STRUCTURES OF CNTs- $\mu$ Al <sub>2</sub> O <sub>3</sub> .....	48
2.3.1 <i>Variation of CNT length</i> .....	50
2.3.2 <i>Variation of CNT diameter and number density</i> .....	52
2.3.3 <i>Raman spectroscopy of the three hybrid structures</i> .....	55
2.4 THERMAL REINFORCEMENT OF CNTs- $\mu$ Al <sub>2</sub> O <sub>3</sub> HYBRIDS.....	57
2.4.1 <i>Introduction</i> .....	57
2.4.2 <i>Experimental</i> .....	59
2.4.2.1 Preparation of CNTs- $\mu$ Al <sub>2</sub> O <sub>3</sub> /Epoxy composites .....	59
2.4.2.2 Measurement of thermal conductivity .....	61
2.4.3 <i>Results</i> .....	63
2.4.4 <i>Numerical simulation of thermal reinforcement</i> .....	65
2.5 CONCLUSION .....	70

## CHAPTER III

STUDIES ON FORMATION MECHANISM OF MULTIFORM CNTs- $\mu$ Al <sub>2</sub> O <sub>3</sub> HYBRID STRUCTURES .	71
3.1 INTRODUCTION .....	71
3.2 INFLUENCES OF CVD PARAMETERS .....	72
3.2.1 <i>Catalyst precursor</i> .....	73

3.2.1.1 Thermal decomposition of ferrocene .....	73
3.2.1.2 Influence of ferrocene concentration in xylene.....	75
3.2.1.3 Influence of the ferrocene-xylene solution feed rate .....	79
3.2.2 <i>Carbon sources</i> .....	81
3.2.2.1 Adding Acetylene at high temperatures .....	82
3.2.2.2 Adding Acetylene at relatively low temperatures .....	87
3.2.3 <i>Temperature</i> .....	90
3.2.3.1 Xylene as carbon source .....	90
3.2.3.2 Xylene-acetylene as carbon sources .....	95
3.2.4 <i>Hydrogen ratio</i> .....	101
3.2.4.1 Hybrids from xylene decomposition at relatively high temperatures .....	101
3.2.4.3 Hybrids from the decomposition of xylene/acetylene mixture.....	105
3.2.4.1 Hybrids from acetylene decomposition at relatively low temperatures.....	108
3.3 EFFECTS OF SUBSTRATE PROPERTIES .....	110
3.3.1 <i>Effect of substrate morphology</i> .....	110
3.3.2 <i>Effect of particle size</i> .....	113
3.3.3 <i>Effect of microparticle structures and surface properties</i> .....	115
3.3.4 <i>CNT growth on heat-treated <math>\mu Al_2O_3</math></i> .....	121
3.4 CNT GROWTH DYNAMICS.....	125
3.4.1 <i>Connection of CNT and <math>\mu Al_2O_3</math></i> .....	125
3.4.2 <i>Growth kinetics of CNTs on alumina microparticles</i> .....	127
3.5 SELF-ORGANIZATION MECHANISM .....	130
3.5.1 <i>Crystal steps determined heterogeneous CNT growth</i> .....	130
3.5.2 <i>Nano-cantilever model</i> .....	138
3.6 CONCLUSION .....	145

## CHAPTER IV

GAS PHASE CHEMICAL REACTION KINETICS IN CVD REACTOR.....	147
4.1 INTRODUCTION.....	147
4.2 CVD PROCESS ANALYSIS .....	148
4.2.1 <i>CVD reactor geometry</i> .....	148
4.2.2 <i>Chemistry and kinetics of chemical reactions</i> .....	149
4.2.2.1 Decomposition of xylene .....	150
4.2.2.2 Pyrolysis of acetylene .....	151

4.2.2.3 Decomposition of ferrocene .....	152
4.2.3 <i>Thermodynamics and transport properties</i> .....	153
4.2.3.1 Fluid thermodynamic properties.....	153
4.2.3.2 Transport properties.....	154
4.2.3.2.1 <i>Dynamic viscosity</i> .....	154
4.2.3.2.2 <i>Mass diffusivity</i> .....	155
4.2.3.2.3 <i>Thermal conductivity</i> .....	157
4.3 MODELING OF GAS PHASE REACTION KINETICS .....	157
4.3.1 <i>Governing equations</i> .....	157
4.3.2 <i>Isothermal reaction kinetics</i> .....	159
4.3.3 <i>Reaction kinetics in the CVD reactor</i> .....	161
4.3.3.1 Non-uniform mass transport.....	161
4.3.3.2 Chemical species concentration fields.....	162
4.3.3.2.1 <i>Comparisons between experimental measurement and simulation</i> .....	162
4.3.3.2.2 <i>Xylene as carbon source</i> .....	163
4.3.3.2.3 <i>Xylene and acetylene as carbon sources</i> .....	166
4.3.3.3 Effective Iron and carbon species distribution .....	167
4.3.3.4 <i>Two end injections of the ferrocene-xylene solution</i> .....	172
4.4 CONCLUSION .....	175
<b>GENERAL CONCLUSION AND PERSPECTIVES</b> .....	177
<b>APPENDICES</b> .....	181
<b>REFERENCES</b> .....	185

# Acronyms and Symbols

## Acronyms

AFM	Atomic Force Microscope
CNTs	Carbon Nanotubes
CVD	Chemical Vapor Deposition
DSC	Differential Scanning Calorimetry
FET	Field-Effect Transistors
HRTEM	High Resolution Transmission Electron Microscope
LIBs	Lithium-Ion Batteries
LJ	Lennard-Jones (12-6) potential
MWCNTs	Multi-walled Carbon Nanotubes
SEM	Scanning Electron Microscope
SWCNTs	Single-walled Carbon Nanotubes
TC	Thermal conductivity
TEM	Transmission Electron Microscope
XRD	X-ray diffraction
VdW	Van der Waals

## Symbols

$c_i$	species $i$ concentration
$C_p$	specific heat
$D_{AB}$	binary diffusion coefficient
$D_i$	diffusion coefficient
$Ea$	activation energy
$f_{H2}$	hydrogen ratio
$H$	enthalpy of reaction
$h$	molar enthalpy
$I_D / I_G$	Raman spectrum intensity ratio between D and G band of CNT

---

$K$	chemical reaction equilibrium constant
$k$	chemical reaction rate constant
$L_{CNT}$	CNT length
$L/D$	aspect ratio of carbon nanotube
$M$	molecular weight
$n$	the exponent for temperature dependence of A
$Q$	heat source term
$p$	pressure
$Re$	Reynolds number
$R_g$	gas constant, $8.314 \text{ J mol}^{-1} \text{ K}^{-1}$
$r$	reaction rate
$S$	entropy of reaction
$s$	molar entropy
$\mathbf{u}$	velocity vector, $\mathbf{u}=(u, v)$
$\mu Al_2O_3$	micrometer alumina spherical particles
$wt\%$	weight fraction
$T$	temperautre
$T_g$	glass transition temperature
$t$	time
$\alpha$	thermal diffusivity
$\varepsilon$	maximum depth of the potential well
$\eta$	dynamic viscosity
$\theta$	angle
$\kappa$	thermal conductivity
$\mu$	species dipole moment
$v_{ij}$	stoichiometric coefficients (negative for reactants and positive for products)
$\rho$	density
$\sigma$	characteristic length

# General introduction

As one brilliant star in nanotechnology, carbon nanotubes (CNTs) have attracted worldwide attention in last decades. They have many potential applications in a wide range of fields such as aerospace, energy storage, biotechnology and electronics. This is mainly due to their extraordinary mechanical properties ( $\sim 100$  times stronger than steel at one-sixth the weight), thermal conductivity ( $\sim 8$  times higher than that of copper), and electrical properties (comparable to that of copper). The remarkable properties along with their quasi-1D tubular structures, the large aspect ratios and the low density, make CNTs promising candidates for multifunctional reinforcement in composite materials. Especially, the composites with good thermal conductivity have huge application potentials in printed circuit boards, connectors, thermal interface materials, heat sinks and other high-performance thermal management systems. A great improvement of the thermal conductivity of the composites has been obtained compared with that of pure polymer. However, the reported properties are still far from the expectation values. This is mainly due to imperfect dispersion of CNTs in the matrix, and high thermal contact resistance between CNTs.

To overcome these barriers, functionalization or surface treatments (e.g. using surfactants, acids) of CNTs have been widely used to improve the dispersion of CNTs in the polymer composites. However, it has been commonly realized that surface modifications can degrade the CNTs intrinsic properties.

An alternative way is to produce multi-scale hybrid materials by combining CNTs and micrometer materials. The CNT dispersion could be improved by using the hybrid structures as fillers. The effective interfacial connection between CNTs and the micrometer materials generates a considerable improvement of multifunctional properties of the composites. However, the formation mechanisms of the multiform hybrid structures have not been reported.

In order to resolve the issues mentioned above, in this thesis we propose the *in situ* control of the organization of CNTs on micrometer ceramic particles during their growth by chemical vapor deposition (CVD). Due to their excellent thermal conductivity, alumina particles are chosen as micrometer substrates in order to develop the hybrid structures for thermal reinforcement in composites. We investigate furthermore the formation mechanisms of

multiform hybrid structures, and the involved chemical reaction kinetics in CVD reactor, for the purpose of large scale production of the desired structures in a controlled way.

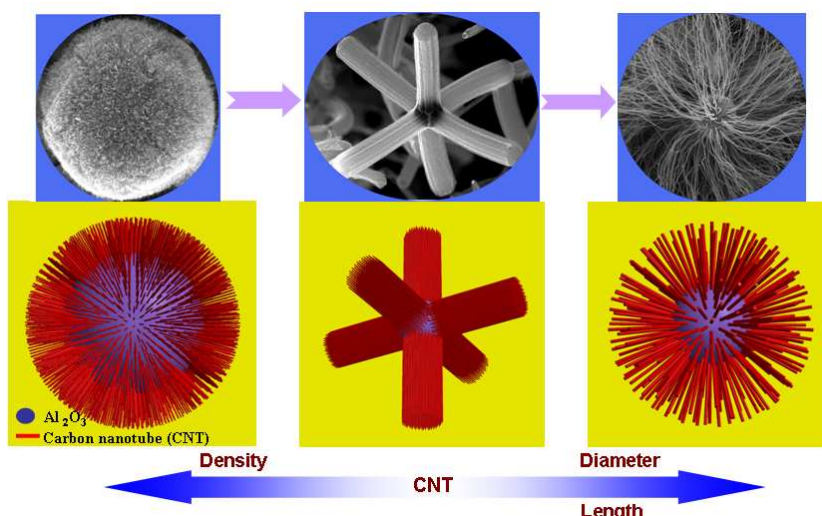
This thesis is divided into four chapters:

The first chapter reviews the state of the art of research in CNT structures, properties and applications, and CNT growth mechanisms in CVD, as well as CNT-based nano-micro hybrid structures.

The second chapter introduces three types of hybrid structures consisting of well-organized CNTs on alumina microspheres ( $\mu\text{Al}_2\text{O}_3$ ) (shown in the figure below). The excellent thermal performance of CNTs- $\mu\text{Al}_2\text{O}_3$  hybrids in epoxy matrix is then characterized.

The third chapter presents the detailed investigation on the roles played by CVD parameters and alumina microparticles in the construction of multiform hybrid structures. A particular attention is paid to the correlative effects of these parameters. The self-organization mechanism of CNTs on  $\mu\text{Al}_2\text{O}_3$  is uncovered by various characterizations including X-ray diffraction, Raman spectroscopy, scanning electron microscopy and transmission electron microscopy.

The forth chapter studies gas phase chemical reaction kinetics in CVD reactor by numerical simulation which takes into account the physical transport phenomena. The non-uniform growth of hybrid structures in the reactor is explained by the space-dependent concentration distribution of species, especially that of ferrocene.



*Three distinct nano-micrometer hybrid structures obtained by grafting CNTs on spherical alumina microparticles by chemical vapor deposition method. The arrows show the variation tendency of the hybrid structures with CNT diameter, length and number density.*

# Chapter I

## Carbon nanotubes and their hybrid materials

### 1.1 Background

Carbon is one of the elements that form the basis of lives on earth. It has the amazing ability to subtly bind with a wide range of elements to form millions of molecules with diverse and complex structures like DNA, proteins, fats, and carbohydrates, etc. These diverse organic compounds furthermore result in the wonderful biodiversity in nature. Besides, as major energy resources carbon-based fossil fuels, such as coal, natural gas and petroleum are also of great importance in modern civilization.

The properties of carbon are a direct consequence of its specific electronic structure ( $1s^22s^22p^2$ ) and multiple orbital hybridizations ( $sp^1$ ,  $sp^2$  and  $sp^3$ ). When forming a molecule, a  $sp^1$  hybridized carbon atom can form two sigma ( $\sigma$ ) bonds and two pi ( $\pi$ ) bonds, a  $sp^2$  hybridized one forms three  $\sigma$  bonds and one  $\pi$  bond, and a  $sp^3$  hybridized one forms four  $\sigma$  bonds. The number and nature of the bonds finally determine the geometry and properties of carbon allotropes.<sup>[1]</sup>

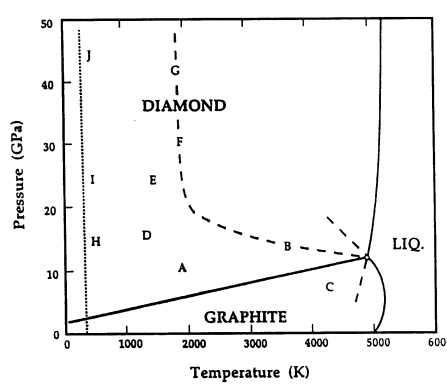


**Figure 1.** Temperature-pressure phase diagram of carbon.(for detailed information see ref. [2])

Pure carbon exists in several forms of allotropes, which are thermodynamically stable at different regions of temperature and pressure, as shown in Fig. 1<sup>[2]</sup>. Diamond and graphite are the two most commonly known ones. The former is made up of repeating units of  $sp^3$  hybridized carbon atoms bonded to four other carbon atoms (Fig. 2a). Each carbon atom is in

a rigid tetrahedral network where it is equidistant from its neighboring carbon atoms. The crystal structure of diamond is a face-centered cubic lattice. Graphite consists of parallel graphene sheets of  $sp^2$  hybridized carbon atoms (Fig. 2b). In each sheet, carbon atoms are strongly connected through  $\sigma$  and  $\pi$  bonds to three nearest neighbors to form a hexagonal network (Fig. 2c). The sheets are held together by weak Van der Waals (VdW) forces. Graphite is the most stable form of carbon under ambient conditions, while diamond is stable at higher temperatures and pressures. The graphite/diamond/liquid triple point is at about 12 GPa/5000 K. Other regions of the phase diagram show stability ranges for other types of carbon, like hexagonal diamond, hexagonal carbynes, and liquid carbon, etc.<sup>[3]</sup>

Due to their specific structures, diamond and graphite have exceedingly different properties. The large binding energy between carbon atoms ( $717 \text{ kJ mol}^{-1}$ ) in diamond results in its extremely high melting temperatures ( $\sim 5000 \text{ K}$ )<sup>[2]</sup> and unparalleled hardness—the hardest natural material known. Diamond has also a marvelous thermal conductivity (5 times that of copper at room temperature)<sup>[4]</sup> and extraordinary optical characteristics (the most popular gemstone). Unlike diamond, graphite is such a soft material that it is commonly used in drawing pencil and as dry lubricants. In addition, graphite is an electrical conductor, and is widely used, for instance, in electrodes.

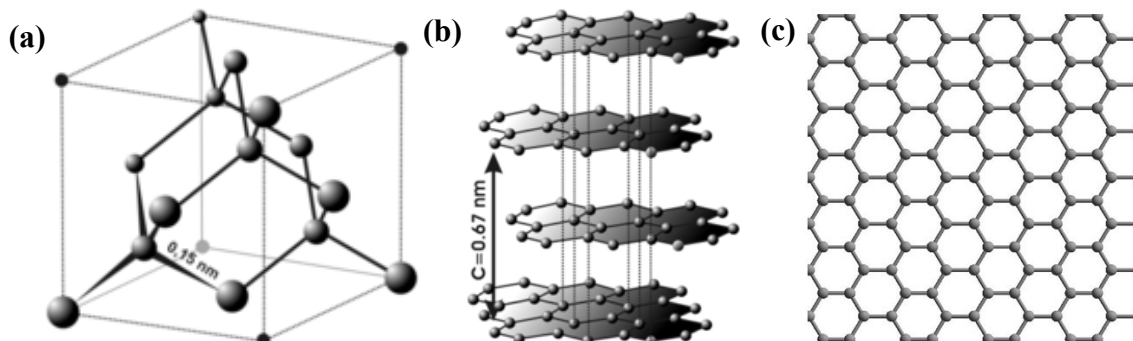


**Figure 2.** Crystal structures of diamond (a), graphite (b) and graphene (c). (from: University of Wisconsin-Madison)

Fullerenes are another kind of carbon allotropes which are closed-cage carbon molecules in the form of a hollow sphere, ellipsoid, or tube. Each atom is trigonally linked to its three near neighbors by the bonds that delineate a polyhedral network, consisting of 12 pentagons and  $n$  hexagons. (Such structures conform to Euler's theorem for polyhedrons in that  $n$  may be any number other than one including zero.) Fullerenes were named after an American architect Richard Buckminster Fuller, because the appearance of spherical fullerenes

resembles the geodesic domes he designed. The best known and most stable fullerene-buckminsterfullerene C<sub>60</sub><sup>[5]</sup>, was discovered in 1985 by R. Curl, H. Kroto and R. Smalley who were then awarded the 1996 Nobel Prize in chemistry. One C<sub>60</sub> molecule contains 60 carbon atoms which form a truncated-icosahedral structure consisting of twelve pentagonal rings and twenty hexagonal rings, like a soccer ball (Fig. 3a). The mean diameter of one C<sub>60</sub> molecule is 6.83 Å. The C<sub>60</sub> crystal has a face-centered-cubic lattice structure under ambient pressure at room temperature, in which the C<sub>60</sub> molecules are held together by weak Van der Waals forces (Fig. 3b).

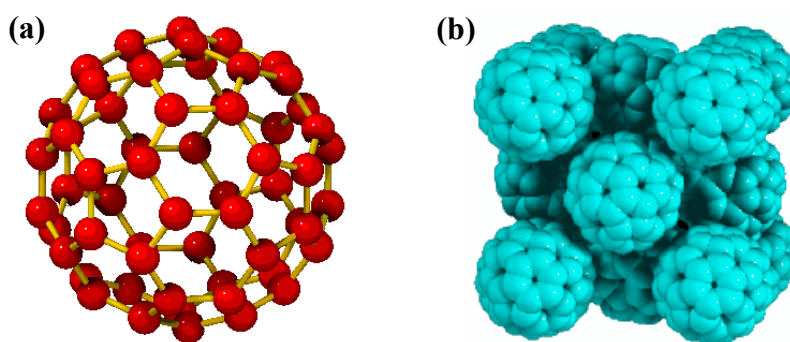


**Figure 3.** C<sub>60</sub> molecule (a) and its crystal unit cell (b). (from: Stony Brook University)

The success in synthesis of macroscopic amounts of fullerenes in 1990<sup>[6]</sup> makes it possible to extensively investigate their properties both in laboratory and in industry. Consequently, numerous novel physical and chemical properties of C<sub>60</sub> have been discovered. Moreover, a variety of fullerene derivatives have also been synthesized by attaching hydrogen or halogen atoms or organic groups in fullerene molecules. The fullerenes doped with alkali metal atoms have been reported to exhibit superconductivity at relatively high temperatures (potassium-doped at 18 K<sup>[7]</sup>, Cs<sub>2</sub>Rb-doped at 33 K<sup>[8]</sup>).

Successive discoveries of fullerene molecules and their fascinating properties stimulated the unprecedented enthusiasm in carbon material research. In 1991, Iijima observed using high resolution transmission electron microscopy (HRTEM) helical graphitic carbon nanotubules (Fig. 4a), which were produced using an arc-discharge evaporation method similar to that used for fullerene synthesis<sup>[9]</sup>. These nanotubes consist of multiple concentric graphitic sheets often capped at two ends. On each sheet, the carbon atom hexagons are arranged in a helical fashion about the tube axis. In fact, as early as 1952 Radushkevich and Lukyanovich<sup>[10, 11]</sup> had already reported tubular carbon filaments with nanosized diameter (Fig. 4b) in the *Journal of Physical chemistry of Russia*; In 1976, M. Endo from Japan<sup>[12]</sup>, collaborating with A. Oberlin in France, reported also the observation of carbon nanotubes (CNTs) by electron microscopy (Fig. 4c).

However, due to the limitations from experimental equipments, fundamental theory, international research context, language, etc.<sup>[11]</sup>, these latter reports did not generate such tremendous impact as did by the one of Iijima who first characterized in detail the helical structure of nanotubes.

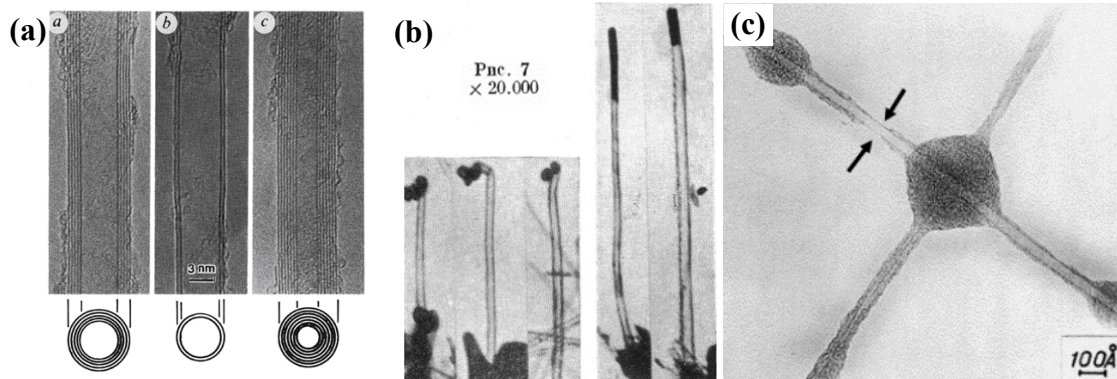


**Figure 4.** TEM observations of carbon nanotubes reported by Iijima in 1991[9] (a), Radushkevich in 1952[10] (b), and Endo in 1976[12] (c).

In 1993, single-walled carbon nanotubes (SWCNTs) were first independently reported by Iijima et al.<sup>[13]</sup>, from NEC, and Bethune et al.<sup>[14]</sup> from IBM in California. Significantly different from multi-walled carbon nanotubes (MWCNTs), SWCNTs are composed of only one graphite sheet, as shown in Fig. 5. In the following two decades, due to their unique structures and extraordinary properties CNTs have greatly attracted worldwide attention.

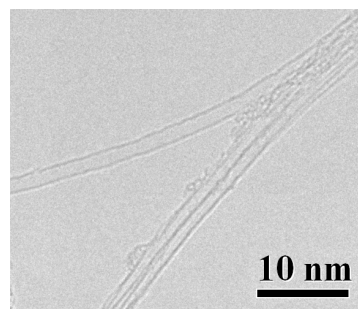


**Figure 5.** High resolution TEM image of a SWCNT produced by arc discharge.

## 1.2 Carbon nanotube structures and properties

### 1.2.1 Structures

In general, CNT is categorized into two classes according to the number of graphene layers in one nanotube: SWCNT and MWCNT.

A SWCNT could be seen as a rolled-up cylinder of a graphene<sup>[15]</sup> sheet. It has a diameter typically on the order of 1-1.4 nm and a length from micrometers to centimeters<sup>[16]</sup>. In contrast, a MWCNT consists of multiple concentric cylinders of rolled-up graphene sheets. The interlayer spacing is ~3.4 Å, close to that of graphite, i.e. 3.35 Å. MWCNTs have varying diameters (from several to hundred nanometers) and lengths (a few micrometers to several centimeters), depending on the production technique used. Because of their quasi-1D structures, CNTs have ultra high aspect ratio (length to diameter), up to 28,000,000:1<sup>[16]</sup>.

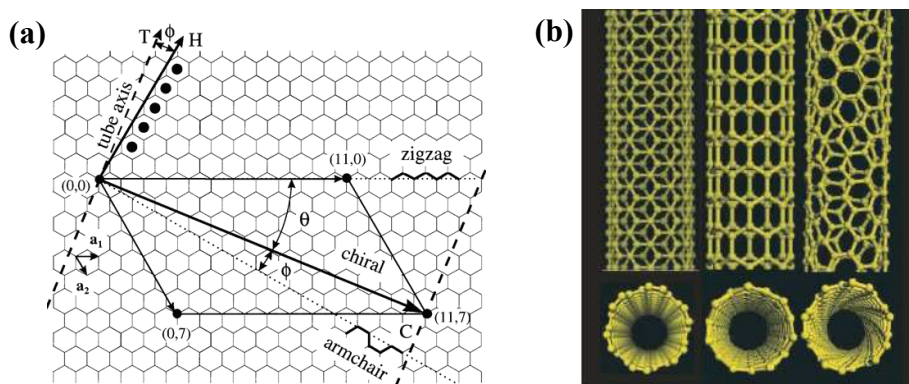


**Figure 6.** (a) 2D graphene sheet with vectors<sup>[17]</sup>, and (b) three chiralities of carbon nanotube: “armchair”, “zigzag” and “chiral” (from left to right).<sup>[18]</sup>

As shown in Fig. 6a, a CNT could be constructed by wrapping up a single graphene sheet such that two equivalent sites of the hexagonal lattice coincide. The vector  $\mathbf{C}$ , called chiral vector, is defined by a pair of integers ( $n, m$ ) and two basis vectors  $\mathbf{a}_1$  and  $\mathbf{a}_2$  of the honeycomb lattice,  $\mathbf{C}=n\mathbf{a}_1+m\mathbf{a}_2$ . The length ( $L_C$ ) of the chiral vector  $\mathbf{C}$  is directly related to the tube diameter  $d$ ,

$$d = \frac{L_C}{\pi} = \frac{\sqrt{n^2 + m^2 + nm}}{\pi} a,$$

where  $a$  is the length of unit vector, 2.46 Å. The chiral angle is defined either with respect to the zigzag axis ( $\theta$ ) or to the armchair axis ( $\varphi=30-\theta$ ), by

$$\tan \theta = \frac{\sqrt{3}m}{2n+m}, (0 \leq |\theta| \leq 30^\circ).$$

The tube axis is indicated by the vector  $\mathbf{T}$  normal to  $\mathbf{C}$ . Therefore, the integers  $(n, m)$  uniquely determine the tube diameter and the chiral angle. A ‘zigzag’ tube is formed when  $m=0$  ( $\theta=0^\circ$ ), and an ‘armchair’ one when  $n=m$  ( $\theta=30^\circ$ ). The other types of tubes are ‘chiral’, that is, when  $0 < \theta < 30^\circ$ . Thus, we can see that there are infinite possibilities in the type of carbon nanotube structures. This feature makes it possible to produce appropriate carbon nanotubes according to the need of applications.

SWCNTs are commonly observed in the form of ‘ropes’ held together by VdW forces<sup>[19, 20]</sup>. As shown in Fig. 7, individual SWCNTs packed into a close-packed triangular lattice with a constant of  $\sim 17$  Å. The binding energy between adjacent tubes is approximately 0.5 eV per nanometer of contact length. In addition, the density, lattice parameter, and interlayer spacing of one rope are very weakly dependent on the chirality of the tubes in the mat<sup>[21]</sup>. As a good estimate, the lattice parameter in CNT ropes (bundled nanotubes) is  $d + 0.34$  nm, where  $d$  is the tube diameter given above. First-principles calculations by Delaney et al.<sup>[20]</sup> showed that a broken symmetry of the (10, 10) tube caused by interactions between tubes in a rope induces a pseudo gap of about 0.1 eV at the Fermi level. This pseudo gap strongly modifies many of the fundamental electronic properties. They predicted a semimetal-like temperature dependence of the electrical conductivity and a finite gap in infrared absorption spectrum.

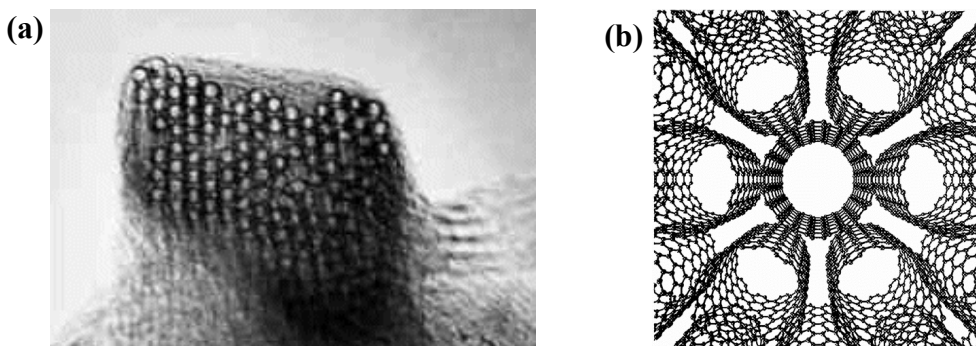


**Figure 7.** (a) Crystalline ropes of metallic CNTs made of about 100 SWCNTs of uniform diameter<sup>[19]</sup>; (b) perspective view of a rope of (10,10) carbon nanotubes<sup>[20]</sup>.

### 1.2.2 Properties

It is well known that material properties directly depend on its structure. The unique tubular nanostructure endows CNTs plenty of remarkable mechanical, electronic, thermal

properties.

### 1.2.2.1 Mechanical properties

Because of the strong  $sp^2$  bonds between carbon atoms and the perfect tubular structure, carbon nanotubes are expected to have extraordinary mechanical properties including high strength, high stiffness and high flexibility.<sup>[22-24]</sup>

Exceptionally high Young's modulus and strength have been measured for both individual SWCNT and MWCNT using different methods. In the calculations, CNT is normally seen as a structural element such as beam and shell models. By measuring the amplitude of the intrinsic vibration of an individual CNT in transmission electron microscope, the evaluated Young's modulus for an isolated MWCNT and SWCNT were 1.8<sup>[25]</sup> and ~1.25 TPa<sup>[26]</sup>, respectively. Wong et al.<sup>[27]</sup> measured MWCNT mechanical properties using atomic force microscopy (AFM) by treating the nanotube as a “cantilever nanobeam”, as demonstrated in Fig. 8a. MWCNTs were pinned at one end to molybdenum disulfide ( $MoS_2$ ) surface. The bending force was measured versus displacement along the unpinned lengths. The evaluated Young's modulus and bending strength were ~1.26 TPa and 14.2 GPa, respectively. Yu et al. performed direct tensile loading tests of SWCNT ropes and MWCNTs in a “nanostressing stage” operated inside a LEO 1530 scanning electron microscope, as shown in Fig. 8b. The Young's modulus obtained ranges from 320 to 1470 GPa (mean 1002 GPa) for SWCNT<sup>[28]</sup> and from 270 to 950 GPa for MWCNT<sup>[29]</sup>.

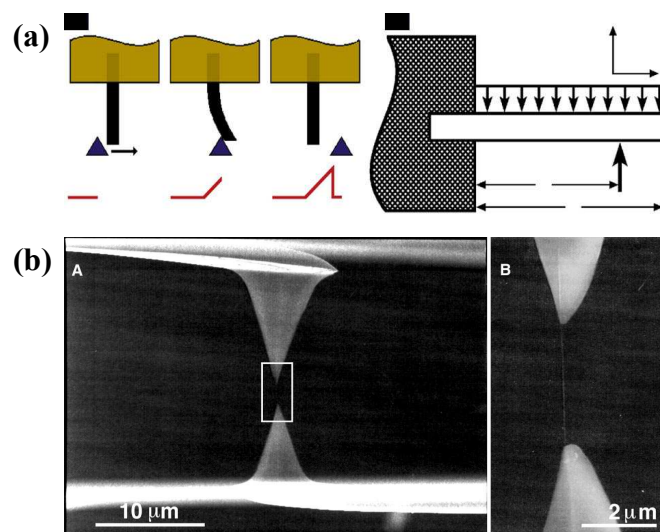


**Figure 8.** (a) Cantilever nanobeam model: Nanomeasurement of CNT mechanical properties by bending a CNT with an AFM tip by Wong et al.<sup>[27]</sup>. (b) Tensile loading test of individual MWCNT<sup>[29]</sup>.

Theoretical evaluation of the Young's modulus could be obtained either by directly computing the mechanical response or by deriving analytically<sup>[30]</sup>. The Young's modulus can be written as the second derivative of the strain energy divided by equilibrium volume. Continuum elastic theory predicts a  $1/R^2$  variation of the strain energy, with an elastic constant equal to  $C_{11}$  of graphite (which corresponds to the Young's modulus parallel to the basal plane), independent of the tube diameter<sup>[24, 31]</sup>. Therefore, in the classical approximation, the Young's modulus of CNT is not expected to vary when wrapping a graphene sheet into a cylinder<sup>[24]</sup>.

The elastic properties of CNTs were investigated by Lu et al.<sup>[32]</sup> using an empirical force-constant model. It was found that for SWCNTs and MWCNTs the elastic moduli were insensitive to structural details such as helicity, radius, and number of walls. The Young's modulus (~1 TPa) and shear modulus (~0.5 TPa) calculated were comparable to that of diamond. Yu et al.<sup>[28]</sup> reported the tensile strength values ranging from 13 to 52 GPa and a maximum tensile strain of 5.3 % for SWCNT bundles measured by tensile load experiment. The results are close to the prediction made by Nardelli et al.<sup>[33]</sup> using molecular dynamics simulation. Tensile testing of MWCNTs<sup>[29]</sup> showed that only the outmost layer breaks during the loading process and the corresponding tensile strength ranges from 11 to 60 GPa.

In summary, despite of the divergence of the values reported in the literature, individual CNT (SWCNT and MWCNT) ultimately exhibit admirable mechanical properties. Table 1 shows a comparison of the properties of SWCNTs and MWCNTs with these of stainless steel and Kevlar (a very strong a para-aramid synthetic fiber). Obviously, CNTs are the strongest and stiffest material in terms of tensile strength and elastic modulus, respectively.

**Table 1.** Comparison of mechanical properties

Material	Young's Modulus (TPa)	Tensile strength (GPa)	Elongation at break (%)	Density of solid (g cm <sup>-3</sup> )
SWCNT	~1	13–53	16	~1.3–1.4 <sup>[21]</sup>
MWCNT	0.8–0.9	11–150		
Stainless Steel	~0.2	~0.65–3	15–50	~7.8
Kevlar	~0.15	~3.5	~2	~1.44

### 1.2.2.2 Thermal properties

The specific heat and thermal conductivity of CNTs are determined primarily by phonons, because the electronic density of states is so low that the thermal transport via "free" electrons is negligible at all temperatures<sup>[34]</sup>. The measurements yielded linear specific heat and thermal conductivity above 1 K and below room temperature while a T<sup>0.62</sup> behavior of the specific heat below 1 K.<sup>[35]</sup>

Because of their small quasi-1D geometry and strong  $sp^2$  bond structure, CNTs are very good thermal conductors along the tube axis, exhibiting a property known as "ballistic conduction". Molecular dynamics simulations<sup>[36, 37]</sup> predicted an unusually high thermal conductivity (TC) value  $\sim$ 3000-6600 W m<sup>-1</sup> K<sup>-1</sup> for an isolated nanotube at room temperature. Those values are comparable to the TC of a hypothetical isolated graphene monolayer or diamond. Direct measurements on individual CNTs showed that the room temperature TC of a MWCNT is more than 3000 W m<sup>-1</sup>K<sup>-1</sup><sup>[38]</sup>, and the one of a metallic SWCNT is about 3500 W m<sup>-1</sup> K<sup>-1</sup><sup>[39]</sup>. These values are  $\sim$  8 times higher than the TC of copper, 385 W m<sup>-1</sup> K<sup>-1</sup>, which is an excellent thermal conductor. However, for CNT bulk mat consisting of aligned CNT array prepared by CVD, the measured thermal conductivity was only  $\sim$ 20 W m<sup>-1</sup> K<sup>-1</sup><sup>[40]</sup>, suggesting that thermally opaque junctions between tubes severely limit large-scale diffusion of phonons.

### 1.2.2.3 Electronic properties

The electronic properties of CNTs are predominately determined by intralayer interaction, rather than by interlayer interactions between multilayers within a single carbon nanotube or between two different nanotubes<sup>[41]</sup>. Depending on chirality, SWCNTs can behave as metals or semiconductors, even if they have early identical diameters. Nanotubes with  $n = m$  (armchair nanotubes) are always metallic. If  $n - m$  is a multiple of 3, then the nanotube is semiconducting with a very small band gap ( $\sim$  10 meV), otherwise the nanotube is a moderate semiconductor with band gaps ( $\sim$  0.5 eV for typical diameter of 1.5 nm). For the same-chirality semiconducting nanotubes, the band gap is inversely proportional to the diameter,

$$E_{gap} = 2\gamma_0 a_{c-c}/d$$

where  $\gamma_0$  is the C-C tight-binding overlap energy,  $a_{c-c}$  is the nearest neighbor C-C distance (0.142 nm) and  $d$  is the tube diameter.<sup>[17]</sup>

Four probe measurements on individual MWCNTs showed a range of electronic behavior

(metallic, semiconducting and semimetallic) [42, 43]. Although MWCNT is composed of several cylinders of different helicity, the conduction property of MWCNT is unique. And ballistic electron transport at room temperature [44] and the Aharnov-Bohm effect [45] were observed. Electron transport measurements on individual SWCNTs [46] showed that the electrical conduction occurs through well separated and discrete electron states that are quantum-mechanically coherent over distance of at least 140 nm. The measurement results proved that SWCNTs indeed act as quantum wires. Calculations by White et al. [47] showed that, unlike normal metallic wires, conduction electrons in armchair nanotubes experience an effective disorder averaged over the tube's circumference, leading to electron mean free paths that increase with nanotube diameter. This increase should result in exceptional ballistic transport properties.

Thess et al. [19] measured the resistivity of the ropes of metallic SWCNTs to be in the order of  $10^{-4} \Omega \text{ cm}$  at 300 K using four-point probe technique. They noted that the ropes were the most highly conductive carbon fibers known. In addition, SWCNTs have a carrier mobility of  $\sim 10,000 \text{ cm}^2 \text{ V}^{-1} \text{ s}^{-1}$ , which is better than that of silicon, and they can carry an electrical current density of  $\sim 4 \times 10^9 \text{ A cm}^{-2}$ , which is three orders of magnitude higher than a typical metal, such as copper or aluminum [48].

### 1.2.3 Potential and current applications

The integrity of perfect structure, unique geometry and amounts of exceptional properties undoubtedly makes CNTs of great significance in nanotechnology. Since the first detailed characterization of CNT structure using HRTEM by Iijima in 1991 [9], many potential applications in a wide range of fields have been proposed for CNTs. These applications include the use of CNTs as conductive and high-strength composites, energy storage and energy conversion devices, sensors, field emission displays and radiation sources, hydrogen storage media, nanometer-sized semiconductor devices, probes, interconnects and bio-engineering. [18] Thanks to world widely collaborative efforts in past two decades, huge progress has been made in CNT applications. And several applications have been commercialized such as CNT application in polymers and in lithium-ion batteries (LIBs) [49]. In particular, the significant advance in CNT synthesis techniques promotes to do various property and application studies with pure high quality CNTs. Here, we will briefly introduce three major applications of CNTs in the fields of composites, energy storage and electronic devices.

### 1.2.3.1 Carbon nanotube composites

The quasi-1d tubular structures together with the large aspect ratios, low density and various remarkable properties make CNTs promising candidates for reinforcement in composite materials. Since the first report on CNT/epoxy composites in 1994,<sup>[50]</sup> many kinds of CNTs/polymer composites have been studied by employing different kinds of polymer as matrix, such as epoxy, poly (methyl methacrylate) (PMMA), polyvinyl alcohol (PVA), polyvinyl chloride (PVC), polypropylene (PP), polyethylene (PE), polyamide 12 (PA12) and polystyrene (PS)<sup>[51]</sup>.

In general, Young's modulus and tensile strength of CNT/polymer composites are found to increase with nanotube loading, dispersion and alignment in matrix<sup>[52-54]</sup>. Dalton et al.<sup>[55]</sup> fabricated the super-tough composite fibers (of 5 µm in diameter and ~100 m in length) consisting of 60 wt % SWCNTs and PVA by optimizing the coagulation-based carbon nanotube spinning method<sup>[56]</sup>. The fibers had a tensile strength of 1.8 GPa, which matches that of spider silk. Their toughness is higher than any natural or synthetic organic fibre discovered so far, such as spider dragline silk, Kevlar and graphite fiber. In addition, they used these fibers to make supercapacitors of 10 µm in diameter and woven them into textiles. This fibre supercapacitor provided a capacitance (5 F g<sup>-1</sup>) and energy storage density (0.6 W h kg<sup>-1</sup> at 1 V) that are comparable to those of large commercial supercapacitors. Miaudet et al.<sup>[57]</sup> reported that the super-tough fibers made from SWCNTs and PVA by a wet-spinning method could absorb 870 J g<sup>-1</sup> with a strain-to-failure up to 430 %, and those spun out of MWCNTs and PVA have a toughness of 690 J g<sup>-1</sup> and a strain-to-failure ratio up to 340 %. Furthermore, they demonstrated that hot-drawing treatment could greatly improve the energy absorption of the fibers at low strain and make them resistant to moisture, due to the improvement of the nanotube alignment and of the crystallinity of the PVA. Based on their excellent properties, the CNT/polymer composites could be used in many fields, including actuators, microelectrodes, electronic textiles, aerospace, sports and automotive.

The application of CNTs as electrically conducting components in multifunctional polymer composites has been successfully realized and commercialized<sup>[18]</sup>. Several orders of magnitude enhancement in electrical conductivity has been achieved with just a very small loading (0.1 wt % or less<sup>[58]</sup>) of nanotubes, while maintaining the other performance aspects of the polymers such as optical clarity, mechanical properties, low flow viscosities, etc.<sup>[52]</sup> These conductive composites have a variety of applications such as electrostatic dissipation, electrostatic painting, electromagnetic interference shielding, printable circuit wiring, and

transparent conductive coating.

Nanocomposites with good thermal conductivity have huge application potentials in printed circuit boards, connectors, thermal interface materials, heat sinks and other high-performance thermal management systems<sup>[52]</sup>. The outstanding thermal conductivity of individual CNT makes it excellent filler in polymer composites. The great improvement of the composite thermal conductivity has been obtained compared with that of pure polymer<sup>[59-61]</sup>. However, the results reported are still far below the prediction value evaluated from the intrinsic thermal conductivity of nanotubes and their volume fraction. This is mainly attributed to the high interfacial thermal resistance both between two CNTs and between CNTs and matrices<sup>[62]</sup>.

### 1.2.3.2 Energy storage

CNTs are desirable alternative electrode materials because of their excellent electrical properties, good electrochemical stability and highly accessible surface area. Thus, CNTs have been used as electrodes in supercapacitors, actuators, Li-ion batteries, solar and fuel cells<sup>[49]</sup>.

Supercapacitors with CNTs have a high capacitance (180 and 102 F g<sup>-1</sup> for SWCNT and MWCNT electrodes, respectively), high power densities (20 kW kg<sup>-1</sup> at energy densities of ~7 W h kg<sup>-1</sup> for MWCNT electrodes) and extraordinarily short discharge time (7 ms for 10 MWCNT capacitors connected in series which operated at up to 10 V)<sup>[18, 63]</sup>. These supercapacitors could be used for applications that require much higher power capacities than batteries, and much higher storage capacities than ordinary capacitors.

Electromechanical actuators based on sheets of SWCNTs were shown to generate higher stress than natural muscle, and higher strain than high-modulus ferroelectrics<sup>[64]</sup>. The actuators function at low voltages of a few volts, compared with ~100 V used for piezoelectric stacks and more than 1000 V used for electrostrictive actuators.

CNTs also have great potential as the electrodes in lithium-ion batteries because of their reversible capacity up to 1000 mA h g<sup>-1</sup>. CNT reinforced anode materials have been commercialized in LIBs<sup>[65]</sup>. Homogeneously dispersed CNTs in synthetic graphite (~ 3 wt. %) give rise to continuous conductive network as well as mechanically strong electrode, resulting in doubled energy efficiency of LIBs. Furthermore, nitrogen-doped CNTs have also shown efficient reversible energy storage in LIBs (480 mA h g<sup>-1</sup>), higher compared to commercial carbon materials used for LIBs (330 mA h g<sup>-1</sup>). In addition, vertically aligned nitrogen-doped CNTs can act as a metal-free electrode with much better electrocatalytic activity, long-term operation stability, and tolerance to crossover effect than platinum for oxygen reduction in

alkaline fuel cells<sup>[66]</sup>.

CNTs are also promising fillers for the development of lightweight, flexible polymeric solar cells<sup>[67]</sup>. Their high aspect ratio allows the formation of a percolating network of nanotubes at low doping levels in polymer composites.

Finally, super CNT springs<sup>[68]</sup> could ultimately have an energy density - a measure of the amount of energy that can be stored in a given weight of material - more than 1,000 times that of steel springs, and comparable to that of the best LIBs. The foam-like films of vertically aligned CNTs<sup>[69]</sup> exhibit much higher compressive strength, recovery rate, and sag factor, and the open-cell nature of nanotube arrays gives excellent breathability. These films may be useful as compliant and energy-absorbing coatings.

### 1.2.3.3 *Electronic devices*

Remarkable properties of CNTs make them promising electronic materials which could be used in field-effect transistors (FET) and interconnects<sup>[49]</sup>. In 1998, the Delft group built the first room temperature single-SWCNT field-effect transistor by connecting a single semiconducting nanotube to two metal electrodes<sup>[70]</sup>. They demonstrated that semiconducting SWCNTs have a channel conductance that can be modified by orders of magnitude ( $\sim 10^5$ ) by an externally applied gate voltage, very similar to that of MOSFET. Further reduction of FET size has to be realized by constructing entire electronic circuits from interconnected nanotubes. Such heterojunction devices have been demonstrated by grafting a metallic nanotube to a semiconducting one<sup>[18]</sup>. In addition, the synthesis of multiply branched and interconnected low effect nanotubes with targeted helicity would be one revolutionary advance for nanoelectronics<sup>[18]</sup>.

Metallic nanotubes could be one of ideal interconnects in nanoelectronic circuits<sup>[49]</sup>. CNTs can withstand high current densities up to  $10^{10} \text{ A cm}^{-2}$ , more than 1000 times of that of copper. Thus, a bundle of closely packed parallel metallic CNTs, or a large defect-free MWCNT is proposed to be used for the next generation of interconnects.

Carbon nanotubes possess the following properties favorable for field emitters: (1) high aspect ratio, (2) small radius of curvature at their tips, (3) high chemical stability and (4) high mechanical strength<sup>[72]</sup>. Electron field emission from an isolated MWCNT<sup>[73]</sup> and from a MWCNT<sup>[74]</sup> film was first demonstrated in 1995. Nanotubes provide stable emission, long lifetimes, and low emission threshold potentials<sup>[72]</sup>. These characteristics make them useful in the fabrication of flat panel displays. Samsung released of a 4.5 inch diode type flat panel display in 1999<sup>[71]</sup>, as shown in Fig. 9b. After that, the display prototypes of larger sizes have

been gradually demonstrated, including a 9 inch (23 cm) red-blue-green color display that can produce moving images. In 2008, they demonstrated the world's first CNT-based active matrix electrophoretic display e-paper.

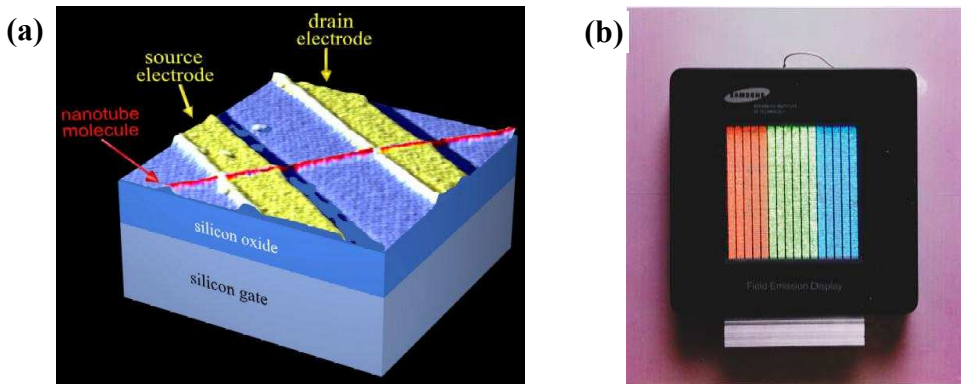


**Figure 9.** (a) Diagram of a carbon nanotube transistor: a SWCNT (red; about 1 nanometer in diameter) bridges two closely separated platinum electrodes (labeled in yellow as "source" and "drain" electrodes; spaced 400 nm apart) atop a silicon surface coated with an insulating silicon oxide layer.(from: Delft Institute of Technology) (b) Samsung 4.5 inch SWCNT flat panel display at color mode with red, green, and blue phosphor columns<sup>[71]</sup>.

### 1.3 Chemical vapor deposition synthesis of CNTs

#### 1.3.1 Introduction to CNT synthesis

In general, three components are required for CNT synthesis: carbon source, heat source and catalyst precursor. During the last two decades, a variety of techniques have been explored to produce CNTs, including electric arc discharge<sup>[9, 13, 75-77]</sup>, laser ablation<sup>[19]</sup>, chemical vapor deposition (CVD)<sup>[78-80]</sup>, ball milling<sup>[81]</sup>, diffusion flame<sup>[82-84]</sup>, electrolysis<sup>[85-88]</sup>, use of solar energy<sup>[89]</sup>, heat treatment of a polymer<sup>[90]</sup>, and low-temperature solid pyrolysis<sup>[91]</sup>. Among them, electric arc discharge, laser ablation and CVD are the three most widely used methods.

Arc discharge takes a significant role both in the research of fullerenes and CNTs. As we have indicated previously, CNTs were first observed in 1991 in the graphitic cathode deposits formed in electric arc discharge. The synthesis of CNTs in gram quantities using arc discharge<sup>[75]</sup> greatly promoted the advance of the research on CNT properties and applications. This method creates nanotubes through arc-vaporization of two graphite rods placed end to end, separated by approximately 1 mm, in an enclosure that is usually filled with inert gas (helium, argon) at low pressure (between 50 and 700 mbars). A potential of ~20 V is typically applied

between two electrodes, and the current is typically of 50 to 100 A. The average temperature in the interelectrode plasma regions is of the order of 4000 K<sup>[92]</sup>. Carbon atoms or small clusters from the vaporized graphite anode condense, either on the surface of the cathode or on the wall of the furnace, into nanotubes or other types of carbon, like amorphous carbon, multilayer graphite etc. In particular, transition metal (Fe, Co, Ni, Y...) or their alloys (Co-Ni, Ni-Y, Co-Fe...) catalyst powders are needed to add in the anode electrode for producing SWCNTs. Arc discharge is one of easiest ways to produce CNTs in large scales.<sup>[75, 93]</sup> In general, CNTs produced by this way have a good graphitization degree due to high synthesis temperatures. However, purification procedures have to be followed after the synthesis in order to separate CNTs from the impurities in as-produced soot.<sup>[42, 94]</sup>

Laser ablation is also a high temperature physical vaporization method, which was the first technique used to generate fullerene clusters in gas phase<sup>[5]</sup>. In this process,<sup>[19, 95]</sup> a graphite target doped with catalytic metals is placed in the middle of a quartz tube that is heated to a given temperature (~1200 °C) under inert atmosphere (He, Ar...). A laser beam (typically a YAG or CO<sub>2</sub> laser) is then introduced through a window and focused onto the target. CNTs are generated from evaporated carbon, and finally conveyed by the buffer gas to a water-cooled copper collector. One main advantage of this method is the production of high quality and high purity CNTs with controlled diameter. However, the process is expensive because it involves high purity graphite rods, high power lasers and low yield of CNTs.

As indicated above, both arc discharge and laser ablation rely on the evaporation of carbon atoms from solid graphite targets at temperatures higher than 3000 K. Furthermore, the nanotubes products are tangled together, along with impurities. These make CNTs difficult to large-scale applications.

In contrast, CVD is increasingly important for CNT applications because it allows the selective growth of CNTs on substrate at medium temperatures in a controlled way. Besides, it allows the bulk production of CNTs<sup>[96]</sup>. These characteristics of CVD are particularly important to their applications in semiconductor field. Furthermore, CVD exhibits one unparalleled advantage in one step direct construction of various CNT-based architectures with multifunctional properties.

In the following parts, we will concentrate on discussing about the CNT synthesis by CVD method, which is also the technique used in this thesis. A short review will be firstly given about the CVD principle and the effect of various parameters on CNT growth, then, CNT formation mechanism and production of CNT hybrid structures will be followed in the next two parts.

### 1.3.2 Principle of chemical vapor deposition

CVD is an important technique for surface modification and new material production. The process involves homogeneous gas phase reactions and heterogeneous chemical reactions on or near the vicinity of a heated substrate surface leading to the deposition of powders or films<sup>[97]</sup>. Typically, a CVD system consists of three main parts: vapor precursor supply system, CVD reactor and effluent gas handling system. The main function of CVD reactor is to heat substrate to the deposition temperature under desired atmosphere. There are a wide range of reactor configurations such as horizontal, vertical and barrel<sup>[97]</sup>.

Fig.10 shows the key steps involved in a CVD process. The first one is the generation (1) and transport (2) of active gaseous reactant species; Second, the gaseous reactants undergo gas phase reactions forming intermediate species (3); Third, absorption and heterogeneous reactions (4) occur at the gas-solid interface; Fourth, diffusion and crystallization result the growth of film (5); Finally, non reacted gaseous precursors and by-products (6) are exhausted out of the reactor (7). Thus, we could see that CVD is a complex process, which comprises thermodynamics, kinetics and mass transport phenomena.

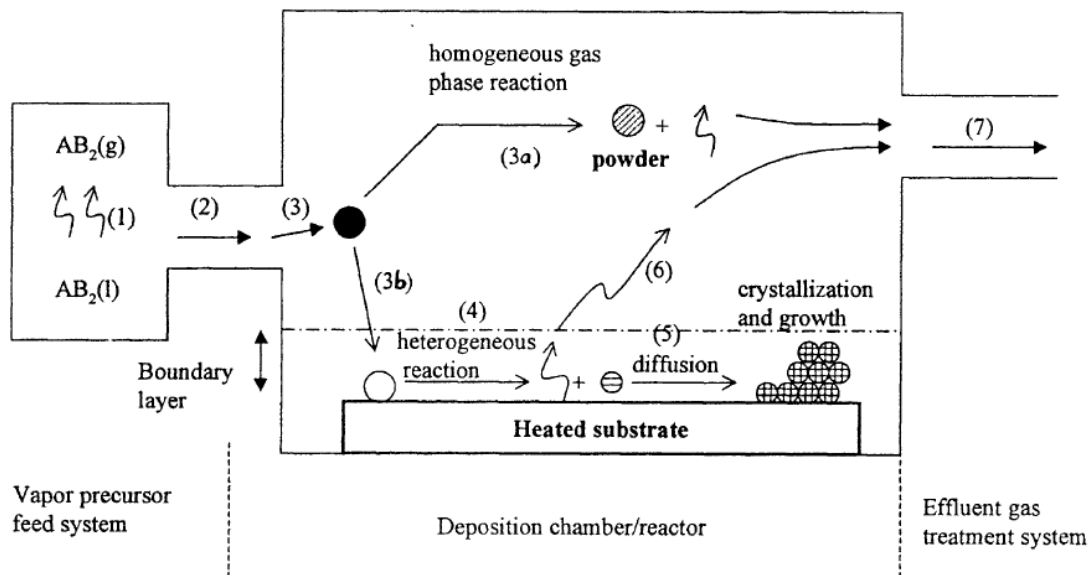


**Figure 10.** Schematic illustration of the key CVD steps during deposition<sup>[97]</sup>.

### 1.3.3 Catalytic CVD synthesis of CNTs

#### 1.3.3.1 Introduction

As early as 1959, CVD was applied to produce carbon filaments and fibers by thermal decomposition of carbon-containing gas on metal catalysts<sup>[98]</sup>. However, it was not recognized that this technique could be used to synthesize CNTs until 1993 when Jose-Yacaman et al.<sup>[99]</sup> demonstrated the success of synthesizing MWCNTs by catalytic decomposition of acetylene over iron particles at 700 °C. At the same period, Endo et al.<sup>[100]</sup> also reported pyrolytic CNTs produced by thermal decomposition of hydrocarbon vapor (benzene) at ~1100°C. It was in 1996 when Dai et al.<sup>[101]</sup> first reported the synthesis of SWCNTs by disproportionation of carbon monoxide at 1200 °C in the presence of molybdenum particles of a few nanometers in size.

The equipment used in catalytic CVD is typically a horizontal quartz tube heated by an electric furnace, as schematically shown in Fig. 11. CNTs can be produced using a wide range of metal catalysts and hydrocarbon sources.<sup>[102, 103]</sup> Carbon sources could be gas (CH<sub>4</sub>, C<sub>2</sub>H<sub>2</sub>, C<sub>2</sub>H<sub>4</sub> etc.), liquid (alcohol, benzene, toluene, xylene, etc.) or solid (camphor, naphthalene, etc.). They, together with carrier gases (Ar, N<sub>2</sub> etc.) are injected into the reactor through an injection system. The catalyst particles (Fe, Ni, Co, etc.) could be either previously deposited on the substrate or in situ produced from catalyst precursors. Then, the catalyst particles are heated to sufficiently high temperature (500-1200 °C) to decompose the carbon sources, in the presence of protection gas (H<sub>2</sub>, NH<sub>3</sub>, etc.). A variety of materials could serve as substrate for nanotube growth, including Al<sub>2</sub>O<sub>3</sub>, SiO<sub>2</sub>, SiC, MgO, Zeolite etc.

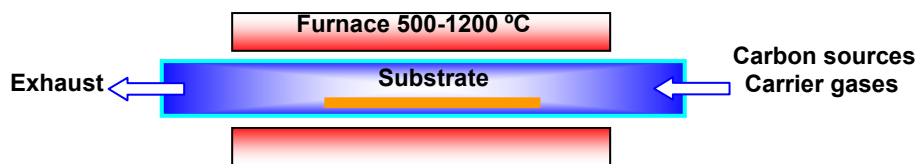


**Figure 11.** Schematic of catalytic CVD reactor.

In general, the catalytic CVD process of CNT synthesis consists in the thermal decomposition of carbon sources (hydrocarbons or other carbon-containing species) on the surface of nanosized catalyst particles supported on substrates. CNT geometry and structure could be influenced by all parameters involved in the process. In the following parts, we will briefly review the research on the influence of catalysts, carbon sources, substrates, atmospheres and temperatures on CNT growth.

### 1.3.3.2 Catalysts

As it is well known, metal catalyst particles are one of the essential components for CNT growth. The catalytic activity sensitively depends on metal nature and particle size. Experimental results<sup>[35]</sup> have demonstrated that transition metals such as iron, nickel or cobalt have sufficient catalytic activity for CNT growth. Also, the catalyst activity is size-dependent. Takagi et al.<sup>[104]</sup> demonstrated that any metal, even gold, silver, and copper, could act as catalyst for SWCNT growth when the particles are less than 3 nm in size. Ultimately, catalyst particles are directly related to CNT growth and CNT diameters.<sup>[105-107]</sup>

The chemical activity of a metal element is determined by its valence electrons. The electronic structure of a catalyst is largely responsible for its interaction with hydrocarbons<sup>[108]</sup>, which includes electronic charge transfer between catalyst and adsorbed hydrocarbon molecules(Fig.12). The change of the electronic structure of adsorbate will result in the dissociation of the adsorbate molecules. As the transition metals have non-filled 3d shells, they consequently show high catalytic activity for dissociating hydrocarbons. Furthermore, the specific electronic structure of each metal results in different catalytic activities. Iron, for example, is more efficient than nickel and cobalt to decompose hydrocarbon. In contrast, copper, a metal with its 3d shell completely filled, was observed to have less catalytic activity than iron.<sup>[109]</sup>

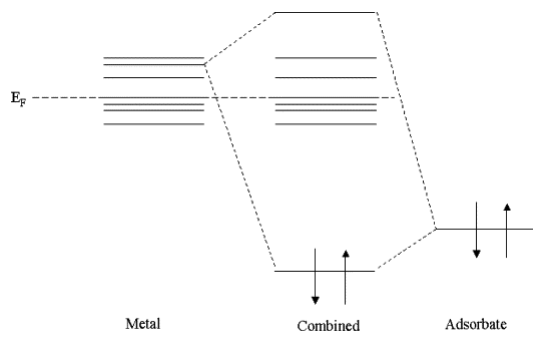


**Figure 12.** Schematic illustration of electronic interactions of metal catalyst and hydrocarbon adsorbate. A filled orbital on the adsorbate overlaps with an empty one on the metal.<sup>[108]</sup>

The catalyst activity in CNT formation is closely associated with their preparation methods and CVD conditions. Up to now, a variety of methods have been applied to prepare catalyst particles<sup>[108]</sup>. One of the key objectives is to control the size of particles. Nanometer catalysts could be previously deposited on substrate or embedded into support before the decomposition of hydrocarbons. Various techniques could be selected depending on the nature

of catalyst precursors. Catalyst particles could be formed: (1) by calcinating metal salt solutions such as acetates or nitrates<sup>[110, 111]</sup> ( $\text{Fe}(\text{NO}_3)_3 \cdot 9\text{H}_2\text{O}$ ,  $\text{Ni}(\text{NO}_3)_2 \cdot 6\text{H}_2\text{O}$ ,  $\text{Co}(\text{NO}_3)_2 \cdot 6\text{H}_2\text{O}$ ...), (2) by heating thin film metals of Fe, Co and Ni deposited by sputtering or evaporation<sup>[107, 111-113]</sup>, (3) by roughening metal surfaces<sup>[103]</sup> with various methods (such as mechanical roughening, electrochemical etching, plasma etching, ion bombardment, oxidization, rusting, etc.), (4) by using colloidal metal or oxide particle<sup>[106]</sup>, or (5) by using aerogel supported metal catalysts<sup>[114, 115]</sup>. Alternatively, catalyst nanoparticles could also be formed by floating catalyst method<sup>[103]</sup>, that is, by in situ thermally decomposing organometallic compounds (ferrocene<sup>[116-119]</sup>, cobaltocene<sup>[120]</sup>, nickelocene<sup>[121]</sup>), Iron(II) phthalocyanine ( $\text{C}_{32}\text{H}_{16}\text{FeN}_8$ )<sup>[122]</sup>, or metal carbonyl complexes (iron pentacarbonyl)<sup>[123]</sup> during the pyrolysis of carbon source. This method permits to easily introduce catalyst precursors into CVD reactors in the form of vapor by carrier gas. In parallel, ferrocene could also be first dissolved into a carbon source solution and then injected into the reactor. Owing to high CNT productivity, the floating catalytic CVD is commonly used for continuous bulk/mass production of nanotubes/nanofibers by CVD<sup>[103]</sup> (this technique will be discussed in details in the latter parts).

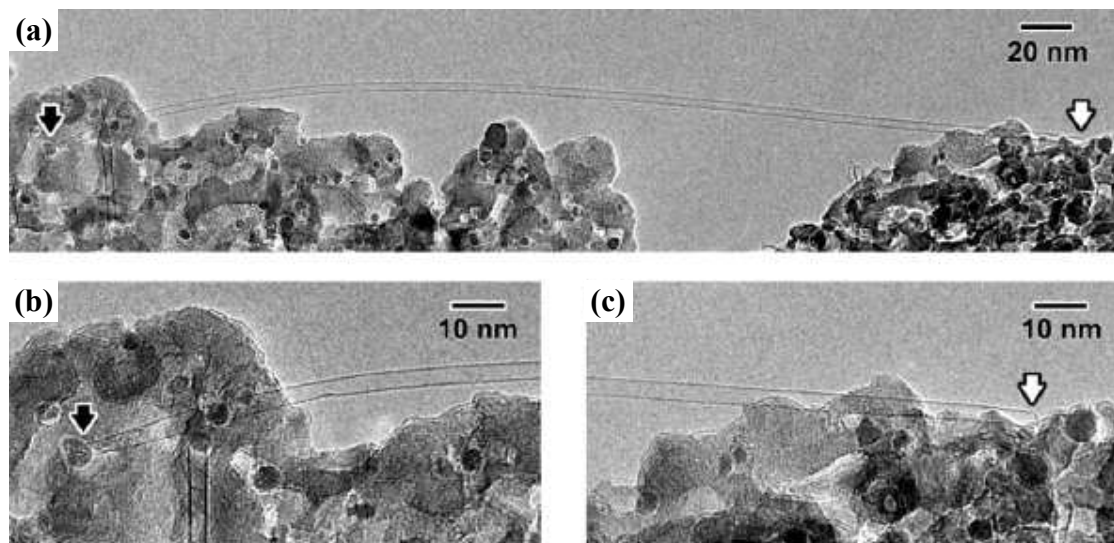


**Figure 13.** (a) a long MWCNT with both ends imaged by TEM. (b) and (c) are magnified images showing the ends (solid and hollow arrows) of the SWNT.<sup>[127]</sup>

The activity of metal catalysts in CNT synthesis shows a “size-effect”. It has been demonstrated that the diameter of CNTs is associated with that of catalyst nanoparticles, and an increases with particle size.<sup>[101, 106, 109, 124-129]</sup> Fig. 13 shows a TEM image obtained by Zhang et al.<sup>[127]</sup> Isolated SWCNTs were grown on discrete catalytic nanoparticles with diameters in the range of 1–3 nm by CVD. It can be clearly seen that the diameters of the SWCNTs are strongly

correlated to the size of the nanoparticles to which the nanotubes are connected. In general, SWCNTs grow from small metal nanoparticles ( $\leq \sim 5$  nm); while MWCNTs are formed from larger catalyst particles.<sup>[106, 125, 127]</sup> The particles with too large sizes are normally inactive to catalyze the growth of nanotubes<sup>[101]</sup>.

Besides particle size, catalyst stability and carbon solubility could also affect CNT growth. It was found that the addition of molybdenum in transition metals (iron, cobalt and nickel) promoted the formation of CNTs<sup>[130, 131]</sup> by stabilizing the catalyst. Furthermore, metal carbides, e.g. iron carbide ( $Fe_3C$ ), have been detected in iron nanoparticles during CNT growth processes, and it was therefore proposed that  $Fe_3C$  might be an intermediate in the growth process<sup>[132, 133]</sup>. This indicates that carbon solubility in metal catalyst particles might play a significant role in CNT growth. However, other experiments showed that the catalytic activity of pure  $Fe_3C$  for the decomposition of acetylene is negligible.<sup>[134]</sup> Moreover, Herreyre et al<sup>[135]</sup> reported that the formation of  $Fe_3C$  in catalyst particles was correlated to the decrease of reaction rates and the poisoning of catalysts in disproportionation of carbon monoxide on  $Fe_2O_3$  at 808 K. Therefore, the roles of metal carbides in CNT growth are still a subject of debate.

In addition, crystallographic orientations of the nanoparticles might also play a role in the CNT growth, for example, in determining CNT chirality.<sup>[108]</sup>

### 1.3.3.3 Substrates

A variety of supports have been used to synthesize CNTs, including  $SiO_2$ <sup>[109, 131, 136, 137]</sup>,  $Al_2O_3$ <sup>[115, 131]</sup>,  $MgO$ <sup>[138]</sup>,  $CaCO_3$ <sup>[139]</sup>, porous Zeolite<sup>[140]</sup> and anodic aluminum oxide(AAO)<sup>[141, 142]</sup>, graphite<sup>[109]</sup>, etc. However, it was found that catalyst particles supported on different substrates result in various CNT structures and morphologies, as well as different yields.<sup>[131, 143]</sup>

Apparently, substrates serve as “holder” of catalyst particles. The substrate greatly influences the catalyst particle size, and thereby the diameter of CNTs. For example, Zeolites have a porous structure that could accommodate catalyst particles in their small pores. Consequently, catalyst particles with a narrow size distribution were obtained on the substrate, and their diameter is limited to the pore size of substrate. Using zeolite particles as a floating catalyst support, Hayashi et al.<sup>[140]</sup> have successfully synthesized small freestanding SWCNTs, which has a diameter of about 0.43 nm (Fig. 14). On the contrary, metal catalyst particles have larger mobility on flat substrates, so that they generally agglomerate together to form bigger particles.

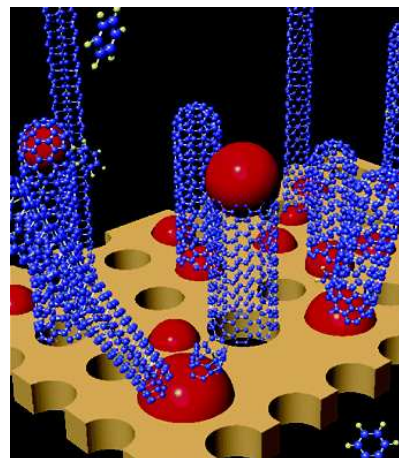


**Figure 14.** Schematic of free-standing SWCNTs grown by using zeolite particles (brown base) as a floating catalyst support (red balls indicate catalyst particles).<sup>[140]</sup>

The interaction between catalysts and substrate materials is of great importance to CNT growth. The strength of the interaction has a direct influence on CNT growth mode. As described by Baker and Sinnott et al,<sup>[144, 145]</sup> “bottom-growth” (or “root-growth”) and “tip-growth” could be seen during CNT growth process depending on the interaction strength between catalyst and substrate (Fig. 15). The interaction is generally characterized by the contact angle at the growth temperature, analogous to “hydrophobic” (weak interaction) and “hydrophilic” (strong interaction) surfaces.<sup>[103]</sup>

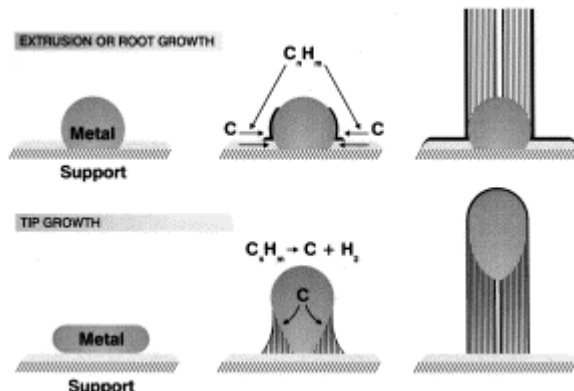


**Figure 15.** Schematics of root-growth and tip-growth modes for carbon filament growth<sup>[145]</sup>.

It is worth noting that catalyst nanoparticles are often generated from compounds containing transition metals, like oxides, salts or metallocenes, etc. The formation of nanoparticles involves a series of chemical and physical phenomena, including chemical bond formation and dissociation, mass transfer, catalyst crystallization. Therefore, for a given metal catalyst, the CNT growth depends not only on substrate chemical nature but also the CVD conditions used. For example, Ren et al<sup>[105]</sup> demonstrated that the aligned CNT array of several square centimeters was grown on nickel-coated glass below 666 °C using acetylene as carbon

source and ammonia as dilution gas. They found that CNTs grew only when NH<sub>3</sub> was introduced first, followed by C<sub>2</sub>H<sub>2</sub>, or when both C<sub>2</sub>H<sub>2</sub> and NH<sub>3</sub> were introduced at the same time. Otherwise, no growth of CNTs was found.

The crystallinity of substrate also exhibits an influence on the selective growth of oriented CNTs. Ward et al.<sup>[146]</sup> studied in detail the influence of substrate on nanotube growth by decomposing methane at 950 °C. Aluminum–iron–molybdenum multi-layer thin films were deposited on various substrates, including (0 0 1) p-type silicon, ‘over-etched’ (001) silicon, porous (001) silicon, poly-silicon on (001) silicon, poly-silicon on PECVD silica, 6-H SiC, (001) MgO, (0001) SiO<sub>2</sub>, (0001) Al<sub>2</sub>O<sub>3</sub> and ‘spun-on’ alumina film. It was found that the roughness and the crystallinity of substrates greatly affected the distribution of the size of iron particles, and consequently determined the selective growth of SWCNTs. Su et al.<sup>[147]</sup> reported the preferred 2D orientations of SWCNTs grown by CVD of methane on silicon-based surfaces at 900 °C. The SWCNTs grown on Si (100)-based surfaces took two perpendicular directions, but those grown on Si (111)-based surfaces took three preferred directions that were separated by 60°. Molecular simulations indicated that the observed orientations were the result of interactions between the nanotubes and the substrate surface lattices. The growth of SWCNTs was guided by the surface lattice to follow a potential minimum path. Han et al.<sup>[148]</sup> also reported the growth of aligned SWCNTs on *a*-plane and *r*-plane sapphire substrates using ferritin as the catalyst. Similarly, the CNTs of micrometers in length grew on *a*-plane sapphire normally to the [0001]direction. In contrast, no orientation was achieved for growth on the *c*-plane and *m*-plane sapphire, or when Fe films, instead of ferritin, were used as the catalyst. Maret et al.<sup>[149]</sup> reported the preferential growth of nanotubes along [110] and [1̄10] directions on a single-crystal MgO (001) surface. The nanotubes were grown at 900 °C by CVD using a mixture of carbon monoxide and hydrogen. The Co catalyst nanoparticles self assembled on MgO under ultra high vacuum conditions. They attributed the directional growth of CNTs to the interactions between oxygen atoms of the MgO substrate and carbon nanotubes.

#### 1.3.3.4 Carbon sources

In addition to carbon monoxide<sup>[101, 123, 150]</sup>, a large variety of hydrocarbons have been used as carbon feedstock to synthesize CNTs by CVD. The most commonly used ones include acetylene<sup>[113]</sup>, methane<sup>[131, 151-153]</sup>, ethylene<sup>[150, 154]</sup>, benzene<sup>[119]</sup>, toluene<sup>[120]</sup>, xylene<sup>[155]</sup>, pyrene<sup>[154]</sup>, butane<sup>[116]</sup>, cyclohexane<sup>[121, 156]</sup> and anthracene<sup>[157]</sup>.

At CNT synthesis temperatures, carbon source mainly decomposes according to the

following two ways: homogenous thermal decomposition in gas phase and catalytic decomposition on catalyst particles. The thermodynamic stability of carbon sources will influence their pyrolysis. Variation of the Gibbs function ( $\Delta_f G$ ) during the decomposition reaction of hydrocarbons into graphite and hydrogen is opposite to the Gibbs free energy of the formation of hydrocarbons at reaction temperatures. Fig. 16 plots the  $\Delta_f G$  of decomposition of the commonly used hydrocarbons (data from ref 158). The stability of carbon sources increases with the variation of the Gibbs energy. The term pyrolytic is defined as converting the carbon source to solid carbon as the main product and to different volatile compounds as by products<sup>[103]</sup>. For example, the pyrolytic reaction producing elementary carbon from methane is thermodynamically unfavorable at temperatures below 800 K. Therefore, methane is commonly used as carbon sources for SWCNT growth at higher temperatures. It could also be derived from the plot that acetylene is a carbon source thermodynamically unstable at low temperatures. Hernadi et al.<sup>[159]</sup> reported the production of CNTs by catalytically decomposing different carbon containing compounds over transition metals (Fe, Co, Ni, Y) supported on silica. The catalytic reactions were carried out at the temperatures ranging from 700 to 800 °C. It was found that the highest yields of CNTs were obtained using acetylene as carbon source. According to the CNT yields, the reactivity order of the carbon containing compounds is: acetylene > acetone > ethylene > n-pentane > propylene >> methanol=toluene >>methane. This order is different from the one expected by the free energies of formation of the compounds (acetylene > ethylene > toluene > propylene > methane > n-pentane > methanol > acetone). That means the pyrolytic reactions in gas phase are not the only rate-determining factor in CNT production. In fact, the varied activities of catalyst particles for different carbon sources have to be taken into account. In addition, as CVD is a complex chemical system with no-equilibrium reactions, the process is also significantly influenced by chemical kinetics and mass transport phenomena.

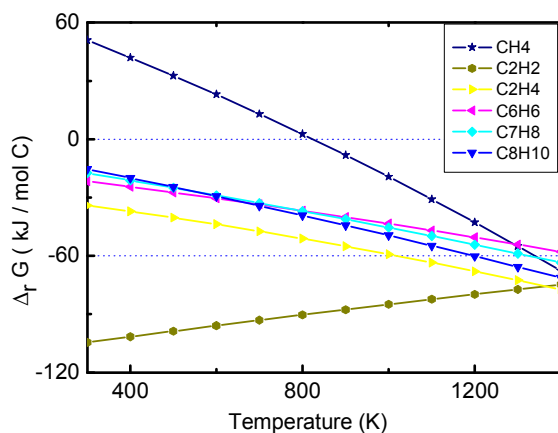


**Figure 16.** Inverse free Gibbs energy of formation of some commonly used carbon sources.

### 1.3.3.5 Atmosphere

The carrier gases commonly used in CNT synthesis by CVD include argon<sup>[160]</sup>, helium<sup>[161]</sup>, nitrogen<sup>[162, 163]</sup>, hydrogen<sup>[12, 164]</sup> and ammonia<sup>[105]</sup>. Hydrogen usually serves as a protective gas to prevent the oxidation of catalyst particles during CNT growth. In addition, hydrogen can also reduce the rate of dehydrogenation reactions, and thus prevent the formation of less ordered and thermodynamically stable carbon structures<sup>[165]</sup>. Therefore, a few amount of hydrogen (in general ~10 %) is added in inert gas during CNT synthesis by floating CVD.<sup>[155, 166]</sup>

Juang et al.<sup>[167]</sup> studied the effect of NH<sub>3</sub> on the growth of CNTs in atmospheric thermal CVD at 900 °C. Argon, NH<sub>3</sub> and methane were used as diluting, reactive and carbon source gases, respectively. It was found that NH<sub>3</sub> enhanced the catalyst (Ni) activity by preventing it from passivation.

The addition of oxygen containing species such as water (H<sub>2</sub>O), carbon dioxide (CO<sub>2</sub>), oxygen (O<sub>2</sub>) in carrier gas could lead to the synthesis of high quality CNTs.<sup>[168, 169]</sup> Cao et al.<sup>[170]</sup> reported the synthesis of aligned CNTs by floating CVD in presence of water vapor. Certain amounts of distilled water were added into the ferrocene dissolved xylene solution. They found that a small amount of water was helpful to eliminate amorphous carbon in the final product, and to further open CNT caps by oxidation. Hata et al.<sup>[168]</sup> reported the efficient synthesis of high-dense vertically aligned SWCNTs, as shown in Fig. 17, using water (~150 ppm) assisted ethylene CVD method. The produced CNT forests with carbon purity above 99.98% had heights up to 2.5 millimeters. They argued that a small amount of water in CVD enhances the activity and lifetime of the catalysts by preventing amorphous carbon coving the catalysts.<sup>[168, 171]</sup> Vertically aligned dense SWCNTs have also been synthesized by an ethanol CVD method<sup>[172]</sup>. The above studies demonstrate that oxygen-containing species have significant influences on CNT growth. Zhang et al.<sup>[169]</sup> have further studied the roles played by hydrogen and oxygen in CNT growth by CVD. They found that adding oxygen (~ 1%) to methane in the CVD returned the high efficient growth of densely packed SWCNTs. They revealed the role of oxygen in the CNT growth is to balance C and H radials and, specifically, to provide a C-rich and H-deficient condition which favors the formation of *sp*<sup>2</sup>-like graphitic structures.

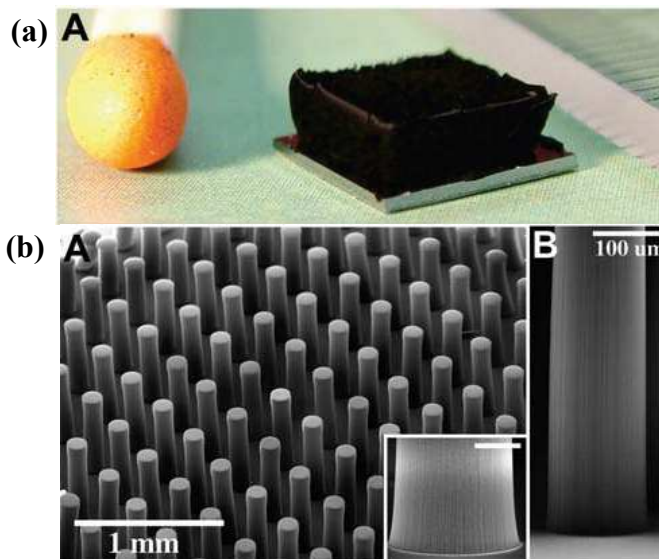


**Figure 17.** (a) SWNT forest grown with water-assisted CVD: a 2.5-mm-tall SWNT forest on a 7-mm by 7-mm silicon wafer. A matchstick on the left and ruler with millimeter markings on the right is for size reference. (b) SEM images of organized SWNT structures-cylindrical pillars (A and B).<sup>[168]</sup>

Sulfur is another additive which is often introduced in CVD processes for enhanced production of CNTs. Cheng et al.<sup>[119]</sup> reported that sulfur is a CNT growth promoter. The addition of thiophene in floating CVD atmosphere promoted the reproducible growth of SWCNTs, and increased the yield of either SWCNTs or MWCNTs under different growth conditions. Valles et al.<sup>[173]</sup> reported that the use of sulfur containing catalyst enhanced the growth of helical CNTs. Furthermore, it was also found that adding sulfur in the form of thiophene vapor favors the growth of Y-shaped carbon nanotubes (YCNTs) under certain hydrocarbon flow conditions.<sup>[173, 174]</sup>

In addition, doping CNTs by substitution with other chemical elements is believed to be a promising approach for tailoring the electrical and optical properties of nanotubes. Because such substitution can introduce donor or acceptor states near the Fermi level. Boron (B) and nitrogen (N) are two commonly used doping elements. Doping by either B or N alone tends to produce metallic behavior.<sup>[175]</sup> And the B and N co-doped MWCNTs possess a bandgap that is adjustable by chemical composition and atomic configuration.<sup>[175]</sup> The N-doped or/and B-doped CNT could be synthesized by the addition of nitrogen precursors or/and boron precursors in CVD. For instance, Wang et al.<sup>[176]</sup> directly synthesized B and N codoped MWCNTs via a bias-assisted hot filament CVD process. Based on the pure CNT synthesis procedure,  $B_2H_6$  and ethylenediamine were additionally fed with methane during the nanotube growth over the powdery MgO-supported Fe-Mo bimetallic catalyst.

### 1.3.3.6 Temperature

Temperature is an essential parameter which has significant influences not only on catalyst activity, but also on CNT geometry, purity, yields and growth kinetics.<sup>[177]</sup> Higher the synthesis temperature is, more active the catalysts are, much easier the combination of catalyst particles becomes. The agglomeration of catalyst particles will therefore result in the increase of the diameter of CNTs.

Besides, the CNT synthesis temperatures should also be chosen according to the carbon feedstocks used. Low temperatures are favorable to reduce the formation of undesired carbon deposits such as amorphous carbon. As we know, the amorphous carbon is deposited from the thermal decomposition of carbon feedstock gas, whereas CNTs are grown from the catalytic decomposition.<sup>[103]</sup> On the other hand, high temperatures are desired for the production of CNTs with good crystallinity. As the diffusion of carbon through the catalyst particles is a thermally activated process, high temperatures promote the growth of CNTs at a high rate, which is desirable for the mass production of CNTs. In general, there is a compromise between obtaining high purity and high crystallinity of CNTs. Taking floating CVD for example, the synthesis of MWCNTs is usually conducted at temperatures below 800 °C, but the production of SWCNTs is at higher temperature.<sup>[178]</sup>

## 1.4 CNT growth mechanisms in CVD

### 1.4.1 General mechanism

Large-scale production of CNTs with well-defined configurations relies on the clear understanding of their growth mechanism. In the last two decades, a considerable progress has been made in the CNT mechanism research, especially, in in-situ observation of CNT growth with HRTEM. However, supplementary works are still required for a better understanding of the mechanism.

“Vapor-liquid-solid” mechanism<sup>[145, 179, 180]</sup> is the first model employed to explain the CNT growth in CVD. In fact, this model is an extension of the one that Baker et al.<sup>[144]</sup> proposed to describe the growth of carbon fibers by catalytic decomposition of carbon feedstock, as shown in Fig. 15. According to this model<sup>[144, 145]</sup>, carbon feedstock first decomposes on the front-exposed surfaces of the metal particle into hydrogen and carbon which then dissolves in the metal particles. Next, the carbon diffuses through the particle and is precipitated on the

opposite half to form tubular fiber having similar diameter to the metal particle size. Comparing with other forms of carbon such as graphitic sheets with open edges, tubular structure with no dangling bonds is energetically favorable<sup>[181]</sup>. Such a process will continue until the front tip of the catalyst particle is deactivated due to the formation carbon layer around it. The rate limiting step in this mechanism is believed to be the diffusion of carbon species from the front side to the rear side. Two probable driving forces of carbon diffusion are suggested to be the temperature gradient and the concentration gradient<sup>[144]</sup>. The temperature gradient in the particle is thought to be created by the exothermic decomposition of hydrocarbons at the exposed front faces and endothermic deposition of carbon at the rear faces, which are initially in contact with the support surface. Depending on the catalyst-substrate interactions, CNTs could grow according to two different modes, as shown in Fig. 15<sup>[144]</sup>. The weak interactions result in the tip growth mode whereas the strong ones yield the root-growth mode.

This primary model could give a rough explanation to some phenomena observed in CNT growth. For instance, it indicates the important role of the catalytic decomposition of carbon feedstock, the influence of the catalyst particle size on CNT diameter, and the formation of metal carbides during CNT growth, etc. However, the model is far from perfect to well describe the complex CNT nucleation and growth processes. Obviously, it does not take into account the “nanosize-effect” of catalyst particles.

The first effect of the particle size is on the catalyst melting point and physical state during CNT nucleation and growth. Take iron nanoparticles as an example. Considering that most CVD processes are conducted at temperatures far below the melting temperature of iron (1534 °C), and below the iron-carbon eutectic temperature (1147 °C), it is therefore reasonable to expect that iron particles are in solid state during CNT growth. However, for nanosized metal particles, the melting temperature  $T_m$  is dependent on their size (radius,  $r$ ). The dependence relationship could be approximately estimated based on the Kelvin equation as<sup>[182]</sup>,

$$T_m = T_0 \exp\left(-\frac{2\sigma_{sl}V}{r\Delta H_{fus}}\right),$$

where  $T_0$  is the bulk melting temperature (1811 K);  $\Delta H_{fus}$  is the latent heat of fusion (13.8 kJ mole<sup>-1</sup>);  $V$  is the molar volume of a metal molecule, which can be calculated from the density ( $7.87 \times 10^3$  kg m<sup>-3</sup>);  $\sigma_{sl}$  is the surface tension between liquid and solid (0.86 J m<sup>-2</sup>). It could be estimated that at commonly used CVD temperatures (500-800 °C) the metal particles with diameters less than 2-3.5 nm are expected to be in liquid state. Besides, nanoparticles also exhibit a melting point drop in the hydrocarbon gas atmosphere.<sup>[183]</sup> After dissolving certain amounts of carbon, the above evaluated diameter values might be increased a little. On the other

hand, it was reported that the melting point of metal nanoparticles is also dependent on catalyst-substrate interaction. For example, the melting point of nickel cluster increases with increasing the catalyst-substrate interaction.<sup>[184]</sup> If the temperatures above carbon-metal eutectic point are used, CNTs would grow according to the vapor-liquid-solid mechanism where diffusion through a liquid-phase particle is responsible for the synthesis of filaments. Otherwise, for instance, catalyst nanoparticles in solid state, or locally molten on the surface, the mechanism is not applicable.

The second effect of particle size is on the CNT growth modes. Recently, Gohier et al.<sup>[185]</sup> demonstrated that for the examined metal particles the CNT growth mode switches from “tip-growth” for large particles ( $>>5$  nm) to “base-growth” for smaller ones ( $<5$  nm). SWCNTs and nanotubes with few walls (typically  $<7$  walls) grew from their base, while larger multi-walled nanotubes were fed with carbon via their tips which support the catalyst particles. In this research, CNTs were grown by a plasma assisted catalytic CVD using cobalt, nickel and iron catalyst particles in different sizes.

Thus, the “Yarmulke” mechanism was then proposed by Dai et al.<sup>[101]</sup> to reflect the specific characteristics of nanoparticles—very high surface energy. Since nanoparticles have a high percentage of surface atoms, it is energetically favorable for an excess carbon in CVD to assemble a graphene cap on the particle surface, with its edges strongly chemisorbed to the metal. Because the basal plane of graphite has an extremely low surface energy (10-20 times smaller than most metals), the total surface energy diminishes. Once the smallest yarmulke has formed, new arriving carbon continuously inserts into the region between the tube edge and the catalytic particle. The driving force for the extrusion of CNTs is believed to originate from the decrease in the free energy in the assembling reaction that occurs at the interface of the metal nanoparticle catalyst<sup>[186]</sup>.

Although above progresses made, the description of CNT nucleation and growth is still far from clear. The following key questions remain suspended in controversy. First, whether is the catalyst a liquid or a solid during CNT growth? Due to the high surface energy, area, and mobility<sup>[103]</sup>, the metal nanoparticles behave completely differently than their bulk metal form. Thus, the second question is whether it is prerequisite for catalyst particles to be in liquid state for the growth of CNTs by CVD. Then, how does the catalyst particle behave during CNT nucleation and growth? How do the carbon atoms dissociated on the catalyst particle diffuse in order to form one CNT, through bulk diffusion or surface diffusion? Are there metal carbides generated during CNT growth? If yes, what is their role for the nanotube growth?

In-situ time-resolved HRTEM provides an efficient tool which permits us to observe and

record with sufficient spatial and temporal resolution the dynamics of CNT nucleation and growth at the atomic scale. Hence, Ajayan said<sup>[187]</sup>, this is a long-awaited solution to the mystery of nanotube growth. Helveg et al.<sup>[188]</sup> recorded, in real time, CNT growth from methane decomposition over supported nickel nanocrystals (5- 20 nm) at ~500 °C inside a high resolution transmission electron microscope. As shown in Fig. 18, the CNT growth was driven by periodic shape changes (between spherical and elongated) of the nickel nanocrystals. The shape variations were driven by the reactions between the catalyst and the carbon source vapor. Specifically, the nucleation and growth of graphene layers were found to be assisted by a dynamic formation and restructuring of mono-atomic step edges at the nickel surface in elongated form. The contraction was attributed to the fact that the increase in the Ni surface energy can no longer be compensated by the energy gained when binding the graphitic fibre to the Ni surface. Density-functional theory calculations demonstrated that step edges act as growth centers for graphene growth mainly because carbon binds more strongly to such sites than to sites at the closepacked facets on Ni. The transport of C atoms from the free Ni surface to the sites at the graphene-Ni interface was the rate limiting step for the nanofibre growth. In this observation, CNTs grew following a tip-growth mechanism.

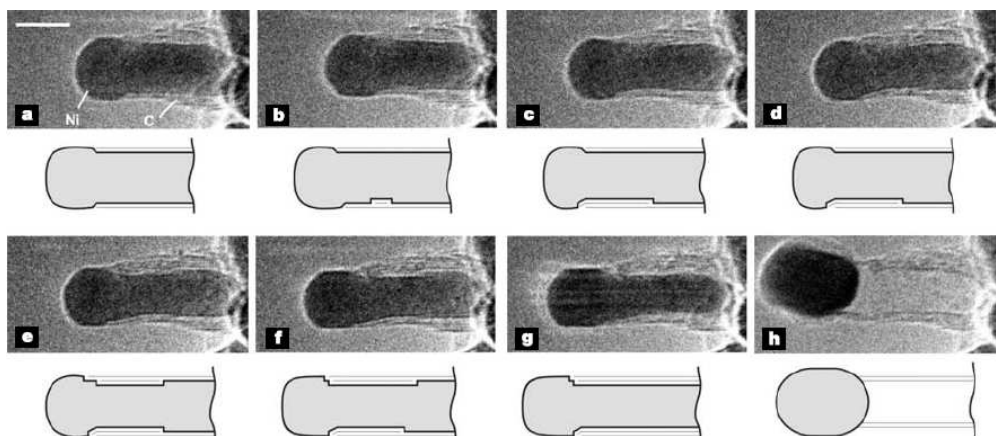


**Figure 18.** Images a–h illustrate the elongation/contraction process of one nickel nanocrystal. Drawings are included to guide the eye in locating the positions of mono-atomic Ni step edges at the C–Ni interface. The images are acquired *in situ* with  $\text{CH}_4:\text{H}_2=1:1$  at a total pressure of 2.1 mbar with the sample heated to 536 °C. Scale bar, 5 nm.<sup>[188]</sup>

Lin et al.<sup>[189]</sup> studied the SWCNT growth by the catalytic decomposition of acetylene over a Ni-MgO catalyst at 650 °C using an *in situ* ultrahigh vacuum transmission electron microscope under a pressure of  $\sim 4 \times 10^{-6}$  Torr. They observed that SWCNTs preferentially grew on smaller sized catalyst particles (diameter  $\leq 6$  nm) via base-growth mechanism, whereas larger catalyst particles favored nanocage formation. The study of the growth

dynamics of a SWCNT showed the existence of an incubation period prior to rapid growth. Furthermore, selected area electron diffraction showed that the nickel particles remained as metallic Ni, instead of forming nickel carbides  $\text{Ni}_3\text{C}$  during CNT growth. Similarly, Wako et al.<sup>[190]</sup> also observed the three stages (incubation, growth and termination) of the CVD growth of a SWCNT on  $\text{SiO}_2$  substrate using *in situ* scanning electron microscopy (SEM). In particular, cobalt-filled apo-ferritin was used to disperse the Co catalysts on the substrate, and thus to minimize the overlapping of the grown SWCNTs.

Hofmann et al.<sup>[96]</sup> studied the decomposition process of acetylene over  $\text{SiO}_x$ -supported Ni and Fe catalysts by an atomic-scale environmental transmission electron microscope (Fig. 19). It was revealed that the nanoparticles showed crystalline fringe contrast and high deformability before and during nanotube formation. *In situ* time-resolved X-ray photoelectron spectroscopy analysis of the CNT growth was carried out under  $\text{C}_2\text{H}_2$  atmosphere ( $\sim 2 \times 10^7$  mbar) at  $580^\circ\text{C}$ . The evolution of the C 1s core level spectrum revealed a transition from chemisorbed carbon to carbide carbon and to a  $sp^2$ -bonded carbon network. A SWCNT nucleated by lift-off of a carbon cap. The cap stabilization and nanotube growth according to base-growth mechanism involved the dynamic reshaping of the catalyst nanocrystal itself. For carbon nanofiber, the graphene layer stacking was determined by the successive elongation and contraction of the catalyst nanoparticle at its tip, resulting in a tip-growth mode.

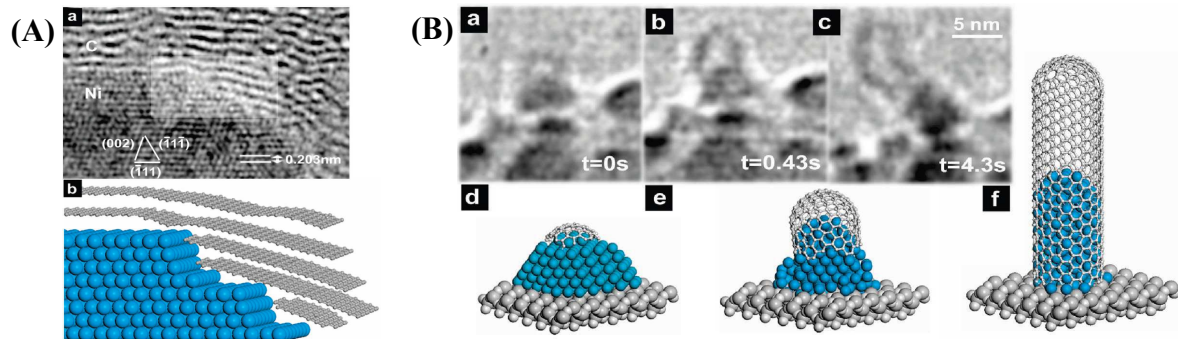


**Figure 19.** (A) (a) HRTEM image of Ni-C interface at the tip of a CNF grown *ex situ* at  $700^\circ\text{C}$  in 2.7:1  $\text{NH}_3:\text{C}_2\text{H}_2$  at 5.2 mbar total pressure. (b) Schematic ball-and-stick model of area highlighted in (a). (B) (a-c) Environmental TEM image sequence of Ni-catalyzed CNT root growth recorded in  $8 \times 10^{-3}$  mbar  $\text{C}_2\text{H}_2$  at  $615^\circ\text{C}$ . (d-f) Schematic ball-and-stick model of different SWNT growth stages.<sup>[96]</sup>

Rodríguez-Manzo et al.<sup>[191]</sup> *in situ* observed the formation of SWCNTs by irradiating a MWNT-metal-MWNT heterojunction<sup>[192]</sup> with an intense electron beam( $10^3 \text{ A cm}^{-2}$ ) in a transmission electron microscope. Fig. 20a demonstrated the process of the formation, elongation, and breakage of a SWCNT with the separation of a metal into two halves. During

the processes at temperatures ranging from 450 to 700 °C, the metal remained crystalline in face-centered cubic (fcc) structure. In addition, they investigated the growth of SWCNTs from highly curved surfaces of transition metal particles that were saturated with carbon. They concluded that high curvature (radius less than 3 nm) is a necessary condition for nanotube growth, and that the local solubility of carbon in the metal determines the nucleation of nanotubes. Furthermore, the absence of a cap to the CNT nucleation indicated that the nanotube structure is not necessarily defined by the formation of a cap with a certain size. Instead, the diameter and structure of the nanotube are controlled by the shape and size of the catalyst particle.

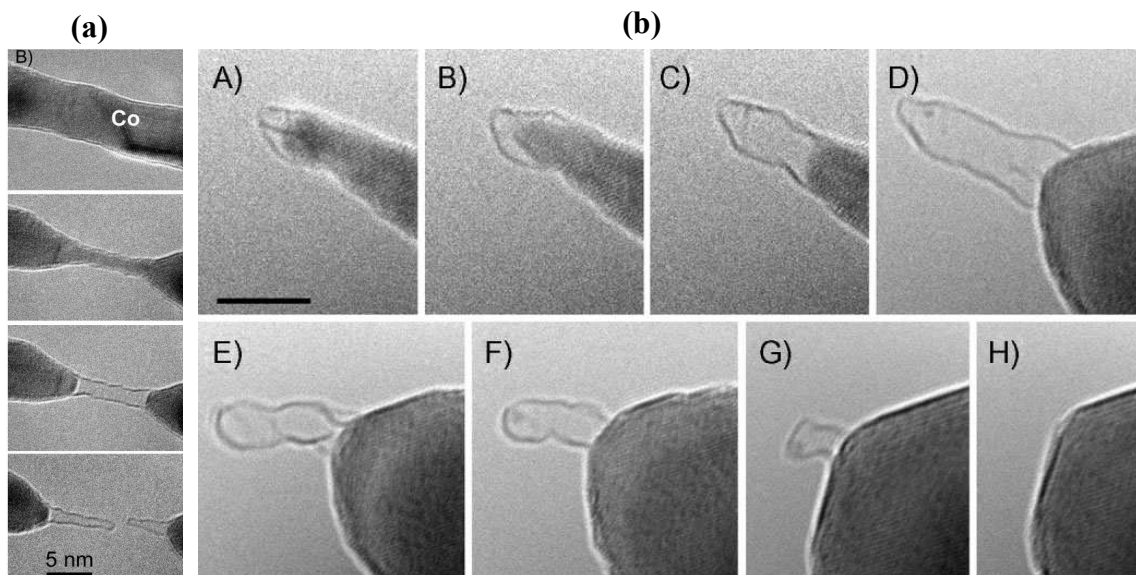


**Figure 20.** (a) A SWCNT formation and breakage by irradiating a MWNT-Co-MWNT heterojunction with an intense focused electron beam at 600 °C. (b) A SWNT grows from a sharp Ni tip that was obtained from a broken double-cone structure, and re-ingests into the blunt Ni particle after rounding of the metal tip at 470 °C. [191]

**In summary**, in-situ HRTEM observation of CNT growth reveals that catalyst particles with high local curvature surface are an essential condition for CNT formation. The nucleation and growth of graphene layer are driven by the dynamic formation and restructuring of monoatomic step edges at catalyst surface through the diffusion of metal atoms. The growth of CNTs is rather related to the amplitude and frequency of the reshaping process of catalyst nanocrystal. The diameter and structure of nanotubes are controlled by the geometry, size and orientation of catalyst particles. However, the reshaping process of catalyst particles needs a foreign driving force, which could be either the carbon deposition reaction between catalyst and carbon sources, or the energy in other forms such as irradiation. The catalyst particles both in

solid and liquid states could catalyze the formation of CNT. Carbon atoms could diffuse through catalyst particle though bulk-diffusion or (and) surface-diffusion, depending on the initial state of catalyst particle, carbon sources, and the used experimental conditions such as pressure and temperature. The rate determining step of CNT growth might be the amplitude and frequency of the catalyst particle reshaping along CNT axial direction, as well as the carbon adsorption, diffusion or precipitation on the catalyst particles.

#### **1.4.2 Mechanism in floating catalytic CVD**

The growth of CNTs by floating catalytic CVD is distinguished from other CVD processes by in situ formation of catalyst particles during the decomposition of hydrocarbons. In general, transition metal catalysts (Fe, Ni, Co) nucleate from the decomposition of catalyst precursors like organometallic compounds (ferrocene<sup>[112-115]</sup>, cobaltocene<sup>[120]</sup>, nickelocene<sup>[121]</sup>) and iron pentacarbonyl<sup>[123]</sup>. These catalyst precursors, either dissolved in liquid carbon source solution or evaporated by heating, are fed into CVD reactor by carrier gas. Normally, the process is carried out under atmospheric atmosphere. Thus, reductive gas such as hydrogen is also added as protective gas during catalyst formation and CNT growth. Specifically, the catalyst formation in floating CVD is sensitively dependent on CVD parameters, including temperature, substrate, carbon sources and protective gas.

Vertically aligned CNT arrays were synthesized by pyrolyzing the solutions of Fe(C<sub>5</sub>H<sub>5</sub>)<sub>2</sub> and C<sub>6</sub>H<sub>6</sub><sup>[193, 194]</sup>, Fe(C<sub>5</sub>H<sub>5</sub>)<sub>2</sub> and C<sub>7</sub>H<sub>8</sub><sup>[195]</sup>, or Fe(C<sub>5</sub>H<sub>5</sub>)<sub>2</sub> and C<sub>8</sub>H<sub>10</sub><sup>[155, 196]</sup> at the temperatures of ~ 850 °C. The produced CNTs are highly crystalline and with a large diameter, ~100 nm (outer diameter). In addition, these procedures give a relatively high CNT growth rate, as high as ~50 μm min<sup>-1</sup> <sup>[196]</sup>.

The growth of CNTs in floating CVD follows the common mechanism: bottom-up growth. That is, CNTs nucleate and grow from the surface of substrate where catalyst particles are located. Li et al.<sup>[197]</sup> reported the selective growth of stacked multiple layers of vertically aligned CNTs on silicon oxide substrate by decomposing a solution of ferrocene/xylene at 770 °C (Fig. 21a). It was demonstrated that each layer of CNTs nucleated and grew from the original substrate surface at the bottom of the existing multiple stacks of CNTs. The stacked layers of aligned nanotubes acted as fully permeable membranes for the downward diffusion of growth precursor vapors, allowing growth to occur at the buried solid interface. The preexisting multiple nanotube stacks lifted up to accommodate the vertical growth of fresh layers, allowing the formation of nanotube towers extending in millimeter lengths. At the same time, Pinault et al.<sup>[198]</sup> also reported the similar phenomenon. Aligned MWCNTs were synthesized by

aerosol-assisted catalytic CVD through sequential injections of aerosols containing both carbon and catalyst precursors. Each sequence was traced by a specific duration or precursor mixture. It was demonstrated that any sequence involved the growth of a new layer on the substrate surface by lifting up any pre-existing one. The continuous feeding of the catalyst precursor was prerequisite to the continuous CNT growth, and the catalyst was playing its role mainly on the substrate surface. By alternatively injecting  $^{13}\text{C}$ -enriched benzene/ferrocene solution, it was demonstrated that the produced CNT array carpet was composed of four stacked parts with different  $^{13}\text{C}/^{12}\text{C}$  ratio, as shown in Fig. 21b. The stacking order was consistent with the chronology of the injection sequences of the solution. This result proved that carbon species diffused through the whole carpet thickness and subsequently feed the origin of the nanotube growth located on the surface substrate. [198]

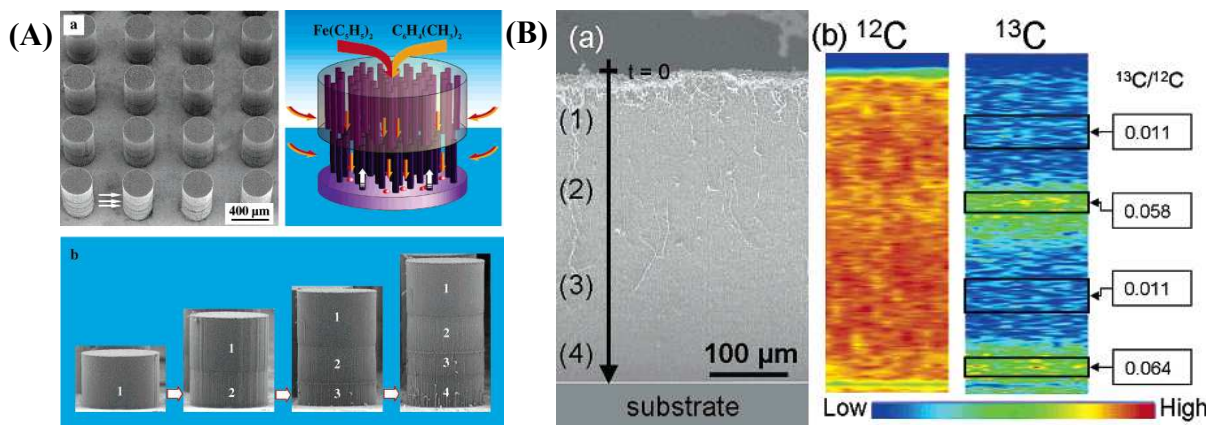


**Figure 21.** Base-growth mechanism of CNTs in floating CVD process: (A) SEM image of an array of 4-stack nanotube pillars selectively grown on patterned silicon oxide substrate by the CVD of xylene/ferrocene solution. The fully grown stack gets lifted up as the new layer grows underneath, on the buried substrate. The height of each stack corresponds to these deposition times (CNT growth rate is typically  $\sim 10 \mu\text{m min}^{-1}$ ). [197] (B) SEM image of a cross section of one aligned MWCNT array synthesized by alternatively injecting  $^{13}\text{C}$ -enrich benzene/ferrocene solution at  $850^\circ\text{C}$  (CNT growth rate was  $\sim 21 \mu\text{m min}^{-1}$ ), and  $^{12}\text{C}$  and  $^{13}\text{C}$  mapping along the MWCNT layer length showing four separated regions with different  $^{13}\text{C}/^{12}\text{C}$  ratios. [198]

In general, CNT grown by floating CVD have one iron particle located at its root. Heresanu et al.<sup>[199]</sup> studied the nature of the catalyst particle generated from the pyrolysis of the aerosols of ferrocene/toluene under Ar atmosphere (no reductive gas). Different ex-situ measurements on the quenched samples demonstrated the iron-based catalyst particles were carbon-rich and oxygen-free, and might be supersaturated carbon-metal particles. However, catalyst particles were oxidized to Fe<sub>3</sub>O<sub>4</sub> or γ-Fe<sub>2</sub>O<sub>3</sub> during the normal cooling process. Pinault et al.<sup>[195]</sup> investigated the early stages of the growth of CNTs by the same process. It was found

that a layer of iron oxide nanoparticles ( $\text{Fe}_2\text{O}_3$  or  $\text{Fe}_3\text{O}_4$ ) was first formed on Si substrate before the growth of CNTs. Even though the oxides are due to residual oxygen in the reactor, the results show that the formation of metal catalyst form metallocene first takes place on substrate surface, and then the produced catalyst particles catalyze the decomposition of carbon sources to produce CNTs. In addition, CNTs produced by floating CVD are partially filled with iron nanoparticles in the  $\gamma$  phase with a face-centered cubic crystal structure.<sup>[156, 200]</sup> The nanoparticles exhibits a preferential crystallographic  $<110>$  axis along the nanotubes<sup>[156]</sup>, and might accelerate the growth of nanotube arrays<sup>[196]</sup>.

## **1.5 CNT based hybrid materials**

### **1.5.1 Introduction**

As discussed previously, the unique structure and remarkable properties of individual CNTs make them excellent candidates in diverse applications. On the other hand, the fact that CNTs are insoluble in all solvents and are easy to agglomerate together has imposed great limitations to their applications<sup>[201]</sup>. Many efforts have been made to modify CNT surface structure through chemical treatments in order to integrate them into inorganic, organic, and biological systems<sup>[201]</sup>. In the meantime, a wide range of nanotube based hybrid materials have also been developed by the combination of CNTs with other materials. These hybrid materials with attractive features exhibit promising applications in the fields of nanobiotechnology, energy conversion/fuel storage, catalysis, electronic nanodevices etc.<sup>[202]</sup>

### **1.5.2 CNTs-based hybrid materials**

The first kind of CNT-based hybrid structure is CNT-polymer composites which are constructed by the combination of CNTs and different polymers. In the composites, the CNTs serve as multifunctional fillers, and the polymer is used as matrix. As introduced in section 1.2.3.1, these hybrid materials have been largely researched in laboratory and in industry for a variety of applications.

The second kind of the hybrid materials is formed by the combination CNTs and metallic or semiconducting nanoclusters.<sup>[202-204]</sup> Metal nanoparticles such as Pt, Au and Rh possess unique electronic, optical, magnetic and catalytic properties. The combination of CNTs with these nanoparticles may lead to a successful integration of their properties in the produced hybrid materials.<sup>[205, 206]</sup> Herein, CNTs serve as supporting materials for the deposition and

stabilization of the nanoparticles. These hybrid materials have several potential applications in gas sensors, biosensors, electronic nanodevices, polymer electrolyte fuel cells, heterogeneous catalysis, etc.<sup>[202]</sup> The produced heterojunctions between CNTs and semiconductor nanoparticles such as CdSe quantum dots (QDs), CeTe QDs and SnO<sub>2</sub> have attractive applications in biological labeling, solar cell, light emitting devices, etc.<sup>[202]</sup>

Another type of the hybrid materials is developed by the attachment of biomolecules on CNTs, or by the interaction of biomolecules and cells with CNTs.<sup>[207-209]</sup> The combination of the conducting properties of CNTs and the recognition properties of the biomaterials gives rise to new bioelectronic systems such as biosensors. Such hybrid structures include the heterojunctions of CNTs-proteins, CNTs-DNA and CNTs-cells. Besides, there are also the hybrid structures constructed by filling the inner cavities of SWCNTs by other elements, such as fullerenes (C<sub>60</sub>, C<sub>70</sub>, ...), metallofullerenes (La<sub>2</sub>@C<sub>80</sub>, Gd@C<sub>82</sub>, ...), pure elements (Ru, Ag, Au,...), biomolecules (small proteins-lactamase, DNA, RNA, ...), etc.<sup>[201, 210]</sup>

Among all the CNT-based hybrid structures, the CNT-polymer hybrid materials are of particular importance. The electrical and thermal conductivities and the mechanical properties of the polymer composites<sup>[211-213]</sup> could be considerably improved by the addition of CNTs. However, the multifunctional properties of the composites are still far from expectations<sup>[214]</sup>. This is mainly due to the imperfect dispersion of CNTs in the matrix, and the lack of efficient load and charge transfers between the interface of matrix and filler<sup>[215]</sup>. Since CNTs have large aspect ratios, they are always organized into aggregates. It is extremely difficult to separate individual nanotubes during the mixing with polymers or ceramic matrix. Especially, when the weight fraction of nanotubes is high in the composites, the large surface area of nanotubes results in a very high viscosity of the nanotube-polymer mixtures. To overcome such barriers and to maximize the advantage of nanotubes as reinforcing materials in composites, surface functionalization<sup>[216]</sup> or chemical treatments<sup>[52]</sup> (e.g. using surfactants, acids) of the CNTs have been widely used. Nevertheless, it has been commonly accepted that these surface modifications can degrade the intrinsic properties of CNTs<sup>[52]</sup>. Further efforts are still needed to make in order to close the gap between the high expectations and moderate performance of CNT-based composites.

### 1.5.3 Nano-micro hybrid structures

#### 1.5.3.1 Introduction

On the contrary to chemical surface modification method, multi-scale combination of CNTs and micrometer supports seems to be an alternative way to overcome such obstacles. In particular, the micro supports could be either micrometric ceramic particles or various fibers. Instead of conventionally mixing two kinds of materials in a random way, CNTs are individually grafted on the surface of the microscopic supports to form the nano-micro hybrid structures. Fig. 22 demonstrates two types of the hybrid structures CNTs- $\mu$ Fiber and CNT- $\mu$ Al<sub>2</sub>O<sub>3</sub>, which are generated by grafting CNTs on carbon fibers and alumina spheres with diameters in micrometer, respectively.

The nano-micro hybrid structures have a reinforced interface between each CNT and the micrometer support. We could easily manipulate the nanotubes by simply controlling micrometer materials. At the same time, rather than in entangled state, CNTs could be distributed on the surface of micrometer particles or fibers in a separated state. This is desired to avoid the agglomeration of CNTs and to obtain good dispersion in composites. Furthermore, the nano/micro, nano/macro, and micro/macro micrometer reinforcements in the composites favor to transfer efficiently the loads between the matrix and the fillers. Thus, enhanced properties are expected to achieve by using the hybrid materials as fillers in composites. Indeed, the composites reinforced with CNT/carbon fibers<sup>[217]</sup> or CNT/micro SiC particles<sup>[218]</sup> showed a noticeable improvement of the interfacial strength between the matrix and reinforcements. Besides, the unique combination of two kinds of materials of different scales favors the development of the composites with multifunctional properties.

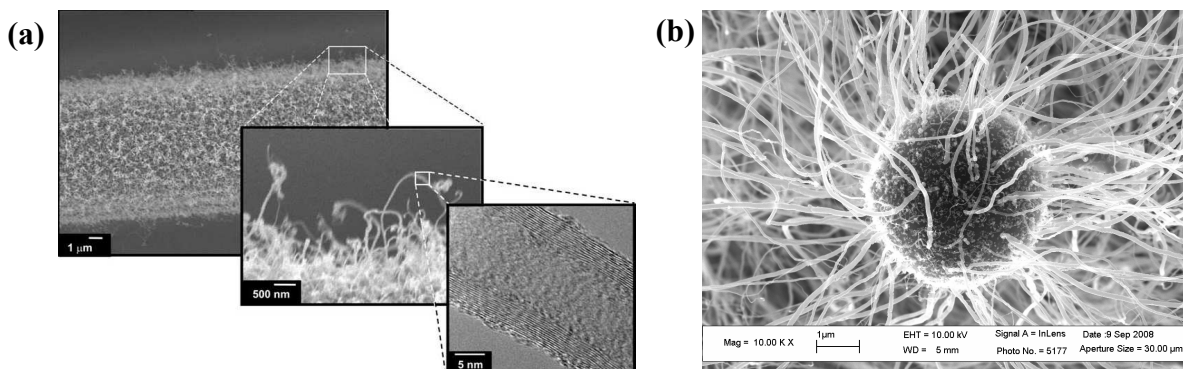


**Figure 22.** Two types of nano-micro hybrid materials: (a) CNTs- $\mu$ Fiber: MWCNTs grafted on carbon microfibers<sup>[219]</sup>; (b) CNT- $\mu$ Al<sub>2</sub>O<sub>3</sub>: MWCNTs grafted on alumina microspheres.

### 1.5.3.2 *In-situ CVD synthesis*

In-situ grafting of CNTs on the surface of micrometric substrates could be realized by CVD method.<sup>[217, 218, 220]</sup> Unlike the CNT growth on flat substrate, the organization of CNTs on micrometer-size particles depends on both the substrate properties, including their size, morphology and their structure, and on the CVD synthesis parameters used, such as carbon source, catalyst precursor, gas atmosphere, hydrogen ratio, temperature, growth time, gas flow etc.

The submicron SiO<sub>2</sub> spheres (diameter: ~ 0.5-1 μm) and CNT hybrid structures, reported by Huang<sup>[221]</sup>, were obtained by pyrolyzing iron (II) phthalocyanine at 800-1000 °C. Then, isolated CNTs were perpendicularly grown on the surface of high curvature SiO<sub>2</sub> particles. Selective growth of aligned CNTs was also obtained on the photolithographically patterned SiO<sub>2</sub> particles. The hybrid structure of CNTs and micro SiC particles was synthesized by Ci et al.<sup>[218]</sup> using floating CVD. CNTs were directly grown on the surface of micro SiC particles (size in 1-4 μm and 10-20 μm) by decomposing a ferrocene-xylene mixture at 650-850 °C under N<sub>2</sub>/H<sub>2</sub> (10:1) atmosphere. Large scale growth of vertically aligned CNT arrays on big diameter (~700 μm) ceramic spherical particles have been reported by Zhang et al.<sup>[222, 223]</sup> and Xiang et al.<sup>[224]</sup> using ethylene or liquefied petroleum gas as carbon source, and ferrocene as catalyst precursor. It was also demonstrated that CNT arrays crack randomly into different bundles on the ceramic particles when the length of CNTs is above 400 μm. The growth of MWCNTs on alumina particles (volumetric diameter ~ 322 μm) supported iron catalyst powders were studied by Philippe et al.<sup>[225]</sup> in a fluidized bed-catalytic CVD, using ethylene as carbon source. The aligned MWCNT mats were first grown around the catalyst grains. Then the entangled CNTs were formed from the particles located inside the porosities of the support, with a fragmentation of the catalyst grains. In addition, hybrid structures of CNTs on ceramic fibers and carbon fibers have been produced by directly growing CNTs using CVD. Afterwards, these hybrid structures have been used to improve mechanical and thermal properties of the composite materials<sup>[217, 226-228]</sup>.

CVD is an efficient method that permits to in situ construct the nano-micro hybrid structures, and in particular, the hybrid structures constituted of CNTs and microscopic ceramic particles. However, the control of CNT organization and orientation in the hybrid structures has not been deeply investigated yet, especially in the case of micro ceramic particles without any pretreatment. The density and the distribution of CNTs have certainly an influence on the multifunctionality of the composite materials, especially on electrical and

thermal properties. Therefore, it is desirable to control CNT arrangements in the hybrid structures for achieving advanced multifunctional composite properties. The widely reported well-aligned CNT architectures, in the forms of arrays of CNT carpets, pillars, forests, etc...<sup>[221, 229-234]</sup>, were generally obtained by exploring pre-patterned substrates or predefining catalyst nanoparticles into certain morphologies on the corresponding substrate. The selective decomposition of carbon sources resulted in different CNT patterns. Obviously, these complex pattern techniques and strict application conditions greatly increase the difficulty and costs of elaborating aligned CNTs. Therefore, it is relevant to propose a facile CVD method to produce multiform hybrid architectures constituted of well organized CNTs and micro ceramic particles without any pretreatment.

### ***1.5.3.3 Enhanced properties***

The nano-micro hybrid materials take advantage of the excellent properties of each component material. They are therefore expected to have more attractive properties and large application potential in structure materials and multifunctional composites which could be used in the aerospace, automotive and sporting goods industries

Thostenson et al.<sup>[217]</sup> studied the reinforcement role of the multiscale hybrid fillers constituted of microscopic carbon fibers grown by nanotubes on their surface. The single-fiber composite tests demonstrated that the CNT/fiber reinforcement improved interfacial load transfer at the fiber/matrix interface, because the presence of CNTs at the fiber/matrix interface improves the interfacial shear strength of the composites. Ci and Bai<sup>[218]</sup> studied the nano-micro multiscale reinforcements in the epoxy composites. The nano/micro hybrid structures were synthesized by directly growing CNTs on the surface of micrometric SiC particles by floating catalytic CVD. Compared with pure epoxy and the SiC particle reinforced epoxy composites, the composites containing 0.5 wt% CNTs/SiC hybrid materials exhibited an increase in Young's modulus (24 %) and tensile strength (15 %). They attributed this improvement in the mechanical properties to the reinforced interfacial behaviors by CNTs.

Besides, the enhanced thermal conductivity of the hybrid structures has also been reported. Han et al.<sup>[235]</sup> reported an increased thermal conductivity of the poly-alpha-olefin nanofluids containing a hybrid sphere/CNT, about 21% incensement at room temperature for particle volume fractions of 0.2 %. Here, the hybrid sphere/CNT was constituted by growing numerous CNTs (~2 μm in length) on the alumina/iron oxide spheres (~70 nm in diameter). In

such hybrid nanoparticles, heat is expected to transport rapidly from one CNT to another through the centre sphere and thus leading to less thermal contact resistance between CNTs when compared to simple CNTs dispersed in fluids. Recently, Naito et al.<sup>[236]</sup> measured the thermal conductivities of high tensile strength polyacrylonitrile (PAN)-based (T1000GB) and high modulus pitch-based (K13D) carbon fibers with CNTs grown on them by CVD using a thermal diffusivity meter. The results showed that the thermal conductivities of both types of fiber were improved by grafting CNTs. The improvement for the CNTs-grafted T1000GB and K13D fibers were 47 % and 30 %, respectively, compared with their original conductivities ( $12.6 \pm 1.0 \text{ W m}^{-1}\text{K}^{-1}$  for T1000GB and  $745.5 \pm 16.0 \text{ W m}^{-1}\text{K}^{-1}$  for K13D).

The enhanced mechanical and multifunctional properties make the nano-micro hybrid materials promising fillers in structure materials and multifunctional composites, which have huge application potentials in aerospace, automotive and sporting goods industries, etc.

## 1.6 Conclusion

In this chapter, we have reviewed some basic knowledge and the state of the art research of CNTs. Briefly, CNTs possess a perfect quasi-1D structure and extraordinary mechanical properties, thermal conductivity and electrical properties. Thus, they have huge application potentials in the fields of composites, electronic devices, bioengineering, etc. Among many synthesis techniques, CVD is of increasing significance for large-scale production of well-controlled CNTs. Besides, it also exhibits an unparalleled advantage in one-step construction of various CNT-based architectures with multifunctional properties. Thanks to the development of in-situ high resolution transmission electron microscopy, the dynamics of CNT nucleation and growth could be recorded at the atomic scale with sufficient spatial and temporal resolution. However, due to the complexity resulted from the multi physical-chemical processes during CVD synthesis, the mechanisms of CNT nucleation and growth are still not clear up to now.

CNTs based hybrid materials are largely investigated because of their novel properties and attractive application potentials in a wide range of fields such as catalysis, energy conversion and biotechnology. Especially, in-situ CVD synthesized multiscale hybrid materials consisting of CNTs and micro particles or fibers are one kind of the most promising materials which could be used as multifunctional fillers in composites. Due to the unique nano-micro hybridization, two great obstacles of CNT based composites - CNT agglomeration and poor interfacial load transfer between filler-filler and filler-matrix, could be easily overcome when employing these hybrid structures as fillers. However, a controlled elaboration

of the hybrid structures has not been reported yet. In consequence, the intrinsic extraordinary quasi-1D properties of CNTs and the unique multifunctional characteristics of the nano-micro hybrid fillers have never been realized in the composites.

In chapter II, we will first demonstrate the multiform well-controlled hybrid structures produced by directly growing CNTs on the surface of alumina microspheres by floating CVD. Then, the outstanding thermal reinforcement of the hybrid materials are obtained by adding them as fillers in polymer composites.

## Chapter II

# Multiform nano-micrometer hybrid structures and thermal transport

### **2.1 Introduction**

The nano-micro hybrid materials based on CNTs and micrometer ceramic particles have tremendous applications in a wide range of fields. Their performance strongly depends on the structures and properties of individual components, as well as the component synergetic corporation. Numerous experiments have demonstrated that undesired agglomeration of CNTs, significant contact resistance and their poor charge transfer interface greatly restrict the improvement of the properties of the composites. Therefore, the organization of CNTs on the micrometer-sized particles is extremely significant to obtain enhanced multifunctional properties of the composites based on the hybrid structures.

In this chapter, we present firstly the multiform hybrid structures consisting of CNTs and alumina microspheres ( $\mu\text{Al}_2\text{O}_3$ ). The CNTs are *in situ* grafted on the surface of  $\mu\text{Al}_2\text{O}_3$  by CVD of iron and carbon precursors. Three distinct types of CNT organization patterns and their evolution are demonstrated. Secondly, in order to examine their thermal performance, the CNTs- $\mu\text{Al}_2\text{O}_3$  hybrid structures are added into epoxy to prepare Epoxy/CNTs- $\mu\text{Al}_2\text{O}_3$  composites. The enhanced thermal conductivities of the composites were obtained at ultra-low CNT weight fractions compared with that of the composites constituted of pristine CNTs and epoxy. This promising result shows the huge application potential of CNTs- $\mu\text{Al}_2\text{O}_3$  as multifunctional fillers. More importantly, the enhanced properties demonstrate the high significance of CNT organization on micro particles to achieve the desired properties. This is also one of the main motivations leading us to further in detail study the formation mechanisms of the multiform hybrid structures in the chapter III.

## 2.2 Experimental

### 2.2.1 Materials

Main materials involved in this study are listed in table 2.

**Table 2.** Information of main materials used in this research

materials	Molecular formula	Physical states	Purity	Notes
Xylene	C <sub>8</sub> H <sub>10</sub>	l*	98.5+%	Assay, isomers plus ethylbenzene, Alfa Aesar
Ferrocene	Fe(C <sub>5</sub> H <sub>5</sub> ) <sub>2</sub>	s*	99 %	Alfa Aesar
Iron(III) chloride	FeCl <sub>3</sub>	s	98 %	Anhydrous, Alfa Aesar
Argon	Ar	g*		Carrier gas
Hydrogen	H <sub>2</sub>	g		Carrier gas
Acetylene	C <sub>2</sub> H <sub>2</sub>	g		Carbon source
Epoxy Resin				Resoltech
Hardener				
Micro alumina particles	Al <sub>2</sub> O <sub>3</sub>	s,(size in 3-10 μm)	99.8%	Containing SiO <sub>2</sub> (800 ppm), Na <sub>2</sub> O (600 ppm), Fe <sub>2</sub> O <sub>3</sub> (150 ppm) and CaO (70 ppm)

\* s, l and g stand for solid, liquid and gas, respectively.

### 2.2.2 Floating CVD equipment and processes

The CNTs- $\mu$ Al<sub>2</sub>O<sub>3</sub> hybrid structures were synthesized by floating CVD in a horizontal quartz tube (110 cm long, inner diameter 45 mm), as shown in Fig. 23a. One layer (~0.5 mm in thickness) of the particles was first homogeneously dispersed on the surface of a quartz plate (3×50 cm<sup>2</sup>), which was then put in the center of the reactor. The CVD reactor was then heated to a given temperature (ranging from 450 to 900 °C) by an electric resistance furnace (60 cm long) under argon and hydrogen atmosphere. Herein, gas flows were accurately controlled by electronic mass flow meters (Bronkhorst, France). After heating the reactor about 30 minutes, the ferrocene-xylene solution was fed by a syringe system and carried into the preheated stable reaction zone by the carrier gases (Ar+H<sub>2</sub>) in the form of spray. In some of experiments, acetylene was additively injected into the reactor in order to adjust CNT

growth. In general, the injection lasted for 10-15 min. At the end, the furnace was cooled down under argon and hydrogen atmosphere ( $1\text{ l min}^{-1}$ ).

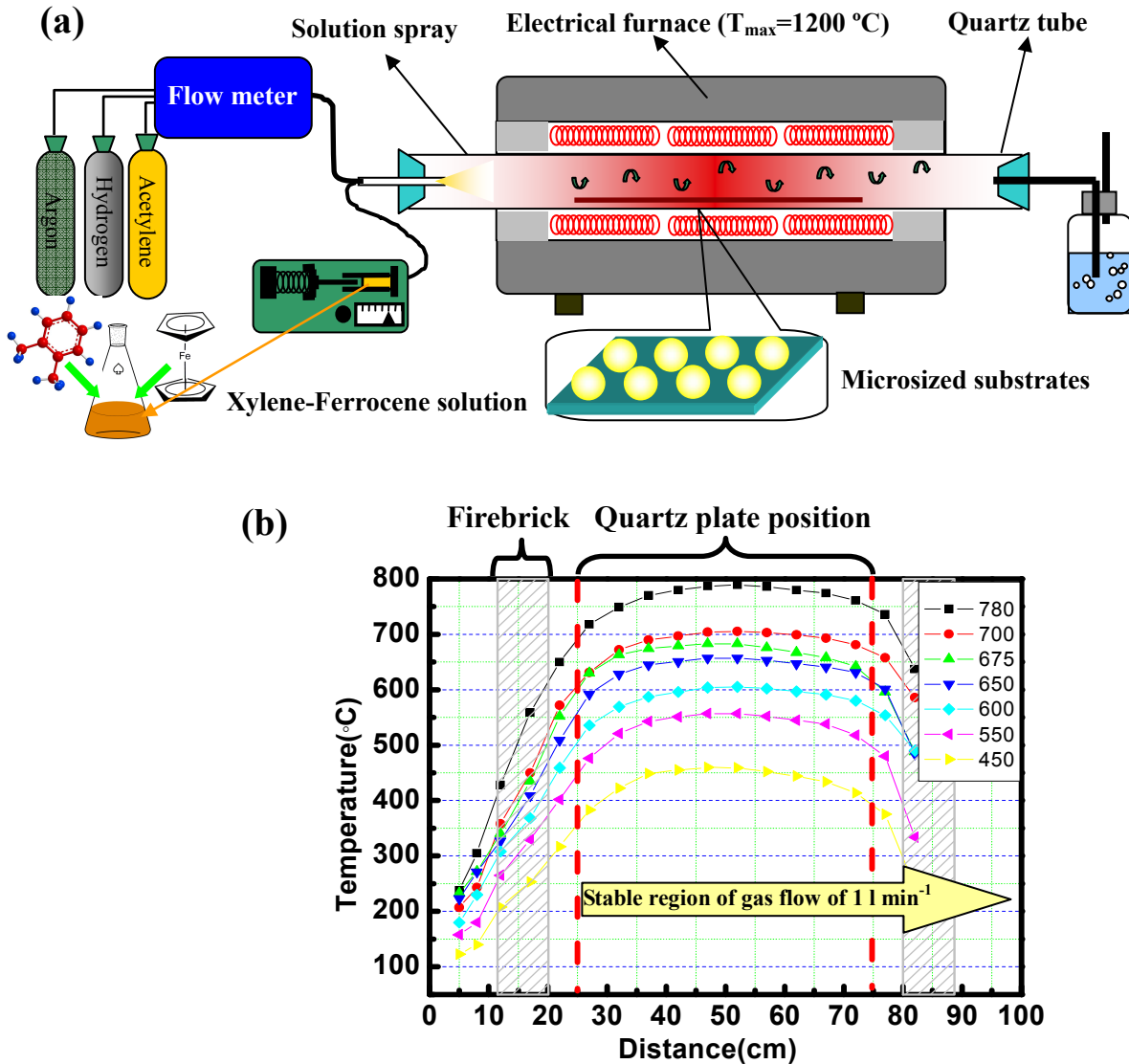


**Figure 23.** (a) Schematic of the CVD system used in this research for the synthesis of the nano-micro hybrid materials. (b) Temperature profiles along the wall of the quartz tube of 46 mm in diameter at the temperatures ranging from 450 to 780  $^{\circ}\text{C}$ . The normal positions of firebrick and quartz plate are indicated in the figure. Gas flow of  $1\text{ l min}^{-1}$  becomes stable after 20 cm, which pass through a thin metal tube with an inner diameter smaller than 1 mm.

The temperature profiles are measured along the wall of the quartz tube at the studied temperatures, as shown in Fig. 23b. The position of quartz plate is marked by two red dot lines between two gray rectangles representing two firebrick regions. As the carrier gases arrive in the reactor by passing through a thin metal tube with diameter smaller than 1 mm,

the gas flow is unstable until to the position of 25 cm where quartz plate is placed. As a consequence, small fluctuations of the temperature are detected in the front part of tube, less than 25 cm for the flow rate of  $1\text{ l min}^{-1}$ . After this position, the temperature becomes stable.

### **2.2.3 Characterization methods**

Mass spectrometry was used to analyze the composition of the exhaust gas during the synthesis of the hybrid structures. The exhaust gas was *in situ* captured using a stainless steel capillary tube and then analyzed by a quadrupole mass spectrometer (MS, Pfeiffer Vacuum, Thermostar<sup>TM</sup> GSD 301 T3). The analysis helps to understand the involved reactions in CNT growth, and to develop the numerical simulation model (chapter IV).

The powder samples were collected at different places on the quartz plate surface. They were then characterized by the following techniques: Scanning Electron Microscope (SEM, LEO Gemini 1530), Transmission electron microscope (TEM, Jeol 1200 EX), High resolution transmission electron microscope (HRTEM, Philips CM20-UT), Raman spectrometer X-ray diffraction (XRD, Siemens D5000, Cu-K $\alpha$  radiation ( $\lambda=1.54069\text{ \AA}$ )), Atomic force microscope (AFM, Digital Instruments Nanoscope IIIa)

## **2.3 Multiform hybrid structures of CNTs- $\mu\text{Al}_2\text{O}_3$**

As we know, the general formation process of the hybrid structures consists in two steps. First, nanoscale catalyst particles are formed on micro alumina spheres by the decomposition of ferrocene. Second, the formed catalyst particles generate MWCNT nucleation and growth. Therefore, the catalyst particles ensure the effective grafting of CNTs on  $\mu\text{Al}_2\text{O}_3$  along their axial direction. This configuration could largely take advantage of the extraordinary axial properties of CNTs, and is therefore favorable to the efficient charge and load transfer in composite materials.

In our research, pristine spherical  $\mu\text{Al}_2\text{O}_3$  particles with no pretreatment are chosen as substrate for the synthesis of the nano-micro hybrid materials. First, alumina is an efficient substrate for CNT growth in CVD process. Second, the big curvature ( $\sim 10^6\text{ rad m}^{-1}$ ) and symmetric geometry of  $\mu\text{Al}_2\text{O}_3$  promote the CNT dispersion. Finally, its excellent thermal conductivity, dielectric properties, wear-resistance and high temperature stability favor it to develop advanced multifunctional hybrid structures for a variety of applications.

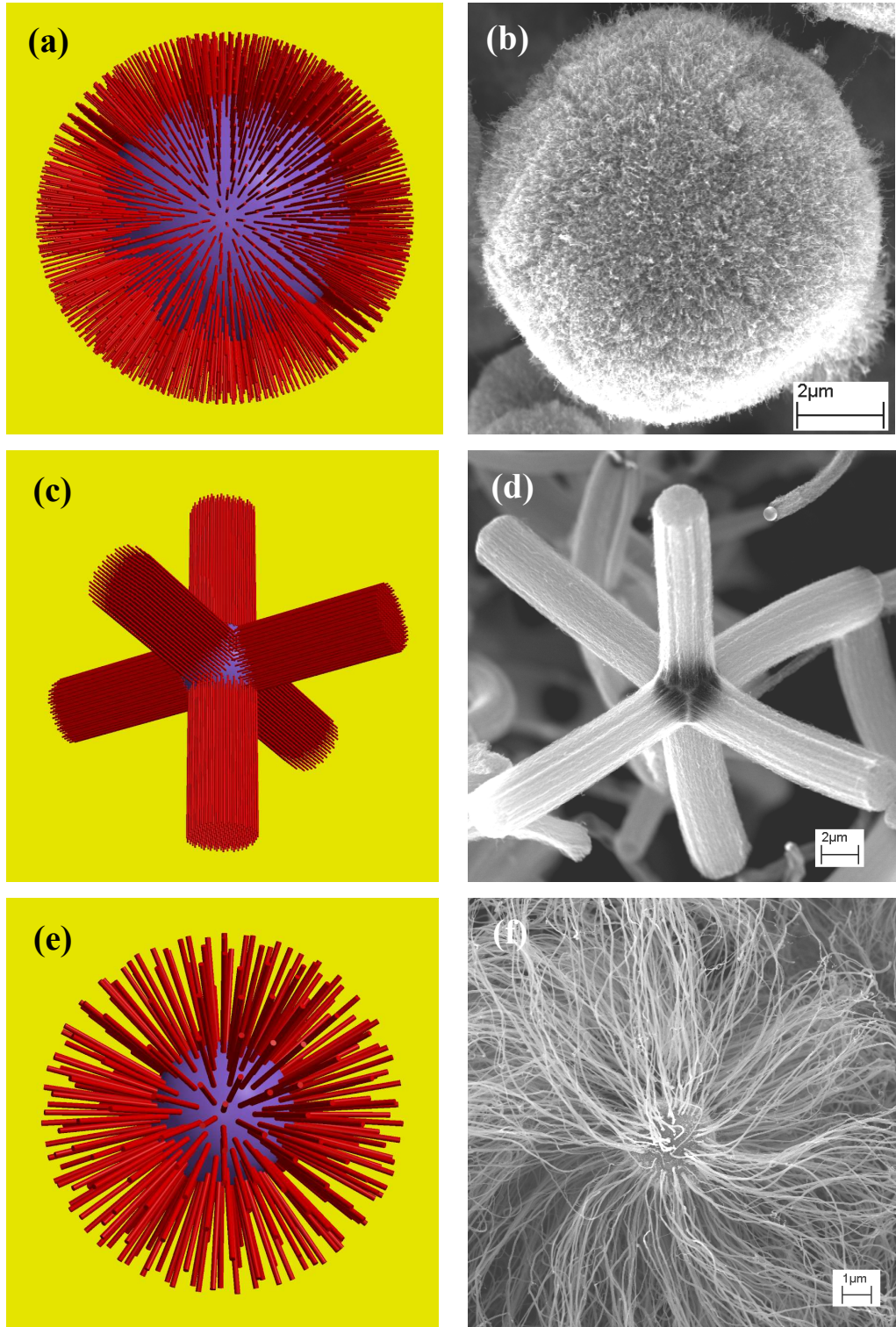


**Figure 24.** Schematics and corresponding SEM images of three distinct CNTs- $\mu\text{Al}_2\text{O}_3$  hybrid structures due to different CNT distribution patterns. (a-b) “short-dense-homogenous”: highly dense and vertically aligned short CNTs homogeneously cover the whole surface of  $\mu\text{Al}_2\text{O}_3$ ; (c-d) “six-branch”: CNTs in independent branches are uniformly distributed in six nearly orthogonal directions. (e-f) “urchin-like”: low area number density and long CNTs get out from  $\mu\text{Al}_2\text{O}_3$  like the spines of sea urchin.

Three obtained hybrid structures with distinct CNT organizations are schematically described as follows: “short-dense-homogeneous”, “six-branch”, and “urchin-like” (Fig. 24).

This classification is based on CNT diameter, length, number density and their organization states. As shown in the schematic, the consecutive structure transformation from “short-dense-homogeneous” to “urchin-like” is like flowering process in nature. As two examples, we will show experimentally the transformations by varying CNT diameter and length through just changing hydrogen ratio and temperature in the CVD process.

### **2.3.1 Variation of CNT length**

Fig. 25 shows different CNT organizations on  $\mu\text{Al}_2\text{O}_3$  and their consecutive transformation with increasing CNT length and aspect ratio (L/D, length/diameter). The aspect ratio is changed by adjusting hydrogen ratio ( $f_{\text{H}_2}$ ) in the total carrier gas flow ( $1\text{ l min}^{-1}$ ). Hydrogen flow varied from  $0.4$  to  $0.1\text{ min}^{-1}$  in series of  $0.4, 0.2, 0.1, 0.05$  and  $0.1\text{ min}^{-1}$ . The CNT synthesis temperature is kept constant at  $550\text{ }^\circ\text{C}$ . Moreover, acetylene is fed at  $10\text{ ml min}^{-1}$  simultaneously with the xylene solution.

In Fig. 25a, CNTs are organized in “short-dense-homogenous” patterns when their lengths are  $\sim 1\mu\text{m}$  and their aspect ratios are  $\sim 100$ . Scanning electron microscopy and Transmission electron microscopy characterizations display homogeneously and vertically aligned CNTs on the surface of the alumina substrate. Such hybrid structures are obtained when  $f_{\text{H}_2}$  is 40 vol. %. However, at the same hydrogen level, the whole continuous CNT layer gradually splits into six equal parts when the aspect ratio is 120 (Fig. 25b). The further decrease of  $f_{\text{H}_2}$  (20 %, 10 % and 5 %) yields to an increase of the CNT average length, and thus to an augmentation of aspect ratio ( $\sim 150$  when  $f_{\text{H}_2} = 20\text{ \%}$  (Fig. 25c);  $\sim 350$  when  $f_{\text{H}_2} = 10\text{ \%}$  (Fig. 25d) and  $\sim 450$  when  $f_{\text{H}_2} = 5\text{ \%}$  (Fig. 25e)). In the absence of hydrogen, six thinner and longer CNT branches grow at the six poles of the spherical alumina microparticle, as shown in Fig. 25f. This is explained by the fact that the decompositions of both catalyst precursor and carbon source are accelerated when hydrogen is removed from the reaction system. Whereas, a supplementary contribution of  $\mu\text{Al}_2\text{O}_3$  substrate to CNT growth is limited.

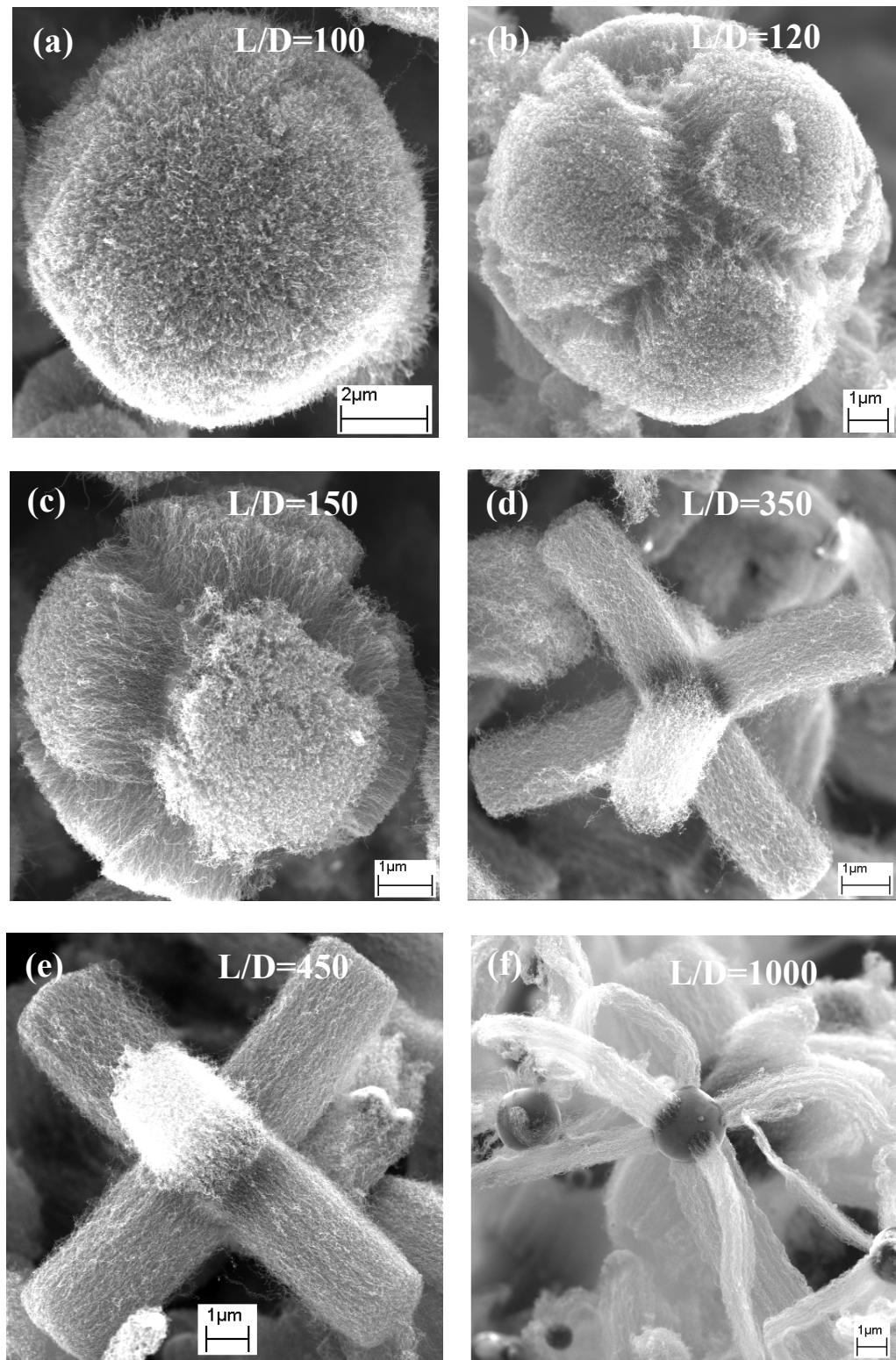


**Figure 25.** SEM images of self organized CNT patterns on  $\mu\text{Al}_2\text{O}_3$  with different aspect ratios (L/D). The hybrid organization changes from “short-dense-homogenous” to “six-branch” when the hydrogen ratio decreases from 40 % to 0. (a) L/D = 100 when  $f_{\text{H}_2}$  is 40 %; (b) L/D = 120 when  $f_{\text{H}_2}$  is 40 %; (c) L/D = 150 when  $f_{\text{H}_2}$  is 20 %; (d) L/D = 350 when  $f_{\text{H}_2}$  is 10 %; (e) L/D = 450 when  $f_{\text{H}_2}$  is 5 %; (f) L/D = 1000 when no  $\text{H}_2$ .

Fig. 26a shows the evolution of CNT aspect ratio with increasing  $f_{\text{H}_2}$  in carrier gas. The lower is the hydrogen ratio, the bigger is the CNT aspect ratio, and finally the more evident is the “six-branch” morphology. However, CNT diameter remains the same value,  $\sim 10 \text{ nm}$  (Fig. 26b), when the hydrogen ratio varies. At the mean while, CNT area number density in the growth regions keeps nearly the same level, except in the absence of hydrogen. Consequently, the increases of CNT length and aspect ratio result in the change of MWCNT organization on  $\mu\text{Al}_2\text{O}_3$  particles, which furthermore produce the variation of the hybrid structures from “short-dense-homogenous” to “six-branch”. Therefore, in this case, the lengths of CNTs are the main factors responsible for their organization on the  $\mu\text{Al}_2\text{O}_3$ . The consecutive variation of the hybrid structures lets us thinking about a natural flowering process.

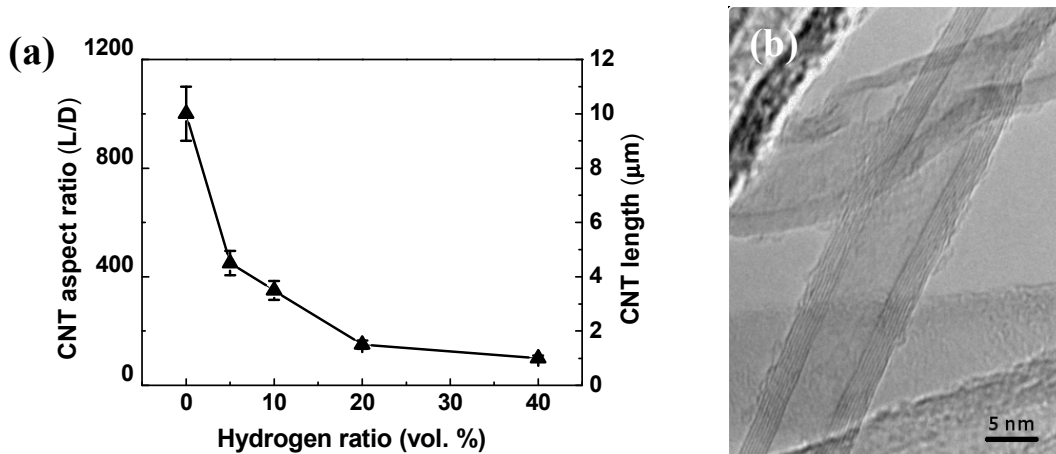


**Figure 26.** (a) The curve represents the evolution of CNT length and aspect ratio with decreasing hydrogen ratio. (b) High resolution TEM image of CNTs obtained when hydrogen ratio is 10 %.

### 2.3.2 Variation of CNT diameter and number density

Fig. 27 shows the different CNT organizations on  $\mu\text{Al}_2\text{O}_3$  and the corresponding consecutive transformations from “six-branch” to “urchin-like” states, with the increase of CNT diameter. These hybrid structures were prepared using xylene as carbon source at temperatures ranging from 550 to 800 °C. The total gas flow rate was fixed to  $0.8 \text{ l min}^{-1}$ , in which hydrogen and argon flow rates were fixed at  $0.08 \text{ l min}^{-1}$  and  $0.72 \text{ l min}^{-1}$ , respectively. Highly dense MWCNTs grown in six different parts are vertically aligned on the  $\mu\text{Al}_2\text{O}_3$  at 550 °C (Fig. 27a), and their diameters and lengths are  $\sim 10 \text{ nm}$  and  $\sim 1 \mu\text{m}$ , respectively. When CNT diameters are around 10 nm (600 °C) or 15 nm (650 °C), they are always

configured in “six-branch” (Fig. 27b and c). However, the “six-branch” structures become less evident when CNT average diameters are ~20 nm (Fig. 28a) at 700 °C (Fig. 27d). Beyond this temperature, the chemical decomposition of ferrocene and xylene is intensified. Finally, both the average diameter and length increase continuously with the temperature, while the area number density decreases. As a result, the “urchin-like” hybrid architecture appears at 750 and 800 °C (Fig. 27e-f).

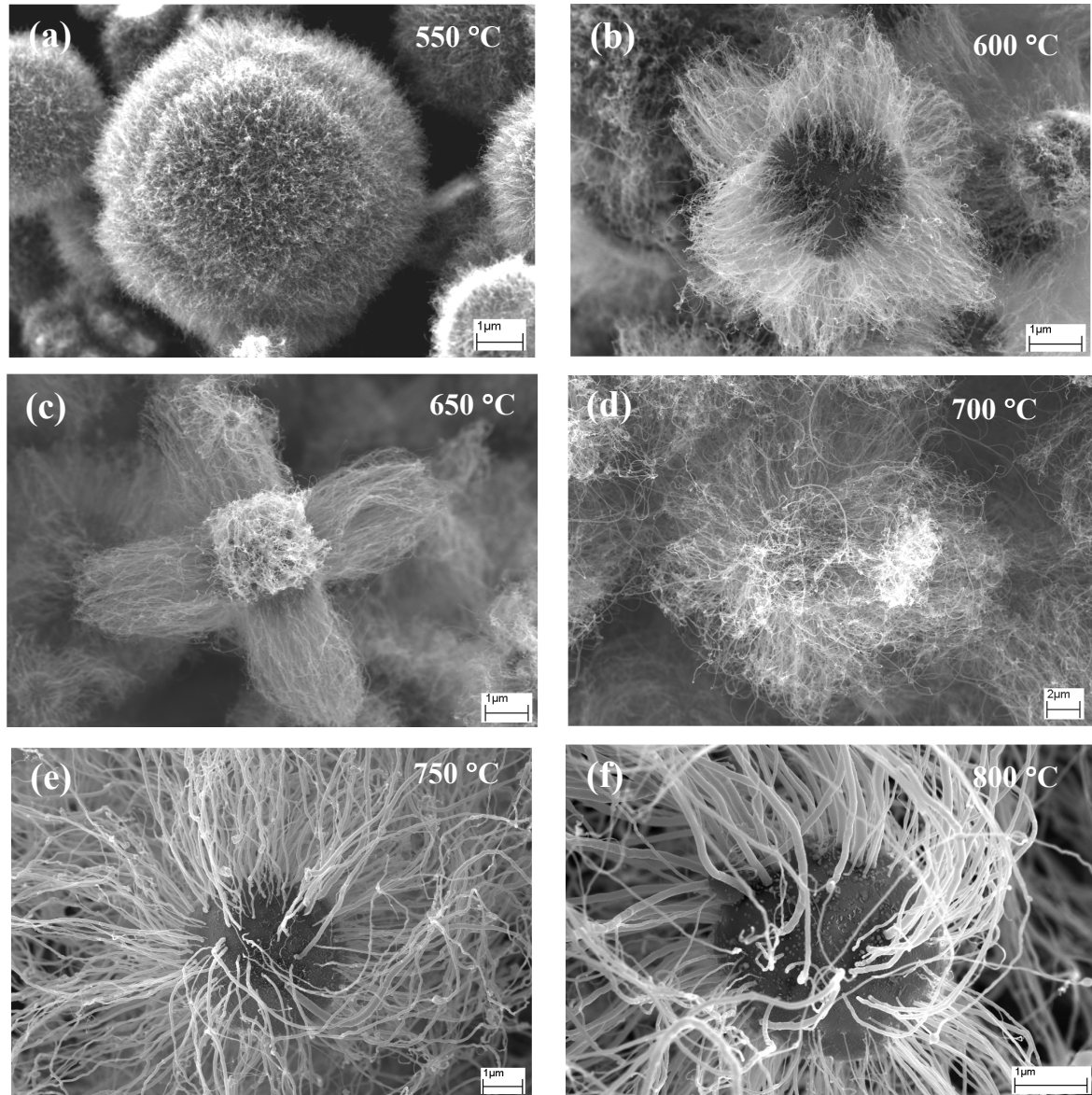


**Figure 27.** SEM images of the self-organized CNT patterns on  $\mu\text{Al}_2\text{O}_3$  obtained at different temperatures. The diameter and length were modulated by increasing the synthesis temperature from 550 to 800 °C with a step of 50 °C, as chronologically represented in images a-f.

The CNT diameters have a considerable augmentation and vary in a large region at these temperatures. Indeed, SEM and TEM observations confirm a decrease of CNT area number density on the surface of  $\mu\text{Al}_2\text{O}_3$ . The influence of the temperature on MWCNT diameter, length and aspect ratio is shown in Fig. 28b. Both diameter and length of CNTs increase continuously with the temperature, and even drastically after 700 °C. Whereas, the CNT aspect ratio in these cases fluctuates in a narrow range from 100 to 300. At this point, it is worth to note that the diameter variations contribute more than the length to the hybrid structuration.

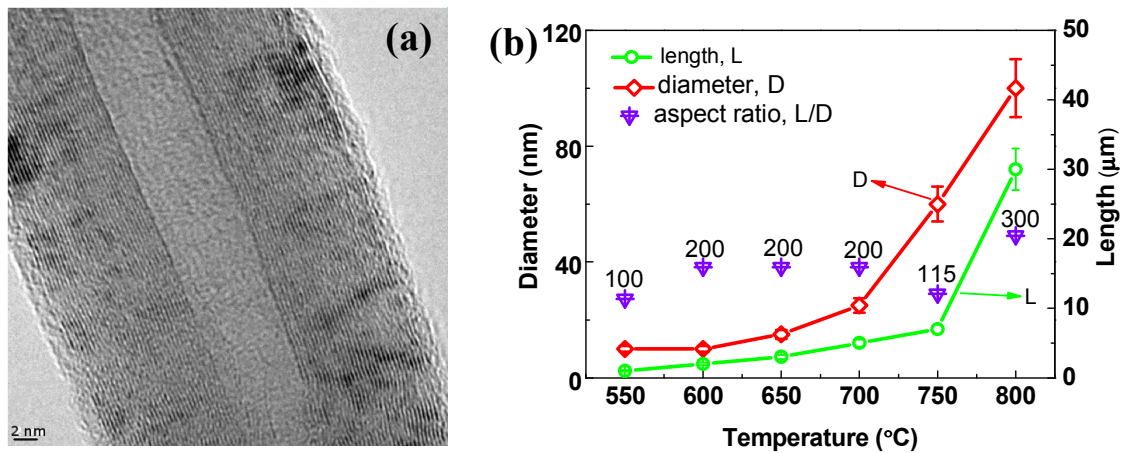


**Figure 28.** (a) High resolution TEM image of one CNT obtained at 750 °C. (b) Temperature dependence of the average diameter, length and the corresponding aspect ratio of CNTs.

It is worth noticing that CNT diameter is generally related to the number density of CNTs on the surface of particles in the catalytic CVD process. This could be previously seen in Fig. 25 and 27. CNTs with small diameters have normally higher density than those with big diameters. The high CNT growth temperature promotes normally the formation of “urchin-like” structures with lower density of CNTs when xylene is used as carbon source.

Sometimes, “urchin-like” hybrid structures with high number density of CNTs could also be seen even at high temperature, especially for the alumina particles located in the front part of the quartz plate. In this area, near the injection zone of carrier gases and carbon source-catalyst precursor solution, higher density catalyst precursors and their decomposed fragments are present. In addition, this zone contains high concentration of decomposed carbon sources which promote the CNT growth at high rates. Consequently, CNTs with high density on micro alumina spheres are formed (Fig. 29a and b). As it is shown, CNTs with high density have still “urchin-like” structures, as in the case of low density. This is different from the previous cases (Fig. 25 and 27), where the high number density of CNTs generates preferentially “six-branch”

structures at low synthesis temperatures. Such “urchin-like” structures show that big diameter CNTs, obtained at high temperatures maintain their vertical alignment on the surface of  $\mu\text{Al}_2\text{O}_3$ , even at high density. This confirms that the diameter contributes more than the number density to the self-organization of CNTs.

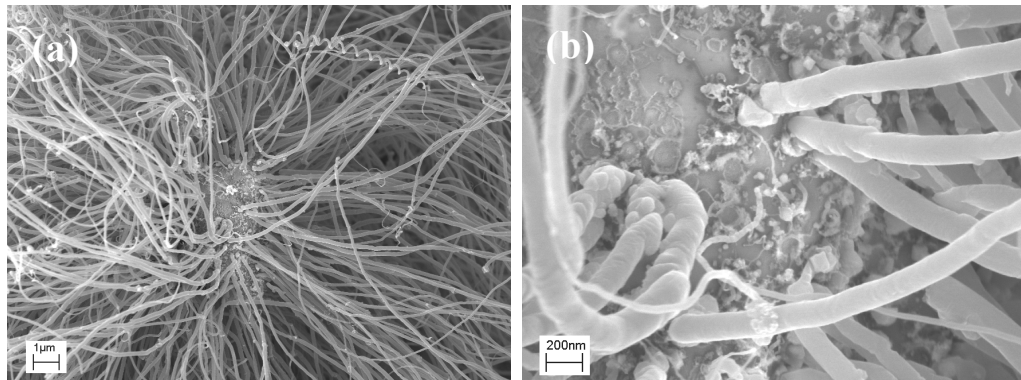


**Figure 29.** “Urchin-like” hybrid structures with high CNT area number density on micro alumina particles. The synthesis was conducted at 800 °C using xylene as carbon source. The solution (ferrocene dissolved in xylene with a concentration of 0.1 g ml<sup>-1</sup>) was injected into the furnace at 0.2 ml min<sup>-1</sup> for 15 min. (a) high CNT area number density: collected from the front of quartz plate (~20 cm before the middle part); (b) high magnification SEM of image a.

### 2.3.3 Raman spectroscopy of the three hybrid structures

Hybrid structures are characterized by Raman spectroscopy in order to understand their chemical structures and homogeneity. The spectra corresponding to the three different hybrid structures and pristine spherical alumina are plotted in Fig. 30. In the case of the “six-branch” and “urchin-like” structures, the commonly evident peaks related to alumina are visible around 220, 286 and 408 cm<sup>-1</sup>, and two slight ones at 610 and 730 cm<sup>-1</sup>. But the peak relative intensity ratios differ for these two types of structures. Furthermore, one significant peak (252 cm<sup>-1</sup>) for “urchin-like” structures disappears in the spectrum of “six-branch” structure. But for “short-dense homogeneous” structure, Raman peaks between 200 and 900 cm<sup>-1</sup> are not visible. This can be attributed to the different CNT coverage levels on alumina surface which influence the accessibility of the excitation laser. Indeed, high density CNTs cover almost the entire surface of the ceramic particles, and thus, no evident signals are detected for the “short-dense homogeneous” structure.

Then, the disorder-induced D-band ( $sp^2$ -hybridized carbon materials) is clearly visible at 1350 cm<sup>-1</sup> in all three cases. The graphite-like G band corresponding to in-plane tangential mode of two carbon atoms in a graphene unit cell is identified around 1581 cm<sup>-1</sup>.<sup>[237]</sup>

Graphitization rate of CNTs in hybrid structures could be evaluated by the half width at half-maximum of G band, the intensity of D band and the relative intensity ratio ( $I_D/I_G$ ).<sup>[238]</sup> A general comparison of the characteristic peaks of CNTs shows that “urchin-like” structures have the highest graphitization rate, in terms of sharper peaks at 1350 and 1580 cm<sup>-1</sup> and the smallest intensity ratio  $I_D/I_G$ .

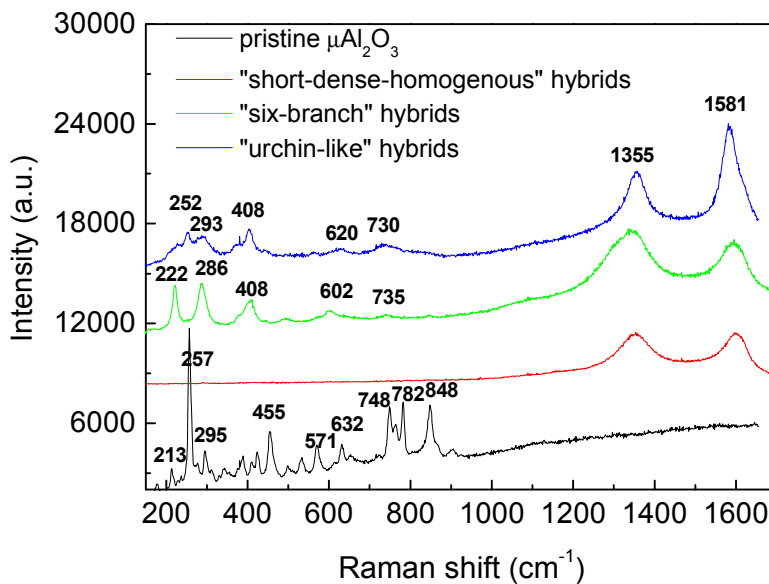


**Figure 30.** Raman spectra of pristine  $\mu\text{Al}_2\text{O}_3$  and hybrid structures with three different morphologies. The spectra were obtained at room temperature using an excitation wavelength of 514.5 nm. The legend indicates: pristine  $\mu\text{Al}_2\text{O}_3$  powders without any treatment and decomposition of carbon; “short-dense-homogeneous” hybrid structures (shown in Fig. 25a) produced at 550 °C using 0.4 l min<sup>-1</sup> H<sub>2</sub> and 10 ml min<sup>-1</sup> C<sub>2</sub>H<sub>2</sub>; “six-branch” hybrid structures (shown in Fig. 25d) produced at 550 °C using 0.1 l min<sup>-1</sup> H<sub>2</sub> and 10 ml min<sup>-1</sup> C<sub>2</sub>H<sub>2</sub>; “urchin-like” hybrid structures (shown in Fig. 27e) produced at 750 °C using 0.1 l min<sup>-1</sup> H<sub>2</sub> and 0.05 g ml<sup>-1</sup> ferrocene in xylene.

## 2.4 Thermal reinforcement of CNTs- $\mu Al_2O_3$ hybrids

### 2.4.1 Introduction

Carbon nanotubes are widely used as thermal filler because of their exceptional intrinsic thermal conductivity (TC) and aspect ratios larger than 1000. The TC of SWCNTs has been reported<sup>[36]</sup> as high as  $6000 \text{ W m}^{-1} \text{ K}^{-1}$  and the one of MWCNTs was experimentally measured at  $3075 \text{ W m}^{-1} \text{ K}^{-1}$  at room temperature<sup>[239]</sup>, which remains above the performances of diamond ( $TC = 2200 \text{ W m}^{-1} \text{ K}^{-1}$ ).<sup>[240, 241]</sup> Therefore the improvement of the TC of composites based on CNTs was extensively investigated through the past years.<sup>[61, 242]</sup> A recent work revealed that a TC of  $0.28 \text{ W m}^{-1} \text{ K}^{-1}$  or a 40% increase had been reached in composites with a 10 % weight fraction (wt%) of CNTs dispersed in polyvinylacetate matrix by using classical sonication method.<sup>[243]</sup> Another optimised configuration was proposed by Haddon and co-workers who brought into play a hybrid filler based on the combination of SWCNTs and graphite nanoplatelets.<sup>[244]</sup> An improved TC of  $1.7 \text{ W m}^{-1} \text{ K}^{-1}$  -about a fivefold increase was obtained for epoxy composites. The hybrid loading mass fraction was as high as 10 %, including 7 wt% graphite nanoplatelets and 3 wt% SWCNTs.

Those weight fractions appear to be far larger than the one of percolation, which should be smaller than 0.1% in CNT reinforced composites.<sup>[49]</sup> The percolation should yield a significant TC augmentation that was never observed so far. A previous investigation on CNT based nanofluids emphasized that the mixture TC remains thirty times lower than the expected theoretical value and much worse at low mass fractions.<sup>[62]</sup> This unsatisfying behaviour was attributed to interfacial contact resistances<sup>[245]</sup>, which several teams tried to decrease, but with little success. It is very plausible that the TC improvement at percolation was never achieved in practice due to insufficient CNT dispersion leading to the predominance of thermal contact resistances.<sup>[62]</sup> Indeed, due to their large aspect ratio, CNTs are so easy to tangle together that a large number of contacts among them produce (fig. 31a). More often, they are also observed in forms of large aggregate even after long time dispersion (Fig. 31b). Therefore, no efficient percolating networks are visible in many cases.<sup>[243]</sup>

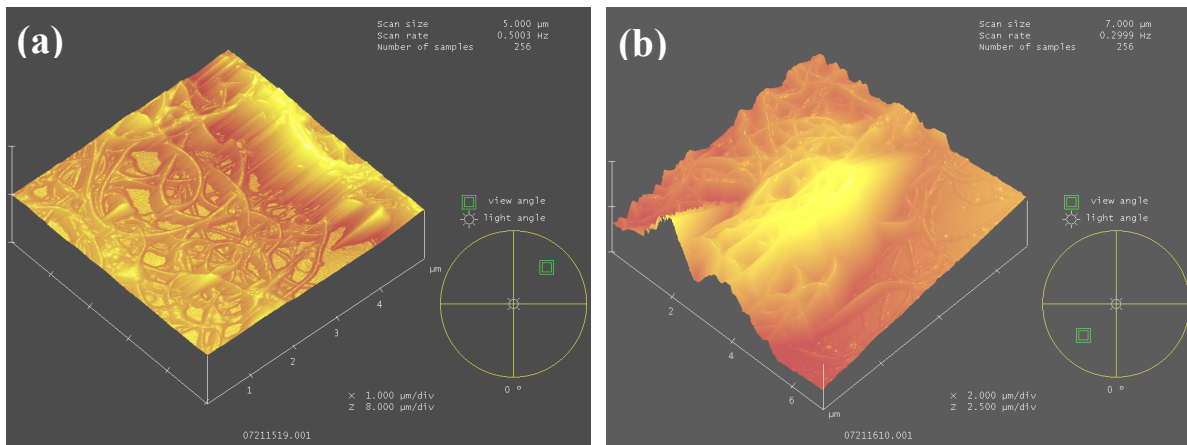


**Figure 31.** AFM images showing a large number of contacts existing among CNTs (a) and one of CNT aggregates (b). CNTs are first ultrasonically dispersed in distilled water for 10 min, and then deposited on a thin film ( $\sim 5 \mu\text{m}$  in thickness) of photoresist AZ5214E coating on a silicon wafer. After, the film is further thinned by centrifugation at 3000 rpm for 30 seconds, and finally hardened through a short exposure of ultraviolet light ( $\sim 6$  seconds).

The nano-micro hybrids could be one attracting solution to improve CNT dispersion and reduce the number of CNT contact. In this part, we test the thermal performance of CNTs- $\mu\text{Al}_2\text{O}_3$  hybrids by adding them in polymers. Optimistically, the experiments show that the epoxy composites with extremely low CNTs weight fraction corresponding to the percolation can have the predicted thermal conductivity values, which are as high as those previously obtained at weight fractions one order of magnitude larger.

The promising properties are indeed attributed to the microarchitecture of CNT- $\mu\text{Al}_2\text{O}_3$  hybrids. These nano-micro fillers provide efficient structures in terms of dispersion and the CNT network within the polymer matrix. The homogeneous dispersion of the CNT- $\mu\text{Al}_2\text{O}_3$  hybrid fillers could be realized by simply implementing a mechanical dispersion, instead of any chemical pre-treatment. In the formed composites, the number of thermal contacts between CNTs is drastically decreased, which greatly limited the phonon conduction between CNTs. Moreover, our numerical modelling reveals that the thermal conductivity of the obtained composites does not depend on the contact resistances between CNTs, but only on the CNTs thermal conductivity and geometry. Indeed, the percolation is generated and the predicted thermal conductivity enhancements of 130 % at CNT mass fractions of only 0.15 %, ten times lower than previous state of the art research is measured.

## 2.4.2 Experimental

### 2.4.2.1 Preparation of CNTs- $\mu\text{Al}_2\text{O}_3$ /Epoxy composites

In order to evaluate the influence of CNT dispersion on the thermal conductivity of the composites, the “urchin-like” CNTs- $\mu\text{Al}_2\text{O}_3$  hybrid structures (as shown in Fig. 32) were chosen as fillers to prepare the CNTs- $\mu\text{Al}_2\text{O}_3$ /Epoxy (Diglycidyl Ether of Bisphenol A, DGEBA) composites. At the mean time, the composites constituted of pristine MWCNTs (with a density of  $1.87 \text{ g cm}^{-3}$ ) and epoxy were also prepared for the purpose of comparison. Two types of fillers were synthesized by the decomposition of a mixture of xylene and ferrocene with concentration of ( $0.05 \text{ g ml}^{-1}$ ) at  $750^\circ\text{C}$  during 15 minutes. However, the synthesized MWCNTs were in the form of carpet. The spherical particles are present in the  $\alpha$ -alumina (hexagonal) crystal phase with an average diameter  $D$  ranging from 2 to  $7 \mu\text{m}$  and a density of  $3.69 \text{ g cm}^{-3}$ . Further Raman spectroscopy was performed on the two types of fillers and pristine  $\alpha\text{-Al}_2\text{O}_3$  (Fig. 33). Specific peaks corresponding to alumina and CNTs were identified in conformity with previous studies.<sup>[246, 247]</sup> The two fillers have similar structures and  $\alpha\text{-Al}_2\text{O}_3$  does not favor the formation of defects in CNTs.

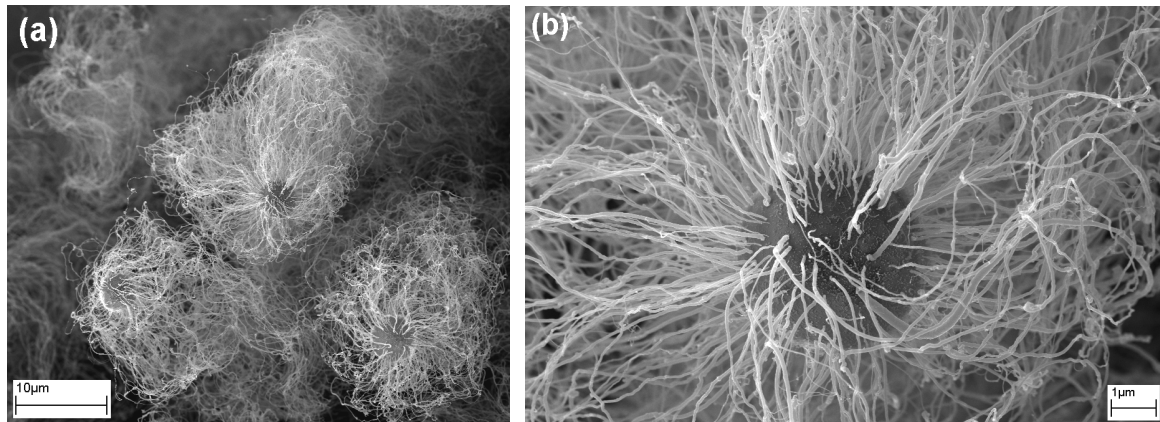


**Figure 32.** SEM images of CNTs- $\mu\text{Al}_2\text{O}_3$  hybrids. Homogenously structured micro-nanometric hybrids are obtained by CVD. The overall diameter of the CNTs- $\mu\text{Al}_2\text{O}_3$  hybrid filler is  $\sim 30 \mu\text{m}$ , the average length and diameter of the MWCNTs are  $13 \mu\text{m}$  and  $40 \text{ nm}$ , respectively. Thermogravimetric analyses indicate that the average wt% of CNTs on one alumina particle is 20 %.

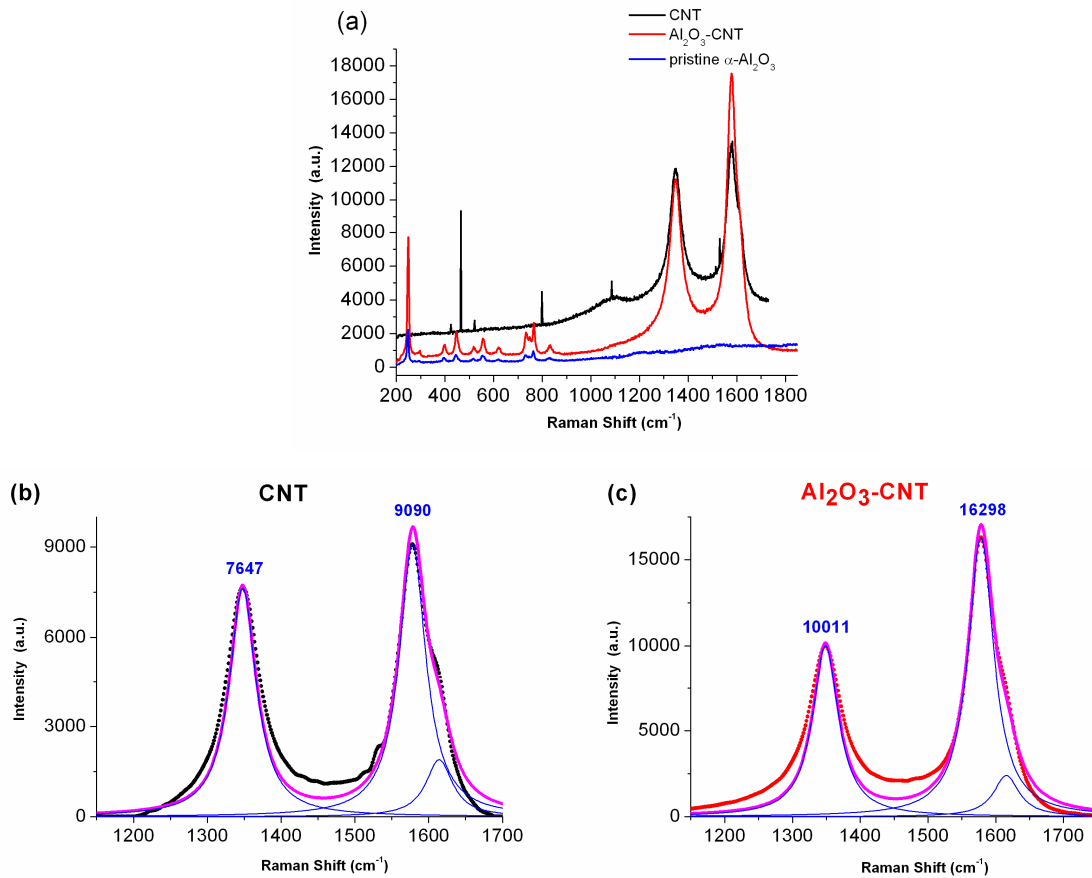


**Figure 33.** Raman spectra of CNTs, CNTs- $\mu$ Al<sub>2</sub>O<sub>3</sub> and pristine  $\alpha$ -Al<sub>2</sub>O<sub>3</sub> particles. (a) For CNT based materials, the disorder-induced D-band ( $sp^2$  –hybridized carbon materials) is clearly visible at 1350 cm<sup>-1</sup>. The graphite-like G band corresponding to in-plane tangential mode of two carbon atoms in a graphene unit cell, is identified around 1580 cm<sup>-1</sup>. Note that the sharp peaks below 1350 cm<sup>-1</sup> are not representative of CNTs. They are only due to diffusion of the silica substrate (microscope slide) where CNT were deposited for analysis. The Raman spectrum (Renishaw) of CNTs- $\mu$ Al<sub>2</sub>O<sub>3</sub> hybrids is determined by the weight modulated sum of the spectra of each component. Therefore, the presence of alumina is justified by the Raman lines below 900 cm<sup>-1</sup>. (b-c) Spectral noises and background broadband deformations from pristine CNT spectrum are removed with the Savitzky-Golay smoothing procedure. Peak fitting under Lorentzian function for D and G-bands indicates intensity ratios  $I_D/I_G$  equal to 0.84 and 0.61, for CNT and CNTs- $\mu$ Al<sub>2</sub>O<sub>3</sub>, respectively. This shows that the CNTs grown on alumina microparticles have better graphitization rate than the pristine ones.

Among the methods cited in the literature for dispersing micrometric or nanometric fillers<sup>[52, 248]</sup>, chemical surface functionalization is widely used.<sup>[249-251]</sup> Nevertheless, hard chemical modifications using surfactants can deteriorate CNTs electrical and thermal properties. Therefore, an alternative method involving mechanical strains is implemented in this work. A solution constituted of fillers and monomer was dispersed thanks to a three-roll mill (Exakt Vertriebs GmbH, Germany) following a well established protocol. A three-roll mill allows for applying controlled pressure and shear forces on the fluid containing the mixture of

CNTs and epoxy resin.<sup>[252]</sup> By controlling the gap between the rolls, their rotation speeds and the residence time of the liquid in the machine, we have finally optimized the dispersion of the fillers, as displayed in Fig. 34. Naturally, the viscosity of the blend decreased due to the mechanical forces applied on it. It has thus been deduced that the nanofiller organization is strongly related to the blending time and the gap between the rolls. Note that a too long blending time generates the detachment of CNTs from the surface of ceramic particles leading the nanofillers to aggregate again.

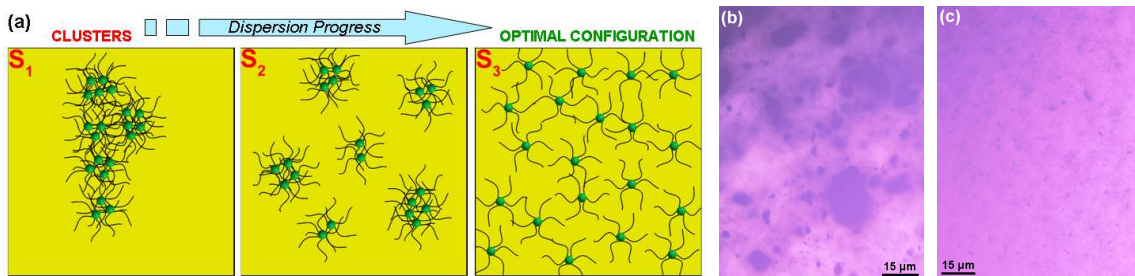


**Figure 34.** Fillers dispersion in epoxy. (a) The schematic represents the spatial arrangements of CNTs- $\mu\text{Al}_2\text{O}_3$  fillers within a polymer. Fillers dispersion is chronologically represented from the state S<sub>1</sub> (beginning of the dispersion process) to S<sub>3</sub> (end). Optical microscope images indicate pristine CNT dispersion in the monomer obtained by using a contrast enhanced silicon wafer after 5 (Fig. 34b, heterogeneous dark areas) and 20 minutes (Fig. 34c, homogeneous medium).

Then, an appropriate amount of hardener at the relevant stoichiometry was added to the latter solution. Afterwards it was cast into an aluminium mould (designed in our laboratory in agreement with ISO 527 and ASTM D638 standards) and followed by successive vacuum in order to remove air bubbles. Samples were cured at room temperature during 12 h. Finally, a postcure at 90 °C for 6 h was performed to ensure complete of curing.

#### 2.4.2.2 Measurement of thermal conductivity

Thermal conductivity characterizations were carried out on nanocomposites (1 mm thick, 10×10 mm<sup>2</sup> cross section) with a non-contact method thanks to a light flash apparatus LFA 447<sup>[245, 253]</sup> at 20 °C. Differential Scanning Calorimetry (DSC) analyses were performed to estimate the samples specific heat  $C_p$  at 20 °C (Tables 3 and 4). The average bulk densities  $\rho$  for the epoxy/CNTs and epoxy/ CNTs- $\mu\text{Al}_2\text{O}_3$  nanocomposites were measured at 1.10 g cm<sup>-3</sup> and 1.13 g cm<sup>-3</sup>, respectively. Finally, the TC  $\kappa$  is calculated from the relation:

$$\kappa = \rho \cdot C_p \cdot \alpha , \quad (1)$$

The thermal diffusivity  $\alpha$  was measured by using the following methodology: first, the front side of the sample was heated by a short Xenon light impulse while an infrared detector measured the resulting temperature rise on the back surface versus time. Secondly, the detector signal was analyzed with the one-dimensional transient heat conduction equation yielding the value of  $\alpha$  within 5 % of accuracy. The measurements were repeated 3 times and excellent reproducibility of the experiments was concluded. DSC analyses were performed on nanocomposites (weights between 5-8 mg) with a Diamond DSC Perkin Elmer. To confirm curing, a first cycle from 30 to 260 °C by a 10 °C min<sup>-1</sup> temperature ramp, and then cooling at 5 °C min<sup>-1</sup> back to 30 °C was realized. The glass transition temperature  $T_g$  and specific heat  $C_p$  were acquired on a second cycle from 0 to 200 °C (heating) and then cooling to 30 °C. Field-emission SEM observations were realized using a LEO Gemini 1530 operated at 5 kV. Nanocomposites were broken in liquid nitrogen and the fractured surface was metalized with tungsten using a Gatan 682 coating system.

**Table 3.** Thermal properties and DSC measurements of Epoxy/CNT nanocomposites at 20 °C

CNT(wt%)	$\rho(\text{g.cm}^{-3})$	$\alpha(\text{mm}^2.\text{s}^{-1})$	$C_p(\text{LFA})^{\text{a}}$	$C_p(\text{DSC})^{\text{b}}$	$T_g(\text{°C})$	$\kappa(\text{W m}^{-1} \text{K}^{-1})$
			(J.g <sup>-1</sup> .K <sup>-1</sup> )	(J.g <sup>-1</sup> .°C <sup>-1</sup> )		
0	1.12	0.13	1.33	1.21	74	0.18
0.06	1.09	0.15	1.36	1.53	70	0.25
0.1	1.11	0.17	1.43	1.25	68	0.24
0.2	1.11	0.16	1.32	1.35	71	0.24
0.4	1.06	0.15	1.40	1.46	67	0.23
0.5	1.11	0.17	1.41	1.39	67	0.26
0.6	1.10	0.18	1.25	1.29	68	0.26
0.7	1.11	0.19	1.25	1.36	70	0.29
0.85	1.10	0.24	1.37	1.33	64	0.35
1	1.11	0.23	1.28	1.36	110	0.35
1.5	1.10	0.25	1.40	1.32	96	0.363

<sup>a</sup> The  $C_p$  (LFA) column refers to specific heat measurements with the LFA apparatus by employing a comparative method based on a differential identification of a known standard sample of alumina.

<sup>b</sup> The  $C_p$  (DSC) column indicates the measurements obtained by a Diamond Perkin Elmer DSC machine. TCs were calculated considering  $C_p$  values measured by DSC rather than the ones obtained by the LFA 447 method, which slightly overestimated the values.

**Table 4.** Thermal properties and DSC measurements of Epoxy/Al<sub>2</sub>O<sub>3</sub>-CNT nanocomposites at 20 °C

CNT(wt%)	ρ (g.cm <sup>-3</sup> )	α (mm <sup>2</sup> .s <sup>-1</sup> )	C <sub>p</sub> (LFA) (J.g <sup>-1</sup> .K <sup>-1</sup> )	C <sub>p</sub> (DSC) (J.g <sup>-1</sup> .°C <sup>-1</sup> )	T <sub>g</sub> (°C)	κ (W m <sup>-1</sup> K <sup>-1</sup> )
0	1.12	0.13	1.33	1.21	74	0.18
0.02	1.13	0.14	1.44	1.39	70	0.22
0.04	1.15	0.20	1.35	1.15	71	0.26
0.06	1.17	0.20	1.21	1.25	72	0.29
0.10	1.10	0.22	1.46	1.39	69	0.34
0.16	1.09	0.28	1.56	1.32	71	0.40
0.2	1.13	0.17	1.11	1.29	98	0.25
0.36	1.13	0.18	1.24	1.26	120	0.26
0.42	1.13	0.18	1.27	1.29	89	0.26

#### 2.4.3 Results

In Fig. 35a and b, the thermal conductivity of the hybrid filler based composite increases rapidly at wt% starting from 0.02 to 0.15% and reaches the value of 0.4 W m<sup>-1</sup> K<sup>-1</sup>, which is 130 % more than the epoxy TC. To our knowledge, none of the previous works proposing CNTs based nanocomposites could succeed in preserving the unique thermal property of one MWCNT when including it as filler in a polymer composite. This increase also proves that the early percolation due to the high aspect ratio of CNTs is adequately generated starting with the smaller microparticles and then involving larger ones. When comparing the TCs of hybrid filler composite materials to those of CNTs based samples, the curves in Fig. 35 reveal that the same thermal conductivity increase appears, but at a weight fraction smaller by one order of magnitude. The comparison with previous experimental data of the literature<sup>[52, 252, 254]</sup> tends to emphasize that our mechanical dispersion process seems to be superior to the ones based on chemical treatment<sup>[254]</sup> (e.g. SDS surfactant) of CNTs, because the TC of our CNTs without any pre-treatment increases at lower wt%. This outcome is supported by previous works showing that CNT dispersion in a thermoplastic polymer is efficiently achieved under mechanical strains.<sup>[255]</sup>

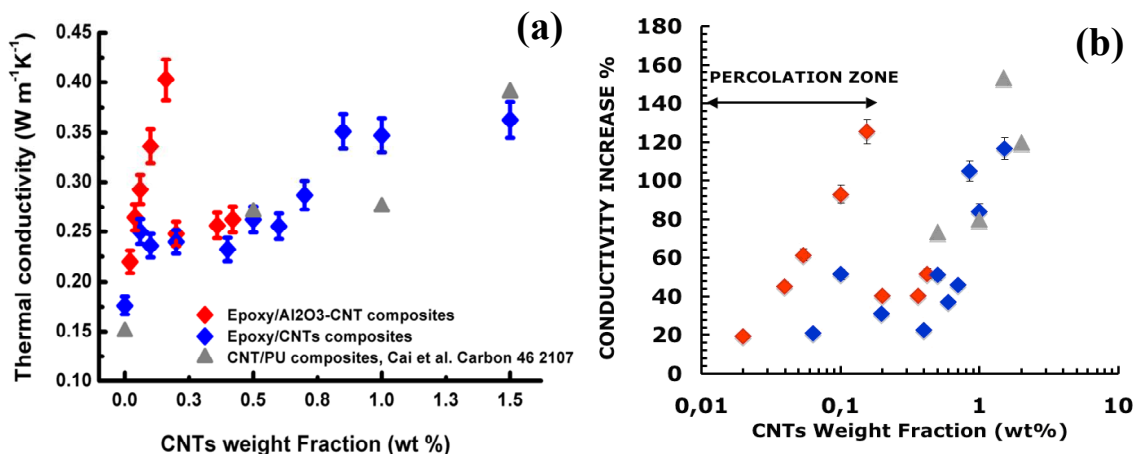


**Figure 35.** (a) Thermal conductivities of the Epoxy/CNTs composites (blue triangles) and the Epoxy/CNTs- $\mu\text{Al}_2\text{O}_3$  composites (red diamonds) versus CNT weight fraction. As a comparison, the thermal conductivities of the CNT-PU composites (pink squares) reported in ref<sup>[256]</sup> were also given. (b) The epoxy TC increases as a function of the CNTs wt%. The one order of magnitude difference in wt% between the hybrid Al<sub>2</sub>O<sub>3</sub>-CNTs and pristine CNTs TC augmentation is clearly emphasized.

After the extraordinary increase of the thermal conductivity for wt% up to 0.15 %, the TC of the hybrid filler based sample drastically decreases to the level of the CNT composites. The first explanation is that the CNT surface becomes so large that the liquid matrix cannot fill all the interstices in such a way that air bubbles with a very low TC remain in the composite. DSC analyses confirm that at high filler loadings, the structure of the polymer matrix is altered, which leads to the disruption of the nanotube-polymer interface, and also to interphase creation.<sup>[257]</sup> This change in behaviour is indicated by the modification of the glass transition temperature  $T_g$  located at 70 °C at low mass fractions but reaching higher values ~ 100 °C for loadings larger than 0.15 %. Such increase of the  $T_g$  attests the earlier arrest of the molecular chain dynamics. During composite preparation, the viscosity of the blend strongly increases for CNT mass fractions larger than 0.15 %, in such a way that the mixing between epoxy and hybrid fillers becomes more difficult to achieve. Ultimately, when nanocomposites have high filler loadings, only few air bubbles are visible during SEM analyses (Fig. 36a). The second explanation is that the area occupied by the CNTs on the microparticle increases more rapidly than the microparticles surface as the wt% increases. Our fabrication process implies that the ratio between both surfaces is indeed proportional to  $\text{wt}^{1/3}$ . When the CNT density on the microparticle surface becomes too high, CNTs agglomerate and form only a few very wide bundles in such a way that the percolation is broken (Fig. 36b). The last reason for the TC diminution at wt = 0.15% is the increase of the number of contacts between CNTs when the mass fraction exceeds the one of percolation.

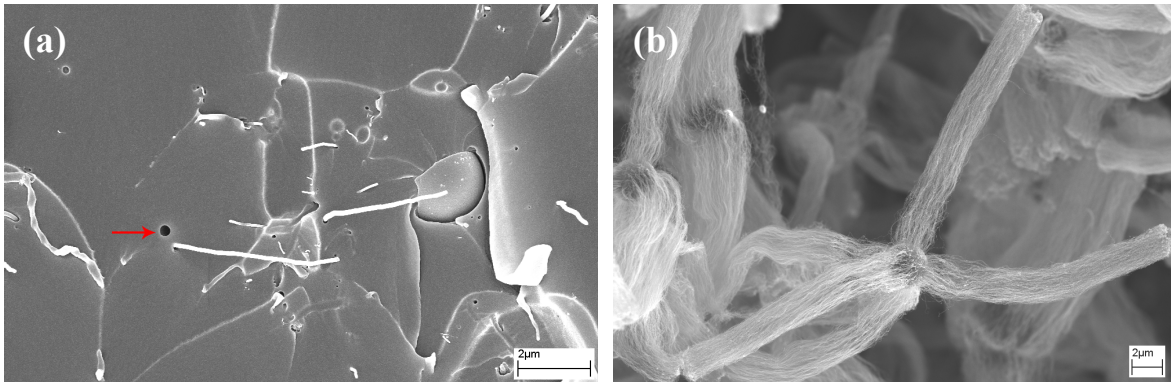


**Figure 36.** (a) SEM image of the fracture surface of epoxy composite loaded at 0.2. The alumina particle is partly visible with surrounding CNTs. Note that some CNTs are pulled off from the alumina particles and others are not visible because the image represents a fracture surface of the composite, broken in liquid nitrogen. The metallization process of the fractured surface for SEM observations explains also the fact that CNTs are detached from the surface of the ceramic particle. An air bubble, with an average diameter of 3 nm is visible, as represented with a red arrow. (b) SEM image of CNTs- $\mu\text{Al}_2\text{O}_3$  hybrids with high CNT density. Fillers with such a configuration yield composites with lower TC than the ones from Fig. 32. Ultimately, in these fillers CNT wt% becomes so large that they tend to aggregate into wide bundles, which breaks the percolation.

Additional fabrication and characterization of epoxy-Al<sub>2</sub>O<sub>3</sub> nanocomposites loaded at 0.5 and 1 wt% have provided TCs of 0.23 and 0.16 W m<sup>-1</sup> K<sup>-1</sup>, respectively. Those figures highlight the degradation of the thermal performances after reaching wt% = 1% even without the presence of CNTs. This result tends to corroborate the evolution of the TC in our CNTs- $\mu\text{Al}_2\text{O}_3$  polymer composites. These explanations might open the path for new improvements but we emphasize that using CNTs at mass fractions larger than the one of percolation does not take advantage of the CNT assets that are put forward in this work.

#### 2.4.4 Numerical simulation of thermal reinforcement

The room temperature TCs of epoxy polymer and  $\alpha$ -alumina particles of  $\kappa_m = 0.17 \text{ W m}^{-1} \text{ K}^{-1}$  and  $\kappa_{\text{Al}_2\text{O}_3} = 46 \text{ W m}^{-1} \text{ K}^{-1}$  respectively, are obtained from the literature and confirmed by our experiments.<sup>[52, 258]</sup> The prediction of  $\kappa$  is conducted in a preliminary stage by deriving the non percolating CNTs- $\mu\text{Al}_2\text{O}_3$  hybrid fillers. The approximations of a small volume fraction  $\eta$  of the filler (<0.3%) and a large filler TC compared to the one of the matrix yield:<sup>[259]</sup>

$$\kappa = \kappa_m \cdot (1 + 3\eta) \quad (2)$$

Note that the contact resistance between the filler and the matrix is neglected, which is a reasonable guess due to the very low TC of the epoxy. Eq. (2) clearly shows (i) that the TC contribution of the hybrid fillers is added to the one of the matrix which supports the idea that the filler contribution is not correlated to the one of the matrix and (ii) that this TC contribution in relative value should not exceed the wt% because  $3\eta \approx \eta\rho_{Al_2O_3}/\rho_{Epoxy} < 1$  wt%. The increase in TC obtained when adding CNTs is larger than 100% instead. The result of Eq. (2) therefore leads to the conclusion that only percolating CNTs are responsible for this outstanding augmentation. Another consequence to Eq. (2) is that the effect on heat conduction of alumina microparticles, if taken as the only filler, is remarkably negligible. This point supports the assertion that the only role of the microparticles is to structure CNTs with optimal dispersion in such a way that it seems sound to compare the TCs of hybrid charges and pure CNT based samples according to their CNT wt%.

First, this model quantifies the nanocomposites TC for a specified microparticle diameter  $D$  by establishing a simple model based on a cubic element of edge length  $L$  that includes one microparticle and its surrounding CNTs, as illustrated in Fig. 37a. We express the thermal resistance in one direction in this volume at the percolation threshold. This resistance is decomposed into the microparticle resistance, the thermal resistances of the CNTs having approximately the same direction as the heat flow and the contact resistance between the CNTs linking two microparticles. It can be easily shown that the microparticle resistance is significantly smaller than the one of CNTs and of the CNTs-CNTs contact. Consequently, the filler TC  $\kappa_F$  arises from the Fourier Law of heat conduction as a function of the CNT length  $L_{CNT}$ , cross section  $S_{CNT}$  and TC  $\kappa_{CNT}$  as well as of the number  $N_{CNTs}$  of CNTs linking two microparticles in the following form:

$$\kappa_F = N_{CNTs} \left[ \frac{2L_{CNT}}{\kappa_{CNT} S_{CNT}} + R_C \right]^{-1} / L = N_{CNTs} \frac{G_{CNT}}{L} \quad (3)$$

The term inside brackets can be identified as the conductance  $G_{CNT}$  associated with two CNTs in contact.  $R_C$ , which represents the contact resistance between two CNTs due to weak Van der Waals interactions, can be derived from reference [260] by rescaling the published data obtained for small CNT diameters by the ratio of the CNT cross sections -the resistance  $R_C$  being inversely proportional to the contact area and the ratio of the contact areas being equal to the ratio of the cross sections-, which provides the value of  $R_C = 9.26 \times 10^6 \text{ K W}^{-1}$ .  $\kappa_{CNT}$  is extracted from reference [38] owing to a linear interpolation depending on the CNT diameter. The obtained value of  $\kappa_{CNT} = 2386 \text{ W m}^{-1} \text{ K}^{-1}$  is kept as a reference. The total number of CNTs noted  $N$  on one microparticle can be deduced from the known ratio of 0.25 between the

mass of the  $N$  and the mass of one microparticle. We assume a homogenous percolation where the microparticles form a cubic lattice in such a way that  $N_{CNTs} = N/6$  CNTs are linked with another microparticle because of the six possible directions available in a cubic lattice. The second neighbours are not percolating and are consequently excluded. The ratio between the contact resistance  $R_C$  and CNTs resistances  $2L_{CNT}/\kappa_{CNT}S_{CNT}$  being in the order of 0.516, we infer that the contributions of the contact resistance and the CNTs resistances are in competition. A noticeable predominance of CNTs resistance can still be established.

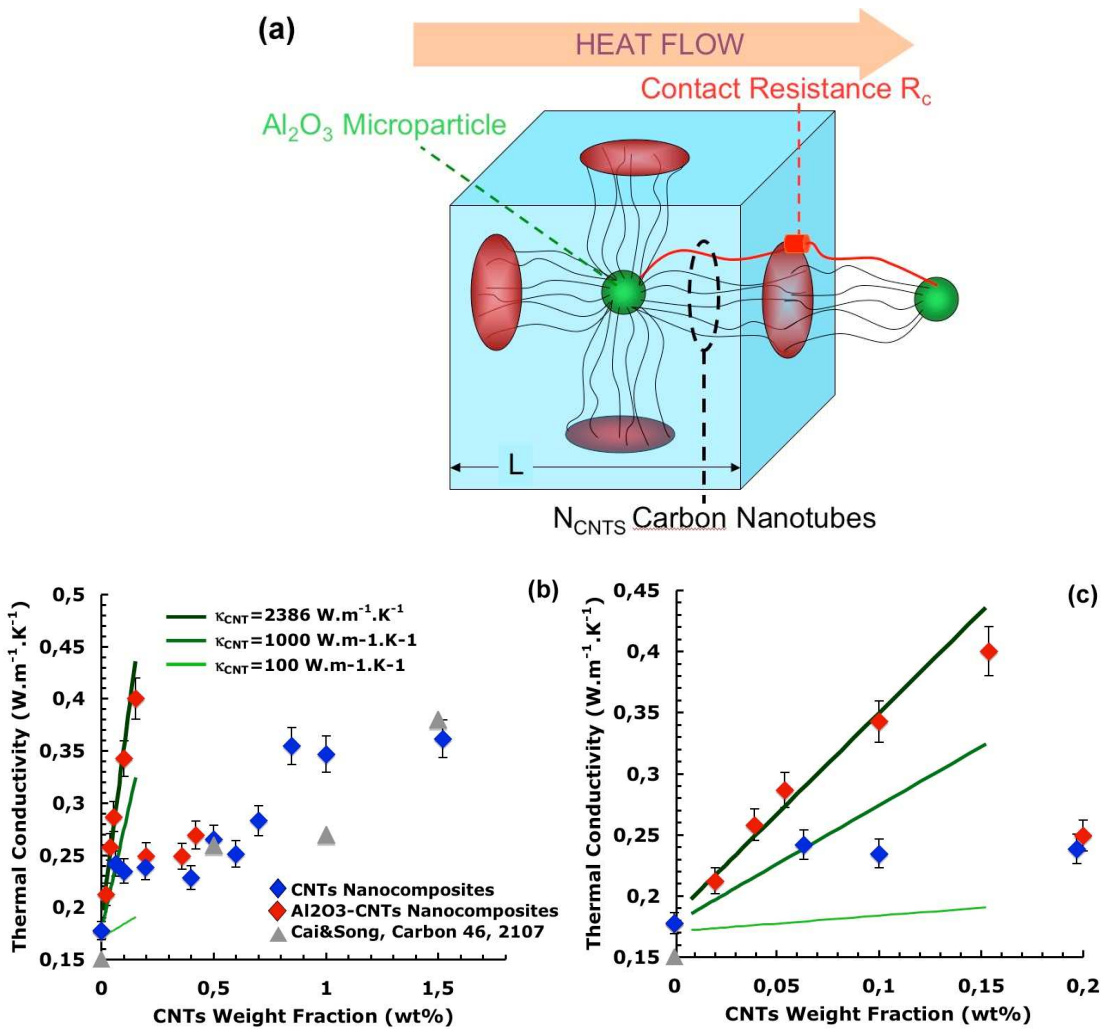


**Figure 37.** (a) Schematic of the cubic element used in the model yielding the hybrid filler TC. (b-d) Nanocomposites TCs versus CNT wt%. In schematic (a), the thermal resistance of the cube is modelled in the direction of the heat flow.  $R_c$  is the thermal contact resistance between two CNTs linking two microparticles belonging to two neighbouring cubes.  $N_{CNTs}$  is the number of those CNTs having the length  $L_{CNT}$ , the cross section  $S_{CNT}$  and the thermal conductivity  $\kappa_{CNT}$ . Note that CNTs with directions perpendicular to the cube front face are not represented. (b-c) The measured TCs of the hybrid  $\text{Al}_2\text{O}_3$  microparticles-CNT fillers (red diamonds) and of the CNTs (blue diamonds) based composites described in this work are reported as well as the recent data from the literature [256] (grey triangles). The prediction of Eq. (6) is also indicated for CNTs

thermal conductivity of  $2386 \text{ W m}^{-1} \text{ K}^{-1}$  (dark green thick line)  $1000 \text{ W m}^{-1} \text{ K}^{-1}$  (green line) and  $100 \text{ W m}^{-1} \text{ K}^{-1}$  (light green thin line). (c) Thermal conductivity enhancement at ultra-low mass fraction of hybrid fillers is clearly identified.

In a second phase, the distribution of the microparticle diameter, which is supposed to be uniform, is taken into account. The values of  $N_{\text{CNT}}$  and  $L = 2L_{\text{CNT}} + D$  at a given microparticle diameter  $D$  are indeed imposed by the homogenous percolation or the equality between  $L$  and the lattice constant of a cubic lattice formed by the microparticles. This equality yields the following mass fraction at percolation:

$$wt = 0.13 \frac{\rho_{Al_2O_3}}{\rho_{\text{Epoxy}}} \left( \frac{D}{L} \right)^3 \quad (4)$$

This simplified expression is obtained by noticing that the CNT mass in the cubic element equals to the mass of one microparticle divided by four. Considering  $D$  in the range of 2 to 7  $\mu\text{m}$ , the corresponding mass fraction is found in the interval of 0.01 to 0.3%. Introducing the mass fraction in Eq. (3) brings the following new expression for the TC:

$$\kappa(wt) - \kappa_m = wt \frac{m_{\text{Epoxy}}}{6m_{\text{CNT}}} \frac{G_{\text{CNT}}}{L} \quad (5)$$

where  $m_{\text{CNT}}$  and  $m_{\text{Epoxy}}$  are the masses of one CNT and of the epoxy included in the  $L^3$  volume, respectively. Starting from the lowest mass fraction where only the smallest microparticles will percolate, we progressively add the contributions of larger microparticles as  $wt$  increases by integrating and normalizing the second term in the RHS of Eq. (5) between the lowest and the running mass fractions,  $wt_{\min}$  calculated from Eq. (4) when  $D = 2 \mu\text{m}$  and  $wt$ , respectively, in order to reach the following expression:

$$\kappa_{\text{tot}}(wt) - \kappa_m = \frac{wt + wt_{\min}}{2} \frac{m_{\text{Epoxy}}}{6m_{\text{CNT}}} \frac{G_{\text{CNT}}}{L} \quad (6)$$

The TC increase appears as proportional to the  $wt\%$  as well as to  $\kappa_{\text{CNT}}$  and  $S_{\text{CNT}}$  and inversely proportional to  $L$  and  $L_{\text{CNT}}$ . The validity of this cumulative description relies on the assumption that the percolating networks based on microparticles with different diameters do not interfere.

As shown in Fig. 37b and c, the agreement between our model and experimental values appears when  $\kappa_{\text{CNT}}$  approaches the reference value of  $2386 \text{ W m}^{-1} \text{ K}^{-1}$ , an optimal match

between the model and the four first points is reached when  $\kappa_{\text{CNT}} = 2180 \text{ W m}^{-1} \text{ K}^{-1}$ , which proves that the TC of the single CNT is retrieved within an inaccuracy range smaller than 10 % in the composite, and that the theoretical percolation limit is also obtained.

In summary, we found the remarkably low percolation threshold and high TC of Al<sub>2</sub>O<sub>3</sub>-CNT filler based nanocomposites taking advantage of the large aspect ratio of CNTs as well as of their unique thermal conductivity. Preserving the thermal conductivity of one MCWNT and observing the theoretical percolation from the thermal conductivity evolution are proven for the first time in this work. This new field of performances is unlocked by generating a CNT microarchitecture as well as by developing a mechanical dispersion. We believe that those structuration and dispersion have significantly reduced the number of thermal contact resistances between CNTs. The result is an excellent CNT dispersion leading to the observed limit properties. We expect very significant impacts for thermal interface materials especially concerning microelectronic devices through the increase of the packaging materials TC. The design of an industrial composite material combining improved thermal performances and satisfying mechanical properties that are not affected by a high filler loading, also becomes achievable.

## 2.5 Conclusion

Multiform nano/micrometer hybrid materials have been produced using floating CVD by in situ grafting CNTs on the surface of  $\mu\text{Al}_2\text{O}_3$ . It is found that CNT organization is strongly dependent on its diameter, length, and area number density on the microparticles. The different organization states result three distinct hybrid architectures: “short-dense-homogeneous”, “six-branch” and “urchin-like”. MWCNTs are initially organized in “short-dense-homogenous” state for small diameter (10 nm) and have low aspect ratio ( $L/D=100$ ), then in “six-branch” for higher aspect ratio due to length increase, and last in “urchin-like” for diameter increase. The consecutive transformations of the hybrid structures, like a flowering process in nature, are demonstrated, for example, by adjusting hydrogen ratio and temperature. Ultimately, the reported multiform hybrid structures can be easily produced in large scales (Appendix 1).

Enhanced thermal conduction is found when the CNTs- $\mu\text{Al}_2\text{O}_3$  is used as fillers in polymer composites. The CNTs- $\mu\text{Al}_2\text{O}_3$ /Epoxy composites show a remarkably low percolation threshold (0.15 wt % CNTs) and high thermal conductivity (130 % enhancement) which is as high as the values previously obtained at wt % one order of magnitude larger. In these composites, well-organized CNTs- $\mu\text{Al}_2\text{O}_3$  structures and homogeneous dispersion of CNTs have significantly reduced the number of thermal contact resistances between carbon nanotubes (CNT), and thus take mostly advantage of the large aspect ratio of CNTs as well as of their unique TC. The multifunctional properties of the CNTs- $\mu\text{Al}_2\text{O}_3$  composites make them promising candidates for various applications in the fields of microelectronic devices or aeronautics.

The nano-micro hybridization presented in this chapter provides one efficient way to control CNT organization states and furthermore improve its dispersion in composites. The resulted CNTs based hybrid materials exhibit the unique multifunctional properties and incomparable advantages over pristine CNTs in the field of composites. Thus, it is encouraged to study in detail their formation mechanisms in order to develop in a large scale these hybrid materials with well-controlled structures.

# Chapter III

## Studies on formation mechanism of multiform CNTs- $\mu$ Al<sub>2</sub>O<sub>3</sub> hybrid structures

### 3.1 Introduction

The CNTs- $\mu$ Al<sub>2</sub>O<sub>3</sub> hybrid structures are promising multifunctional fillers in composites. Their polymer composites have remarkably low thermal percolation threshold. A high reinforcement in thermal conduction of the composites could be achieved using ultra-low mass fraction of CNTs, due to the unique architecture and improved dispersion of CNTs in matrix material. The thermal contact resistance between CNTs in the composites is greatly dependent on their organization in the hybrid structures. Therefore, it is desired to produce well-defined hybrid structures with controlled CNT organization, in order to develop the composites with high thermal performance. The realization of the control over the hybrid structures strongly relies on the understanding of CNT growth processes and their organization mechanism on micro substrates.

In this chapter, we firstly study the influence of CVD parameters on CNT growth on micrometer ceramic particles, and on geometry of CNTs- $\mu$ Al<sub>2</sub>O<sub>3</sub> hybrid structure. The parameters include temperature, catalyst precursor, carbon sources, and hydrogen ratio. Then, we discuss about the significant roles played by the alumina spherical microparticles in the construction of the multiform hybrids. The impacts of microparticle morphology and crystallographic structure are specially pronounced. The next part demonstrates the connection between CNTs and microparticles, and the CNT growth dynamics. Finally, the formation mechanism of multiform hybrid structures is uncovered. The specific surface crystal steps potentially determine the heterogeneous growth of CNTs on  $\mu$ Al<sub>2</sub>O<sub>3</sub>, and the number of CNT branches in the hybrid structures, as well as the branch orientations. The self-assembly of CNTs on  $\mu$ Al<sub>2</sub>O<sub>3</sub> is due to weak Van der Waals interaction forces between neighboring CNTs. The proposed “nano-cantilever” model explains that the CNT self-assembly is greatly dependent on their diameter, length and number density on  $\mu$ Al<sub>2</sub>O<sub>3</sub>.

### 3.2 Influences of CVD parameters

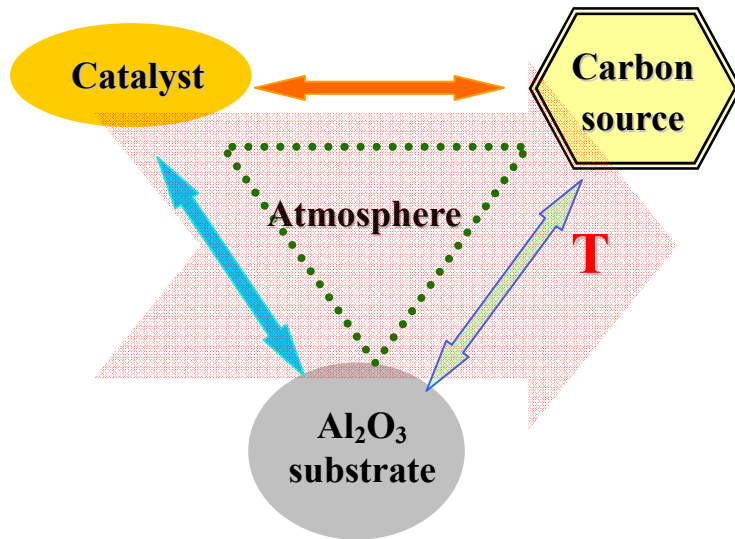


**Figure 38.** Schematic of key parameters and their correlative interactions during the construction of CNTs- $\mu$ Al<sub>2</sub>O<sub>3</sub> hybrid structures by CVD method.

The CNTs- $\mu$ Al<sub>2</sub>O<sub>3</sub> hybrids are obtained by in-situ growing MWCNTs on the surface of the pristine  $\mu$ Al<sub>2</sub>O<sub>3</sub>. Briefly, the construction CVD process mainly consists in the following three steps. First, it is the nucleation and growth of iron particles, which result from the thermal decomposition of catalyst precursor-ferrocene on the  $\mu$ Al<sub>2</sub>O<sub>3</sub> particles. Second, the carbon containing species are catalytically decomposed on the iron nanoparticles to enable CNT growth. Third, the growing CNTs organize into various arrangement states. Different organizations of CNTs result in distinct hybrid structures with varied morphologies. The above processes occur simultaneously in the gas atmosphere inside CVD reactor and on the surface of micro substrates. Thermal decomposition reactions in gas atmosphere serve as indispensable support of catalyst and carbon atoms. They are greatly dependent on temperature, catalyst precursor, carbon sources and atmosphere condition. Meanwhile, the surface properties of substrate might directly determine initial nucleation of catalyst particles and all consecutive surface reactions. There are strong correlative interactions between these factors, and their relationships are schematically shown in Fig. 38.

The following parts will separately present the influence of each CVD parameter on the formation of CNTs- $\mu$ Al<sub>2</sub>O<sub>3</sub> hybrids. The interactive relation and the synergetic corporation of

the parameters are emphasized in order to develop high quality hybrid materials with controlled structures.

### 3.2.1 Catalyst precursor

#### 3.2.1.1 Thermal decomposition of ferrocene

In our studies, ferrocene, Fe(C<sub>5</sub>H<sub>5</sub>)<sub>2</sub>, is used as catalyst precursor for catalytic growth of CNTs on micrometric ceramic particles. It is well known that ferrocene is an organometallic chemical compound having a ‘sandwich’ structure of bis-cyclopentadienyl iron<sup>[261]</sup>. The iron atom in ferrocene is normally assigned to the +2 oxidation state. Each cyclopentadienyl (Cp) ring is then allocated a single negative charge, bringing the number of  $\pi$ -electrons on each ring to six, and thus making them aromatic. These twelve electrons (six from each ring) are then shared with the metal via covalent bonding, which, when combined with the six *d*-electrons on Fe<sup>2+</sup>, results in the complex having an 18-electron, noble gas electron configuration. Consequently, ferrocene is an air-stable solid, whose melting and boiling points are  $\sim$  174 °C and  $\sim$  249 °C, respectively. Meanwhile, it is easy to sublime at temperatures as low as  $\sim$  90 °C<sup>[262]</sup>. Often, ferrocene is used as catalyst precursor in CVD process for catalytic growth of CNTs. It could be vaporized in the first stage of furnace having a low temperature, and then carried by carrier gas into the second reaction zone to grow CNTs. Alternatively, as ferrocene is soluble in most organic solvents, it could also be directly dissolved into carbon source solutions such as xylene, benzene and toluene. Then, the resulted solution is directly injected into CVD reactor with the help of carrier gas. Here, we use the latter method. Concretely, ferrocene is first dissolved into xylene solution, which is then injected into the reactor in the form of spray.

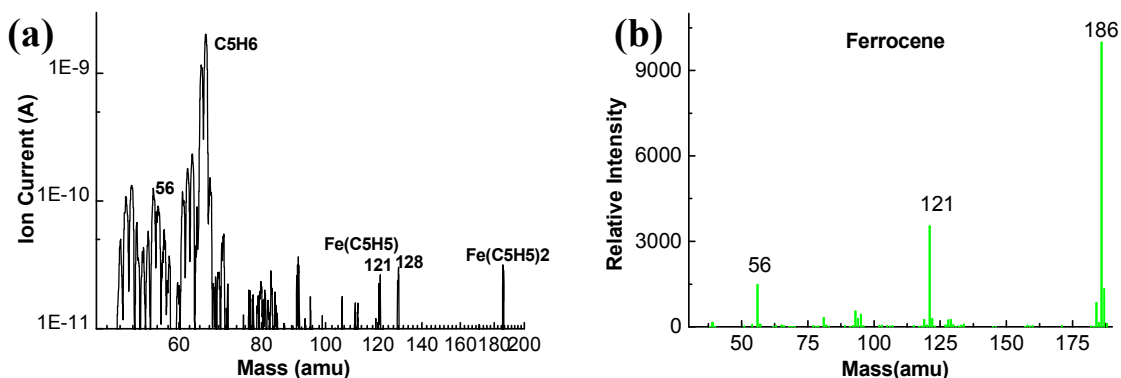
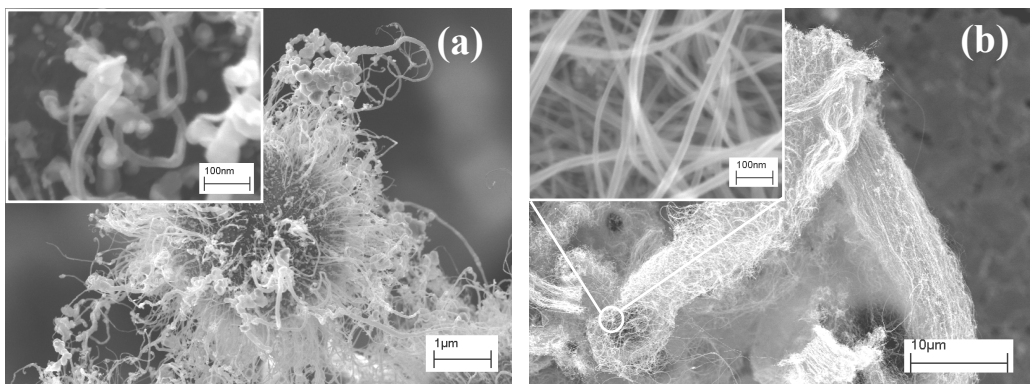


Figure 39. (a) Mass spectrum measured during the thermal decomposition of ferrocene in the center of the quartz tube at 400 °C. (b) Standard mass spectrum of ferrocene (data from NIST).

The thermal decomposition temperature of ferrocene has been reported around 400 °C<sup>[119]</sup>. Fig. 39a shows the mass spectrum of the exhaust gas from the thermal decomposition of ferrocene in the quartz tube at 400 °C. Comparing with the mass spectrum of pure ferrocene (Fig. 38b), it could be seen that cyclopentadiene (C<sub>5</sub>H<sub>6</sub>) is the main decomposition product, in addition to iron.

It is worth noting that the thermal decomposition of ferrocene does not produce pure iron nano particles. The sublimation temperature has considerable influence on the final product structure. A various number of structures have been reported by high temperature pyrolysis of ferrocene at different sublimation temperatures<sup>[262]</sup>. Indeed, in the final products, there exist amounts of CNTs filled with iron particles in their centers, as well as iron particles tightly surrounded by carbon layers. Fig. 40a shows the hybrid structures obtained by the direct decomposition of pure ferrocene at 750 °C under argon (720 ml min<sup>-1</sup>) and hydrogen (80 ml min<sup>-1</sup>) atmosphere. Ferrocene powder was evaporated at a rate of ~30 mg min<sup>-1</sup> in the front of quartz tube at a temperature about 250 °C. The diameter of iron filled CNTs range from 15 to 50 nm, and the length was about 2-2.5 μm. On the other hand, clean CNTs in bundles as long as ~ 130 μm are formed on  $\mu$ Al<sub>2</sub>O<sub>3</sub> at 750 °C (Fig. 40b), when acetylene is fed during the evaporation of ferrocene at lower rate (~ 20 mg min<sup>-1</sup>). The CNT diameter is around 15 nm. This indicates that the nucleation of catalyst particles from ferrocene on  $\mu$ Al<sub>2</sub>O<sub>3</sub> is not an isolated thermal decomposition process. Furthermore, the catalytic growth of CNTs is also dependent on carbon source and CVD atmosphere conditions.



**Figure 40.** (a) SEM images of iron-filled carbon nanostructures and carbon surrounded iron particles formed on  $\mu$ Al<sub>2</sub>O<sub>3</sub> by decomposition of ferrocene at 750 °C. Left-upside: higher magnification SEM image of a local region on the  $\mu$ Al<sub>2</sub>O<sub>3</sub> surface. (b) SEM images of clean and long CNTs grown on  $\mu$ Al<sub>2</sub>O<sub>3</sub> by decomposition ferrocene under C<sub>2</sub>H<sub>2</sub> containing atmosphere.

In the followed studies, one-step injection of ferrocene is used in order to get a better

control on Fe/C ratios in CVD reactor. Ferrocene is dissolved into xylene solution according to certain percentages. The mixture is directly injected by a syringe injector, and then it is carried into the reaction zone by carrier gas.

### 3.2.1.2 Influence of ferrocene concentration in xylene

In the first place, we have studied the influence of ferrocene concentration in xylene solution on the formation of CNTs- $\mu$ Al<sub>2</sub>O<sub>3</sub> hybrid structures at 780 °C. The flow rates of argon and hydrogen were 0.72 and 0.08 l min<sup>-1</sup>, respectively. The ferrocene concentrations used and the corresponding Fe/C ratios are shown in table 5. The ferrocene-xylene solution injection rate was ~0.2 ml min<sup>-1</sup>. The injection lasted for 20 min.

**Table 5.** Concentrations of ferrocene dissolved in xylene solution and corresponding molar ratios between iron and carbon atoms

Parameters	variation range				
Ferrocene concentration (g ml <sup>-1</sup> )	1E-3	5E-3	1E-2	5E-2	1E-1
Fe/C molar ratio	8.28E-5	4.12E-4	8.22E-4	3.98E-3	7.65E-3

Ferrocene concentration ( $c_{\text{ferrocene}}$ ) has a significant influence on CNT growth on  $\mu$ Al<sub>2</sub>O<sub>3</sub>, especially on CNT diameter and length (Fig. 41). Only few CNTs grow on the surface of the microparticles when  $c_{\text{ferrocene}}$  is 0.001 g ml<sup>-1</sup>. These short CNTs are like “spaghettis” which randomly stick on several parts of the particle surface (Fig. 41a). The diameter of CNTs is ~10 nm. When  $c_{\text{ferrocene}}$  increases to 0.005 g ml<sup>-1</sup>, highly dense CNTs tightly cover the whole surface of particles (Fig. 41b). Meanwhile, amounts of small carbon encapsulated iron particles are also deposited both on the surfaces of CNTs and micro particles. CNT diameter is in a range from 15 to 20 nm, and its length is ~2  $\mu$ m. By contrast, when  $c_{\text{ferrocene}}$  is 0.01 g ml<sup>-1</sup>, low density CNTs are vertically deposited on the surface of  $\mu$ Al<sub>2</sub>O<sub>3</sub>, resulting in the “urchin-like” hybrid structures. Compared with the narrow CNT diameter distribution obtained at lower  $c_{\text{ferrocene}}$ , CNTs have the diameters varying in a large range from 15 nm to more than 100 nm, and most of them are larger than 30 nm (Fig. 41c). Besides, the CNT length also increases up to 15  $\mu$ m. With further increasing  $c_{\text{ferrocene}}$  to 0.05 and 0.1 g ml<sup>-1</sup>, the CNT lengths reach up to ~30-50  $\mu$ m, and its number density on  $\mu$ Al<sub>2</sub>O<sub>3</sub> also increases (Fig. 41d). Because of their big lengths, vertically aligned CNTs incline toward the direction where there

is less limitation during their growth, like the gap among  $\mu\text{Al}_2\text{O}_3$ . However, no obvious difference has been noticed in CNT growth at the above two  $c_{\text{ferrocene}}$ . Fig. 40e shows the CNT diameter distribution at different  $c_{\text{ferrocene}}$ . It could be seen that low ferrocene concentrations ( $c_{\text{ferrocene}} < 0.01 \text{ g ml}^{-1}$ ) promote the formation of CNTs which have a narrow diameter distribution, and small lengths. By contrast, CNTs with large diameters are found on  $\mu\text{Al}_2\text{O}_3$  when  $c_{\text{ferrocene}}$  is more than  $0.01 \text{ g ml}^{-1}$ . Moreover, the diameter distribution enlarges with increasing  $c_{\text{ferrocene}}$ . At the same time, CNT length also increases with  $c_{\text{ferrocene}}$  in a nonlinear way.

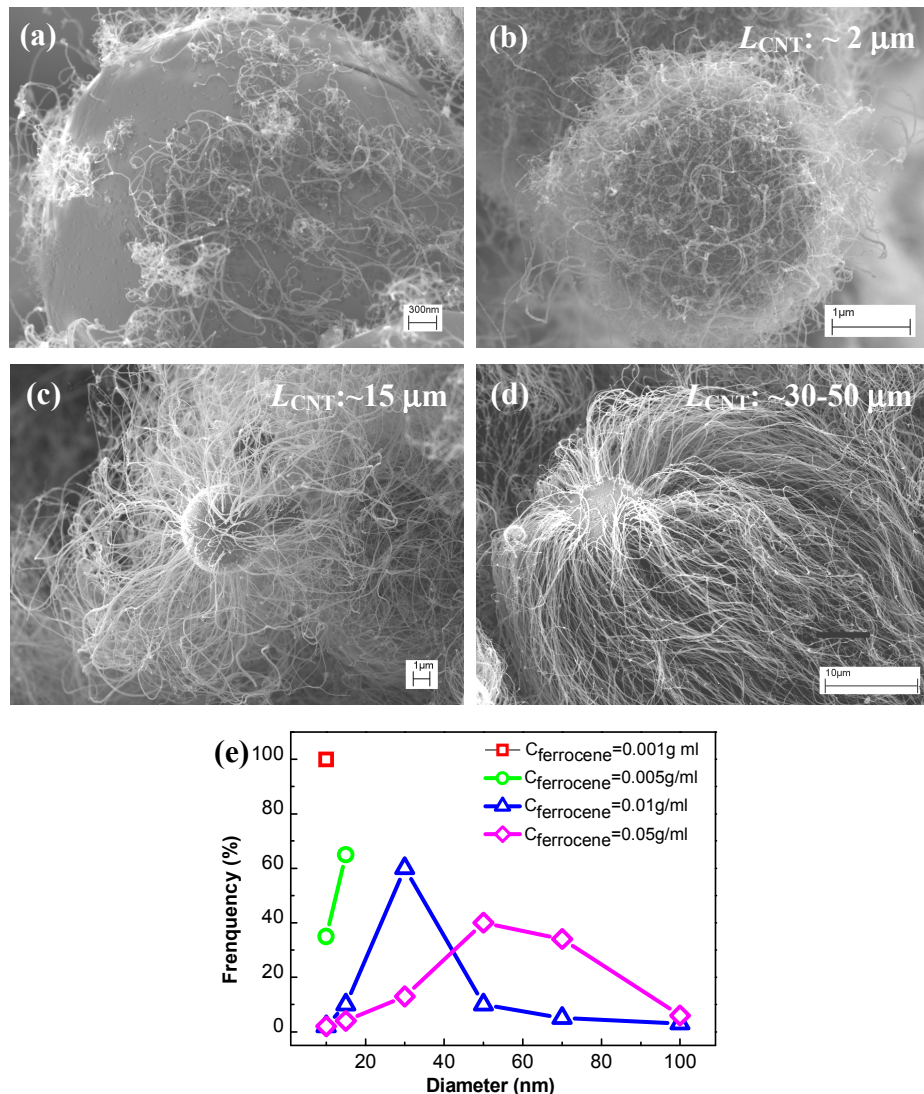


**Figure 41.** SEM Images of CNTs- $\mu\text{Al}_2\text{O}_3$  hybrid structures obtained at different ferrocene concentrations: (a)  $0.001 \text{ g ml}^{-1}$ , (b)  $0.005 \text{ g ml}^{-1}$ , (c)  $0.01 \text{ g ml}^{-1}$ , (d)  $0.05 \text{ g ml}^{-1}$ .  $L_{\text{CNT}}$  indicates the CNT length. (f) CNT diameter distributions at different  $c_{\text{ferrocene}}$ .

The above results demonstrate the significant role of  $c_{\text{ferrocene}}$  in CNT growth on  $\mu\text{Al}_2\text{O}_3$ .

The size distribution of final iron catalyst particles shows a  $c_{\text{ferrocene}}$  dependency at the studied conditions. High Fe/C ratio solutions result normally large iron particles, which in turn produce CNTs with large diameters. Moreover, CNTs growth dynamics are also related to  $c_{\text{ferrocene}}$  when only xylene is used as carbon source at 780 °C. It is found that large iron particles mostly promote to grow long CNTs, vice versa. The CNT diameter and growth rate are directly related to  $c_{\text{ferrocene}}$ .

Another interesting fact is the variation of CNT number density with  $c_{\text{ferrocene}}$ . When  $c_{\text{ferrocene}}$  is 0.001 g ml<sup>-1</sup> (Fe/C ratio 8.28E-5), a few of thin CNTs are formed. Then highly dense CNTs grow on  $\mu$ Al<sub>2</sub>O<sub>3</sub> when the Fe/C ratio increases to 4.12E-4. However, when  $c_{\text{ferrocene}}$  is equal to 0.01 g ml<sup>-1</sup>, low density CNTs with large diameters are found. Then, the further increase of  $c_{\text{ferrocene}}$  results again in an increase of CNT density. This phenomenon confirms again the intervention of carbon source in catalyst nucleation process. Also, it indicates that when  $c_{\text{ferrocene}}$  is high, there might be the combination of small catalyst particles at CNT nucleation stage in order to form large catalyst particles.

Fig. 42 shows the variation of the relative intensity ratios of MS peaks with ferrocene concentration. These MS peaks correspond to xylene and the decomposition products of ferrocene and xylene such as toluene (C<sub>7</sub>H<sub>8</sub>), benzene (C<sub>6</sub>H<sub>6</sub>), cyclopentadienyl (C<sub>5</sub>H<sub>5</sub>), acetylene (C<sub>2</sub>H<sub>2</sub>), methane (CH<sub>4</sub>). It is well known that MS ion currents are directly correlated with the concentrations of the corresponding components including the molecule fragments from ionization, and the products from gas phase decomposition. The relationship between ion current and component concentration can be described by equation (3-1):

$$I_i = NF \cdot S_i \cdot C_i = \varepsilon_i \cdot C_i \quad (3-1)$$

where  $I_i$  and  $C_i$  correspond to the ion current and the concentration of component  $i$ , respectively. NF and  $S_i$  are the normalization factor and calibration factor of the component  $i$ , which can be combined into a linear coefficient  $\varepsilon_i$ . In our research, argon is the most abundant gas, which has a volume percentage more than 80 % in the reactor atmosphere. Therefore, its corresponding MS current intensity at m/z= 40 is chosen as the reference for the calculation of the relative relation of other products. The relationship between relative intensity ( $I_i/I_{Ar}$ ) and relative concentration ( $C_i/C_{Ar}$ ) of the component  $i$  can be described as:

$$\frac{I_i}{I_{Ar}} = \frac{\varepsilon_i}{\varepsilon_{Ar}} \cdot \frac{C_i}{C_{Ar}} = \varepsilon'_i \cdot \frac{C_i}{C_{Ar}} \quad (3-2)$$

Then, the concentration of component  $i$  can be calculated as follows:

$$C_i = \frac{1}{\varepsilon'_i} \cdot \frac{C_{Ar}}{I_{Ar}} \cdot I_i \quad (3-3)$$

Fig. 42 shows that the relative intensity of each component decreases with the increase of the ferrocene concentration in xylene solution until 0.05 g ml<sup>-1</sup>. This indicates that ferrocene favors the decomposition of carbon source, and thus the production of CNTs. Beyond, one significant variation of peak intensity is observed compared with the peak intensities at 0.05 g ml<sup>-1</sup>. It is known that the increase of ferrocene concentration generates the augmentation of the Fe/C molar ratio. Thus, the feeding of a sufficient amount of iron is necessary to obtain a high CNT growth rate, and to increase their coverage on  $\mu$ Al<sub>2</sub>O<sub>3</sub>. The CNTs with a large diameter could only be obtained when the Fe/C molar ratio is more than 8.22E-4 at the used conditions. The further increase of Fe/C ratio produces the CNTs with larger diameters and higher density on  $\mu$ Al<sub>2</sub>O<sub>3</sub>. This corresponds well to the decrease rates of the component relative intensity ratios shown in Fig. 42. When the Fe/C molar ratio is larger than 3.98E-3, small variation of carbon source decomposition indicates one balance reached between the iron and carbon interaction in gas phase. In addition, little variation in CNT production yield indicates a saturated stable catalyst formation rate on  $\mu$ Al<sub>2</sub>O<sub>3</sub> at the researched conditions.

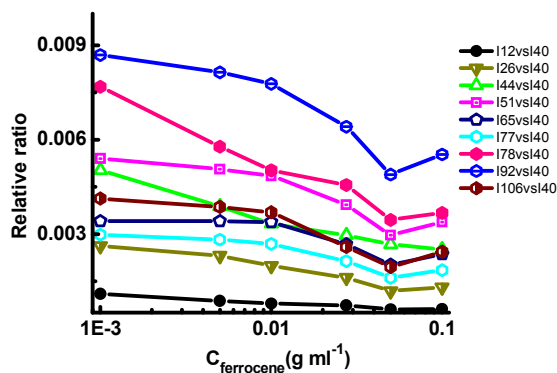


**Figure 42.** Relative ratios between the intensities of MS peaks corresponding to xylene decomposition products and that of Ar at  $m/z = 40$ , obtained at different  $c_{ferrocene}$ .

### 3.2.1.3 Influence of the ferrocene-xylene solution feed rate

The influence of the ferrocene-xylene solution injection rate on CNT growth on  $\mu$ Al<sub>2</sub>O<sub>3</sub> is investigated at 550 °C in the presence of acetylene. The concentration of ferrocene in the solution is about 0.05 g ml<sup>-1</sup>, and the flow rate of acetylene is 6 ml min<sup>-1</sup>. The solution injection rates are listed in table 6. As C<sub>2</sub>H<sub>2</sub> is much more active than xylene at 550 °C, the Fe/C molar ratios are calculated according to the mole of iron in ferrocene and that of carbon in ferrocene and C<sub>2</sub>H<sub>2</sub>. The total gas flow rate is 1 l min<sup>-1</sup>, containing 5 % hydrogen and 95 % argon.

**Table 6.** Feed rate of ferrocene-xylene solution and corresponding molar ratios between iron and carbon

Parameters	variation range			
Solution feed rate(ml min <sup>-1</sup> )	0.05	0.1	0.17	0.27
C <sub>2</sub> H <sub>2</sub> flow rate (ml min <sup>-1</sup> )			6	
Fe/C molar ratio <sup>a</sup>	0.020	0.033	0.046	0.058

a: Fe/C molar ratio is the ratio between iron in ferrocene and carbon in ferrocene and C<sub>2</sub>H<sub>2</sub>

The hybrid structures obtained at different solution feed rates are presented in Fig. 43. It is found that  $\mu$ Al<sub>2</sub>O<sub>3</sub> spheres are densely covered by CNTs with lengths ~ 0.2 μm when the solution feed rate is 0.05 ml min<sup>-1</sup>. When the feed rate is higher than 0.05 ml min<sup>-1</sup>, the “six-branch” structures are dominant in the final products. The length of CNT bundles has narrow variation (about 4-4.5 μm) with the further increase of the solution feed rate. The same phenomenon is observed in CNT density on  $\mu$ Al<sub>2</sub>O<sub>3</sub>. This could be explained by the following reasons. First, the strong interference of acetylene yields small catalyst particles with homogeneous size during the deposition of iron on the surface of  $\mu$ Al<sub>2</sub>O<sub>3</sub>. Second, certain Fe/C molar ratios are required for obtaining high CNT growth rate. As its active chemical feature, acetylene could very easily decompose into carbon on catalyst particles even at relatively low temperatures. Therefore, when the Fe/C ratio is about 0.020, the low iron ratio in the reactor greatly limits the catalyst formation rate, which in turn influences the carbon deposition from acetylene. A big jump in CNT growth rate has been observed when the Fe/C ratio is over 0.033. Beyond this value, the CNT growth rate becomes stable even a further increase of the Fe/C ratio. This indicates the maximum growth rate of CNTs in the presence of sufficient carbon and iron precursors at the used temperatures. At the different solution injection rates, the CNT diameter keeps almost at the same level, varying from 6 to 10 nm.

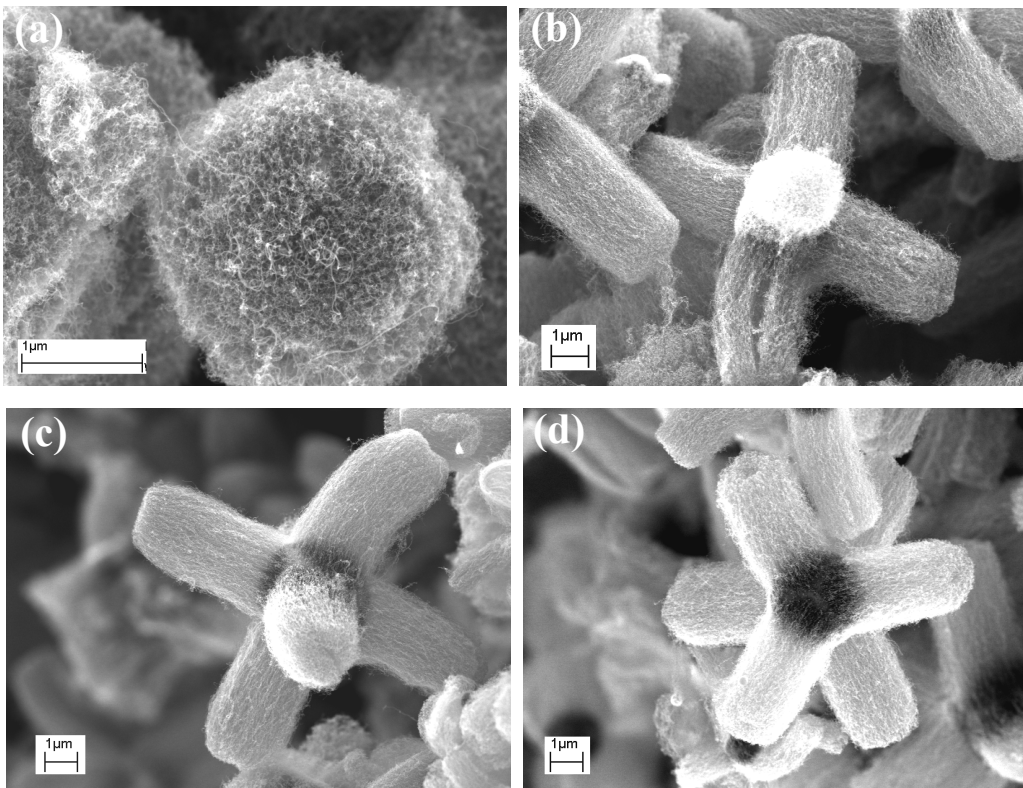


**Figure 43.** SEM images of CNTs- $\mu$ Al<sub>2</sub>O<sub>3</sub> hybrid structures obtained at 550 °C with different ferrocene-xylene solution feed rates: (a)  $\sim 0.05 \text{ ml min}^{-1}$ , (b)  $\sim 0.1 \text{ ml min}^{-1}$ , (c)  $\sim 0.17 \text{ ml min}^{-1}$ , (d)  $\sim 0.27 \text{ ml min}^{-1}$ . The flow rate of C<sub>2</sub>H<sub>2</sub> was 6 ml min<sup>-1</sup>, which corresponds to 6 vol. %.

Fig. 44 shows the variation of the MS ion currents of the main products in the reactor when the solution feed rates are varied from 0.05 to 0.27 ml min<sup>-1</sup>. Although a constant flow rate of acetylene is used, a small variation is detected at m/z 26 due to the increase of ferrocene and xylene feed rate. The variation of the curve slope shows that more acetylene is consumed at the higher solution injection rates. We observed an evident increase of the ion current at m/z 106, which corresponds to xylene, but minor variations are noted at the other masses. Obviously, the augmentation of xylene quantity in the system will consequently increase the detected ion intensities at the corresponding masses. Furthermore, the ion intensity ratios (lower part in Fig. 44) show unnoticeable variations with the increase of solution feed rate. Thus, it could be concluded that the augmentations of the ion currents at m/z 15, 26, 52, 65, 78, 92 and 106 are attributed to the increased amount of xylene. However, only few amount of benzene due to the decomposition of xylene is discharged because of the increase of the solution feed rate. Therefore, under the given hydrogen and acetylene ratios, the increase of ferrocene quantity accelerates the CNT growth. Consequently, we observe an evolution of the CNT length, as described above.

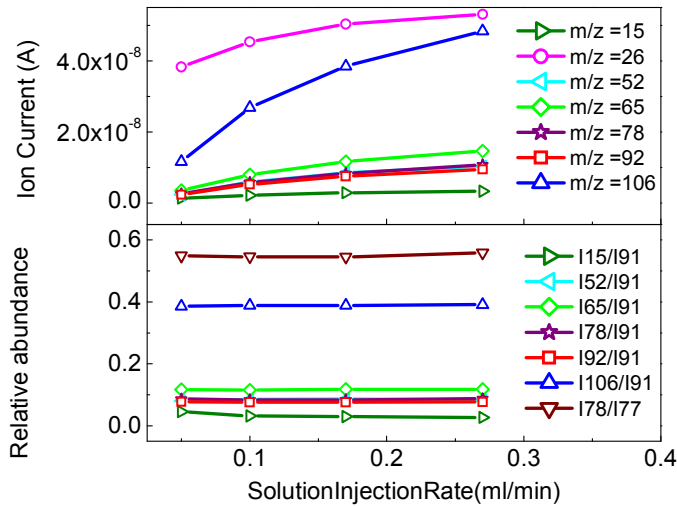


**Figure 44.** Mass spectra analysis on the influence of ferrocene-xylene solution feed rates on the growth of CNTs. The upper part of the figure demonstrates the variations of the ion currents of the main products at m/z 15, 26, 52, 65, 78, 92 and 106. The lower part indicates the variations of the ratios between the ion currents at m/z 15, 26, 52, 65, 78, 92, 106 and the one at m/z 91. In addition, the ratios between the ion intensities at m/z 77 and 78 are also plotted.

**In summary**, ferrocene plays an essential role in CNT growth on  $\mu$ Al<sub>2</sub>O<sub>3</sub> and the formation of the CNTs- $\mu$ Al<sub>2</sub>O<sub>3</sub> hybrid structures. Its concentration and feed rate significantly influence catalyst nucleation, CNT diameter, and CNT growth dynamics. When xylene is used as carbon source at relatively high temperature (780 °C), high ferrocene concentrations (Fe/C ratios) promote the growth of CNTs having large diameters and lengths. The diameter varies in a wide range. The “urchin-like” CNT- $\mu$ Al<sub>2</sub>O<sub>3</sub> hybrid structures are formed when  $c_{\text{ferrocene}}$  is higher than 0.01 g ml<sup>-1</sup>. When acetylene is used as carbon source at relatively low temperature (550 °C), high ferrocene-xylene solution injection rates accelerate the growth of thin CNTs with homogeneous diameter. These CNTs self-organize into “six-branch” structures on  $\mu$ Al<sub>2</sub>O<sub>3</sub> when the Fe/C ratio is more than 0.033.

### 3.2.2 Carbon sources

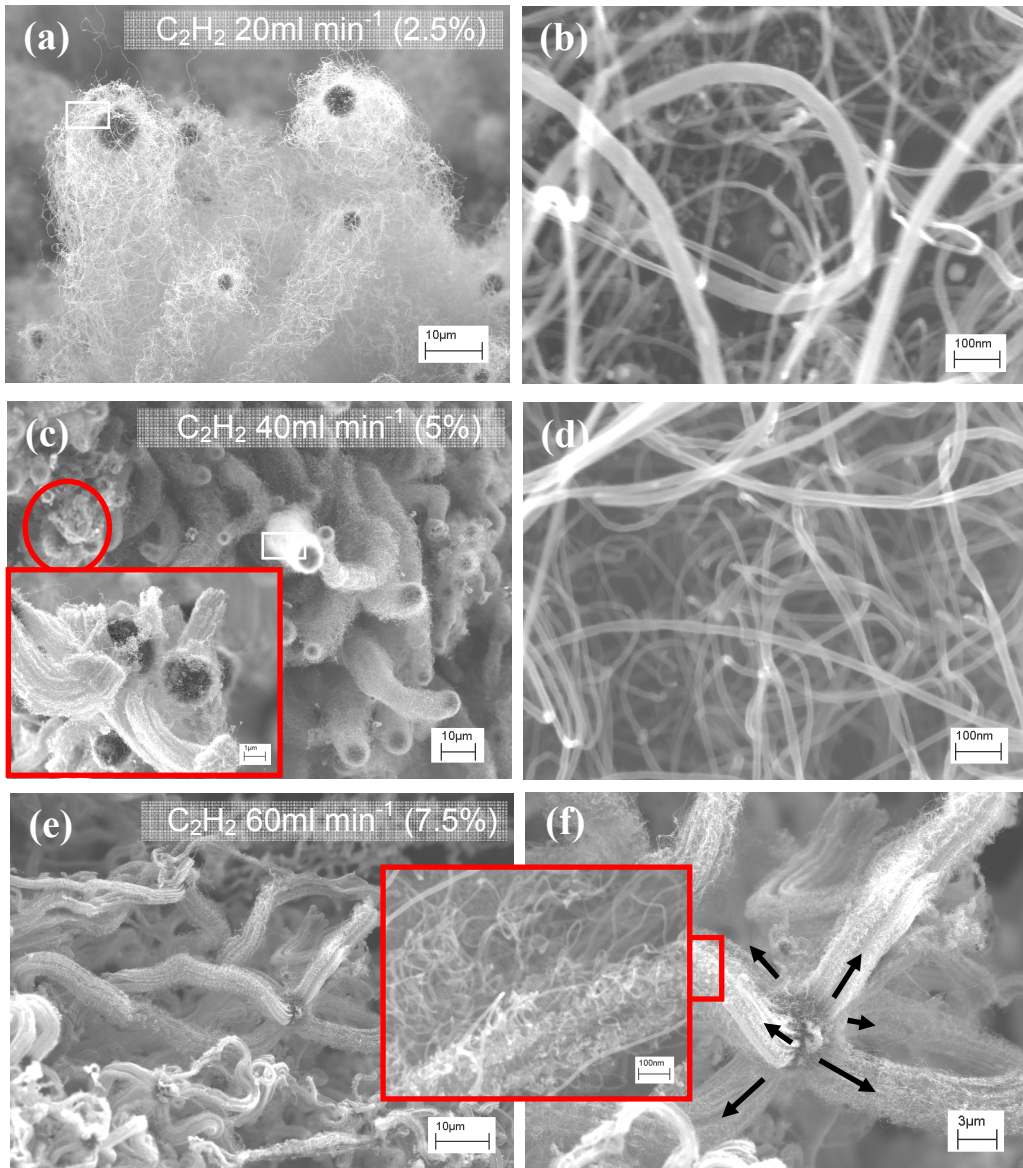
As we have demonstrated in the previous part, the “urchin-like” hybrid structures could be synthesized by the decomposition of xylene solution dissolving certain percent ferrocene at relatively high temperatures. However, the diameter of CNTs in the obtained hybrid structures always varies in a large range, from 10 nm to more than 100 nm. Although the hybrid structures

consisting of homogenous CNTs have also been obtained at relatively low temperatures, the CNT growth rate is very weak. Moreover, the CNT crystallinity is not so good. On the other hand, acetylene is an active carbon source which has been widely used to synthesize CNTs which have homogenous diameters, and relatively high growth rates, as shown in Fig. 40b. However, little research has been reported in the literature about the production of CNTs using mixed carbon sources which are composed of two hydrocarbons with extremely different properties. One, acetylene, is highly active hydrocarbon in gas state, but the other, xylene, is a liquid hydrocarbon with a relatively high thermodynamic stability.

In the following two parts, we will discuss about the influence of the addition of acetylene on the hybrid morphologies, and the diameter and growth rate of CNTs.

### ***3.2.2.1 Adding Acetylene at high temperatures***

The influence of the addition of acetylene on the hybrid structures is first investigated at 780 °C. Acetylene and the xylene solution dissolving ferrocene (0.05 g ml<sup>-1</sup>) are spontaneously injected into the CVD reactor. The solution feed rate is ~ 0.2 ml min<sup>-1</sup>. The total gas (Ar+H<sub>2</sub>+C<sub>2</sub>H<sub>2</sub>) flow is ~ 0.8 l min<sup>-1</sup>, in which the hydrogen fraction is kept constant, ~10 %. Three different C<sub>2</sub>H<sub>2</sub> flow rates studied are 20, 40 and 60 ml min<sup>-1</sup>, corresponding to three volume fractions ~ 2.5, 5 and 7.5 %, respectively. The injection of two carbon sources is stopped spontaneously after 15 min.



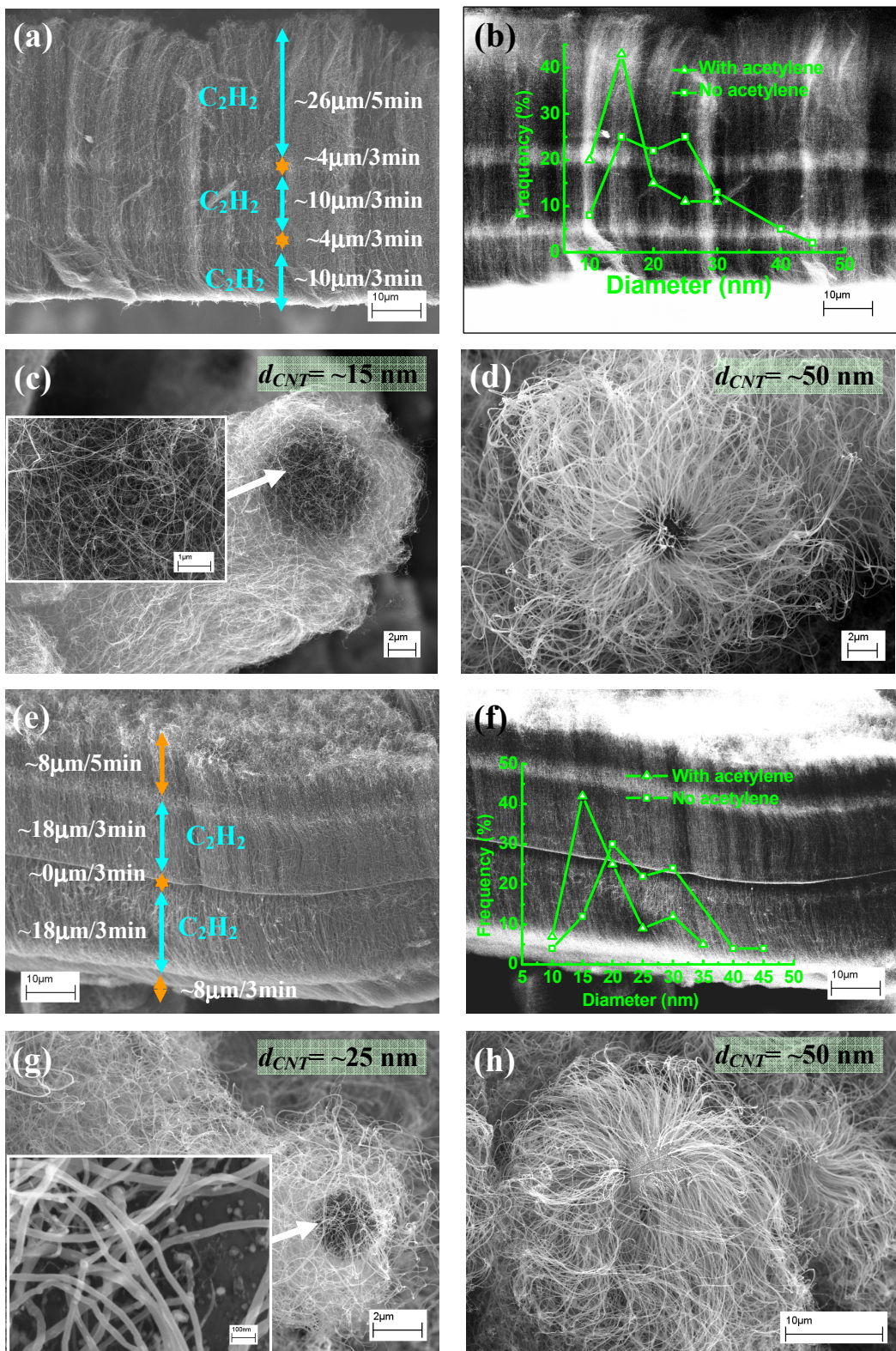
**Figure 45.** SEM images of the CNTs- $\mu$ Al<sub>2</sub>O<sub>3</sub> hybrids obtained by adding different volume percentage of acetylene ( $f_{C_2H_2}$ ) in carrier gas at 780 °C. (a-b)  $f_{C_2H_2} = 2.5\%$ : (b) the high magnification of the region marked by the white square in (a). (c-d)  $f_{C_2H_2} = 5\%$ : the hybrid structures containing very dense CNTs assembling in a bundle, and amounts of aggregates consisting of the alumina particles covered by highly dense CNTs and amorphous carbon depositing on CNTs (Inserted high magnification SEM image of the region marked by a red square). (e-f),  $f_{C_2H_2} = 7.5\%$ : the hybrid structures consisting of six branch CNT bundles (marked by six arrows in (f)) on  $\mu$ Al<sub>2</sub>O<sub>3</sub>. And each bundle contains highly dense CNTs and amorphous carbon, shown in the inserted figure.

Fig. 45 shows the different CNTs- $\mu$ Al<sub>2</sub>O<sub>3</sub> hybrid structures obtained by adding different volume concentrations of acetylene in the atmosphere. The alumina microparticles are found to be covered by dense CNTs growing in different spatial directions (Fig. 45a) when  $f_{C_2H_2} = 2.5\%$ . The CNT length is  $\sim 60 \mu\text{m}$ . The CNT arrangement in these structures is greatly disordered, compared with the regular CNT arrangement in the hybrid structures obtained without

acetylene at 780 °C (Fig. 41d). But the diameter of the CNTs obtained with the addition of acetylene has a narrower distribution range, from 10 to 40 nm (Fig. 45b), instead of the range from 10 to 100 nm in the case without acetylene. Furthermore, a few of carbon capsulated iron particles are found on the surface of  $\mu$ Al<sub>2</sub>O<sub>3</sub>. However, the CNTs assemble into a bundle with a length of ~ 60  $\mu$ m when  $f_{\text{C}_2\text{H}_2}$  increases to 5% (Fig. 45c). The alumina particles are closely surrounded by highly dense CNTs, and they locate in the front of each CNT bundle. A closer observation of the particle surface (Fig. 45d) shows that CNTs have homogenous diameter (~ 15-20 nm), and randomly cross over each other. Besides, amounts of aggregates are also formed, which consists of the alumina particles covered by bundles with highly dense CNTs and amorphous carbon (Inserted high magnification image in Fig. 45c). When higher volume fractions of acetylene is used ( $f_{\text{C}_2\text{H}_2}=7.5\%$ ), the CNTs assemble into six distinctive bundles of 60  $\mu$ m in length (Fig. 45e), in which thin CNTs (~10 nm) are randomly tangled together, and accompanied by huge amounts of amorphous carbon (inserted image in Fig. 45f). Moreover, it is found that the six CNT bundles arrange in an orthogonal way on the alumina particles (Fig. 45f).

As it is shown, the addition of higher percent acetylene promotes to the formation of more amorphous carbon during CNT growth. But, certain percentages of acetylene are necessary to feed sufficient carbon sources for the growth of CNTs at a high rate. Due to its low pyrolysis activation energy, acetylene could pyrolyze into solid carbon in gas phase at high temperatures. High  $f_{\text{C}_2\text{H}_2}$  also favors the formation of amorphous carbon during CNT growth. Therefore, the control of acetylene concentration is desired in order to produce the hybrid structures consisting of homogeneous CNTs without impurities.

Another evident effect of the addition of acetylene is the reduction of the CNT diameter distribution range. At the researched temperatures, the higher the volume fraction of C<sub>2</sub>H<sub>2</sub> is, the smaller the average diameter of CNTs is. As we have discussed early, the diameter of CNTs is strongly related to that of catalyst particles. The homogeneous CNTs with a small diameter indicate again the intervention of acetylene in the formation of iron catalyst particles.



**Figure 46.** Influence of the addition of  $\text{C}_2\text{H}_2$  (2 vol %) in carrier gas on the CNT growth on quartz plate and  $\mu\text{Al}_2\text{O}_3$  at 750 °C. (a-d) Carbon source injection time sequence: 5 min ( $\text{C}_8\text{H}_{10} + \text{C}_2\text{H}_2$ ) - 3 min ( $\text{C}_8\text{H}_{10}$ ) - 3 min ( $\text{C}_8\text{H}_{10} + \text{C}_2\text{H}_2$ ) - 3 min ( $\text{C}_8\text{H}_{10}$ ) - 3 min ( $\text{C}_8\text{H}_{10} + \text{C}_2\text{H}_2$ ). Images a and b show the multilayer CNTs on quartz plate and their secondary electron image, respectively; Images c and d demonstrate the growth of CNTs on  $\mu\text{Al}_2\text{O}_3$  located in the regions of 0-5 cm and 20-30 cm, respectively. (e-h) Carbon source injection time sequence: 5 min ( $\text{C}_8\text{H}_{10}$ ) - 3 min ( $\text{C}_8\text{H}_{10} + \text{C}_2\text{H}_2$ ) - 3 min ( $\text{C}_8\text{H}_{10}$ ) - 3 min ( $\text{C}_8\text{H}_{10} + \text{C}_2\text{H}_2$ ) - 3 min ( $\text{C}_8\text{H}_{10}$ ). Images

*e* and *f* show the multilayer CNTs grown on quartz plate and their secondary electron image, respectively; Images *g* and *f* demonstrate the growth of CNTs on  $\mu$ Al<sub>2</sub>O<sub>3</sub> located in the regions of 0-5 cm (*g*) and 20-30 cm (*h*).

The influence of C<sub>2</sub>H<sub>2</sub> on the CNT growth is further studied by multiple discontinuous injections of acetylene at 750 °C. The xylene solution containing 0.05 g ml<sup>-1</sup> ferrocene is continuously fed during the whole process of 17 min, whereas acetylene is discontinuously fed in the interval of 3 min. Argon and hydrogen flow rates are 0.8 and 0.2 l min<sup>-1</sup>, respectively. The two following different cases are studied.

In the first case, carbon source injection time sequence is 5 min (C<sub>8</sub>H<sub>10</sub>+ C<sub>2</sub>H<sub>2</sub>) -3 min (C<sub>8</sub>H<sub>10</sub>) -3 min (C<sub>8</sub>H<sub>10</sub>+ C<sub>2</sub>H<sub>2</sub>) -3 min (C<sub>8</sub>H<sub>10</sub>) -3 min (C<sub>8</sub>H<sub>10</sub>+ C<sub>2</sub>H<sub>2</sub>). C<sub>2</sub>H<sub>2</sub> is first injected 5 min and then stopped for 3 min. Then, the 3 min injection of acetylene repeats two times at the interval of 3 min. Fig. 46a shows one CNT carpet of ~54  $\mu$ m in thickness. The multiple layer CNT structure is clearly demonstrated by secondary electron image (Fig. 46b), in which two white bands of 4  $\mu$ m corresponds to two CNT growth periods without acetylene. The different contrast is mainly due to large amounts of iron particles produced during these periods. According to the layer thicknesses, the initial CNT growth rate with acetylene is estimated about ~5.2  $\mu$ m min<sup>-1</sup>. This rate is quite higher than the CNT growth rates in the periods without acetylene (~ 1.3  $\mu$ m min<sup>-1</sup>), and higher than these in the two growth periods with acetylene (~ 3.3  $\mu$ m min<sup>-1</sup>). The inserted diameter distribution curves demonstrate that the addition of acetylene favors to decrease CNT diameter. The high CNT growth rates in the first 5 min with acetylene might be due to fewer obstacles to the arrival of catalyst and carbon source precursors on the substrate surface. However, no CNT layers are found on  $\mu$ Al<sub>2</sub>O<sub>3</sub>, as shown in Fig. 46c and d. CNTs organize into different states depending on their deposition position. The ultra-highly dense CNTs align into one large bundle on the alumina microparticles located in the front part of quartz plate (Fig. 46c). The CNT diameter is very homogeneous, ~15 nm. However, CNTs with low number density are found on the particles placed in the middle region of the plate. The CNTs form the “urchin-like” structures with the particle in the core position. The CNT diameter has a large distribution range varying from 20 to 70 nm, and the mean diameter is ~ 50 nm. The hybrid structures are very similar to these obtained without adding acetylene at 780 °C (Fig. 41d). This indicates that the influence of acetylene on CNT growth is weakened in the latter region of the reactor in the reactor at high temperature.

In the second case, carbon source injection time sequence is as follows: 5 min (C<sub>8</sub>H<sub>10</sub>) -3 min (C<sub>8</sub>H<sub>10</sub>+ C<sub>2</sub>H<sub>2</sub>) -3 min (C<sub>8</sub>H<sub>10</sub>) -3 min (C<sub>8</sub>H<sub>10</sub>+ C<sub>2</sub>H<sub>2</sub>) -3 min (C<sub>8</sub>H<sub>10</sub>). The ferrocene-xylene

solution is first injected for 5 min, and then the feeding of acetylene (flow rate 20 ml min<sup>-1</sup>) of 3 min is carried out 2 times at the interval of 3 min. Figures 46e-f show the multiple layers of CNT carpet obtained on the quartz plate. A layer of CNTs with a thickness of ~ 8  $\mu$ m are grown from the decomposition of xylene and ferrocene in the first 5 min, with a growth rate of ~ 1.6  $\mu$ m min<sup>-1</sup>. The CNT growth rate increases to 6  $\mu$ m min<sup>-1</sup> when acetylene is added into the reactor. A very thin layer mainly consisting of iron particles surrounded carbon is formed when the injection of acetylene is stopped. There is nearly no CNT growth in the followed 3 min. The reinjection of acetylene activates the growth of CNTs at the same rate of 6  $\mu$ m min<sup>-1</sup>. This phenomenon shows once again that the addition of acetylene accelerates CNT growth. The CNT diameter distribution comparison curves (Fig. 46f) show that CNTs grown in the presence of acetylene have smaller diameters and a narrower distribution range than that of CNTs grown without acetylene. The CNT growth on  $\mu$ Al<sub>2</sub>O<sub>3</sub> is similar to that in the first case: large “bundle-like” structure in the front part (Fig. 46g) and “urchin-like” hybrid structures in the middle part (Fig. 46h). But the CNT density in the “bundle-like” structure is much lower than that in first case (Fig. 46g and c). Furthermore, the CNT diameter (~ 25 nm) is also larger than the one in the first case (first injecting acetylene).

The above comparison experiments demonstrate that the addition of a certain percentage of acetylene is helpful to accelerate CNT growth and to narrow its diameter distribution range. Furthermore, different initial carbon sources could also affect the diameter distribution of CNTs in hybrid structures. At relatively high temperatures, a strong influence of acetylene on CNT growth takes place mainly in the front part of the reactor. Beyond certain distance, CNT growth is mainly resulted from the pyrolysis intermediates of xylene and acetylene.

### 3.2.2.2 Adding Acetylene at relatively low temperatures

The influence of C<sub>2</sub>H<sub>2</sub> is also investigated at 550 °C. As discussed in the previous part, the high density CNTs could be obtained on  $\mu$ Al<sub>2</sub>O<sub>3</sub> at this temperature. The ferrocene-xylene solution was always fed at the rate of 0.2 ml min<sup>-1</sup> for ~ 15 min.

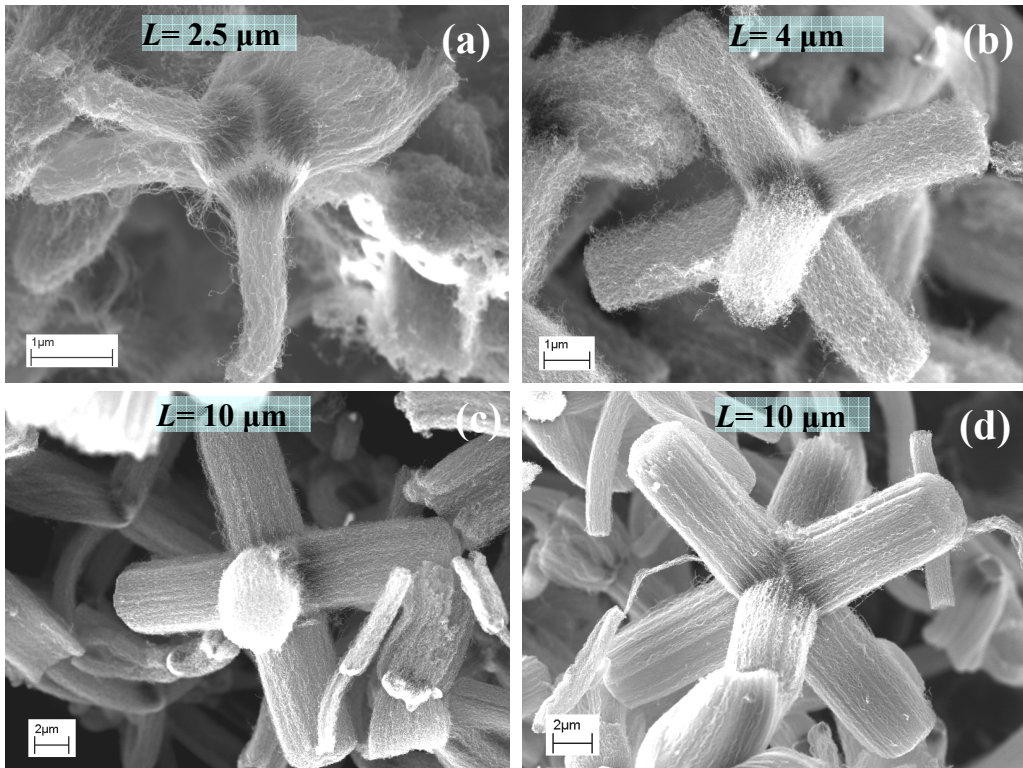


**Figure 47.** SEM images of the CNTs- $\mu$ Al<sub>2</sub>O<sub>3</sub> hybrid structures obtained at 550 °C using different C<sub>2</sub>H<sub>2</sub> concentrations: (a) 6 ml min<sup>-1</sup> (0.6 %), (b) 10 ml min<sup>-1</sup> (1 %), (c) 20 ml min<sup>-1</sup> (2 %) and (d) 40 ml min<sup>-1</sup> (4 %).

Fig. 47 shows the hybrid structures obtained using different C<sub>2</sub>H<sub>2</sub> concentrations varying from 0.6 to 4 vol. %. It can be seen that the hybrid structures always consist of regularly separated CNT bundles on  $\mu$ Al<sub>2</sub>O<sub>3</sub>, and CNTs have a narrow diameter distribution ranging from 6 to 10 nm, at different acetylene concentrations. However, the CNT density and the CNT bundle length increase consecutively, from  $\sim 2.5$  to 10  $\mu\text{m}$ , with increase of C<sub>2</sub>H<sub>2</sub> concentration. This indicates that the addition of acetylene promotes the nucleation of iron catalyst particles from ferrocene at low CNT synthesis temperatures. Additionally, high concentration C<sub>2</sub>H<sub>2</sub> feeds more effective carbon sources to catalyst particles, and thus accelerates CNT growth rate.

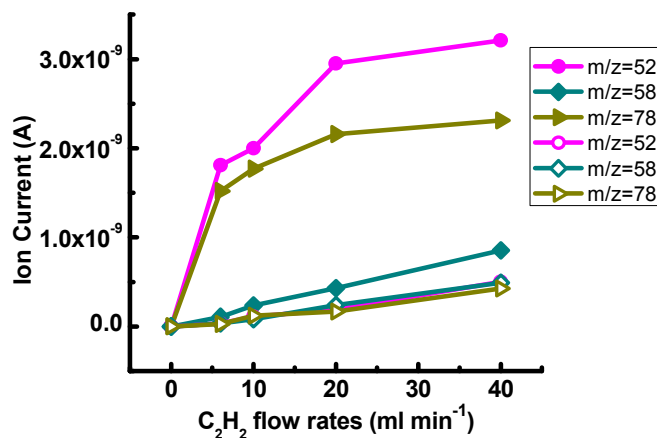


**Figure 48.** Comparison of the MS ion intensities at  $m/z$  52, 58 and 78 under different  $C_2H_2$  concentrations with (solid symbols) and in the absence (hollow symbols) of ferrocene-xylene solution at 550 °C.

Fig. 48 shows the three most evident variations of the ion intensities at  $m/z$  52, 58 and 78 under different  $C_2H_2$  concentrations are shown in Fig. 48. For comparison, their ion current intensities in the absence of ferrocene-xylene solution are also given. At each acetylene concentration, the ion current intensity is always higher with ferrocene-xylene solution than without. This indicates that the presence of this solution provides additional ion contribution at corresponding masses. High  $C_2H_2$  concentrations yield an increase of the difference in ion intensities at each mass. However, except the ion intensity at  $m/z$  58, the augmentation exhibits a nonlinear increase: fast from 0.6 to 2 %, and then slow beyond 2 %. The nucleation of small iron particles is intensified when the  $C_2H_2$  concentration increases. This may promote the growth of CNTs with high density.

**In summary**, the addition of acetylene in reactor atmosphere significantly modulates the CNT growth from the decomposition of ferrocene-xylene solution. First, the addition of acetylene could narrow the diameter distribution of CNTs synthesized at high temperatures. This is realized by the interference of acetylene in catalyst particle formation on the microparticles. Due to its high chemical activity, acetylene could efficiently provide effective carbon for CNT growth once the catalyst particle size reaches a critical value. According to our observation, this catalyst particle critical value is about 5 nm. On the other hand, its high activity makes it very easy to form amorphous carbon in gas phase, especially, at high temperatures. Furthermore, the strong influence of acetylene is found in the front part of the reactor. Beyond certain distance, its impact is weakened with the distance. This is a competitive result from the fluid dynamics of carrier gas and the chemical kinetics of acetylene reactions. At relatively low temperatures, enhanced CNT growth rates have been obtained by the addition of

acetylene. The synthesized “six-branch” CNTs- $\mu$ Al<sub>2</sub>O<sub>3</sub> structures contain the homogenous CNTs with diameters ranging from 6 to 10 nm.

### **3.2.3 Temperature**

In general, CNT nucleation and growth rates are dominated by the substrate surface properties and the pyrolytic reactions occurring in the gas phase. As a decisive thermodynamic parameter, temperature has significant influences on the thermal decomposition of ferrocene and carbon sources. The former process generates the formation of iron particles. The latter one provides the continuous feeding of effective carbon species for CNT growth. In the following two parts, we will discuss about the temperature influence on the formation of CNT- $\mu$ Al<sub>2</sub>O<sub>3</sub> hybrid structures using xylene and xylene-acetylene as carbon sources.

#### **3.2.3.1 Xylene as carbon source**

The influence of temperature is first studied using xylene as carbon source. The temperature is varied from 550 to 900 °C with the interval of 50 °C. The ferrocene concentration in xylene solution is 0.05g ml<sup>-1</sup>. The flow rates of argon and hydrogen are 0.72 and 0.08 l min<sup>-1</sup>, respectively. The injection of the solution lasts for 15 min.

As demonstrated in Fig. 27, the “six-branch” hybrid structures transfer to the “urchin-like” ones with the increase of CNT growth temperature from 550 to 800 °C. At the same time, The CNT lengths increase continuously with the temperature. The CNT diameters are inclined to increase and vary in a large region (Fig. 28). A further increase of the temperature results in much longer and larger CNTs, ~150 μm in length and ~50-100 nm in diameter at 850 °C (Fig. 49). Whereas, by comparing with the hybrid structures obtained at lower temperatures, the number density of CNTs on  $\mu$ Al<sub>2</sub>O<sub>3</sub> is greatly decreased. Moreover, CNT arrangement on the substrate surface also changes from a vertically aligned state to a random one. Often, it is found that several small alumina particles are attached to a large one. However, the hybrid structures are completely changed when the temperature is increased to 900 °C. Only a few of CNTs decorated with iron particles are formed on  $\mu$ Al<sub>2</sub>O<sub>3</sub>(Fig. 49b). Instead, The higher magnification SEM (Fig. 49c) of one selected region on the surface of  $\mu$ Al<sub>2</sub>O<sub>3</sub> and its corresponding secondary electron image (Fig. 49d) demonstrate that the alumina microspheres

are densely covered by amorphous carbon balls. Each ball encapsulates a small iron particle sized in a range from 10 to 20 nm. It is worth mentioning that the CNT diameter is similar to the iron particle size, and no CNT with large diameter is found. This result is coherent with that reported by Eres et al<sup>[263]</sup>, that is, the CNT growth with ferrocene losses vertical alignment at 900 °C, and the growth rate exhibits a dramatic steep drop. This is mainly due to the enhanced gas-phase thermal decomposition of Fe(C<sub>5</sub>H<sub>5</sub>)<sub>2</sub> above 850 °C, which immediately produces iron particles in gas phase before ferrocene molecule arrival on substrate surface. The enhanced thermal decomposition of carbon sources at high temperatures could also accelerate the carbon deposition on the forming iron particles. One direct consequence is the presence of a large amount of carbon encapsulated iron particles on the outside walls of CNTs and on the surface of micro alumina (Fig. 49b-d).

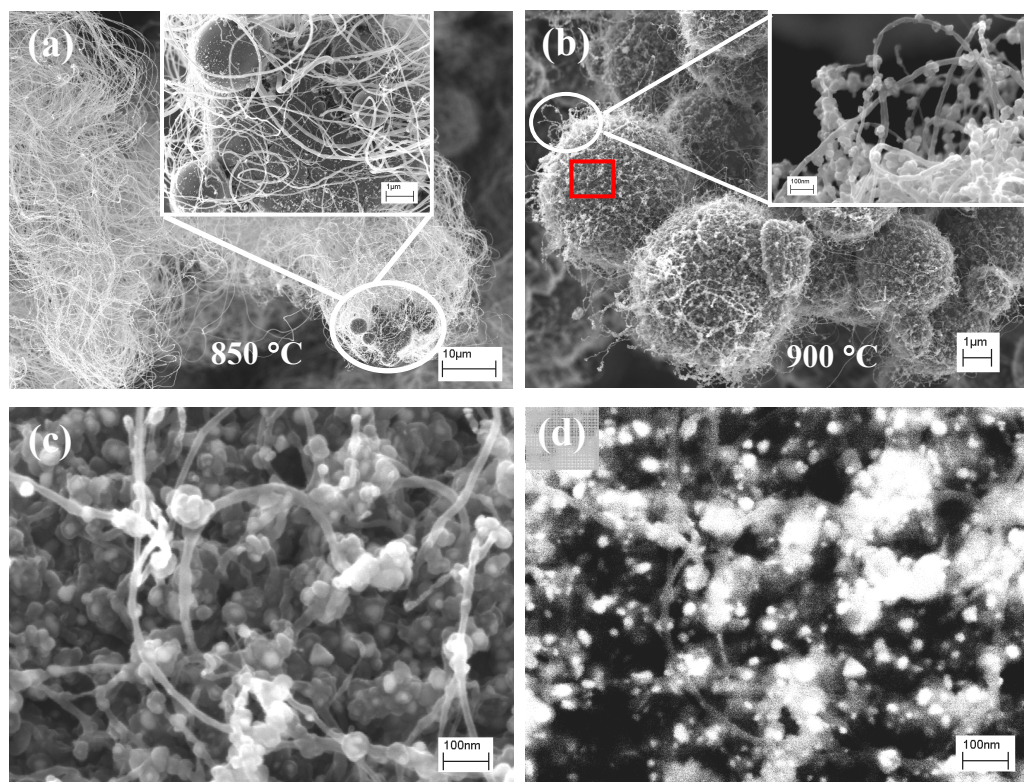


**Figure 49.** SEM images of the hybrid structures obtained at high temperatures. (a) Hybrid structures synthesized at 850 °C. Inserted high magnification image shows the irregular CNT arrangement and its low number density on one  $\mu$ Al<sub>2</sub>O<sub>3</sub> attached by several small ones. (b) Hybrid structures synthesized at 900 °C: CNTs are decorated with plenty of small iron particles on their surface (Inserted higher magnification image). (c-d) High magnification of the selected red zone in (b) and its corresponding secondary electron image.

The temperature dependence of the CNTs- $\mu$ Al<sub>2</sub>O<sub>3</sub> hybrid structures reveals the significance of the generation rate of catalyst particles. The iron particle formation is mainly

determined by the thermal decomposition of ferrocene and the interaction between ferrocene and carbon sources. These two processes are strongly temperature-dependent.

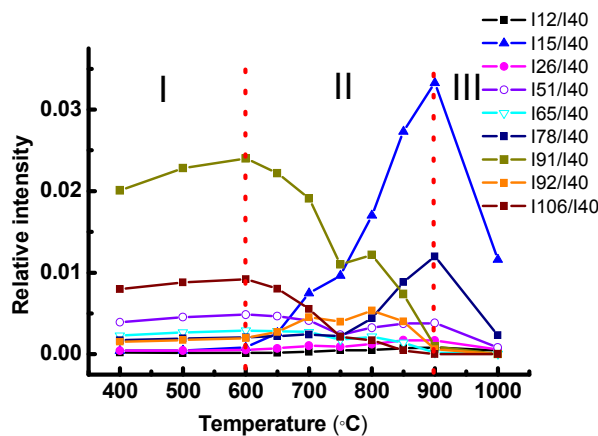


**Figure 50.** MS analyses of the three different temperature regions of xylene decomposition, ranging from 400 to 1000 °C. Two red dot lines indicate two critical temperatures of the decomposition of the solution.

Fig. 50 shows the main MS intensity peaks which have evident variations when the temperature increases from 400 to 1000 °C. From the figure, it could be seen that with the temperature increase, the decomposition process of the ferrocene-xylene solution undergoes three different periods, marked by two red dot lines. The slight augmentation of the curves from 400 to 600 °C due to might be the incomplete evaporation of the solution spray droplets at low temperatures. In fact, only a little of xylene decomposes into toluene at this temperature range. This could be seen from the variation of the intensity ratios of  $I_{106}/I_{91}$  (Fig. 51a) and  $I_{92}/I_{106}$  (Fig. 51b). The MS of pure o-xylene has the two strongest ion intensity peaks at m/z 91 and 106 (see Appendix 2), which are attributed to the species  $C_7H_8^+$  and  $C_8H_{10}^+$ . In the MS of toluene, there is also a characteristic peak at m/z 91 corresponding to toluene molecule. In Fig. 51a, a slight decrease of the intensity ratio  $I_{106}/I_{91}$  indicates a weak decomposition (~3 % at 600 °C) of xylene when the temperature is between 400 and 600 °C. On the other hand, a slight near linear increase (~2.5 % at 600 °C) of  $I_{92}/I_{106}$  is found at this temperature period (Fig. 51b). Furthermore, no variation of  $I_{78}/I_{92}$  could be seen with the increase of the temperature from 400 to 600 °C (Fig. 51c). This indicates that no benzene is produced at these temperatures. Therefore, the decomposed xylene is almost completely transferred into toluene when the temperature is lower than 600 °C.

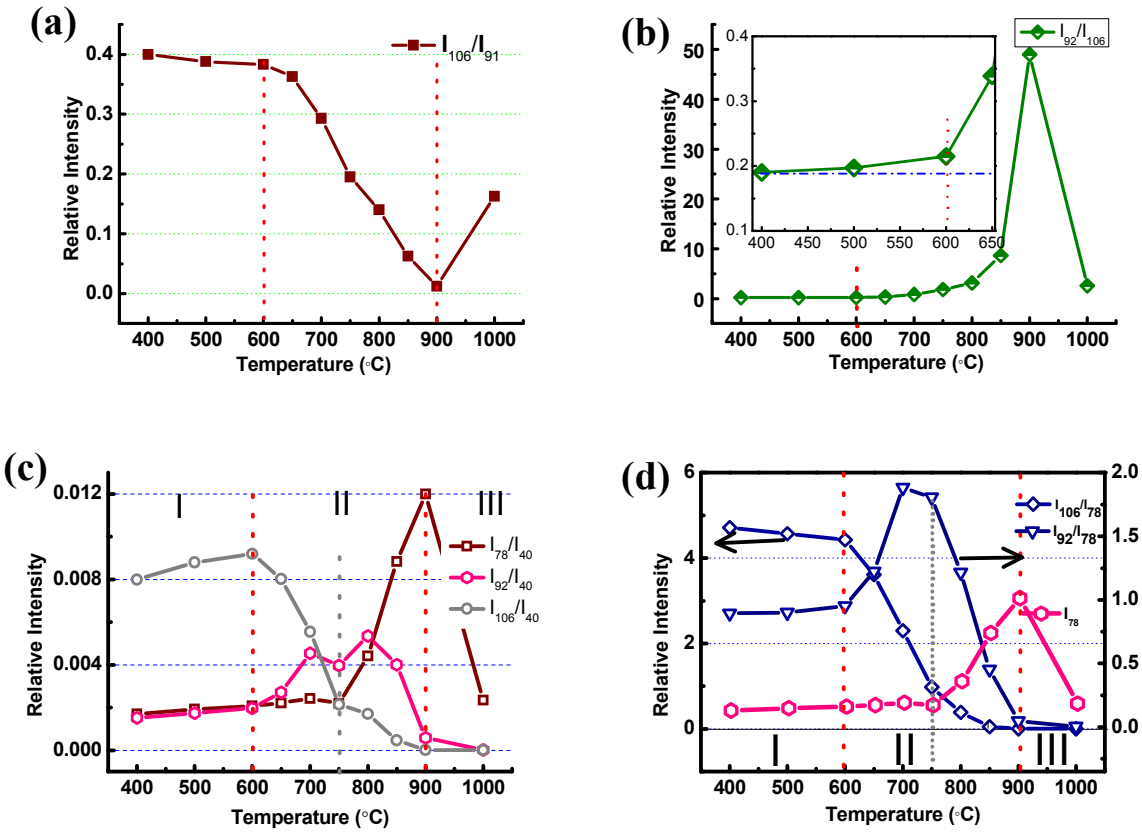


**Figure 51.** MS analysis of the decomposition of xylene solution containing 0.05 g mL<sup>-1</sup> ferrocene at the temperatures ranging from 400 to 1000 °C. Two red dot lines indicate two critical temperatures of the decomposition of the solution. (a) The ratios between the ion intensities at  $m/z=106$  ( $C_8H_{10}^+$ ) and  $m/z=91$  ( $C_7H_7^+$ ). (b) The ratios between the ion intensities at  $m/z=92$  ( $C_7H_8^+$ ) and  $m/z=106$  ( $C_8H_{10}^+$ ). The inserted figure is the amplification of the curve between 400 and 650 °C. (c) The relative ratios between the ion intensities at  $m/z=106$  ( $C_8H_{10}^+$ ),  $m/z=92$  ( $C_7H_8^+$ ),  $m/z=78$  ( $C_6H_6^+$ ) and  $m/z=40$  ( $Ar^+$ ). (d) The relative intensity ratios of  $I_{106}/I_{78}$  and  $I_{92}/I_{78}$ . For comparison, the ion intensity curve of  $I_{78}/I_{40}$  is plotted at the bottom of figure.

In the second stage, the decomposition of the xylene solution increases when the temperature varies from 600 °C to 900 °C. Fig. 50 shows the quasi-linear decreases of the ion intensities at  $m/z$  106( $C_8H_{10}^+$ ) and 91( $C_7H_7^+$ ), whereas the increases of the ones at  $m/z$  78 ( $C_6H_6^+$ ) and 15( $CH_3^+$ ), with the increase of the temperature. However, the  $I_{92}$  ( $C_7H_8^+$ ) first shows an increase from 600 to 800 °C, and then a decrease from 800 to 900 °C. The evident increase of  $I_{78}$  ( $C_6H_6^+$ ) could only be seen after 750 °C. Moreover, the intensity ratio  $I_{106}/I_{91}$  decreases in a nearly linear way from 0.38 to 0.01 with the increase of the temperature from 600 °C to 900 °C (Fig. 51a). The decreasing  $I_{106}/I_{91}$  indicates that there are certainly the generation of  $C_7H_8$  species in gas phase due to the increased decomposition of  $C_8H_{10}$ . At the same time, the ratio  $I_{92}/I_{106}$  undergoes a firstly slow linear increase from 0.2 at 600 °C to 1.85

at 750 °C, and then a dramatic one above 750 °C (Fig. 51b). This means that there remain a few amounts of xylene in the gas phase above 750 °C. The further observation (Fig. 51c) of the variation of the ion intensities at m/z 106, 92 and 78 show that most xylene is transferred into toluene from 600 to 750 °C. At this temperature region, there is a very weak augmentation of benzene concentration. Whereas, the rapid augmentation of I<sub>78</sub> indicates the increased production of benzene in a linear way, with the increase of temperature from 750 to 900 °C. Benzene could be produced from either the residual xylene, or the generated toluene. As shown in Fig. 51c, both the I<sub>78</sub>/I<sub>40</sub> and I<sub>106</sub>/I<sub>40</sub> decrease with the increase of the temperature. However, the former exhibits a slower decrease rate than the latter. The similar phenomena are also seen from the variations of the relative intensities of I<sub>106</sub>/I<sub>78</sub> and I<sub>92</sub>/I<sub>78</sub> (Fig. 51d). Therefore, it could be deduced that most benzene is produced from the decomposition of toluene. At 900 °C, the concentration of benzene is significantly higher than this of toluene, which is further greatly higher than that of xylene (Fig. 51b and d). In addition, the ion intensities at m/z=12(C<sup>+</sup>) and 26 (C<sub>2</sub>H<sub>2</sub><sup>+</sup>) have a weak increase with the temperature. Whereas, the intensity at m/z=51 first decreases in the temperature range from 600 to 750 °C, and then increases. This is mainly due to the variation of the concentrations of toluene and xylene in the gas phase.

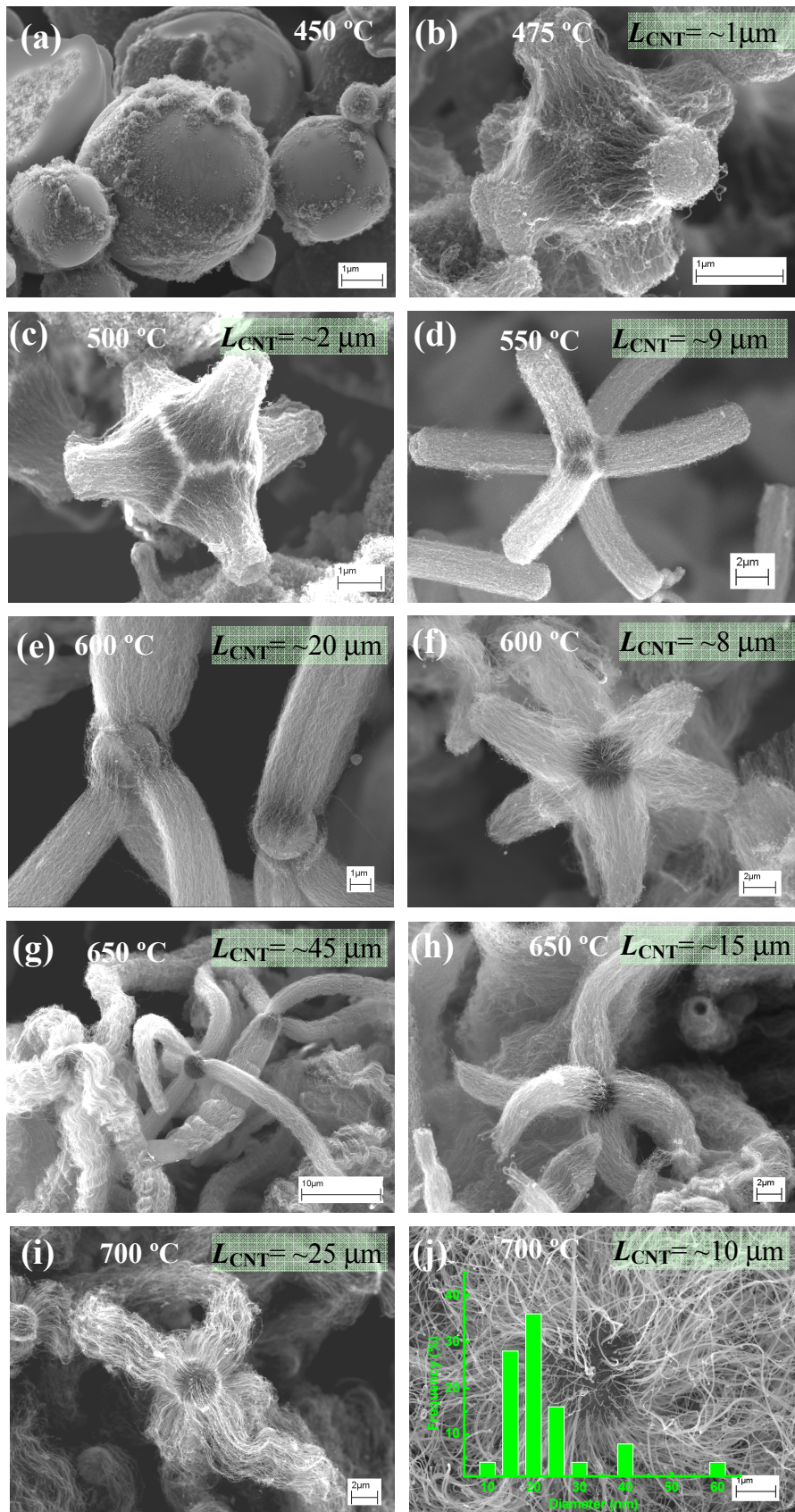
In the third temperature region ( $T \geq 900$  °C), the benzene concentration becomes to decrease, and the residual toluene is continuously decomposed. When the temperature is equal to 1000 °C, the levels of benzene and toluene in the residual gas are very weak, near zero. However, there remains a little of xylene in the gas. This results in an increase of the ratio I<sub>106</sub>/I<sub>91</sub> (Fig. 51a) and a decrease I<sub>92</sub>/I<sub>106</sub> (Fig. 51b). Moreover, the species CH<sub>3</sub> and CH<sub>4</sub> formed from the decomposition of xylene and toluene are largely consumed at 1000 °C.

In summary, the ferrocene-xylene solution undergoes a complex decomposition process when the temperature varies in the range from 400 to 1000 °C. The whole temperature region could be divided into 3 major zones. In the first region ( $T \leq 600$  °C), there is only a little of xylene decomposed at the used conditions. As a result, short CNTs with small diameter are grown on  $\mu$ Al<sub>2</sub>O<sub>3</sub> at a very weak rate. In the second region ( $600 \leq T \leq 900$  °C), the increased pyrolysis rates of xylene and its subsequent products such as toluene promote the growth of CNTs with large diameters and lengths. However, the high decomposition rates at 900 °C also promote the direct formation of amorphous carbon in gas phase. Beyond this temperature, there are no CNTs grow on  $\mu$ Al<sub>2</sub>O<sub>3</sub> at the researched conditions.

### 3.2.3.2 Xylene-acetylene as carbon sources

The effect of temperature is also studied in the range from 450 to 700 °C when the xylene-acetylene mixture is used as carbon source. It is reported that the lowest decomposition temperature of ferrocene is around 400 °C.<sup>36</sup> But, no CNT growth is observed on  $\mu$ Al<sub>2</sub>O<sub>3</sub> particles under our experimental conditions. Ferrocene, concentrated at 0.05g ml<sup>-1</sup>, was dissolved in xylene, which was fed into the furnace at a rate of ~0.2 ml min<sup>-1</sup>. In the mean time, C<sub>2</sub>H<sub>2</sub> was fed at a flow rate of 20 ml min<sup>-1</sup>. The feeding of the ferrocene-xylene solution and acetylene lasted for 15 min. Argon and hydrogen served as carrier gases at flow rates of 0.88 and 0.1 l min<sup>-1</sup>, respectively.

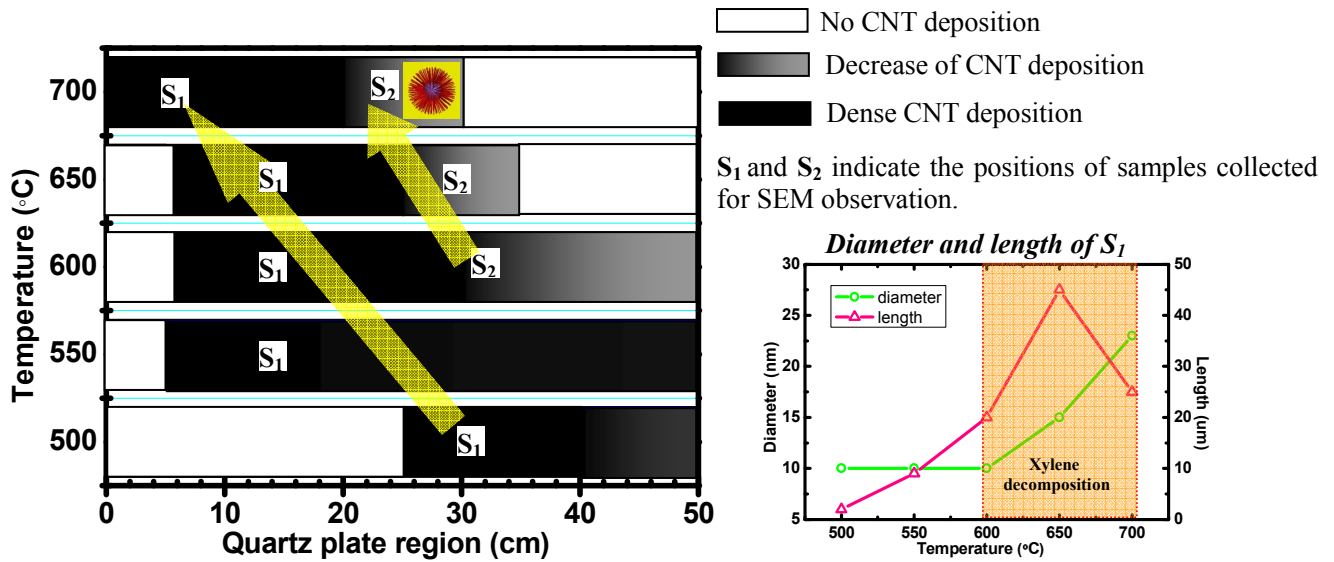
Fig. 52 displays the SEM images corresponding to the CNTs- $\mu$ Al<sub>2</sub>O<sub>3</sub> hybrid structures obtained at the temperatures ranging from 450 to 700 °C. Only few short CNTs are grown on  $\mu$ Al<sub>2</sub>O<sub>3</sub> at 450 °C, and their distribution pattern looks like an inscribed cube inside an alumina sphere (Fig. 52a). The deficient CNT growth indicates that at this temperature ferrocene has a weak decomposition rate. In contrast, the hybrid structures consisting of six CNT bundles are abundantly observed in the final products when the temperature is beyond 450 °C (Fig. 52b-i). At the low temperatures from 475 to 550 °C, the CNT bundles are regularly distributed in the six orthogonal directions. The CNT length consecutively increases from ~2  $\mu$ m at 450 °C to ~9  $\mu$ m at 550 °C, but CNT diameter remains around 10 nm. The CNT bundles obtained at 550 °C is also quite different from these at lower temperatures. CNTs in the bundles obtained at 550 °C are nearly parallel to each other. Whereas, the CNT bundles obtained at the lower temperatures are contracted at their ends.



**Figure 52** SEM images of CNTs- $\mu$ Al<sub>2</sub>O<sub>3</sub> hybrid structures obtained using 20 ml min<sup>-1</sup> C<sub>2</sub>H<sub>2</sub> and 0.2 ml min<sup>-1</sup> ferrocene-xylene solution at the following temperatures: (a) 450 °C, (b) 475 °C, (c) 500 °C, (d) 550 °C, (e-f) 600 °C, (g-h) 650 °C and (i-j) 700 °C. Images f, h and j are SEM images of the hybrid structures collected in the latter regions of the quartz plate. The CNT bundle lengths at different temperatures are indicated in each

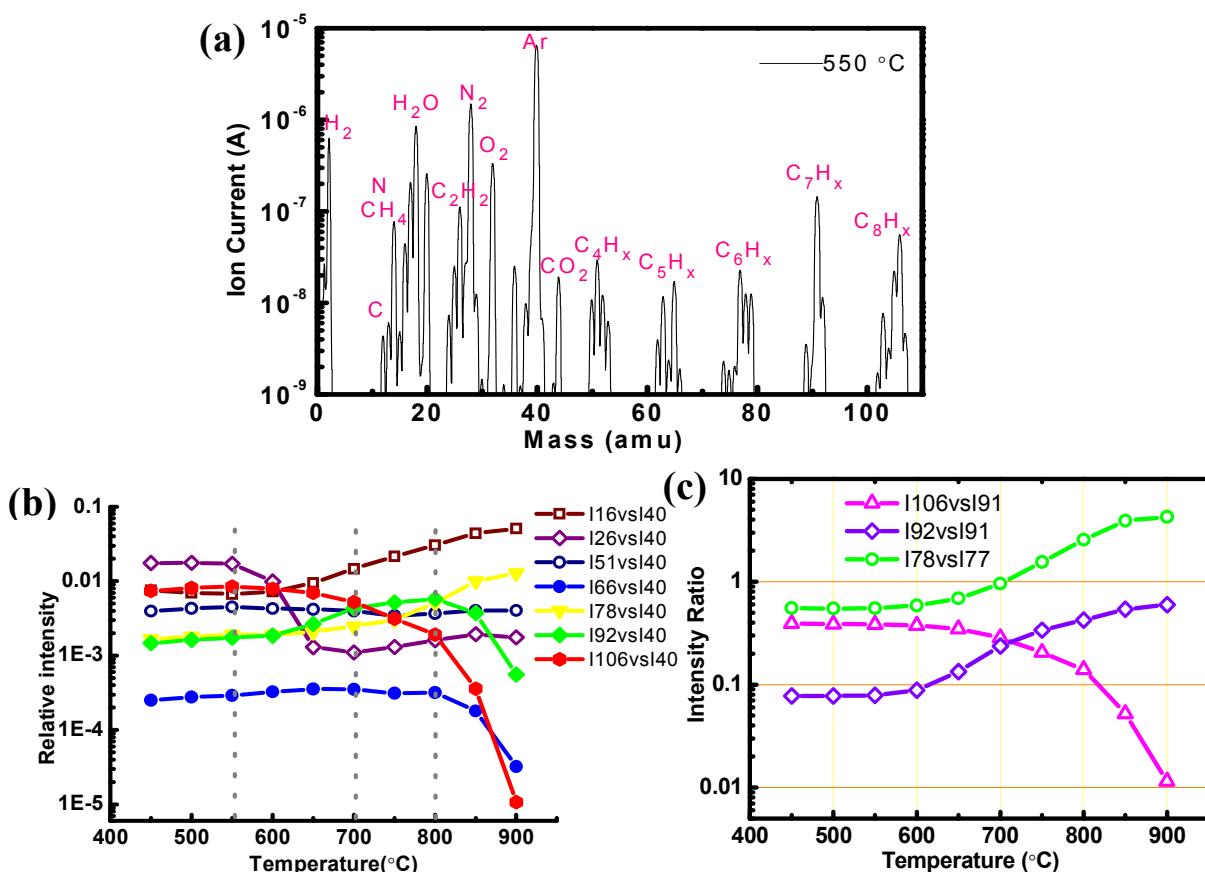
figure.

High density CNTs are observed on the  $\mu$ Al<sub>2</sub>O<sub>3</sub> placed in the quartz plate between 5 and 20 cm at 600 °C (Fig. 52e). The CNT length is ~20  $\mu$ m and its diameter remains ~ 10 nm. However, CNTs grown on the microparticles beyond 30 cm is much shorter in length (~8  $\mu$ m) but larger in diameter ranging between 10 -15 nm. Similarly, the long CNT bundles around 45  $\mu$ m are found on the alumina microparticles located between 5 and 20 cm at 650 °C, but shorter bundles on the particles located in the range of 20-30 cm. However, the diameter of CNTs in the different regions has little variation, ranging between 10 -15 nm. Beyond this temperature, the CNT density evidently decreases on the  $\mu$ Al<sub>2</sub>O<sub>3</sub> which are located at the first 10 cm of the quartz plate. The bundles have a reduced length, ~ 25  $\mu$ m. Moreover, a variation of CNT diameter is also observed from 5 to 15 nm. Most of CNTs have diameters ranging from 10 to 15 nm. No CNT bundle could be observed on the  $\mu$ Al<sub>2</sub>O<sub>3</sub> located in the latter region of the reactor. The CNTs of 10  $\mu$ m in length arrange in all directions on  $\mu$ Al<sub>2</sub>O<sub>3</sub>, forming the “urchin-like” hybrids. The diameter distribution bar diagram (inserted in Fig. 52j) shows that most CNTs have diameters ranging from 15 to 25 nm, and a few of CNTs have a big diameter of 40 nm, or even 60 nm.



**Figure 53.** Schematic of CNT deposition on alumina microparticles dispersed on quartz plate at different growth temperatures. The color change represents the variation of CNT deposition quantity. Two yellow arrows show the increasing tendencies of CNT diameter. The figure at right bottom shows the variations of CNT diameter and length with temperature.

Fig. 53 shows the distribution of CNTs obtained at the temperatures from 500 to 700 °C on  $\mu$ Al<sub>2</sub>O<sub>3</sub> particles which are homogenously dispersed on the surface of quartz plate of 50 cm in length. We can see that the starting deposition position of CNTs moves toward the front of quartz plate with increasing temperature. As indicated in the figure, the decomposition of xylene becomes intense after 600 °C. This could explain why CNT diameter largely increases after this temperature, especially at 700 °C. At the same time, the highly dense CNT deposition region narrows with the increase of temperature after 550 °C. This is mainly due to the increased consumption rates of ferrocene at higher temperatures. The following MS measurements give us more explanations.



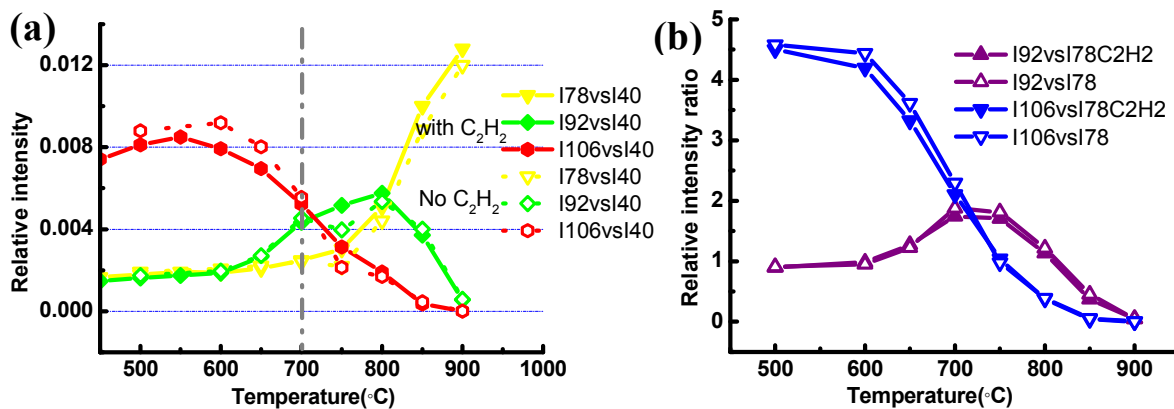
**Figure 54.** (a) Mass spectra of the exhaust gas at 550 °C. (b) Evolution of the ion currents at masses ( $m/z$ ) corresponding to the predominant fragments formed during the reactions. (c) Relative intensity ratios of the fragments of  $C_6H_5$ ,  $C_6H_6$ ,  $C_7H_7$ ,  $C_7H_8$ ,  $C_8H_{10}$ , showing the decomposition of xylene and the production of benzene.

Fig. 54a shows the mass spectra of the exhaust gas produced by the decomposition of the acetylene and xylene mixture at 550 °C. The ion current peaks at  $m/z$  40(20) and 2 are attributed

to the carrier gases Ar and H<sub>2</sub>, respectively. The ones at m/z 44, 32, 28 and 14 correspond to the components of residual air such as CO<sub>2</sub>, O<sub>2</sub> and N<sub>2</sub>, respectively. Acetylene and xylene are identified by their specific molecular peaks at m/z 26 and 106, respectively. Finally, the fragments C<sub>4</sub>H<sub>x</sub>, C<sub>5</sub>H<sub>x</sub>, C<sub>6</sub>H<sub>x</sub>, C<sub>7</sub>H<sub>x</sub> (subscript x indicates integral numbers) resulting from the pyrolysis in furnace or ionizations in mass spectrometer are displayed in the spectra.

Fig. 54b shows the evolution of the ion currents at the masses corresponding to C<sub>8</sub>H<sub>10</sub><sup>+</sup> (m/z 106), C<sub>7</sub>H<sub>8</sub><sup>+</sup> (m/z 92), C<sub>6</sub>H<sub>6</sub><sup>+</sup> (m/z 78), C<sub>5</sub>H<sub>5</sub><sup>+</sup> (m/z 65), C<sub>4</sub>H<sub>10</sub><sup>+</sup> (m/z 58), C<sub>4</sub>H<sub>4</sub><sup>+</sup> (m/z 52), C<sub>2</sub>H<sub>2</sub><sup>+</sup> (m/z 26) and CH<sub>4</sub><sup>+</sup> (m/z 16) with the increase of temperature from 450 to 900 °C. Some noticeable intensity changes are observed at m/z 16, 26, 78, 92 and 106, which correspond to the fragments of CH<sub>4</sub><sup>+</sup>, C<sub>2</sub>H<sub>2</sub><sup>+</sup>, C<sub>6</sub>H<sub>6</sub><sup>+</sup>, C<sub>7</sub>H<sub>8</sub><sup>+</sup> and C<sub>8</sub>H<sub>10</sub><sup>+</sup>, respectively. Obviously, C<sub>2</sub>H<sub>2</sub> undergoes a significant change: it first decreases very slowly from 450 to 550 °C, and then abruptly to a constant at 700 °C. The ion current at m/z 106 corresponding to xylene exhibits first a slight increase until 550 °C due to the increasing evaporation of the xylene solution. Then, the current starts to decrease because of the beginning of the decomposition. The intensity at m/z 92 undergoes an important increase from 550 to 800 °C, and then an evident decrease after 800 °C. This indicates that toluene begins to largely decompose after this temperature. However, the monotonous increase of the relative intensity at m/z 78 indicates the continuous generation of benzene in the reactor, especially after 700 °C. The intensity at m/z 66 corresponding to the fragment of C<sub>5</sub>H<sub>6</sub><sup>+</sup> starts to decrease significantly only when the temperature is larger than 800 °C.

Furthermore, the decomposition of xylene and the generation of toluene and benzene can be more precisely evaluated from the evolution of the relative ratios between the intensities at m/z 106, 92, 91, 78 and 77. According to the standard spectra library provided by Pfeiffer Vacuum, the relative intensity ratios are different in the spectra of xylene, toluene and benzene. They are as follows: I<sub>106</sub> / I<sub>91</sub>: ~0.577 (xylene), I<sub>92</sub> / I<sub>91</sub>: ~0.075 (xylene) and ~0.784 (toluene), and I<sub>78</sub> / I<sub>77</sub>: ~0.661 (xylene) and ~6.938 (benzene). The evolutions of the I<sub>106</sub> / I<sub>91</sub>, I<sub>92</sub> / I<sub>91</sub> and I<sub>78</sub> / I<sub>77</sub> (Fig. 54c) show that xylene does not evidently decompose under these experimental conditions until 550 °C. The decomposition rate of xylene increases quickly after 600 °C. Similarly, it is found that toluene and benzene appear in exhaust gases obtained at temperatures higher than 550 °C. Their concentrations quickly increase. This means a large part of xylene decomposes into toluene and benzene.



**Figure 55.** MS analyses of the impact of acetylene on the decomposition of xylene into toluene and benzene. (a) Comparison of relative intensities at  $m/z$  78 ( $C_6H_6^+$ ), 92 ( $C_7H_8^+$ ) and 106 ( $C_8H_{10}^+$ ) obtained by measuring of the exhaust gases from the decomposition of carbon source with (solid symbols) or no (hollow symbols) acetylene. (b) Relative intensity ratios  $I_{106}/I_{78}$  and  $I_{92}/I_{78}$  in the cases with (solid symbols) or no acetylene (hollow symbols) in the system.

The impact of acetylene on the decomposition of xylene is further demonstrated by comparing the relative intensities at  $m/z$  78 ( $C_6H_6^+$ ), 92 ( $C_7H_8^+$ ) and 106 ( $C_8H_{10}^+$ ) between the two cases with or without acetylene. MS measurements are conducted on the following two kinds of exhaust gases at the temperatures ranging from 450 to 900 °C. In the first case, xylene is used as the only carbon source. In the second case, acetylene is added into the reactor at a flow rate of 20 ml min<sup>-1</sup>. The concentration of ferrocene in xylene solution is 0.05 g ml<sup>-1</sup>. As shown in Fig. 55a, the relative intensity of xylene with C<sub>2</sub>H<sub>2</sub> is lower than that without C<sub>2</sub>H<sub>2</sub> when the temperature is lower than 700 °C. However, no evident difference has been observed in the relative intensities at  $m/z$  78 and 92 between the cases with or no addition of acetylene. Beyond 700 °C, the addition of acetylene produces little variation of the intensities at  $m/z$  92 and 106, but an increasing augmentation of the one at  $m/z$  78. This means that more acetylene is transformed into benzene at high temperatures than at low ones. As shown in Fig. 55b, the intensity ratios  $I_{106}/I_{78}$  and  $I_{92}/I_{78}$  of two cases (with and no C<sub>2</sub>H<sub>2</sub>) also indicate the addition of acetylene generates a slight decrease of the relative abundances of xylene and toluene in the system, compared with that of benzene.

**In summary:** based on the MS analyses and SEM characterizations, it could be concluded that the evolution of hybrid structures is mainly related to the pyrolysis of C<sub>2</sub>H<sub>2</sub> at the temperatures ranging from 450 to 600 °C. The synthesized hybrid structures consist of CNTs in “the six-branch” structures, and the CNTs have a homogeneous diameter, ~10 nm. A further increase of the temperature yields the increased decomposition of xylene. Due to the intensified

decomposition of ferrocene, CNT diameter and length increase with temperature. In turn, the “urchin-like” hybrid structures which consist of CNTs with large diameters are synthesized.

### **3.2.4 Hydrogen ratio**

In this research, the synthesis of the hybrid structures is conducted under ambient atmosphere pressure. The MS measurements demonstrate the presence of a relatively high percentage of oxygen in the system, which could be from air, or impurities contained in carrier gases. It has been proven that a small amount of oxygen enhances catalyst activity and prolongs catalyst lifetime by preventing amorphous carbon formation on the catalyst surface, and thus promotes CNT growth. On the other hand, too much oxygen in reactor could result in the oxidization metal catalyst particles, as well as the consumption of hydrocarbons by the formation and discharge of CO and CO<sub>2</sub> gases. Therefore, hydrogen serving as protective gas is added in floating CVD system for CNT synthesis. However, reactive hydrogen (H•) has been demonstrated to play a negative effect to CNT growth by plasma assistant CVD of methane at a low pressure of 0.3-0.4 torr (1 torr = 133 Pa)<sup>[169]</sup>. Increasing H<sub>2</sub> presence always leads to systematic decrease in SWCNT yield, because high concentrations of H species do not favor the formation and growth of sp<sup>2</sup>-like carbon structures.

In the following part, we will discuss about the influence of hydrogen ratio on the growth of hybrid structures by the thermal decomposition of carbon sources at different temperatures.

#### **3.2.4.1 Hybrids from xylene decomposition at relatively high temperatures**

The influence of hydrogen is studied when xylene is used as carbon source at 780 °C. Ferrocene, concentrated at 0.05g ml<sup>-1</sup>, is dissolved into xylene solution, which is then injected into the reactor at a rate of ~ 0.2 ml min<sup>-1</sup>. The solution feeding time is 12 min. The hydrogen ratio is varied from 0 to 40 % in the carrier gases at a total flow rate of 1 l min<sup>-1</sup>. That is, the used hydrogen flow rates are 0, 0.1, 0.2 and 0.4 l min<sup>-1</sup>. The samples are collected in the region from 1 to 3 cm of the quartz plate.

Fig. 56 shows the hybrid structures obtained with different hydrogen ratios in carrier gases. No presence of hydrogen in the atmosphere favors the formation of long CNTs which are decorated on their outer surfaces with a large number of carbon particles (Fig. 56a). The CNT

diameter mainly varies from 30 to 45 nm. The CNT density on alumina particles is so high that CNTs self assemble as one bundle with a length of  $\sim$  80  $\mu$ m. At the same time, no hydrogen presence in the carrier gases also promotes the generation of a layer of amorphous carbon deposition on the microparticles. This layer containing iron atoms, along with a few of thin and long CNTs (Fig. 56b). However, these impurities are considerably decreased when hydrogen is added in the carrier gases. Few particles are found on CNTs grown with 40 % hydrogen (Fig. 56g-h). Instead, large amounts of iron particles encapsulated by a layer of carbon are deposited on the surface of  $\mu$ Al<sub>2</sub>O<sub>3</sub>, as shown in Fig. 56d, f and h. No evident variation is observed in the CNT diameter and density with the increase of hydrogen ratio. The CNT bundles have a large length, more than  $\sim$ 80  $\mu$ m at different hydrogen ratios. As one part of CNT bundle is often covered by the neighboring hybrid structures, it is very difficult to measure the CNT length variation with hydrogen ratio. But the variation of the thickness of CNT carpets collected on the quartz plate indirectly demonstrates that the presence of hydrogen in atmosphere decreases the CNT growth rate. As shown in Fig. 57, a CNT layer of  $\sim$  350  $\mu$ m in thickness has been obtained in 12 min when no hydrogen is present in atmosphere. That is, the average CNT growth rate is about 30  $\mu$ m min<sup>-1</sup>. As a comparison, the CNT layer thickness decreases to  $\sim$ 110  $\mu$ m, that is, the average growth rate of CNTs is only  $\sim$  9  $\mu$ m min<sup>-1</sup> when 10 % hydrogen is added. Furthermore, it is found that CNT diameter almost keeps the same level at the two conditions mentioned above.

Fig. 58 shows the variation of the MS intensities at m/z 15, 18, 26, 51, 78, 92, 106 and 120 with the increase of hydrogen ratio. These peaks have experienced a noticeable intensity change, and they are attributed to the species CH<sub>3</sub><sup>+</sup>, H<sub>2</sub>O<sup>+</sup>, C<sub>2</sub>H<sub>2</sub><sup>+</sup>, C<sub>4</sub>H<sub>3</sub><sup>+</sup>, C<sub>6</sub>H<sub>6</sub><sup>+</sup>, C<sub>7</sub>H<sub>8</sub><sup>+</sup> and C<sub>8</sub>H<sub>10</sub><sup>+</sup>, respectively. First, the increase of the intensity of H<sub>2</sub>O<sup>+</sup> indicates that high ratios of hydrogen reduce more quantity of oxygen in the reactor. The oxygen is mainly from the carrier gases and air. As indicated early, certain amount of oxygen in reactor promotes CNT growth. This could be one reason of why CNT length decreases with the increase of hydrogen ratio. Second, the decrease of the intensity of C<sub>8</sub>H<sub>10</sub><sup>+</sup> demonstrates that hydrogen promotes the decomposition of xylene at relatively high temperatures. The augmentation of the intensity of C<sub>6</sub>H<sub>6</sub><sup>+</sup> represents the increased concentration of benzene in the exhaust gas at high hydrogen ratios. But the abundance of toluene keeps nearly the same level at different hydrogen ratios. In addition, a slight increase has also been observed in current intensities of the peaks at m/z 30 (C<sub>2</sub>H<sub>6</sub><sup>+</sup>) and 51 (C<sub>4</sub>H<sub>3</sub><sup>+</sup>).

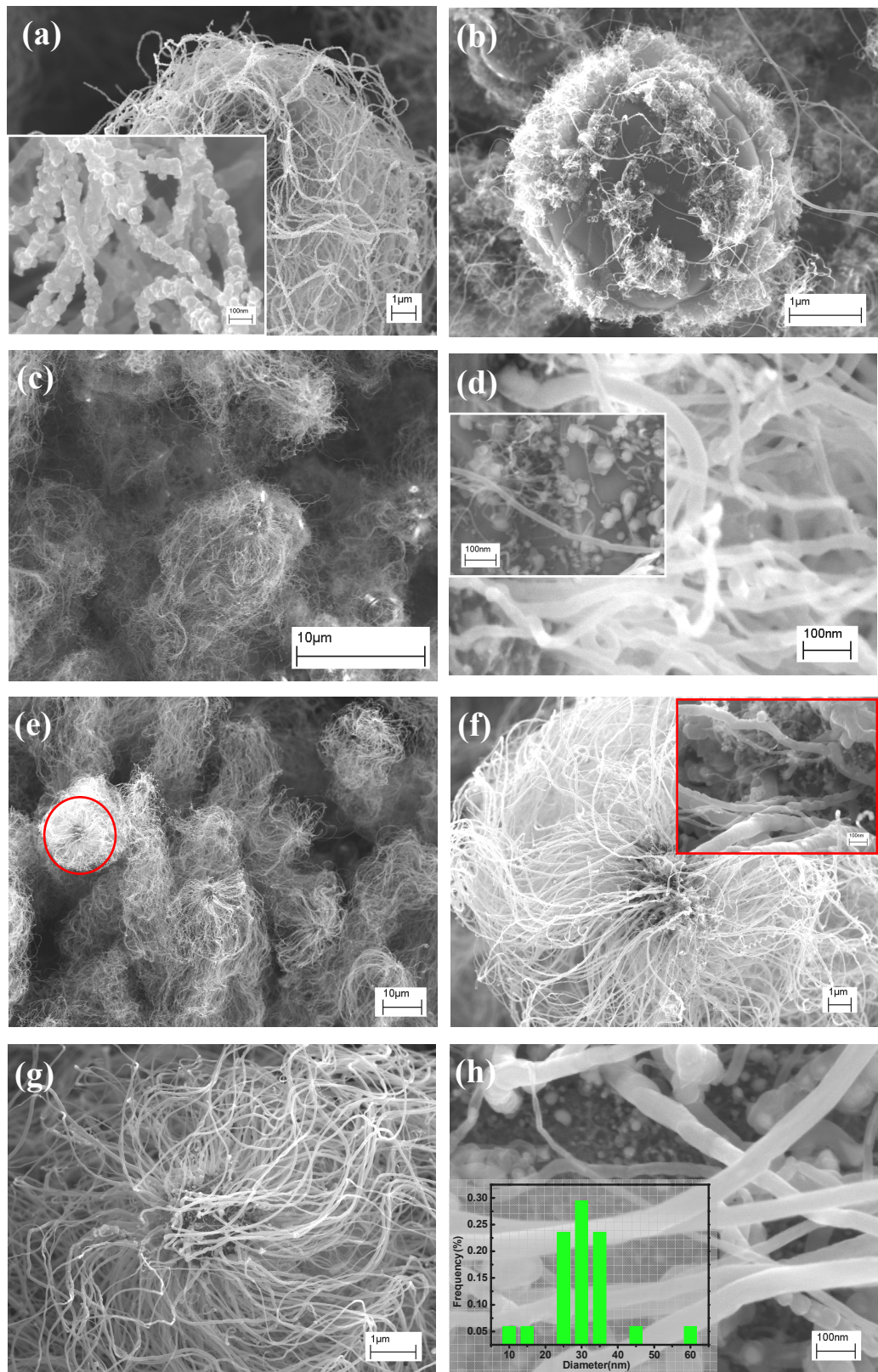


**Figure 56.** SEM images of the hybrid structures obtained with different hydrogen ratios  $f_{H_2}$  at 780 °C. (a-b)  $f_{H_2} = 0$ : large amounts of particles decorating on CNTs (image a), and the alumina particle covered by a thin carbon layer containing iron atoms (image b). (c)  $f_{H_2} = 10\%$  (0.1 l min<sup>-1</sup>). (d) high magnification SEM image of the surface of alumina particle. (e)  $f_{H_2} = 20\%$  (0.2 l min<sup>-1</sup>). (f) high magnification of the circled particle in e. (g)  $f_{H_2} = 40\%$  (0.4 l min<sup>-1</sup>). (h) high magnification of CNTs and alumina particle surface in g, and the inserted bar graph shows CNT diameter distribution.

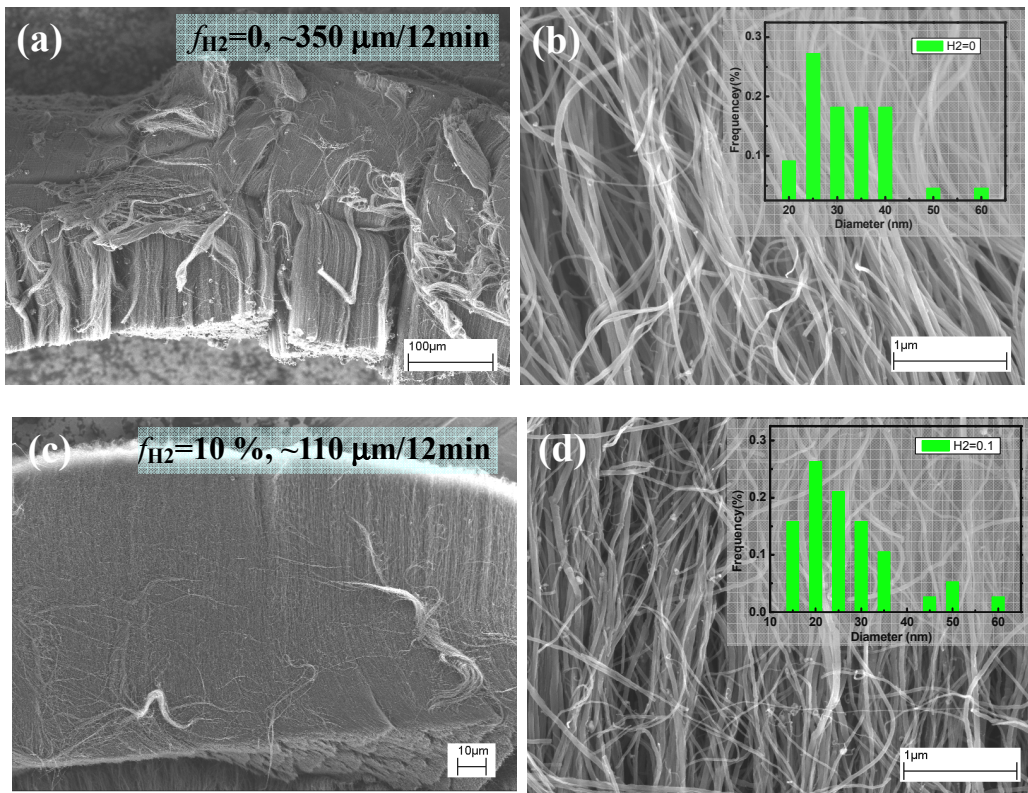


**Figure 57.** SEM images of the CNT carpets obtained with different hydrogen ratios: (a-b)  $f_{H_2}=0$ , and (c-d)  $f_{H_2}=10\%$ . Images b and d are the high magnification of images a and c, respectively. The inserted bar graphs show the distributions of CNT diameters at the two different hydrogen ratios.

The above analyses demonstrate that the reductive hydrogen prevents the formation of amorphous carbon particles during CNT growth when xylene is used as carbon source at relatively high temperatures. High hydrogen ratios in carrier gases promote the decomposition of xylene to benzene, but the decrease of CNT growth rate. The presence of large amounts of carbon layer encapsulated iron particles is due to the insufficient feeding of the effective carbon which could directly contribute to CNT nucleation and growth.

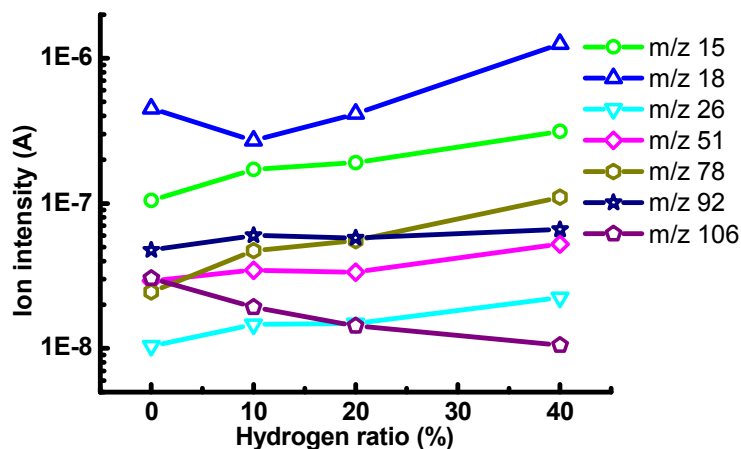


**Figure 58.** Evolution of MS ion current intensity peaks attributed to the fragments  $CH_3^+$ ,  $H_2O^+$ ,  $C_2H_2^+$ ,  $C_4H_3^+$ ,  $C_6H_6^+$ ,  $C_7H_8^+$  and  $C_8H_{10}^+$ , with the increase of hydrogen ratio in CVD reactor.

### 3.2.4.3 Hybrids from the decomposition of xylene/acetylene mixture

In the previous part, we have discussed the influence of hydrogen ratio on CNT growth on  $\mu$ Al<sub>2</sub>O<sub>3</sub> when xylene is used as carbon source. It has been noticed that high hydrogen ratios promote the decomposition of xylene and the formation of aligned CNTs with less impurities such as amorphous carbon particles. However, a large number of iron particles encapsulated by carbon layers are deposited on the surface of  $\mu$ Al<sub>2</sub>O<sub>3</sub>. These particles have sizes similar to the CNT diameters, but they fail to catalyze CNT growth. Consequently, a certain quantity of iron is not contributed to the growth of CNTs. In contrast, iron particles could be sufficiently used to grow CNTs when certain amount of acetylene is added into the reactor. Moreover, the produced CNTs have a homogeneous diameter and a high number density. This indicates that the interaction between catalyst precursor and carbon source strongly influences the catalyst in CNT growth activity.

In this part, we will study the impact of hydrogen ratio on CNT growth using the acetylene/xylene mixture as carbon sources at 780°C. A constant acetylene flow rate, 20 ml min<sup>-1</sup>, is used, that is, 2 % in total carrier gases. The hydrogen ratio is varied from 0 to 40 % in a series of 0, 0.05, 0.1, 0.2 and 0.4 l min<sup>-1</sup>. The ferrocene-xylene solution is injected at a rate of ~ 0.2 ml min<sup>-1</sup> for 12 min.

Fig. 59 shows the hybrid structures obtained with different hydrogen ratios. For comparison, the hybrid structures synthesized at each hydrogen ratio have been collected from several different regions of the quartz plate.

Firstly, it is found that high hydrogen ratios favor the formation of “clean” CNTs without impurities. The hybrid structures synthesized using  $f_{\text{H}_2}=20\%$  and 40 % consist of pure CNTs on  $\mu$ Al<sub>2</sub>O<sub>3</sub>, as shown in Fig. 59a-f. On the other hand, the impurities including amorphous carbon particles and iron particles are observed in the hybrid structures obtained using low hydrogen ratios or no hydrogen, as shown in Fig. 59j-n. These results confirm the important roles played by hydrogen in floating CVD process for the synthesis of CNTs- $\mu$ Al<sub>2</sub>O<sub>3</sub> hybrid structure. High concentration hydrogen prevents impurity formation by lowering the dehydrogenation rates of acetylene, or by recombining with carbon to reproduce hydrocarbon fragments.

Secondly, with the increase of hydrogen ratio the organization of CNTs on  $\mu$ Al<sub>2</sub>O<sub>3</sub> varies from six branches (Fig. 59j, m and n) to one bundle (Fig. 59a, d, g, h and k), and then to the “urchin-like” structures (Fig. 59b-c and e-f). Correspondingly, the mean diameter of CNTs also varies from  $\sim 15$  to  $\sim 30$  nm, and then to  $\sim 60$  nm, respectively. It is worth noting that the CNT diameter also depends on the growth position of CNTs in the reactor. As indicated in Fig. 59, CNTs grown in the front of the reactor show little variation in diameter ( $\sim 15$  nm) with the hydrogen ratio. However, CNTs formed in the middle or back region of the reactor have large diameters, except the one when  $f_{\text{H}_2} = 0$ . The values of 30 and 40 nm in mean diameter are observed for CNTs formed in the region from  $\sim 10$  to  $20$  cm on quartz plate when the hydrogen ratio is 5 and 10 %, respectively. But higher hydrogen ratios (20 and 40 %) result in the CNTs with larger diameter,  $\sim 60$  nm. However, the growth of CNTs in the region after 20 cm is completely different at different hydrogen ratios. For instance, the “urchin-like” hybrid structures are formed when hydrogen ratio is larger than 20 %. In these structures, the CNT average diameter is  $\sim 60$  nm, but their length greatly decreases compared with the ones in the previous regions. In contrast, when the hydrogen ratio is less than 20 %, the growth of CNTs is always accompanied with various different kinds of impurities including carbon-encapsulated iron particles decorated on the outer surface of CNTs (Fig. 1 and n) and these deposited on the surface of  $\mu$ Al<sub>2</sub>O<sub>3</sub> (Fig. 59i). Another one evident difference along the length of quartz plate is the CNT density on  $\mu$ Al<sub>2</sub>O<sub>3</sub>, as shown in the inserted images in Fig. 59. It is found that at various hydrogen ratios the CNT number densities decrease with the increase of the growth position increasing the length. These variations are especially significant when the hydrogen ratio is less than 20 % (Fig. 59g-n).

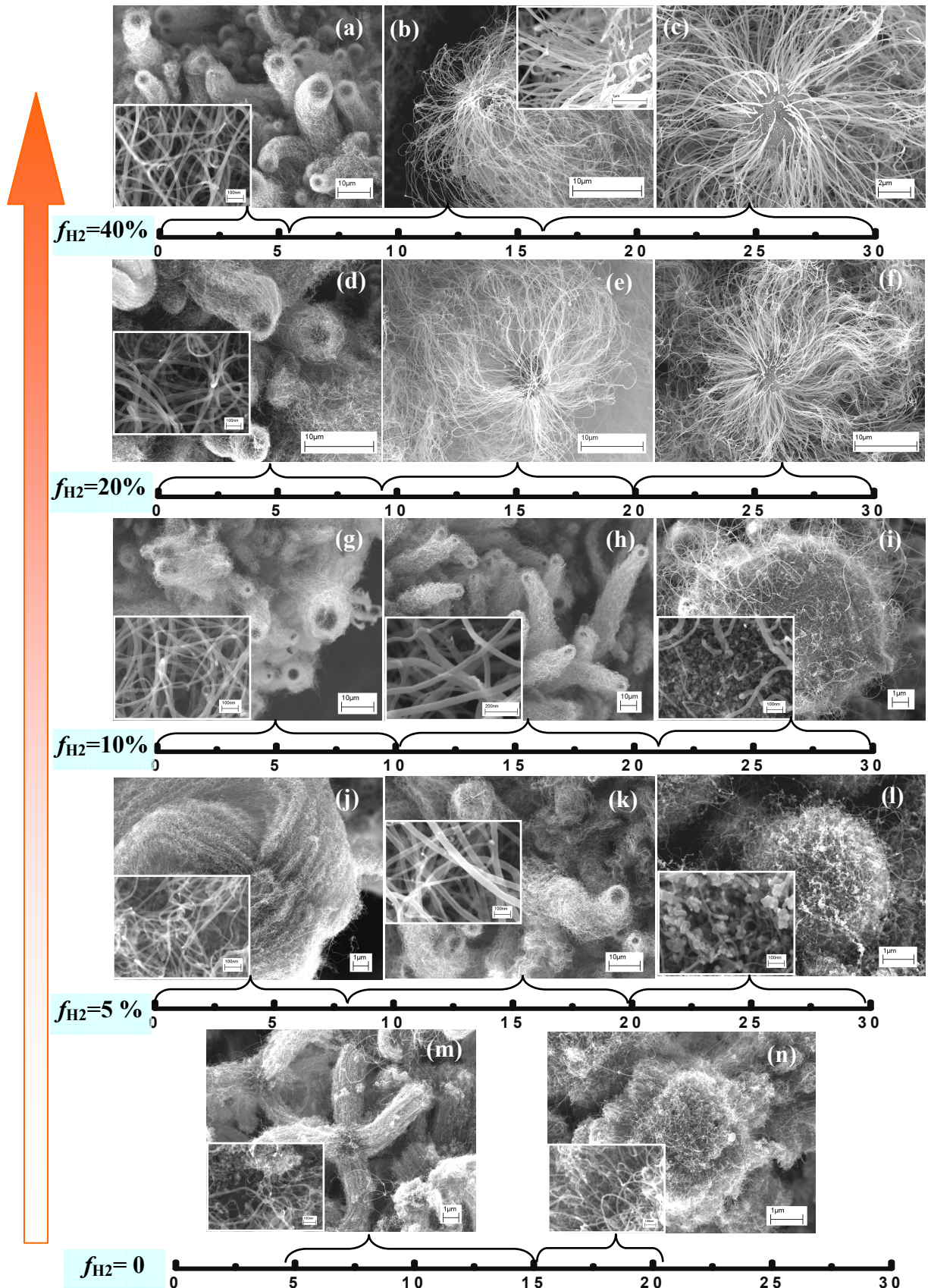


**Figure 59.** SEM images of the hybrid structures synthesized with varied  $f_{H_2}$  from 0 to 40 %. The lines with scales (unit: cm) represent the distribution of hybrid structures along the length of quartz plate at each hydrogen ratio. Acetylene is added as carbon source along with xylene. The total gas flow rate is  $1\text{ l min}^{-1}$ .

The length of CNTs on  $\mu$ Al<sub>2</sub>O<sub>3</sub> varies as does the area number density. That is, they gradually decrease along the CNT growth position on the quartz plate. Indeed, this could be directly seen from the variation of the thickness of deposition on the quartz plate. Always, the thickness decreases with the position of the deposition. Fig. 59m and n show that the CNT length decreases from 7 micrometer in the region of 5-15 cm to 1 micrometer in the region of 15-20 cm when no hydrogen is added in the system. The length of one CNT bundle shown in Fig. 59j is  $\sim$  100  $\mu$ m, but the CNT length in Fig. 59l is only about several micrometers. It is worth noting that CNT length difference along the deposition position becomes less evident with the increase of the hydrogen ratio. For instance, the CNT length of  $\sim$  60  $\mu$ m is measured in the region from 0 to 5 cm, and the one of  $\sim$  35  $\mu$ m is measured for CNTs in the “urchin-like” structures in the back region when hydrogen ratio is 20 %.

The above analyses demonstrate the significant influence of hydrogen ratio on the hybrid structures produced using the acetylene/xylene mixture as carbon source. The hydrogen influence is effectuated by varying the distribution of the concentrations of the effective carbon or iron species which could directly contribute to CNT growth. The variation of the CNTs- $\mu$ Al<sub>2</sub>O<sub>3</sub> hybrid structures along the CNT deposition position demonstrates the influence of hydrogen ratio on chemical kinetics of the decomposition of carbon sources (acetylene and xylene) and catalyst precursor (ferrocene).

### ***3.2.4.1 Hybrids from acetylene decomposition at relatively low temperatures***

The influence of hydrogen ratio on the formation of hybrid structures is also studied by decomposition of the acetylene/xylene mixture at relatively low temperature(50°C). The hydrogen flow rate varies from 0.4 to 0 1 min<sup>-1</sup>, corresponding to the ratio from 40 % to 0. Whereas, a constant acetylene flow rate of 10 ml min<sup>-1</sup> (1 %) is used at various hydrogen flow rates.

The considerable influences on the CNT length and the morphology of the hybrid structures have been observed (Fig. 25). The CNT length decreases nearly exponentially with the increase of hydrogen ratio. At the same time, the “six-branch” hybrid structures transform to “short-dense-homogenous” ones. This proves again the inhibition role of hydrogen in the dehydrogenization of acetylene on the catalyst particles.

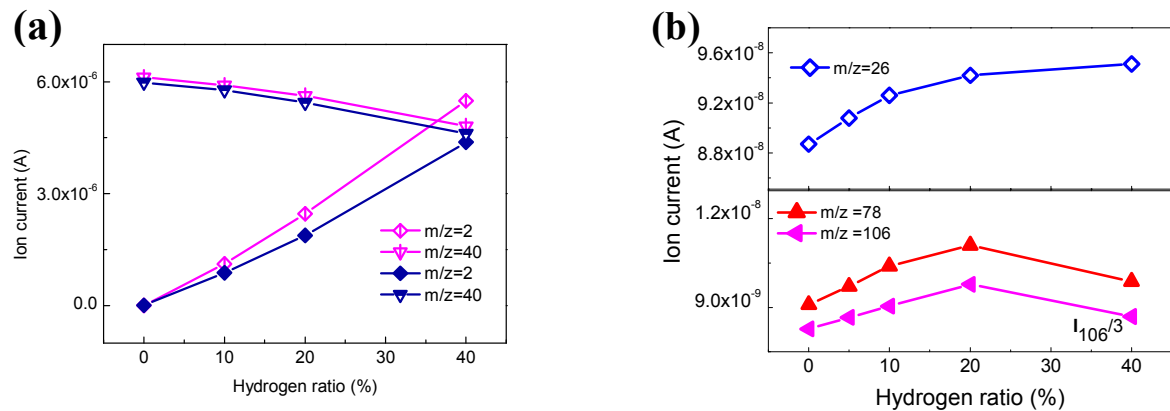


**Figure 60.** MS analyses of the influence of hydrogen ratio on the pyrolysis of acetylene. (a) Comparison of the ion intensities of hydrogen ( $m/z=2$ ) and argon ( $m/z=40$ ) measured at 550 °C before (hollow symbols) and after (solid symbols) the injections of  $C_2H_2$  ( $10\text{ ml min}^{-1}$ ) and ferrocene-xylene solution ( $0.05\text{ g mL}^{-1}$ ). The argon flow rates are  $1-x$  ( $x=0, 0.06, 0.1, 0.2, 0.4\text{ l min}^{-1}$ ), where  $x$  is hydrogen flow rate. (b) Evolution of the ion currents at  $m/z$  26, 78 and 106 with increasing hydrogen ratio. For better display, the intensity at  $m/z$  106 has been divided by 3.

Fig. 60 shows the MS analyses on the decomposition of carbon sources at different hydrogen ratios. The ion current intensities at  $m/z$  2 and 40, corresponding to hydrogen and argon, respectively, were measured using a  $C_2H_2$  gas flow rate of  $10\text{ ml min}^{-1}$ . For comparison, the ion intensities before injecting acetylene and ferrocene-xylene solution were also measured, as shown in Fig. 60a. In the two cases, the intensities at  $m/z$  40 decrease linearly and parallel to each other with increasing the hydrogen ratio and the ones at  $m/z$  2 increase almost linearly. However, an increasing difference is visible for the intensity at  $m/z$  2 with or without acetylene. This difference is attributed to the consumption of hydrogen, by its interactions with carbon sources and catalyst precursor or carbon. It is justified by the fact that the pyrolysis of acetylene in CNT growth is degraded with increasing hydrogen ratio. This could be seen from the gradual increase in ion intensity at  $m/z$  26 (Fig. 60b). In addition, the ion intensity at  $m/z$  78 demonstrates a small variation at different hydrogen ratios, and it reaches a maximum value at 20 % of hydrogen. Nevertheless, the ion intensity is derived from the ionization of xylene during MS measurements. Therefore, the production of benzene during the pyrolysis of acetylene at different hydrogen ratios is negligible.

**In summary**, the hydrogen ratio in carrier gases plays a significant role in the production of the hybrid structures. These influences are greatly dependent on the natures of carbon sources and the used temperatures. First, the addition of hydrogen favors to inhibit the formation of amorphous carbon structures during CNT growth, especially when acetylene is

used as carbon source at relatively high temperatures. Second, a certain amount of hydrogen could prevent the catalyst particles from the oxidation by the oxygen in ambient atmosphere condition. Third, hydrogen decreases the dehydrogenation processes from hydrocarbons, and thus decreases CNT growth rate. Especially, the dehydrogenization of acetylene is greatly suppressed by adding high concentration ratio hydrogen. This helps to decrease the differences produced in CNT growth rate and hybrid structures along the CNT deposition distance in the reactor. At low temperatures ( $T \leq 550$  °C), CNTs grow mainly from the decomposition of acetylene. The hydrogen ratio shows little effect on the CNT diameter. But, its influence on the CNT growth rate is clearly seen from the variation of CNT length and the transformation of hybrid structures.

### ***3.3 Effects of substrate properties***

The contribution of the micrometer substrates to CNT organization is greatly different from that of the large substrates with a flat surface such as quartz plate. In the following parts, we will study the significant roles played by alumina microspheres in the creation of multiform hybrid structures.

#### ***3.3.1 Effect of substrate morphology***

“Carpet-like” CNT arrays are generally grown on large flat substrates by floating CVD. Quartz plate is one of the commonly used flat substrates. Fig. 61 shows one CNT carpet of 100  $\mu$ m in thickness, formed by the decomposition of C<sub>2</sub>H<sub>2</sub> (0.01 l min<sup>-1</sup>) and ferrocene-xylene solution (0.05 g ml<sup>-1</sup>) at 800 °C for 10 min. The flow rates of argon and hydrogen gases are 0.71 and 0.08 l min<sup>-1</sup>, respectively. It could be seen that the “carpet” consists of highly dense CNTs which are approximately parallel to each other, and which are quasi-vertically aligned on the substrate surface. It is worth noting that the flat substrate contains a large number of micrometer crystalline grains, and its general surface curvature is infinitely small, close to zero.

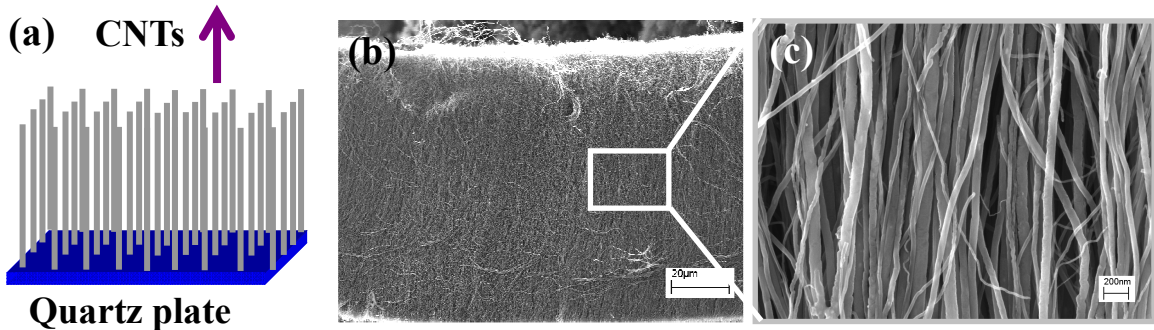


**Figure 61.** (a) Schematic of the growth of CNTs on quartz plates. (b-c) SEM images of highly dense vertically- aligned CNTs grown on quartz plate. c is the high magnification SEM image of the square zone marked in (b).

When micrometer particles are used as substrates, CNT growth varies with individual particle shape. For instance, more CNTs are found to grow on the two sides than on the periphery of the micro alumina plates (Fig. 62a-b). However, when “triangular-prism-like” micrometer alumina particles are used as substrates, few of CNTs could be found on the flat base surface. By contrast, high density CNTs grow on the peripheral side surfaces along three different directions (Fig. 62c). High magnification image (Fig. 62d) shows that the side surfaces are constituted of many regularly arranged small crystalline steps. Fig. 62e shows two alumina micrometer hemispheres separated by CNTs grown perpendicularly on the two internal fracture surfaces. The two CNT cylinders are connected together at the intersection part. Oppositely, CNTs grown on the spherical surfaces organize into several “branches” in different directions.

Based on the SEM results, it can be concluded that the morphology of microparticles has a great influence on CNT organization, and thus on the hybrid structures. In this study, ceramic microspheres with the sizes mainly ranging from 1 to 7  $\mu\text{m}$  are used as substrates to create the nano-micro hybrid structures. Compared with the large plate substrates, the microspheres have a much higher surface curvature ( $\sim 10^6 \text{ rad m}^{-1}$ ) which is favorable to obtain well-dispersed CNTs potentially grown in all spatial directions, like the “urchin-like” CNTs- $\mu$ Al<sub>2</sub>O<sub>3</sub>. This kind of hybrid fillers has an unparalleled advantage in improving the heterogeneity of CNTs-based composite properties.

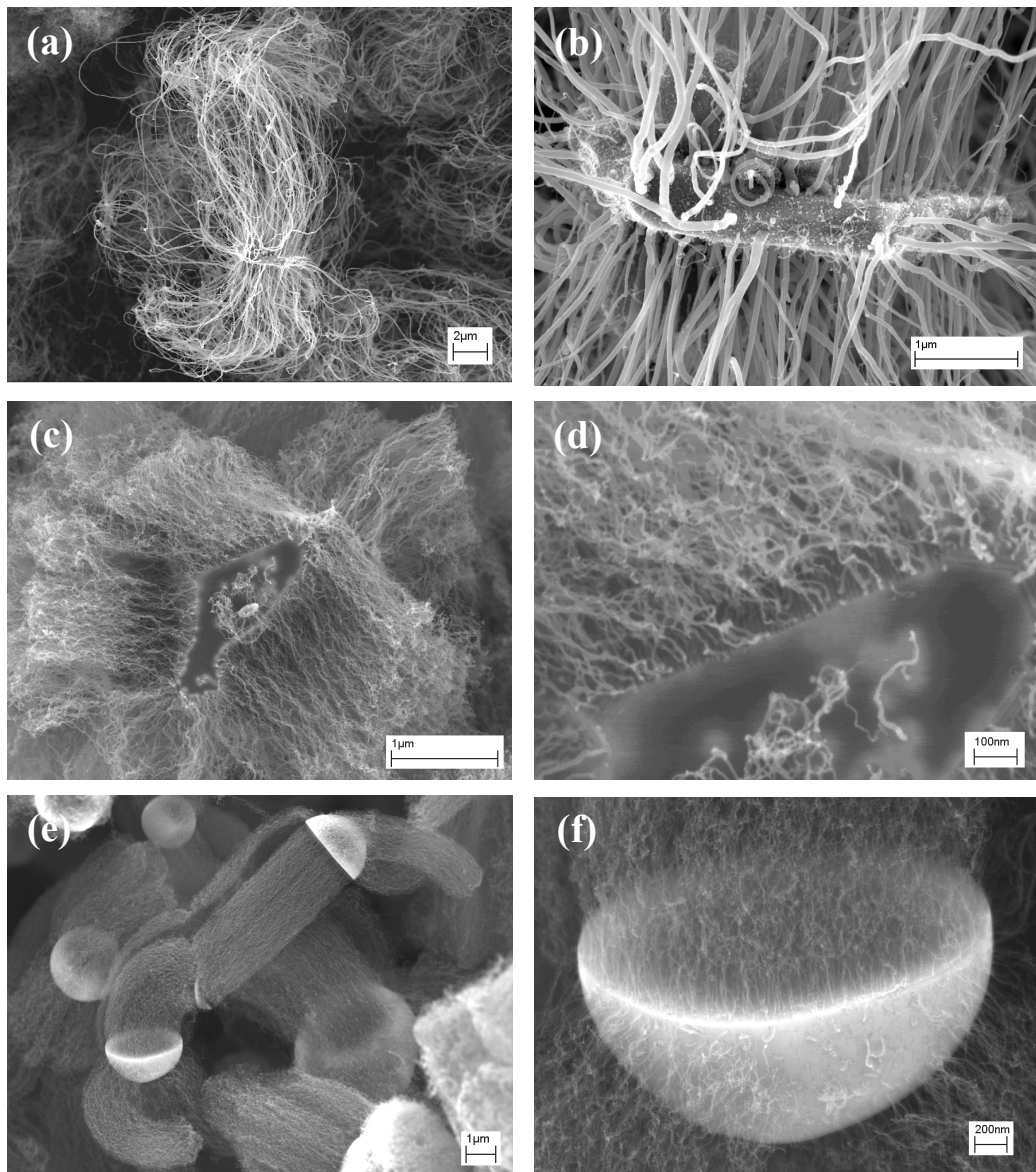


**Figure 62.** SEM images of CNTs grown on the alumina microparticles with different morphologies. (a-b) micrometer plates: ferrocene-xylene solution ( $0.05 \text{ g ml}^{-1}$ ) with  $H_2$  ( $0.1 \text{ l min}^{-1}$ ) and  $Ar$  ( $0.9 \text{ l min}^{-1}$ ) at  $780^\circ\text{C}$ , (b) is the higher magnification of a. (c-d) “triangular-prism-like” micrometer alumina particles: ferrocene-xylene solution ( $0.05 \text{ g ml}^{-1}$ ) with  $C_2H_2$  ( $0.02 \text{ l min}^{-1}$ ),  $H_2$  ( $0.1 \text{ l min}^{-1}$ ) and  $Ar$  ( $0.88 \text{ l min}^{-1}$ ) at  $550^\circ\text{C}$ , (d) is the higher magnification of (c); (e-f) micro alumina hemispheres: the same condition as the previous one, f is the higher magnification of (e).

### 3.3.2 Effect of particle size

The particle size is another parameter that could possibly influence the obtention of regular hybrid structures. We know that the diameter of spherical particles directly relates with their surface area and curvature, which could in turn affect the quantity of CNTs grafted on one  $\mu$ Al<sub>2</sub>O<sub>3</sub> and the CNT density. The variation of local surface structure is pronounced with the increase of the particle size, during their formation process. These heterogeneities might also be an impact factor that generates the variation of the hybrid structures.

Here, we demonstrate, for example, the variation of the “six-branch” hybrid structures with increasing the alumina microparticle diameter from 0.5 to 10  $\mu$ m. The CNTs are synthesized at 600 °C by injecting C<sub>2</sub>H<sub>2</sub> (0.02 l min<sup>-1</sup>) and the ferrocene-xylene solution (0.05 g ml<sup>-1</sup>) during 8 min. The gas flow rates of Ar and H<sub>2</sub> are 0.8 and 0.2 l min<sup>-1</sup>, respectively. Fig. 63 shows the hybrid structures constituted of high density CNTs on the  $\mu$ Al<sub>2</sub>O<sub>3</sub> with different diameters. Only a few CNTs grow on the  $\mu$ Al<sub>2</sub>O<sub>3</sub> with a diameter of 700 nm, as demonstrated in the inserted high magnification SEM image. Moreover, CNTs seem to self-organize into two thin branches which are in fact a combination of several thinner branches with a length of ~ 15  $\mu$ m. The combination is due to the small surface area available CNT growth and the narrow space between CNT branches. When the particle diameter is ~ 1.8  $\mu$ m, the quantity of CNTs on  $\mu$ Al<sub>2</sub>O<sub>3</sub> has a considerable increase, compared with that on the particles of 700 nm. In apparent, CNTs self-assemble into three branches in different sizes. In fact, the large upward branch contains several thinner ones. The combination trace is obviously indicated by the boundaries of thinner CNT branches (marked by the arrows in the corresponding figure). Even though CNT quantity and density greatly increase in each branch, the branch length remains always ~ 15  $\mu$ m. The further increase of microparticle size ( $\phi_{\text{Al}_2\text{O}_3} = 3.5$  and 5  $\mu$ m) results in six nearly orthogonal CNT branches on one particle. Each branch containing density of CNTs has nearly the same bundle size, and the same bundle length of 15  $\mu$ m. However, the hybrid structures with the larger diameter ( $\phi_{\text{Al}_2\text{O}_3} = 7.5$   $\mu$ m) have a varied CNT branch number, not always six. Furthermore, the branch size also varies in a large range, and its morphology becomes irregular.

Therefore, the particle size shows little influence on CNT growth rate at the researched conditions, but considerable one on the morphology of hybrid structures. When the particle

size is too large, CNT bundles with varied numbers can be obtained, and the size of the bundles (CNT numbers) is varied. On the other hand, when the particle is small, low area number density CNT bundles are often combined into one or two bundles when the CNT length is beyond a certain value.

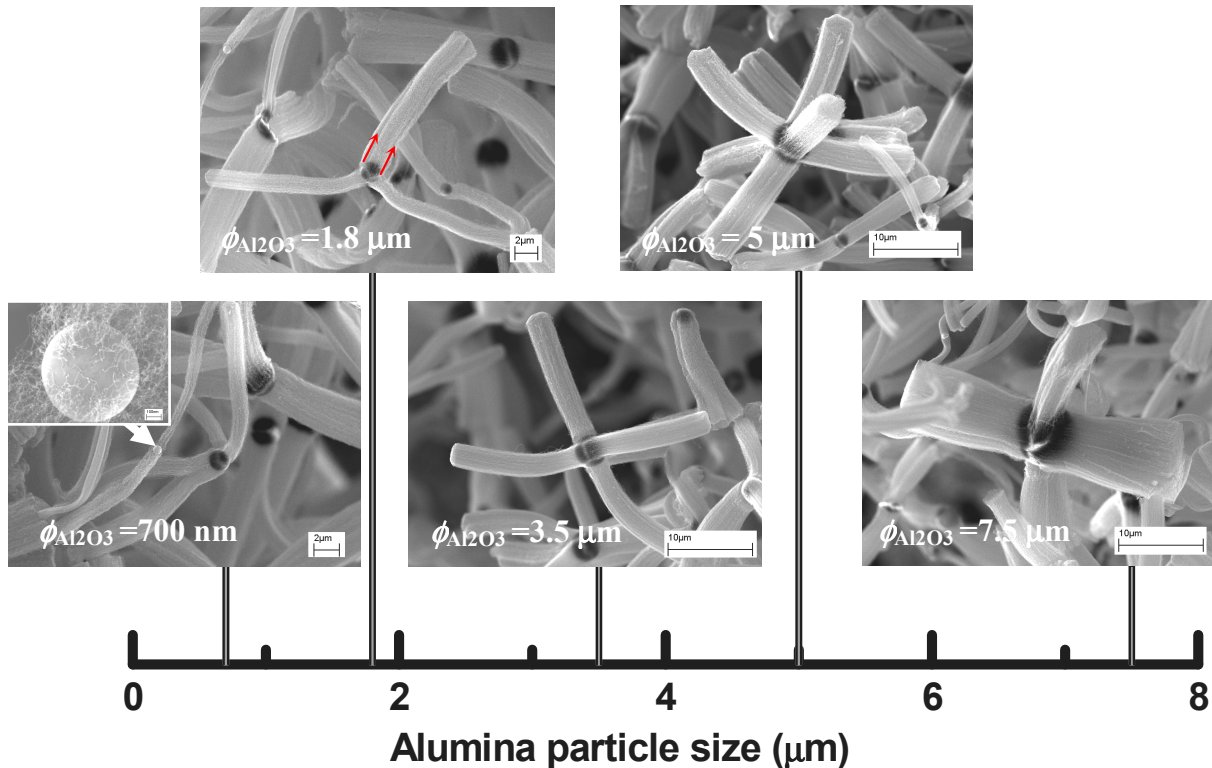


**Figure 63.** SEM images showing the evolution of the “six-branch” high-density CNTs- $\mu\text{Al}_2\text{O}_3$  hybrid structures with the increase of alumina microsphere diameter.

As a comparison, we also demonstrate the impact of the  $\mu\text{Al}_2\text{O}_3$  size on the hybrid structures constituted of CNTs with relatively low number densities and short lengths (Fig. 64). Several CNTs are sparsely dispersed on the small particles of 900 nm in diameter, and no evident bundles could be seen due to too small quantity of CNTs. The branch shape appears to be much clearer when the diameter of alumina microspheres increases up to 1.4  $\mu\text{m}$ . The six-branch hybrid structures are found when the particle size is larger than 2  $\mu\text{m}$ . However, the CNT branches are not well aligned, or even seriously curved on these particles owing to the weak CNT quantity contained in each branch. The “six-branch” hybrid structures become dominant with the further increase of the alumina microparticle size. Moreover, almost the same bundle length around 6  $\mu\text{m}$  is observed on the microparticles with different diameters, except a shorter length of 1.5  $\mu\text{m}$  on the particles of 900 nm in diameter. We can see that the

particle size mainly influences the number of CNTs in each branch. The hybrid structures with small alumina particles contain less CNTs in each branch, and thus show more flexibility than that obtained on the large microparticles. In a word, the particle size exhibits little influence on CNT diameter and growth rate. But the variation of the particle surface area and curvature with diameter could result in considerable variations in CNT quantity and their organization. In general, the well-aligned “six-branch” hybrid structures are observed on the alumina particles with diameters ranging from 3 to 6  $\mu\text{m}$ .

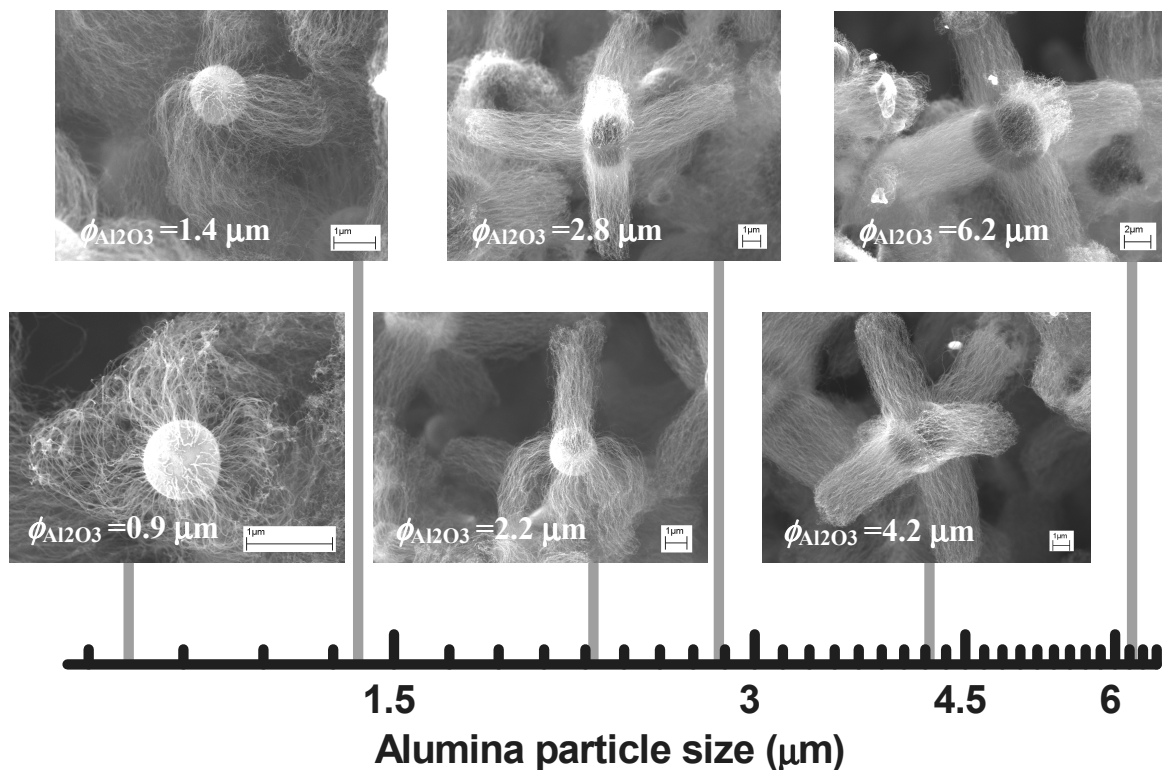


**Figure 64.** SEM images showing the evolution of the “six-branch” CNTs- $\mu\text{Al}_2\text{O}_3$  hybrid structures with the increase of alumina microsphere diameter. The hybrids are constituted of the CNTs with a low number density on  $\mu\text{Al}_2\text{O}_3$ .

### 3.3.3 Effect of microparticle structures and surface properties

Besides, the hybrid structures, especially the “six-branch” ones, are also related to the special structure characteristics of  $\mu\text{Al}_2\text{O}_3$ . The spherical alumina particles were fabricated by melting in a plasma flame irregular alumina particles, which were previously sized and fused. Afterwards, the molten droplets of  $\text{Al}_2\text{O}_3$  were formed into spherical shapes due to

surface-tension effects. As previously reported [264], the alumina particles produced by this way exhibit certain differences in crystallography because of different cooling rates in one particle. Indeed, the X-ray diffraction spectrum (Fig. 65a) shows that the pristine microparticles contain not only thermodynamically stable hexagonal  $\alpha$ -Al<sub>2</sub>O<sub>3</sub>, which is the predominant phase, but also metastable tetragonal  $\delta$  and monoclinic  $\theta$  phases. The spectrum corresponding to the  $\mu$ Al<sub>2</sub>O<sub>3</sub> particles heated at 800 °C reveals that no evident phase-transformations have occurred in comparison with the spectrum of pristine  $\mu$ Al<sub>2</sub>O<sub>3</sub>. Generally, the structure of  $\delta$ - and  $\theta$ -Al<sub>2</sub>O<sub>3</sub> is located within the surface layer due to the rapid quench speed during the solidification of particles.<sup>[265]</sup> This is also proven by the Raman spectrum of the pristine particles (Fig. 65b). The  $\alpha$ -Al<sub>2</sub>O<sub>3</sub> characteristic peaks at 418 and 645 cm<sup>-1</sup> for A<sub>1g</sub> modes and at 378, 433, 451, 578 and 751 cm<sup>-1</sup> for E<sub>g</sub> modes are invisible in the spectrum.<sup>[266]</sup> Whereas, the intensities of Raman shift between 200 and 900 cm<sup>-1</sup>, associated to  $\delta$ - and  $\theta$ -Al<sub>2</sub>O<sub>3</sub>, are more evident. The six evident peaks are present at the positions around 257, 455, 632, 748, 782 and 848 cm<sup>-1</sup>. It indicates that the predominant  $\alpha$ -Al<sub>2</sub>O<sub>3</sub> could be surrounded by a thin layer of  $\delta$ - and  $\theta$ -Al<sub>2</sub>O<sub>3</sub> structure, so that only small amount of  $\alpha$ -Al<sub>2</sub>O<sub>3</sub> can be accessed by the laser source.

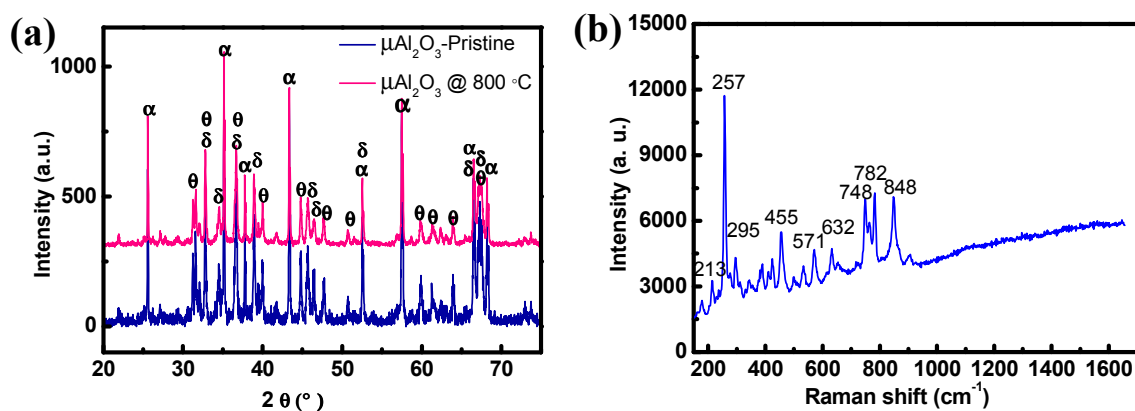


**Figure 65.** (a) XRD spectra of the pristine alumina microparticles and the particles heated at 800 °C during 4h; (b) Raman spectrum of pristine alumina particles.

As reported in references [222, 224, 225], the growths of CNTs on spherical ceramic particles and various fibers generate also the “bundle-like” or “plate-like” structures when the CNT length is larger than certain values. However, in these reported structures, the organizations of CNTs on the substrates are completely random and irregular way. Oppositely, large quantities of the regular “six-branch” structures are surprisingly formed in our case. Moreover, the same

“six-branch” hybrid structures appear under the experimental conditions are varied in a wide range.

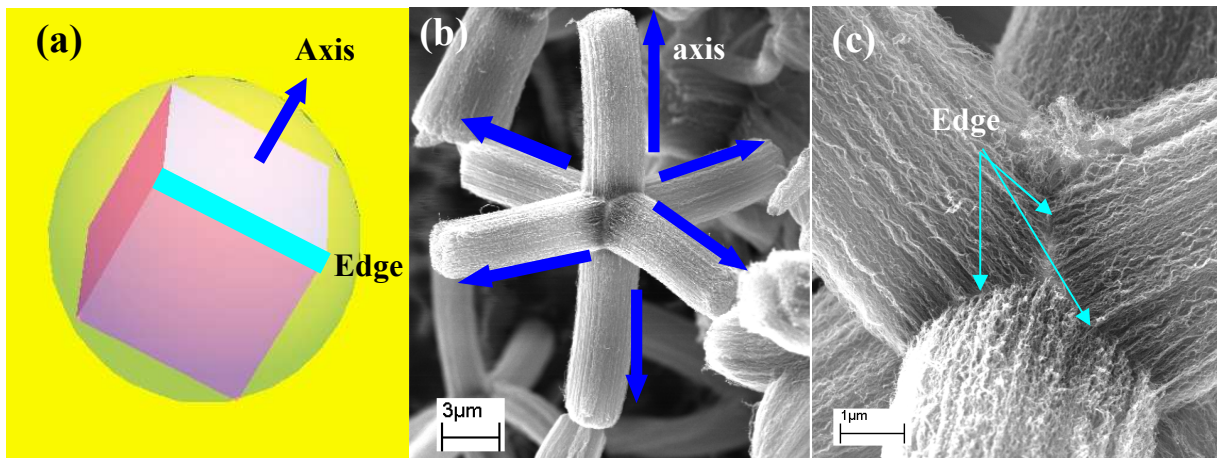


**Figure 66.** (a) Schematic of one  $\mu\text{Al}_2\text{O}_3$  sphere inscribing a cube where six faces correspond to the projections of six CNT bundles along their axis directions, respectively, and which twelve edges correspond to the boundaries between two bundles. (b) Six orthogonal CNT bundles grown on one alumina microsphere; (c) High magnification SEM image showing the boundaries between CNT bundles. The “six-branch” hybrid structures are grown with  $\text{C}_2\text{H}_2$  ( $40 \text{ ml min}^{-1}$ ) at  $550^\circ\text{C}$  during 15 min. The total flow rate of carrier gas was  $1 \text{ l min}^{-1}$  and the concentration of ferrocene in xylene was  $0.05 \text{ g mL}^{-1}$ .

As shown in Fig. 66, the six CNT bundles are orthogonally organized on the surface of one spherical alumina particle. Ideally, an inscribed cube (Fig. 66a) could be gotten by cutting the microparticle along the boundaries formed between two neighbor nanotube bundles. The axes of six nanotube bundles will be perpendicular to the six corresponding faces of the cube. That is, the projection of each bundle along its axis is located inside one corresponding face. Oppositely, the boundary regions on  $\mu\text{Al}_2\text{O}_3$  could also be seen from the distribution of CNTs grown at relatively low temperatures. Fig. 67a shows the CNTs grown by feeding acetylene at a rate of  $10 \text{ ml min}^{-1}$  for 15 min at  $450^\circ\text{C}$ . Their distribution on  $\mu\text{Al}_2\text{O}_3$  forms twelve edges of a cube. Fig. 67b-c show CNTs obtained by injecting acetylene for 3 minutes at  $600^\circ\text{C}$ . By comparing with Fig. 67a, CNT growth gradually expands towards the centers of the square regions. Fig. 67d shows that CNTs self assemble into six-branch structures after 30 minutes growth at  $475^\circ\text{C}$ . In particular, a concave area is observed on the top of each CNT branch. The variation of the CNT distribution shown in Fig. 67 indicates that the nucleation and growth of CNTs on  $\mu\text{Al}_2\text{O}_3$  are not homogeneous processes at relatively low temperatures. They first nucleate and grow in the cube-edge regions, and then expand toward the centers of the faces as indicated by yellow

arrows in Fig. 67. In consequence, the lengths of CNTs located in the centers of six face regions are less than these of neighbor CNTs, resulting in a concave area on the top of each CNT branch.

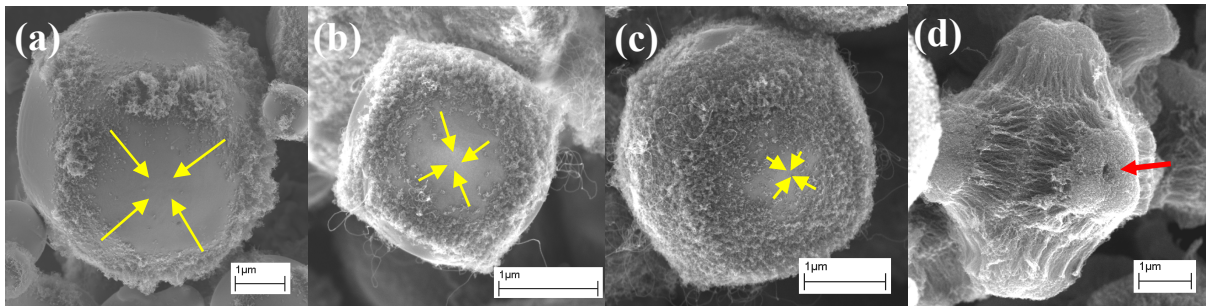


**Figure 67.** SEM images showing the variation of CNT distribution on  $\mu\text{Al}_2\text{O}_3$  spherical particles. The CNTs are grown by feeding acetylene ( $10 \text{ ml min}^{-1}$ ) and hydrogen ( $0.1 \text{ l min}^{-1}$ ): (a) for 15 minutes at  $450^\circ\text{C}$ . (b-c) for 3 minutes at  $600^\circ\text{C}$ . (d) for 30 minutes at  $475^\circ\text{C}$ . The yellow arrows represent the expansion tendency of CNT growth region.

However, the heterogeneous growth of CNTs on the cube-face corresponded region could be eliminated by increasing hydrogen ratios in carrier gases. The same growth rate results in the CNTs with the same length. Consequently, a convex CNT cap could be observed on top of each CNT branch, just as shown in Fig. 68. CNTs in each branch are perpendicularly aligned on its corresponding cube face. However, the growth of CNTs on the whole surface of microparticles is not homogeneous, so that they self organize into six branches.

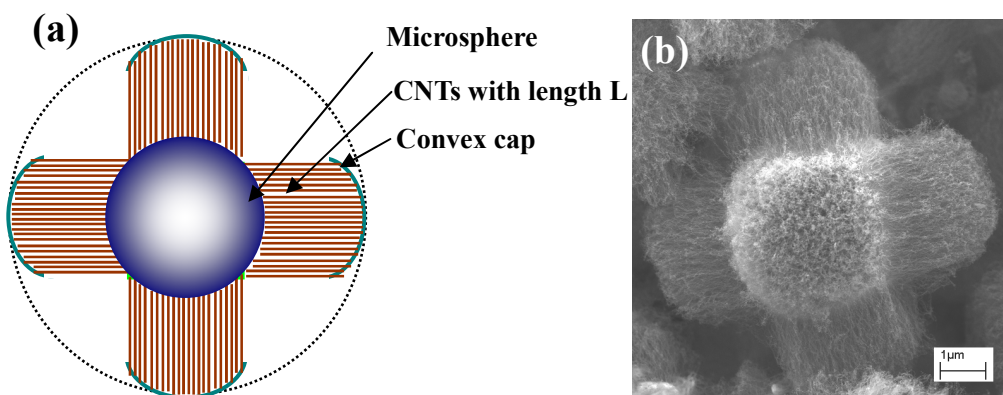


**Figure 68.** (a) Schematic of 2 dimensional view of one  $\mu\text{Al}_2\text{O}_3$  sphere grafted by six orthogonal nanotube branches. In each branch, CNTs have the same length,  $L$ . The blue convex curves indicate the CNT convex caps. (b) SEM image of CNTs grown on  $\mu\text{Al}_2\text{O}_3$  sphere for 20 minutes at  $600^\circ\text{C}$ , using 1% acetylene and 30% hydrogen in the total carrier gases of  $1 \text{ l min}^{-1}$ .

The hidden “cube-like” surface structure of  $\mu$ Al<sub>2</sub>O<sub>3</sub> generates the heterogeneous CNT growth. The heterogeneity might be derived from the following factors. First, the varied chemical compositions (such as impurities, Al and O atoms) in the surface layer of  $\mu$ Al<sub>2</sub>O<sub>3</sub> could result in the different CNT nucleation and growth rates. Second, different surface phase structures generate the variation of CNT growth on the alumina particles. Third, different types of crystal planes might also produce the “six-branch” hybrid structures.

In fact, the micro spherical particles have an alumina purity as high as 99.8 %, as well as SiO<sub>2</sub> (800 ppm), Na<sub>2</sub>O (600 ppm), Fe<sub>2</sub>O<sub>3</sub> (150 ppm) and CaO (70 ppm). The proportion of these impurities in the particles is so weak that XRD measurements could not detect their presence. Thus, it is impossible for so few amounts of impurities to concentrate in certain regular surface region of the alumina particles.

XRD and Raman measurements have detected that the presence of the metastable  $\theta$ -Al<sub>2</sub>O<sub>3</sub> and  $\delta$ -Al<sub>2</sub>O<sub>3</sub> in the particle surface layer. These metastable phases are always present in the particles which have been heat-treated at 800 °C for 4 h. In order to verify the influence of the particle surface composition (Al or O atoms), the alumina microparticles treated by basic or acidic solutions are used for CNT synthesis. The pristine alumina particles of 5 g in mass are ultrasonically washed for 1 hour in 30 ml 5 mol l<sup>-1</sup> NaOH solution. As a comparison, other 5g particles are washed for 3 hours in 45 ml 6 mol l<sup>-1</sup> HCl solution. Then, the solutions are removed after the precipitation of the particles which have been washed several times with distilled water. After being dried in air by heating at 100 °C, the particles are used as substrate to grow CNTs using 0.05 g ml<sup>-1</sup> ferrocene-xylene solution at 750 °C. The gas flow rates of argon and hydrogen are 0.72 and 0.08 l min<sup>-1</sup>, respectively. As shown in Fig. 69a-b, the growth of CNTs on the treated particles is greatly different from the one on pristine particles. In both cases, a thin shell consisting of iron particles and carbon is formed on the surface of particles. It is observed that when the length is beyond a critical value, the CNTs grow out of the shell by breaking it up at certain places. Most CNTs have a diameter ranging from 10 to 20 nm. The growth of CNTs is only observed in some regions of the particle surface. The regions “without CNTs” are smooth under scanning electron microscope. In addition, the CNT growth under a shell has also been observed on the pristine alumina particles at 780 °C when an amount of 3‰ thiophene is added in 0.05 g ml<sup>-1</sup> ferrocene-xylene solution (Fig. 70a). The whole surface of one particle is completely covered by a shell consisting of carbon layer decorated with small iron particles. The shell could be split into several pieces at certain places by the growth of CNTs. Meanwhile, a wavy CNT carpet of ~180  $\mu$ m in thickness is grown on the quartz plate during 15 min. The mean diameter of CNTs is ~ 50 nm. This

indicates that the addition of thiophene could change the deposition rate of iron and carbon on the alumina particle surface. Too fast carbon deposition rate results in a continuous shell instead of carbon nanotubes. Furthermore, an evident boundary indicated in Fig. 70c exists between two surface regions of alumina particle. This boundary reflects the heterogeneous surface structure of  $\mu\text{Al}_2\text{O}_3$ , which results in an evident difference in the amount of deposited iron particles and carbon on the two neighboring regions.

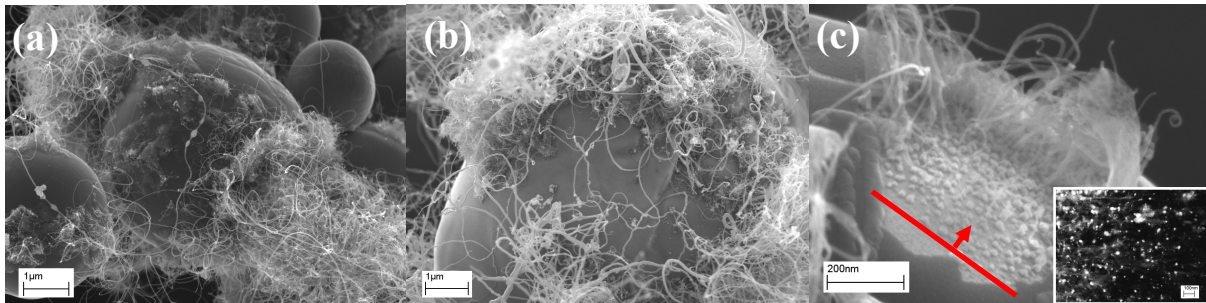


**Figure 69.** SEM images of CNTs grown on the alumina particles treated by NaOH solution (a) and HCl solution (b). (c) CNTs grow on the surface of alumina particles by breaking up a shell consisting to iron particles and carbon (see the inserted image). The red line indicates a regular boundary formed by the deposited particles.

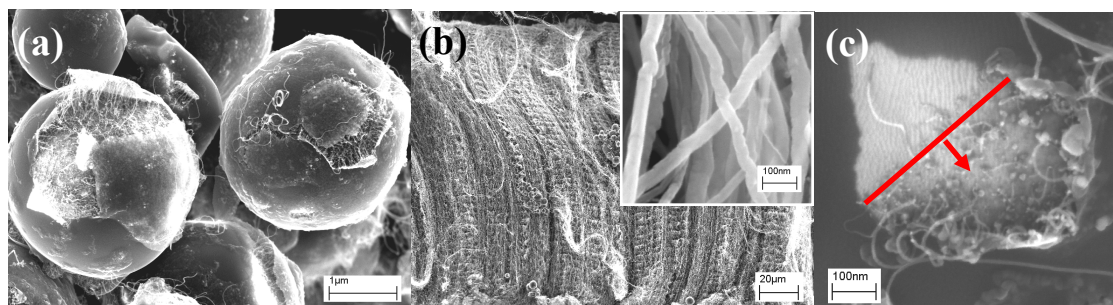


**Figure 70.** (a) SEM image of the CNT growth on  $\mu\text{Al}_2\text{O}_3$  using the ferrocene-xylene solution containing 3 %o thiophene at 780 °C. (b) SEM image of one carpet constituted of wavy CNTs grown on the quartz plate. (c) One small  $\mu\text{Al}_2\text{O}_3$  surface region after removing the cover shell. The red line shows a regular boundary between two regions having varied amounts of carbon encapsulated iron particles and carbon.

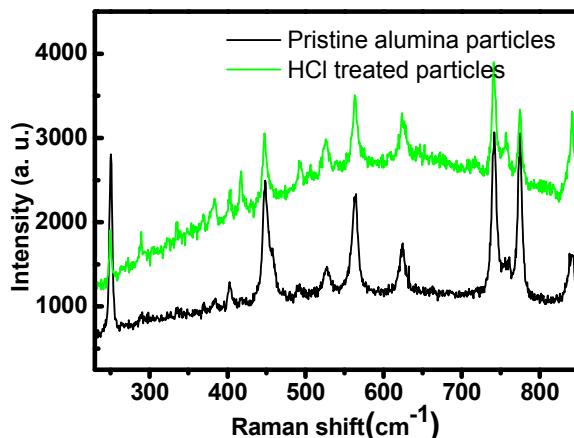


**Figure 71.** Raman spectra of pristine alumina particles and the particles treated with HCl solution.

We have seen that the surface treatments mentioned above could greatly alter the iron and carbon deposition rates which in turn influence the CNT growth on the microparticles. Fig. 71 shows the comparison of Raman spectrum of the pristine particles with that of the particles treated by HCl solution. The differences of two spectra demonstrate the variation of the surface properties of particles due to acid treatment. But, the surface heterogeneity is still present on the treated particles. This means that the heterogeneity comes from the intrinsic structure of the microparticles, instead of the chemical compositions.

### 3.3.4 CNT growth on heat-treated $\mu$ Al<sub>2</sub>O<sub>3</sub>

As concluded in previous parts, the heterogeneous nucleation and growth of CNTs on the  $\mu$ Al<sub>2</sub>O<sub>3</sub> surface originate in the inherent crystal structure of the microparticles. Meanwhile, the pristine microparticles have a multiphase structure. Therefore, the regular distribution of metastable phases in particle surface layer might be one reason that results in the growth of “six-branch” hybrid structures.

It has been reported that the metastable  $\theta$ -Al<sub>2</sub>O<sub>3</sub> and  $\delta$ - Al<sub>2</sub>O<sub>3</sub> could occur structural transformation after moderate heat treatment, and they transform completely to  $\alpha$ -Al<sub>2</sub>O<sub>3</sub> when the heat treatment temperature is higher than 1473 K.<sup>[265]</sup> In order to eliminate these metastable phases, high temperature heat treatment has been carried out on the pristine particles. This treatment could also help to release the surface strain energy generated during the fast particle cooling process. The microspheres were first heated from room temperature to 1350 °C in air at a rate of 330 °C per hour using a high temperature electric furnace. They are then cooled down to room temperature after holding at 1350 °C for 4 h. As shown in Fig. 72, the  $\theta$ -Al<sub>2</sub>O<sub>3</sub> and  $\delta$ -

Al<sub>2</sub>O<sub>3</sub> are nearly completely transformed into  $\alpha$ -Al<sub>2</sub>O<sub>3</sub> after the thermal treatment. Then, the heat-treated  $\mu$ Al<sub>2</sub>O<sub>3</sub> particles are used as substrate to synthesize CNTs under different conditions.

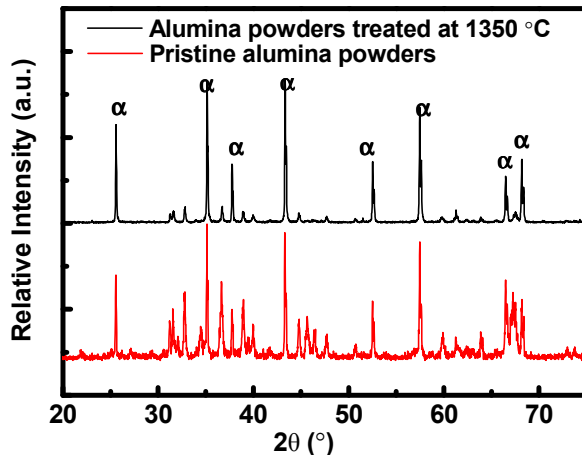


**Figure 72.** X-ray diffraction spectra of the pristine alumina microparticles and the high-temperature heat-treated microparticles

First, the growth of CNTs on the heat-treated microparticles has been conducted using 0.05 g ml<sup>-1</sup> ferrocene-xylene solution at 780 °C. The solution feeding rate is  $\sim$  0.2 ml min<sup>-1</sup>. Varied hydrogen flow rates are used in order to study the influence of hydrogen on CNT growth on the heat-treated microparticles. And hydrogen ratio varies in a sequence of 0, 10 %, 20 % and 40 %. The total carrier gas flow is 1 l min<sup>-1</sup>. The solution feeding lasts for 12 min. Fig. 73 shows the variation of hybrid structures with hydrogen ratio at 780 °C. The CNTs with high density are grown on the heat-treated  $\mu$ Al<sub>2</sub>O<sub>3</sub> particles when the high ratio of hydrogen,  $\sim$ 40 %, is added into the reactor. They align in all directions, rather than in multi-branch structures. With the decrease of the hydrogen ratio, the density of CNTs is also considerably decreased. Moreover, more impurities including amorphous carbon and iron particles are observed on the  $\mu$ Al<sub>2</sub>O<sub>3</sub> surface. In particular, the carbon layer encapsulated iron particles are found on the outer walls of nanotubes. These phenomena are greatly similar to those observed using pristine alumina particles. But the average diameter of CNTs is always around  $\sim$ 40 nm at different hydrogen ratios. The CNT length is failed to evaluate because one part of the bundles is always covered by the neighboring hybrid structures. The CNT diameter variation using the heat-treated particles is also similar to those using the pristine particles.

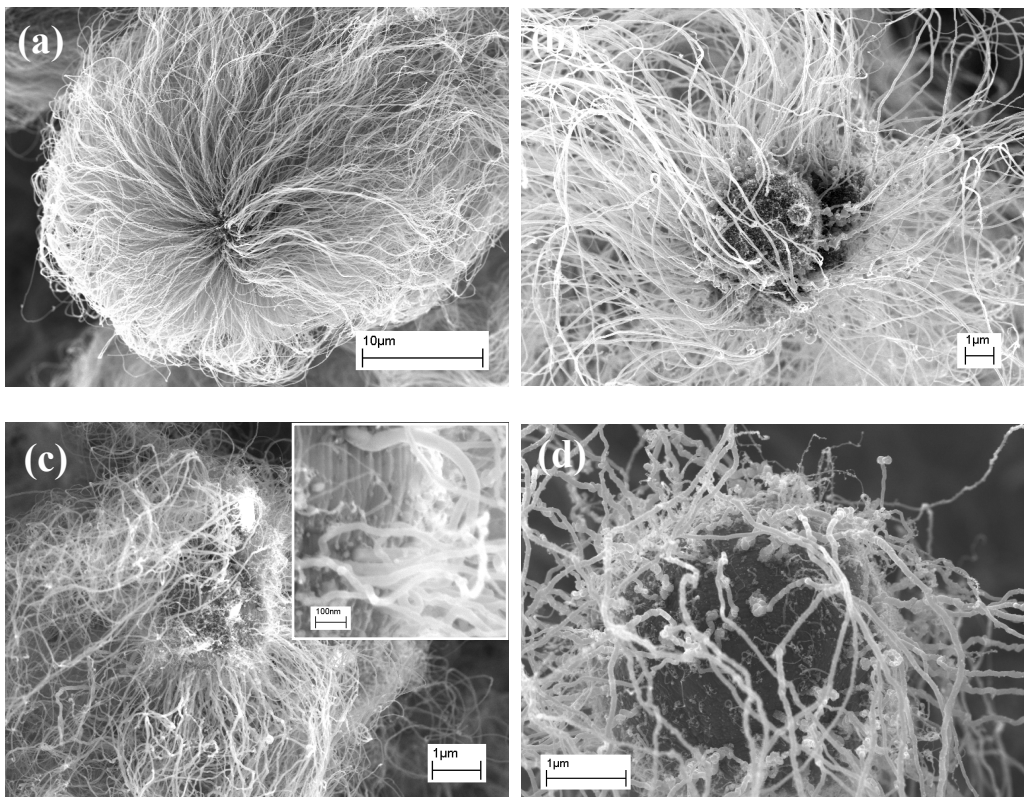


**Figure 73.** SEM images of the hybrid structures constructed by growing CNTs on the high temperature heat-treated  $\mu$ Al<sub>2</sub>O<sub>3</sub> particles at different hydrogen ratios: (a) 40 %, (b) 20 %, (c) 10 % and (d) 0.

Second, the growth of CNTs on the heat-treated microparticles has also been investigated using the acetylene/xylene mixture as carbon sources at 600 °C. The gas flow rates of acetylene, hydrogen and argon used are 0.01, 0.3 and 0.7 l min<sup>-1</sup>, respectively. Ferrocene is dissolved in xylene solution at a concentration of 0.05 g ml<sup>-1</sup>. The solution is fed into the reactor at a rate of ~ 0.13 ml min<sup>-1</sup>. The carbon source feeding time is varied from 1 to 20 minutes in order to investigate the variation of the CNT organization states with its growth time. Fig. 74a-e show the hybrid structures obtained using the injection times of 1, 2, 5, 10 and 20 min, respectively. Similarly, CNTs self assemble into six branches on the surface of the heat-treated particles (Fig. 74a-e). The large lengths make CNT bundles easy to combine with their neighbors. As shown in Fig. 74e, the six CNT bundles adhere to each other when their length is ~54  $\mu$ m. In the researched periods, CNT length is found to increase with injection time in a nearly linear way (Fig. 74f). However, no variation of CNT diameter is observed with increasing the injection time. The six-branch hybrid structures are similar to the ones obtained with the pristine microparticles.

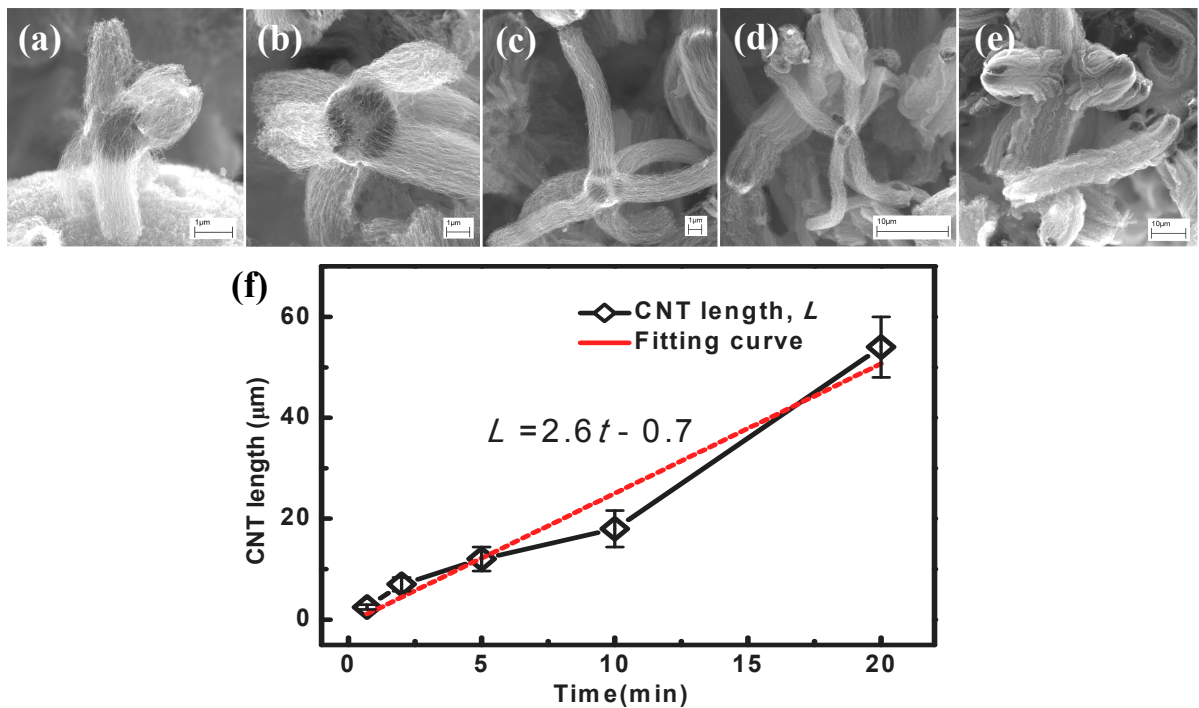


**Figure 74.** SEM images of the hybrid structures constructed by growing CNTs on the heat-treated alumina particles using the mixture of acetylene and xylene as carbon source at 600 °C for the following different injection times: (a) 1 min, (b) 2 min, (c) 5 min, (d) 10 min and (e) 20 min. (f) Evolution of CNT bundle length with the injection time at the studied conditions.

As shown above, both the “urchin-like” structures and the “six-branch” structures are obtained even using the heat-treated particles which are uniquely composed of  $\alpha$ -Al<sub>2</sub>O<sub>3</sub>. CNTs grow in the same way on these particles as on the pristine ones. This confirms that the heterogeneous growth of CNTs, especially the “six-branch” structures originate in the intrinsic crystallographic structures of  $\alpha$ -Al<sub>2</sub>O<sub>3</sub>. The heterogeneous crystal structures vary the nucleation of iron catalyst particles, and thus generate the growth of CNTs in the six separated regions on the surface of alumina microparticles.

### 3.4 CNT growth dynamics

#### 3.4.1 Connection of CNT and $\mu\text{Al}_2\text{O}_3$

Up to now, we have demonstrated a large number of different hybrid structures obtained by in situ growing CNTs on  $\mu\text{Al}_2\text{O}_3$ . In these hybrids, the connection between CNTs and microparticle is due to the catalyst particles which are derived from the decomposition of ferrocene. It is worth noting that the continuous feeding of ferrocene is required to the continuous growth of CNTs. That means the iron quantity in the reactor is gradually augmented with increasing ferrocene-feeding time. Naturally, we would like to ask the following two questions: what about the earliest growth state of CNTs on  $\mu\text{Al}_2\text{O}_3$ , and what do the new coming irons serve for the continuous CNT growth?

First, the initial stage of CNT growth on  $\mu\text{Al}_2\text{O}_3$  is studied by injecting carbon and catalyst precursors in a very short time. As shown in Fig. 75a, small CNTs of  $\sim 70$  nm in length have been obtained by injecting the mixture of ferrocene-xylene solution and acetylene at  $600^\circ\text{C}$  for  $\sim 10$  s. The flow rate of acetylene is  $\sim 10 \text{ ml min}^{-1}$ . The CNTs have a diameter ranging from 5 to 10 nm, which is close to the diameter of CNTs produced with longer growth time. This indicated that the diameter of CNTs is determined at their initial growth stage when the mixture carbon sources are used at relatively low temperatures. Few iron particles are found without growing CNTs. This confirms again the high efficiency of the mixture carbon source to CNT growth. However, the CNTs have a low number density, and they disperse sparsely on the alumina particle surface. Due to the poor electrical conductivity of  $\mu\text{Al}_2\text{O}_3$ , it is very difficult to clearly distinguish out the locations of catalyst particles from such thin CNT by SEM. Therefore, we use the same experimental conditions to grow CNTs on the Surfs® plate (silicon wafer) surface. AFM measurements (Fig. 75c) prove that there exists one catalyst particle at the end of CNT. Thanks to this particle, the CNT is catalyzed to grow, and is fixed on the surface of substrate.

After the nucleation of catalyst particles on substrate, they will catalyze the growth of CNTs according to the “bottom-up” mode. That is, the elongation of CNTs results from carbons precipitated out of the catalyst particles which are located on their roots. The strong interaction between catalyst particles and substrate makes CNTs to attach on the surface of microspheres. The white bright points shown in Fig. 76a show the connections between CNTs and the micrometer substrate. The CNTs of  $\sim 10$  nm in diameter are synthesized using acetylene as carbon source at  $600^\circ\text{C}$ . Fig. 76b and c show the connection between CNTs and

$\mu$ Al<sub>2</sub>O<sub>3</sub> which are realized using xylene as carbon source at 780 °C. It is found that the roots of CNTs contain the catalyst particles with different shapes: angular, cylindrical, conical... Moreover, several catalyst particles are often found at the root of CNT (Fig. 76b). Fig. 76d also shows the elongated iron particles inside the CNT. The detachment of CNTs from the microparticles is realized by the dissociation of the root catalyst particles from the substrate surface, as shown in Fig. 76e-h. The catalyst particles are always found to stick at the nanotube roots. The SEM images show furthermore the combined catalyst particles from several smaller ones. Especially, the combination of the ends of two different carbon nanotubes is found when two corresponding catalyst particles are very close (Fig. 76g-h).

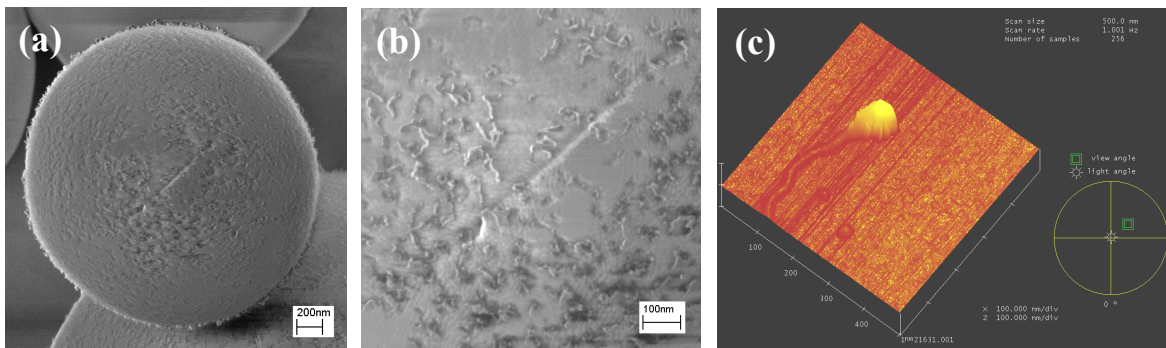


**Figure 75.** (a) SEM images of  $\mu$ Al<sub>2</sub>O<sub>3</sub> after very short time injection of ferrocene-xylene solution and acetylene at 600 °C, (b) high magnification SEM image of a. (c) AFM image of one CNT having an iron particles at one of its ends. The CNTs are obtained on the Surfs® plate surface (SiO<sub>2</sub> layer supported on Si) using the same conditions as the previous ones but longer time (3 min).

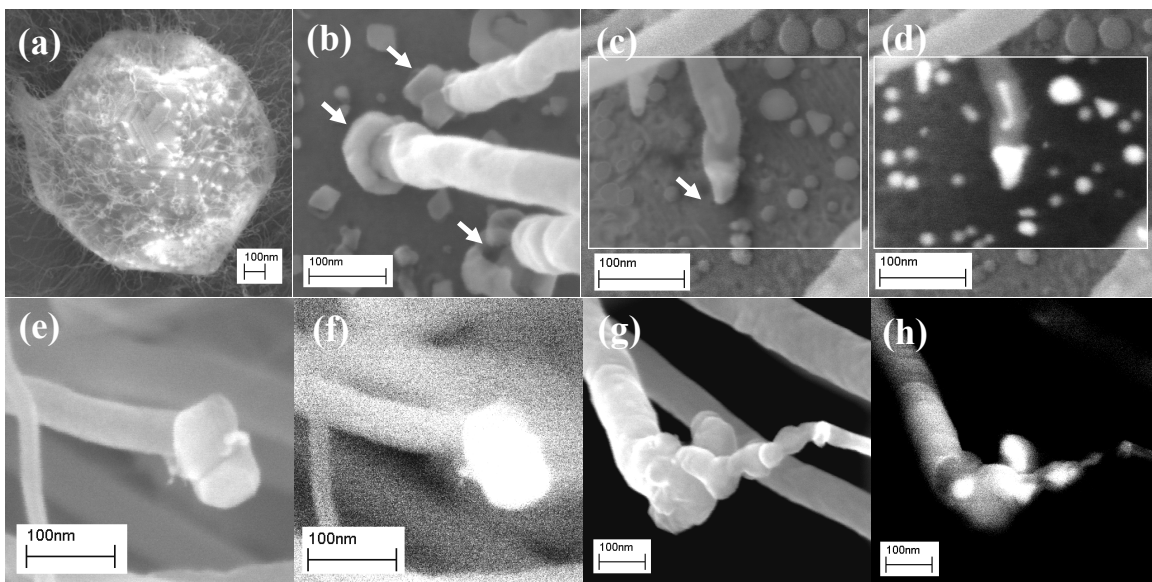


**Figure 76.** (a) SEM images of the hybrid structures consisting of CNTs of 10 nm in diameter and  $\mu$ Al<sub>2</sub>O<sub>3</sub>. The bright points on the surface of  $\mu$ Al<sub>2</sub>O<sub>3</sub> show the connection of each CNT with the microparticle. (b-d) Different morphologies of iron particles which fix CNTs on the surface of microparticles. (e-h) SEM images of the roots of two CNTs disconnected from the substrate. Figures d, f and h are the second electron SEM

images corresponding to the figure c, e and g, respectively.

### 3.4.2 Growth kinetics of CNTs on alumina microparticles

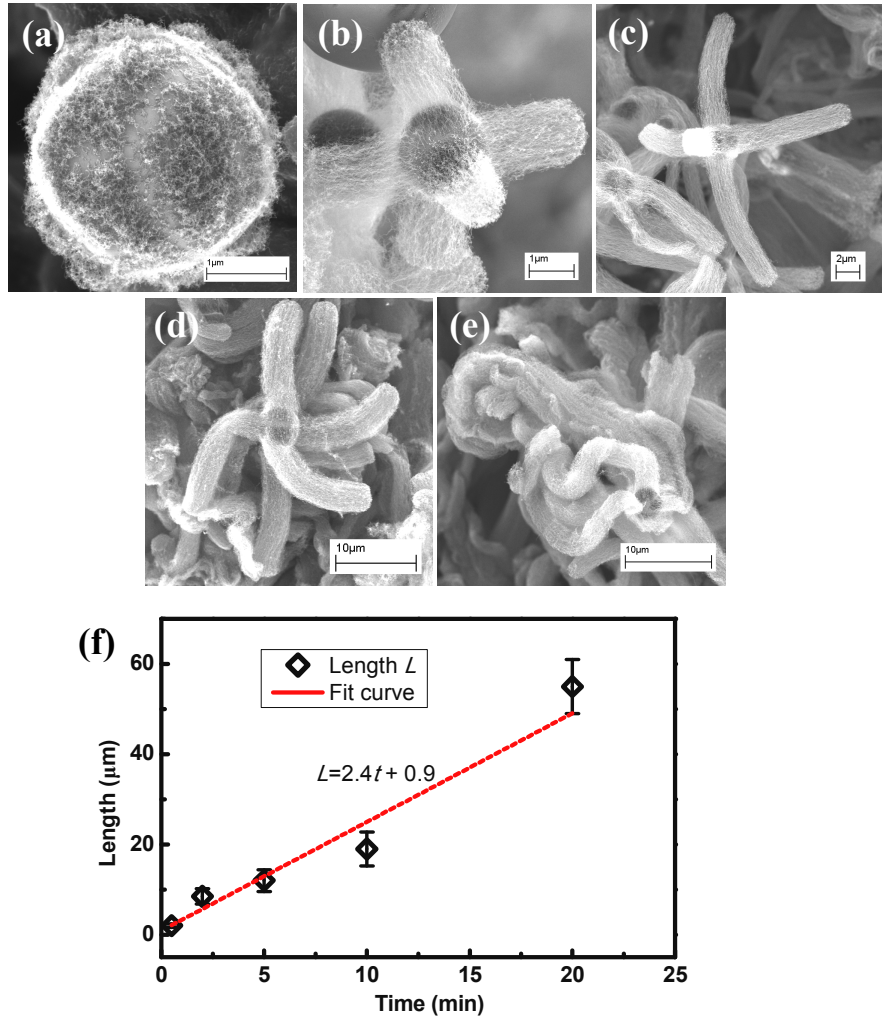


**Figure 77.** Evolution of the morphologies of CNTs- $\mu\text{Al}_2\text{O}_3$  hybrids with growth time. The CNT growth was conducted at 600 °C using 30 vol. % hydrogen, for different times: 1, 2, 5, 10 and 20 min.

The dynamics of CNT growth on pristine  $\mu\text{Al}_2\text{O}_3$  has been investigated by gradually increasing catalyst and carbon precursor feeding time in a sequence of 1, 2, 5, 10 and 20 min. The mixture of acetylene ( $0.01 \text{ l min}^{-1}$ ) and xylene (at an injection rate of  $\sim 0.2 \text{ ml min}^{-1}$ ) is used as carbon source. Argon and hydrogen flow rates are 0.7 and  $0.3 \text{ l min}^{-1}$ , respectively. The evolution of CNTs- $\mu\text{Al}_2\text{O}_3$  hybrids at different growth times is shown in Fig. 77. It is found that under the studied conditions the hybrids have always the “six-branch” structures from a short CNT growth time ( $\sim 1 \text{ min}$ ) to a long one (20 min). The length of CNT branches progressively augments in a quasi linear manner with the growth time (Fig. 77f). This is similar to the case

reported by Zhang et al.<sup>[222]</sup> and Xiang et al.<sup>[224]</sup>. Consequently, the vertically aligned branches with short length (Fig. 77b) grow gradually into the curved ones with irregular wave shapes (Fig. 77e), due to the increased obstacles from the surrounding particles with the increase of CNT length. At the same time, the CNT branches become easier to deform. It should be mentioned that the CNT number densities in bundles obtained at longer growth times are significantly higher than that shown in Fig. 77a. This indicates that at the initial stage of CNT growth the number of catalyst particles on  $\mu$ Al<sub>2</sub>O<sub>3</sub> increases with the catalyst and carbon feeding time.

In addition, we found that amounts of catalyst particles are embedded inside the CNTs. the CNTs obtained at 450 and 500 °C have a low degree of crystallography. Often, they are found deformed at positions where iron particles are contained. Another interesting phenomenon observed is that at several conditions the outer walls of CNTs with large diameters are found noncontinuous, instead of straight, especially, the CNTs synthesized using xylene as carbon sources at high temperatures (Fig. 78).

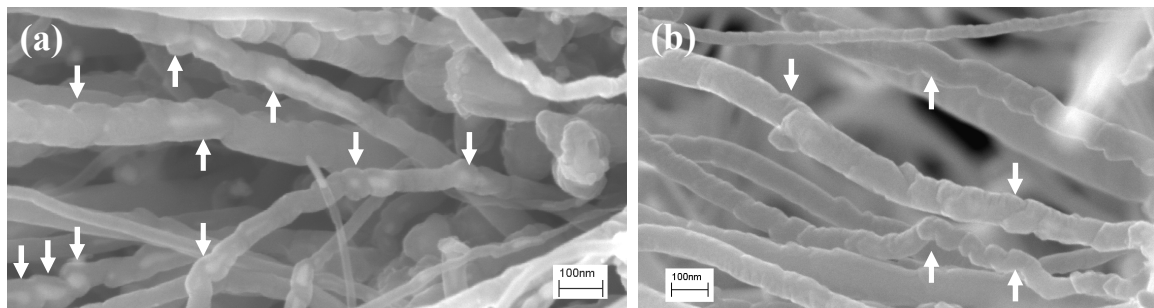


**Figure 78.** SEM images of CNTs having fluctuant outer surface and encapsulating iron particles, obtained using xylene as carbon source at high temperatures.

According to the above phenomena, we propose the following CNT growth model to explain their elongation during the CVD of carbon and catalyst precursors on the alumina microspheres. As shown in Fig. 79, the nucleation and growth of iron catalyst particles is initiated by heterogeneous deposition of ferrocene vapor in certain regions of the surface of  $\mu$ Al<sub>2</sub>O<sub>3</sub> (Fig. 79-I). Simultaneously, the interaction between depositing iron and decomposing hydrocarbons results in CNT nucleation and growth on the catalyst particles (Fig. 79-II). Certainly, catalyst particle size is considerably influenced by carbon source. Then, depending on the chemical kinetics condition in reactor, the following different paths could be followed for further growth of CNTs. Homogeneous deposition of carbon and iron around the formed

catalyst particles could make CNTs to straightly grow forward (Fig. 79-II). Continuous feeding of iron could make the ancient catalyst particle to be encapsulated inside the CNT. The asymmetric deposition of the new coming iron as shown in Fig. 79-IV and -V could change the nanotube growth direction according to the orientation of the new forming catalyst particles. Furthermore, the integration of the carbon-encapsulated iron particles (Fig. 79-VI) would generate the variation of CNT morphology, in particular, the fluctuant outer surface. Finally, the nucleation of iron particles could also take place in the gas phase when the thermal decomposition rate of ferrocene is very high. The nucleated catalyst particles would directly absorb hydrocarbons in gas phase, and then deposit on the outer walls of growing carbon nanotubes (Fig. 79-VII). This phenomenon is often observed at high CNT synthesis temperatures, such as 900 °C.

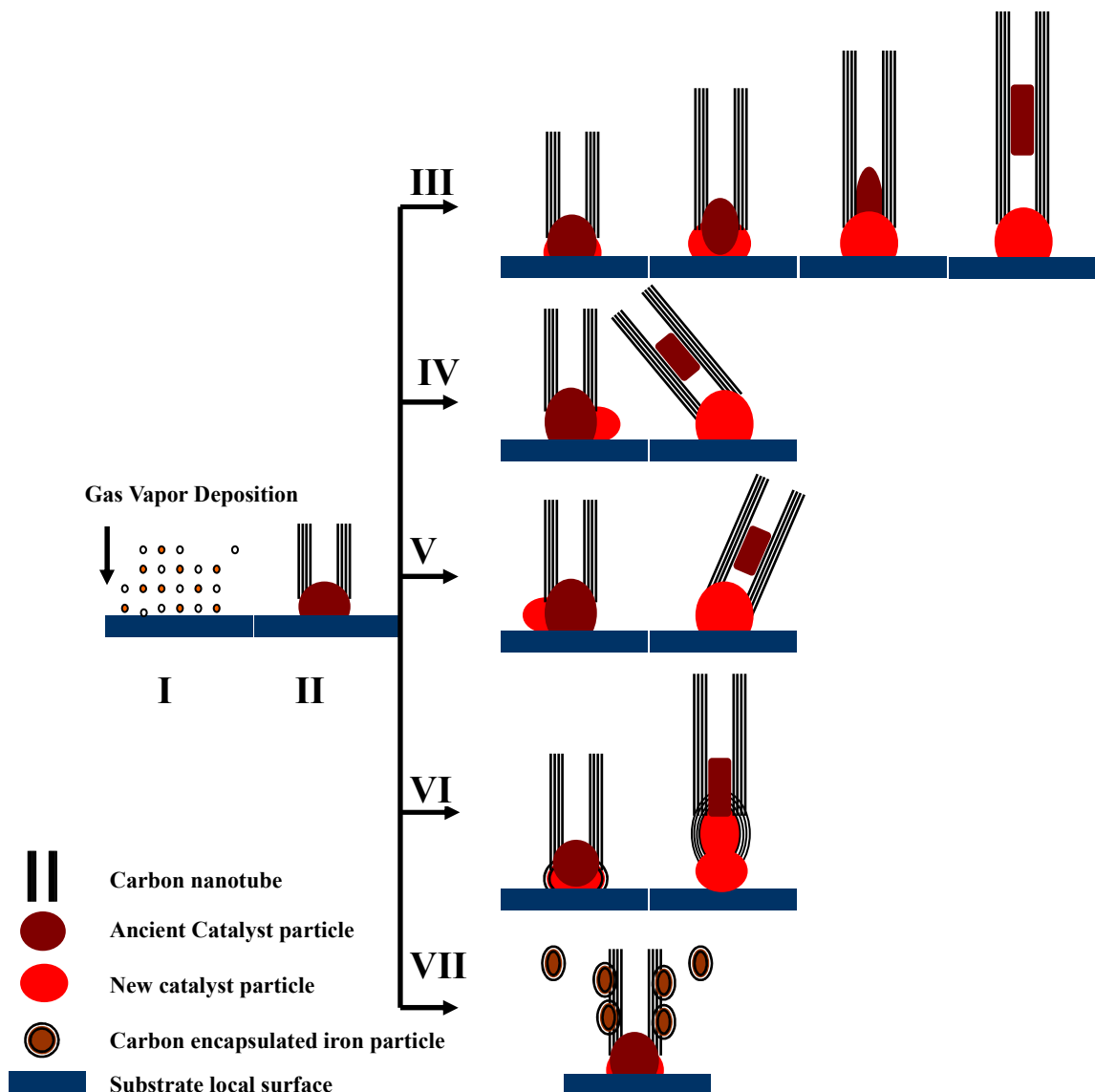


**Figure 79.** Schematic of the models for the growth of CNTs with varied structures on the alumina microparticles.

### 3.5 Self-organization mechanism

#### 3.5.1 Crystal steps determined heterogeneous CNT growth

As we know, the formation of the hybrids is initiated by the nucleation of iron particles on the surface of  $\mu\text{Al}_2\text{O}_3$ . The anisotropy surface structure would certainly generate varied catalyst formation rates, which thus influence CNT nucleation and growth.

Although the alumina microparticles have multi-phase structure, the metastable  $\theta$ - &  $\delta$ - $\text{Al}_2\text{O}_3$  are not the determinative factors for the formation of the “six-branch” hybrid structures. This has been proven by the fact that the similar structures have been obtained using the high temperature treated  $\mu\text{Al}_2\text{O}_3$  and the pristine ones. The six CNT bundles demonstrate a cube-like structure in  $\mu\text{Al}_2\text{O}_3$ . Highly dense CNTs could be formed in the six-face regions, but only few ones in the twelve edge regions. This difference reveals the existence of higher catalyst nucleation ratios at the face regions than at the edge regions.

Fig. 80 shows the six-branch hybrid structures consisting of CNTs and the heat-treated  $\mu\text{Al}_2\text{O}_3$  particles. The CNT synthesis is conducted at 600 °C, with the injection of acetylene at a flow rate of 0.01 l min<sup>-1</sup>. The six CNT branches are regularly aligned on the surface of microparticles. Instead of a smooth sphere, the heat-treated  $\mu\text{Al}_2\text{O}_3$  particle surface is composed of a number of crystalline steps of varied sizes, and some flat regions. This indicates that the fast quench cooling process generates a huge amount of stress on the microparticle surface. The quick solidification of the particles makes them keep the spherical shape of the molten droplet. During the high temperature heat-treatment, the release of the formed stress promotes the reorganization of aluminum and oxygen atoms in order to form most stable crystal structures. The high magnification SEM images demonstrate that the growth of CNTs takes place at crystal step sites, rather than in the flat regions. The direction of CNT branches is strongly dependent on the orientation of the crystal steps. For instance, as shown in Fig. 80b, CNTs are perpendicular to the edges of the crystal steps indicated by two red lines. Moreover, it is found that the CNT number density varies with the crystal step size.

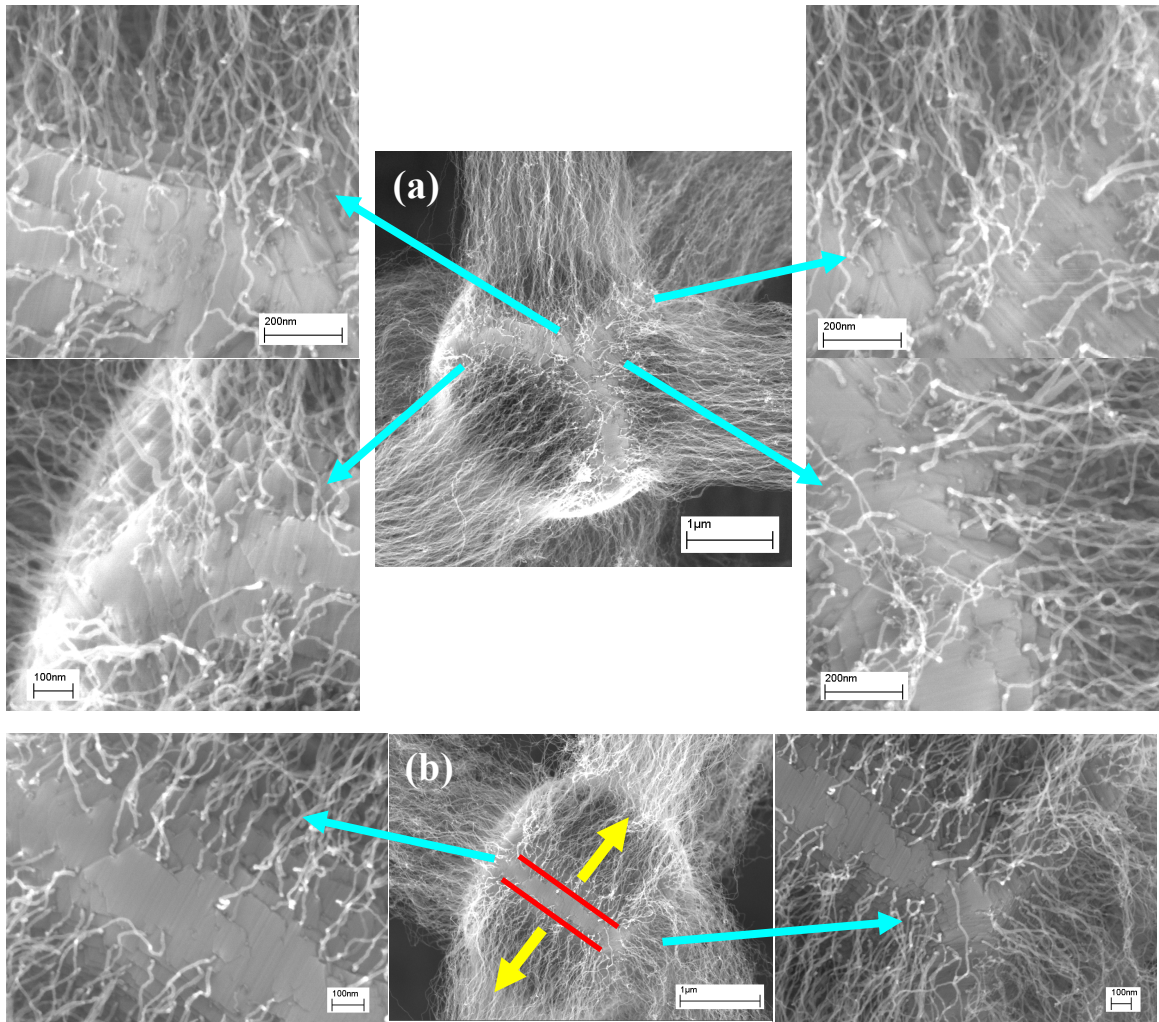


**Figure 80.** (a-b) SEM images of the six-branch hybrid structures consisting of CNTs and heat-treated  $\mu\text{Al}_2\text{O}_3$ . The high magnification images show that CNTs preferentially grow on the step sites rather than on the flat plane area. CNT growth direction is dependent on the orientation of the crystal steps.

The surface morphology of the heat-treated  $\mu\text{Al}_2\text{O}_3$  particles is demonstrated in Fig. 81a. Indeed, the whole particle surface is homogeneously divided into the different regions which have the crystal steps of different sizes and specific orientations. Obviously, the band regions indicated by the arrows contain very few crystal steps, and this is a relatively smooth surface. The regular distribution of these defects-less bands on the microparticle surface forms a cube-like motif. In contrast, a number of crystal steps are observed in the regions surrounded by every four band-like regions (Fig. 81b). The steps stack up one over another, and finally terminate with a small platform at the highest points (red arrow in Fig. 81a). On the other hand, the pristine particles often take on “smooth” surfaces (Fig. 81c). In fact, a closer observation unveils that the pristine particle surface is extremely similar to the one of heat-treated particles. That is, a large number of crystal steps are distributed on the surface. The only difference between the two kinds of particles is that the pristine ones contain a much larger number of

steps of much finer sizes. The surface motif of the pristine particles could be reproduced after deposition of a thin carbon layer containing iron (Fig. 81e). The smooth bands and small crystal steps could be clearly seen in the figure. Therefore, we see another important role played by heat-treatment, that is, to enlarge the size of the hidden surface crystal steps through atom reconstruction. In consequence, the heterogeneous surface nature becomes more evident to observe using SEM on the heat-treated particles. Therefore, the growth of CNTs in the six orthogonal directions is originally determined by the intrinsic surface crystal structure of  $\mu\text{Al}_2\text{O}_3$  particles.

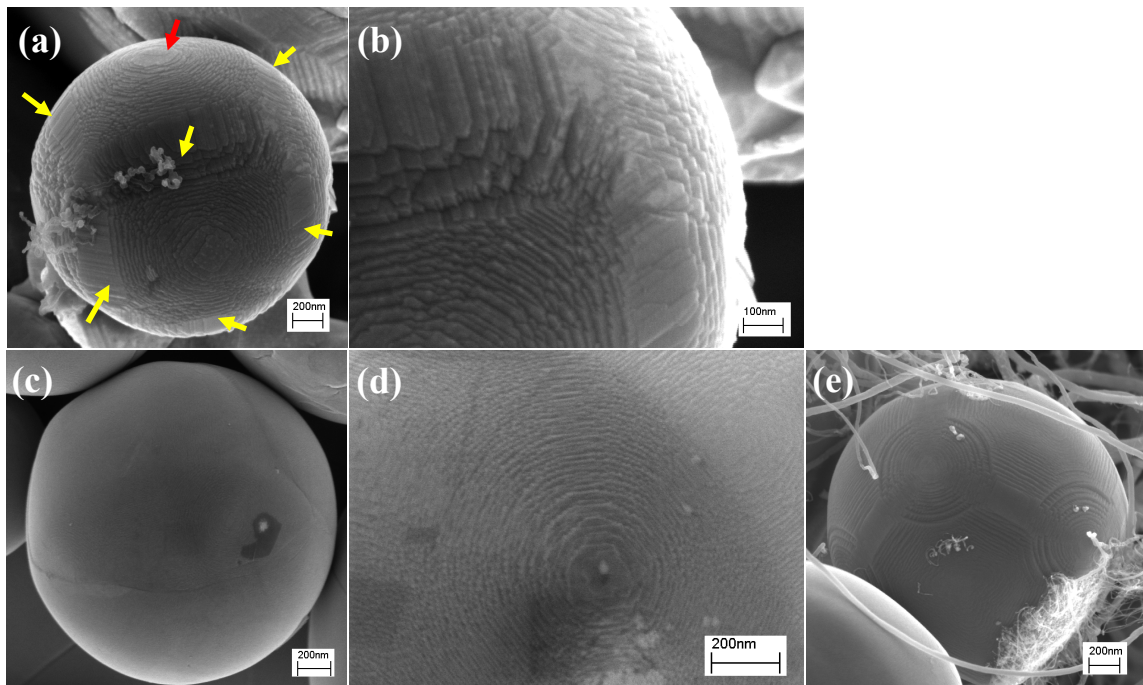


**Figure 81.** SEM images of the surface morphologies of the heat-treated  $\mu\text{Al}_2\text{O}_3$  particles (a-b) and the pristine  $\mu\text{Al}_2\text{O}_3$  particles (c-d). (e) Reproduction of the surface structure of the pristine alumina particles by depositing a thin carbon layer. The yellow arrows in the figure (a) indicate the regions with few crystal steps.

Normally, the particles, larger than 1  $\mu\text{m}$  in diameter, are polycrystalline. This is due to their specific production procedure, that is, the rapid solidification of the molten particles moving at high speeds. The combination of the small molten droplets could take place to form a larger ones. However, these combined small droplets solidify so quickly that the mass diffusion between them is insufficient to form a completely homogeneous particle. This feature has been observed with the heat-treated particles after carbon deposition on their surface, as shown in Fig. 82a-d. In particular, the strong color contrast is found on different regions of the particle surface. The energy dispersive spectroscopy analysis shows that there is no difference in the chemical composition of the two types of grains with different colors. The contrast is due to the different

carbon absorption properties of each contained sub-grain. Furthermore, the “band-like” zones are also observed on the particle surface. They are found to traverse amazingly the different subgrains (Fig. 82b-c). Little difference could be observed between CNT growths on these different subzones (Fig. 82d). This indicates that the surface layer plays a significant role on the formation of CNTs.

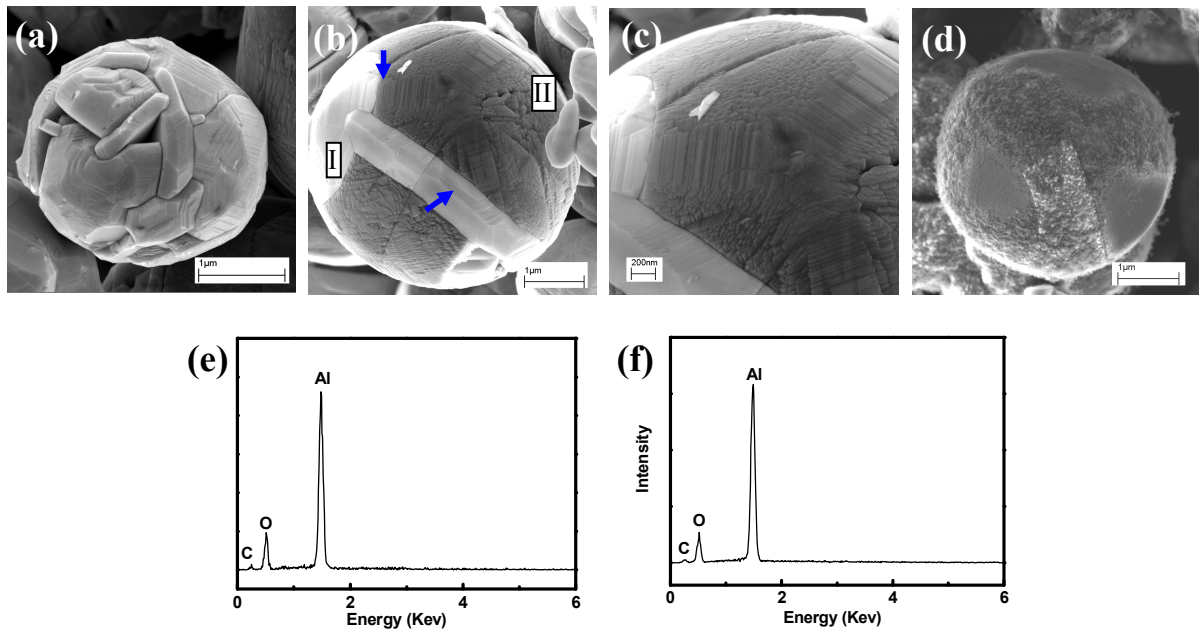


**Figure 82.** (a-c) SEM images of the heat-treated alumina particles composed by several different sub-particles. c is the higher magnification SEM image of b. (d) growth of short CNTs on the particles. (e-f) Energy dispersive spectroscopy analyses of the two kinds of sub-particles with difference colors. The spectra e and f correspond to the white (I) and black (II) particles, respectively.

In order to determine the crystalline orientations of  $\mu$ Al<sub>2</sub>O<sub>3</sub>, the small particles with a diameter less than 1  $\mu$ m are studied, rather than the large polycrystalline ones. That is because the small particles are normally derived from one molten droplet which has homogeneous composition distribution inside the whole particle. Moreover, it is only possible to do the electron diffraction analysis on the small particles in TEM. Their small sizes permit to transmit a sufficient quantity of accelerated electrons. Then, the relationship between the crystal orientation and the CNT growth direction could be brought to light by analyzing the microparticle diffraction pattern (diffraction mode) and the CNT arrangement (image mode). The diffraction analysis procedure is schematically shown in Fig. 83. After the alignment of electron beam, the six-branch hybrid structures should be aligned in order to make at least two CNT branches perpendicular to the electron beam, that is, parallel to the TEM display screen. The transmission electron images of the hybrid structure are taken at the selected magnification.

Then the diffraction is conducted on the whole surface of the particle, or on several selected areas (selected area diffraction mode). Normally, it is done in the regions near the roots of CNT branches. The crystal orientation of  $\mu$ Al<sub>2</sub>O<sub>3</sub> could be determined by the electron diffraction patterns. The organization directions of CNT branches could therefore be established by comparing the TEM images of the hybrid structure and the diffraction patterns of the particle.

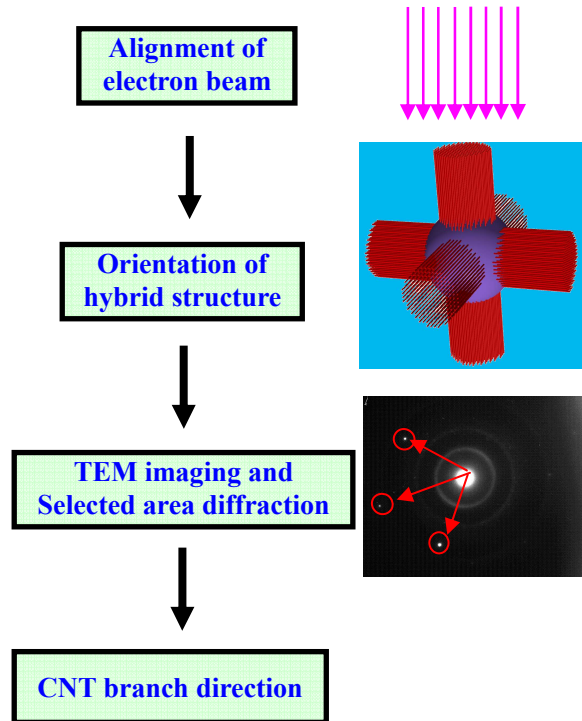


**Figure 83.** Schematic of the procedure of electron diffraction analysis on six-branch hybrid structure

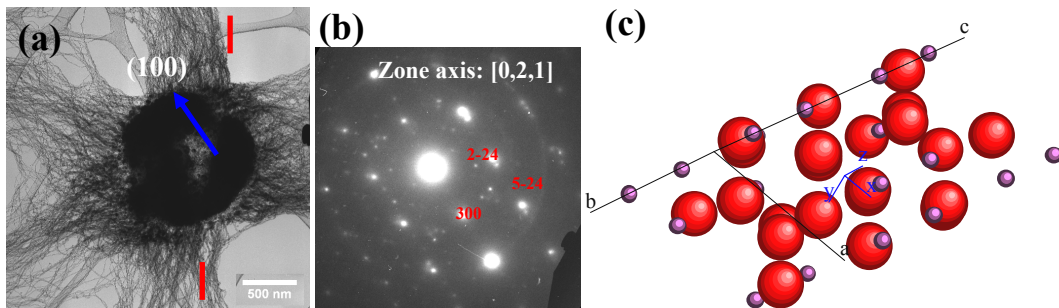
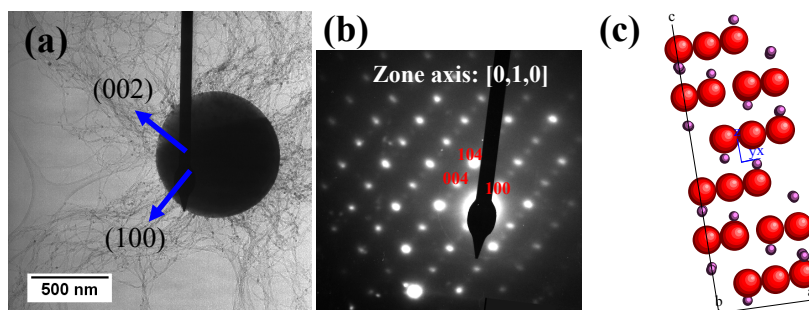


**Figure 84.** (a) TEM image of the hybrid structure, (b) Electron diffraction on the whole  $\mu$ Al<sub>2</sub>O<sub>3</sub> particle, and (c) projection of the  $\alpha$ -Al<sub>2</sub>O<sub>3</sub> primitive cell along the [021] direction, in which the big red balls indicate O<sup>2-</sup> ions, and the small violet ones indicate Al<sup>3+</sup> ions.

A number of diffraction analyses have been conducted on many different alumina particles. Fig. 84a shows the TEM image of one hybrid structure containing six CNT bundles, in which two vertical branches (marked by the red bars) are parallel to the TEM display screen. The

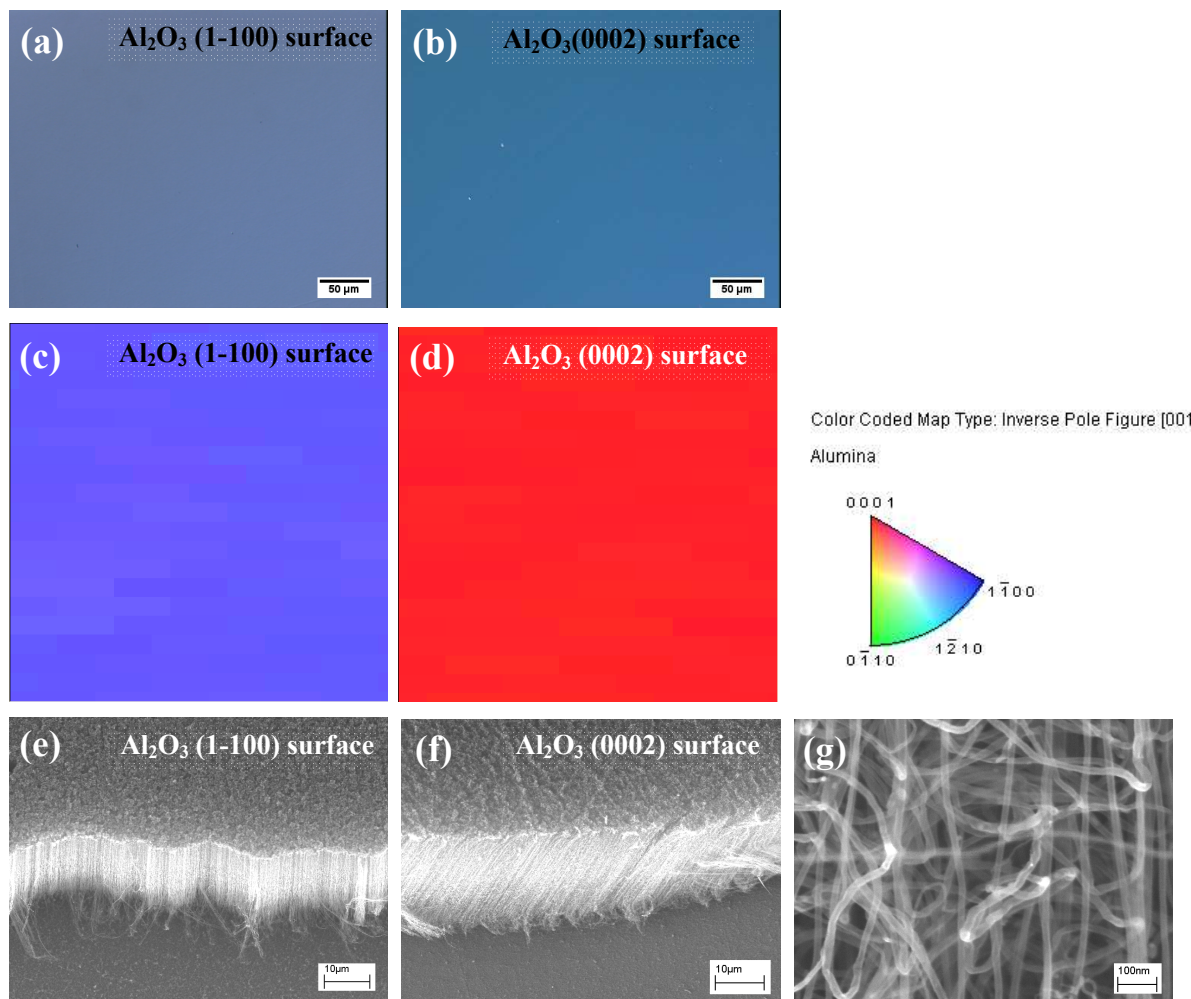
whole alumina particle is selected to do electron diffraction, whose pattern is shown in Fig. 84b. It is worth to mention that the pattern is obtained on the particle, which has been attacked for certain time by converged electron beam. The white area in the center of alumina particle corresponds to the region with weakened thickness. The plane indices corresponding to the diffraction spots are identified as the ones given in the figure. Correspondingly, the diffraction axis is calculated along the [021] direction. The projection of the  $\alpha$ -Al<sub>2</sub>O<sub>3</sub> primitive cell along the axis direction is schematically shown in Fig. 84c. The blue arrow in Fig. 84a denotes the [100] direction. This direction is nearly parallel to the alignment directions of the CNT bundles marked with the red lines. The small difference might be due to a slight deformation of the microparticle, which is resulted by electron attack. This indicates that the particle cube-surface planes belong to planes {100}.

Fig. 85 shows another type of electron diffraction pattern obtained with one small particle which is  $\sim 800$  nm in diameter. The electron diffraction (Fig. 85b) is conducted on the selected area, marked by the TEM beam stop (Fig. 85a). One CNT bundle is grown from this region. Then, the particle is aligned to make two CNT bundles parallel to the TEM display screen. A pattern with well-aligned diffraction spots is obtained. The corresponding plane indices and the projection of the primitive cell are demonstrated in Fig. 85b and c, respectively. The calculated axis direction is [010]. The blue arrows indicating the normal vectors of the (002) and (100) planes exactly point to two CNT bundles (Fig. 85a). This confirms the diffraction result presented in Fig. 84. Furthermore, it shows that CNT bundles could also be formed in the regions where the crystal orientation corresponds to the family of planes {002}. Therefore, the directions of CNT bundles could be normal to  $\alpha$ -Al<sub>2</sub>O<sub>3</sub> {100} and {002} planes.



**Figure 85.** (a) TEM image of the hybrid structure, (b) Electron diffraction on the selected region marked by the beam stop in (a). (c) projection of the  $\alpha$ -Al<sub>2</sub>O<sub>3</sub> primitive cell along the [010] direction, in which the big red balls indicate O<sup>2-</sup> ions, and the small violet ones indicate Al<sup>3+</sup> ions.

Furthermore, CNT growth has also been conducted on alumina single crystals with different types of surface plane. Because it is of significant importance to precisely identify the influence of alumina crystal planes on CNT nucleation and growth. Two samples with  $\alpha$ -Al<sub>2</sub>O<sub>3</sub>(1 $\bar{1}$ 00) and (0002) surfaces are chosen as substrates. The polishing is first done in order to remove the surface defects formed during the cutting of the two single crystals. The optical microscopy images show two smooth sample surfaces (Fig. 86). Then, the electron back scattering diffraction (EBSD) analysis is carried out on the two surfaces. The results proves that the two sample surfaces are exactly (1 $\bar{1}$ 00) and (0002). Next, the two monocrystals are used as substrates to synthesize CNTs using acetylene/xylene mixture as carbon source at 700 °C. The acetylene flow rate is  $\sim$  0.02 l min<sup>-1</sup>. The flow rates of argon and hydrogen carrier gases are 0.9 and 0.1 l min<sup>-1</sup>, respectively. The injection of carbon sources lasts for about 20 min.



**Figure 86.** Characterizations of two alumina single crystals oriented in [1-100] and [0002] directions, and their influence on CNT growth. (a-b) Optical microscopy images of the two monocrystal sample surfaces after polishing. (c-d) Characterization of electron backscatter diffraction (EBSD) on the two sample surfaces. (e-f) SEM images of CNT carpets obtained on the two monocrystal surfaces at 700 °C. (g) high magnification SEM of CNTs shown in figure e.

Fig. 86e-f show two CNT carpets obtained on single crystal  $\alpha\text{-Al}_2\text{O}_3$  ( $1\bar{1}00$ ) and (0002) surfaces. Highly dense CNTs are grown on the above two surfaces. The carpet on the former surface has a thickness of  $\sim 10 \mu\text{m}$ , but  $\sim 20 \mu\text{m}$  on the latter one. A higher CNT growth rate is found on the (0002) surface, about 2 times higher than on the ( $1\bar{1}00$ ) surface. However, the diameter of CNTs obtained on the two surfaces is at the same level,  $\sim 10 \text{ nm}$  (Fig. 86g). In spite of the difference in CNT growth rate, the growth of high density CNTs on the two types of crystal surfaces indicates that the alumina {0002} and {1-100} surfaces have little difference in terms of the nucleation of iron catalyst particles and CNTs at the studied conditions.

This result further confirms that the heterogeneous growth of CNTs in six branches on  $\mu\text{Al}_2\text{O}_3$  originates from the difference in the distribution of crystal steps on the particle surface. Compared with the nucleation of catalyst particles on flat surface, this at crystal step sites requires less energy<sup>[267]</sup>. The regions with a large number of crystal steps are the preferential nucleation sites of iron catalyst nanoparticles. The step size and distribution could significantly influence the distribution of catalyst particles. However, the smooth regions with few crystal steps are not favorable for the growth of catalyst particles and CNTs. In consequence, the arrangement of CNT bundles in the six-branch hybrid structures is determined by the crystal step orientation. The CNT organization in the six bundles is in fact a representation of the intrinsic surface alumina structures of  $\mu\text{Al}_2\text{O}_3$ .

The six-branch CNTs- $\mu\text{Al}_2\text{O}_3$  is related to the cube-like particle surface feature. The formation of the latter is due to the specific production process of alumina microspheres. As mentioned earlier, the spherical particles were fabricated by melting irregular alumina particles in a plasma flame. In general, the cubic part in the center of particles may not be completely molten. Thus, they could serve as nucleation seed during the particle solidification process. The seeds with a regular morphology may consequently generate the difference in the cooling rates of different surface regions.

The cube-like feature and step structures of the  $\mu\text{Al}_2\text{O}_3$  surface are schematically demonstrated in Fig. 87a. The whole sphere surface is divided into six symmetric regions by twelve regularly connected bands (pink zones in Fig. 87a). The twelve pink band zones correspond to the twelve edges of an inscribed cube. In these regions, there are few crystal steps. In contrast, the six regions are composed of a large number of well-organized crystal steps. In each region, the steps could be seen as a series of regularly stacked crystal planes which have different sizes. A small platform is formed near the highest point. Ideally, these planes are parallel to the corresponding cube face, which is probably parallel to crystal planes {0002} and

$\{1-100\}$ . For the material of hexagonal structure, the crystal planes  $\{0002\}$  have the highest atom density, and thus correspond to the most stable planes. As shown in the inserted figure (Fig. 87a), iron catalyst particles preferentially nucleate at the crystal step sites. Large step sizes lead to low catalyst densities, vice versa. Then, high density CNTs are nucleated on the catalyst particles which distribute in the six regions. The orientations of the steps determine the distributions of iron catalyst particles, and furthermore the CNT organization directions. With the growth of CNTs on  $\mu\text{Al}_2\text{O}_3$ , the six orthogonal bundle structures are finally formed (Fig. 87b). At the same time, it worth to remind that this influence of the  $\mu\text{Al}_2\text{O}_3$  surface structures on CNT growth and organization could be modulated by increasing the hydrogen ratios and the synthesis temperature.

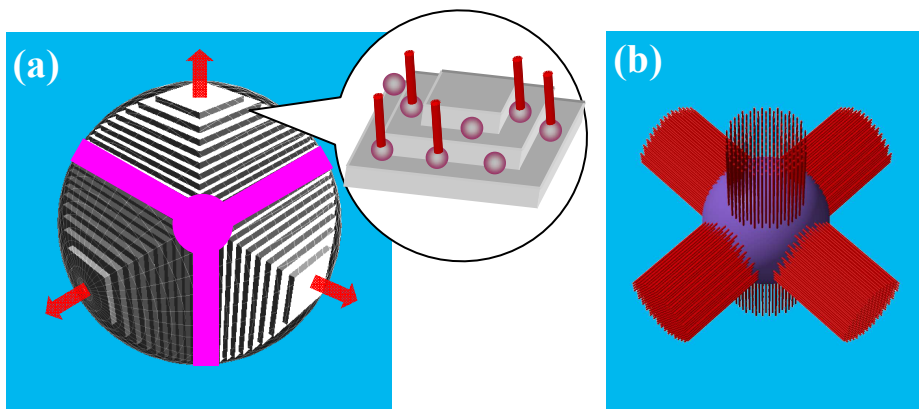


**Figure 87.** Heterogeneous surface structures of  $\mu\text{Al}_2\text{O}_3$  particles and resulted hybrid structures with six CNT bundles. (a) Schematics of the step surface structures of the  $\mu\text{Al}_2\text{O}_3$ . The pink regions correspond to the twelve edges of the inscribed cube. The inserted figure shows the catalyst nucleation and CNT growth at the step sites. Red arrows indicate the CNT bundle directions. (b) Schematic of the hybrid structures consisting in the six CNT bundles on the pristine  $\mu\text{Al}_2\text{O}_3$  with a step structure demonstrated in (a).

### 3.5.2 Nano-cantilever model

It is noticed that CNTs in the hybrid structures possess specific diameter, length and density. It is desirable to propose an appropriate model, which could globally describe the relationship between the geometry and density of CNTs and the organization of hybrid structures. In the following parts, we use a CNT nano-cantilever model to analyze the deflection of a single CNT from vertically-aligned state to the state parallel with its neighboring CNTs (Fig. 88a), due to the weak van der Waals interaction (VdW) forces which promote the formation of CNT bundles.

Indeed, the VdW forces extensively exist in CNT growth process, and in the obtained materials. For instance, they largely contribute the self-assembly of single-walled CNTs into bundles, and the self-folding of one CNT into racket-structures.<sup>[268-271]</sup> Another significant effect of VdW forces is the formation of high density vertically aligned single-walled or MWCNT arrays which are normally produced on flat substrate by CVD method<sup>[80, 231, 272]</sup>. As previously indicated, the exceptional mechanical properties, especially high Young's modulus ( $\sim 1$  TPa)<sup>[35, 273]</sup>, ensure short CNTs high stiffness enough to resist to the bending deformation, and to grow perpendicularly on the surface of the substrate.

In the case of the “short-dense-homogenous” and the “urchin-like” hybrid structures, CNTs grow vertically on the surface of spherical particles. Meanwhile, in “six-branch” structures, CNTs self-assemble into bundle structures, in which parallel CNTs are aligned along six-directions. The deflection of CNTs is a competitive result between the VdW forces and the CNT resistance to bending.

The continuum Lennard-Jones (LJ) model is widely used to evaluate the VdW potential energy of interactions in any types of graphitic structures, including CNTs.<sup>[268, 271, 274]</sup> It was found that the interaction potentials between two arbitrary CNTs have the same curve when plotted in terms of the reduced parameters, the well depth  $\phi(R_0)$  and equilibrium VdW gap ( $R_0-\rho$ ), which is from 3.107 to 3.169 Å.<sup>[268, 274, 275]</sup> As Sun suggested,  $R_0-\rho$  has a value of 3.15 Å.  $R_0$  is the equilibrium spacing at the minimum energy for the two interacting entities;  $\rho$  corresponds to the sum of the diameters of two interacting CNTs. The potential of two parallel and infinitely long single-walled CNTs can be represented by a simple analytical form as suggested by Girifalco<sup>[268]</sup> et al. and Sun et al.<sup>[274]</sup>, as follows:

$$\tilde{\phi}(\tilde{R}) = -\frac{1}{0.6} \left[ \left( \frac{3.41}{3.15\tilde{R} + 0.28} \right)^4 - 0.4 \left( \frac{3.41}{3.15\tilde{R} + 0.28} \right)^{10} \right] \quad (1)$$

where  $\tilde{\phi}(\tilde{R}) = \frac{\phi(R)}{|\phi(R_0)|}$ ,  $\tilde{R} = \frac{(R-\rho)}{(R_0-\rho)}$ ,  $\phi(R)$  is the potential energy of interaction per unit length,

and  $R$  is the perpendicular distance between CNT centers, which could be written as

$$R = \tilde{R}(R_0 - \rho) + \rho. \quad (2)$$

Therefore, the interaction potential between two MWCNTs could be written as:

$$\phi^{AB}(R) = -\frac{|\phi(R_0)|}{0.6} \left( \left( \frac{3.41}{R - \rho + 0.28} \right)^4 - 0.4 \left( \frac{3.41}{R - \rho + 0.28} \right)^{10} \right) \quad (3)$$

At this point, the problem is transferred to how to obtain the value of  $\phi(R_0)$ .

Here, we use the method proposed by Sun et al [274, 275] to evaluate approximately the potential expression. The interaction between two MWCNTs A and B interaction is expressed by an index ( $r_{inner}^A$ ,  $n_A$ )-(  $r_{inner}^B$ ,  $n_B$ ) in the continuum model.  $r_{inner}^A$  and  $r_{inner}^B$  indicate the inner radii for tubes A and B, respectively.  $n_A$  and  $n_B$  stand for the number of layers in tubes A and B, respectively. The interlayer spacing is assumed constant,  $c=3.39$  Å. The potential energy ( $\phi^{AB}$ ) for ( $r_{inner}^A$ ,  $n_A$ )-(  $r_{inner}^B$ ,  $n_B$ ) was calculated by summarizing all the interactions ( $\phi^{ij}$ ) between the i layer of tube A and the j layer of tube B, here  $i=1, 2, \dots, n_A$  and  $j=1, 2, \dots, n_B$ . As proposed by Sun et al. [275], the well depth of two MWCNTs  $\phi_0^{AB}$  could be approximately estimated by:

$$\begin{aligned}\phi_0^{AB} = & \phi_0^{n_A n_B} + 0.13(\phi_0^{(n_A -1)n_B} + \phi_0^{n_A (n_B -1)}) + 0.03(\phi_0^{(n_A -2)n_B} + \phi_0^{(n_A -1)(n_B -1)} + \phi_0^{n_A (n_B -2)}) \\ & + 0.01(\phi_0^{(n_A -3)n_B} + \phi_0^{(n_A -2)(n_B -1)} + \phi_0^{(n_A -1)(n_B -2)} + \phi_0^{n_A (n_B -3)})\end{aligned}\quad (4a)$$

where

$$\phi_0^{ij} = -\sqrt{(3.13 - 37.9\sqrt{R_i^A}) \times (3.13 - 37.9\sqrt{R_j^B})} \quad (4b)$$

$$R_i^t = R_{inner}^t + (i-1) \times c \quad (i=n_t, \dots, n_{t-3}; t=A, B) \quad (4c)$$

The potential terms ( $\phi_0^{AB}$  and  $\phi_0^{ij}$ ) and radii ( $R_i^t$  and  $R_{inner}^t$ ) are in units of meV/Å and Å, respectively.

In our case, CNT diameter is homogeneous in the “short-dense-homogeneous” and the “six-branch” hybrid structures. According to HRTEM observations, CNT has an inner radius of ~25 Å, and contains 8 graphene layers. It is therefore reasonable to assume all the CNTs with the same index, in the form ( $r_{inner}$ , 8). Then, we calculate using equations 4 the potential between any pair of CNTs  $\phi_0^{AB} = -360.72$  meV. Furthermore, the potential  $\phi^{AB}$  could be finally expressed by

$$\phi^{AB}(R) = -\frac{360.72}{0.6} \left[ \left( \frac{3.41}{R-50+0.28} \right)^4 - 0.4 \left( \frac{3.41}{R-50+0.28} \right)^{10} \right]. \quad (5)$$

The force between two MWCNTs resulting from VdW interaction potential is:

$$f(R) = -\frac{d\phi^{AB}(R)}{dR}. \quad (6)$$

Using the above  $\phi^{AB}$  expression, the interaction force  $f(R)$  could be expressed by

$$f(R) = 1.602 \times 10^{-12} \times 705.22 \times \left( \left( \frac{3.41}{R - 50 + 0.28} \right)^{11} - \left( \frac{3.41}{R - 50 + 0.28} \right)^5 \right) (\text{N}/\text{\AA}). \quad (7)$$

Evidently, in all the hybrid structures, MWCNTs are grown on  $\mu$ Al<sub>2</sub>O<sub>3</sub> through base growth mode.<sup>[144]</sup> That is, one end of MWCNTs is fixed on the substrate by catalyst particles, but the other one is free. In order to emphasize the roles of CNT length and diameter in the self-organization mechanism, we assume MWCNT as hollow homogeneous cylindrical cantilever, as done in the earlier experimental and theoretical studies.<sup>[270, 276]</sup> The beam endures an attractive force from adjacent CNT. For vertically-aligned CNT arrays, the distance R between two CNTs could be approximately estimated by  $R \approx 1/\sqrt{N}$ , where N is the CNT area number density. The interaction force of two adjacent CNTs is simply seen as a uniform distributed VdW force,  $f(R)$ , along the length ( $L$ ) of the beam axis, as shown in Fig. 88a.

According to Euler-Bernoulli equation, the deflection of the beam  $u(x)$  at the position x is given by:

$$EI \frac{d^4 u}{dx^4} = f(R) \quad (8)$$

where E is the Young's modulus of CNT and I is the second moment of its cross-section. The moment is:

$$I = \frac{\pi}{64} (d_o^4 - d_i^4) \quad (9)$$

where  $d_o$  and  $d_i$  are the outer and inner diameters of CNT, respectively.<sup>[277]</sup> As we only consider small bending deflection of the short beam ( $\sim 1 \mu\text{m}$ ), the shear force can be neglected. Moreover, we assume the VdW forces as constant along the length of CNT because of the high area number density of CNTs and their small deflection angle. After integrating equation 8, the CNT maximum bending deflection can be expressed by:

$$u_{\max}(L) = \frac{f(R)L^4}{8EI} \quad (10)$$

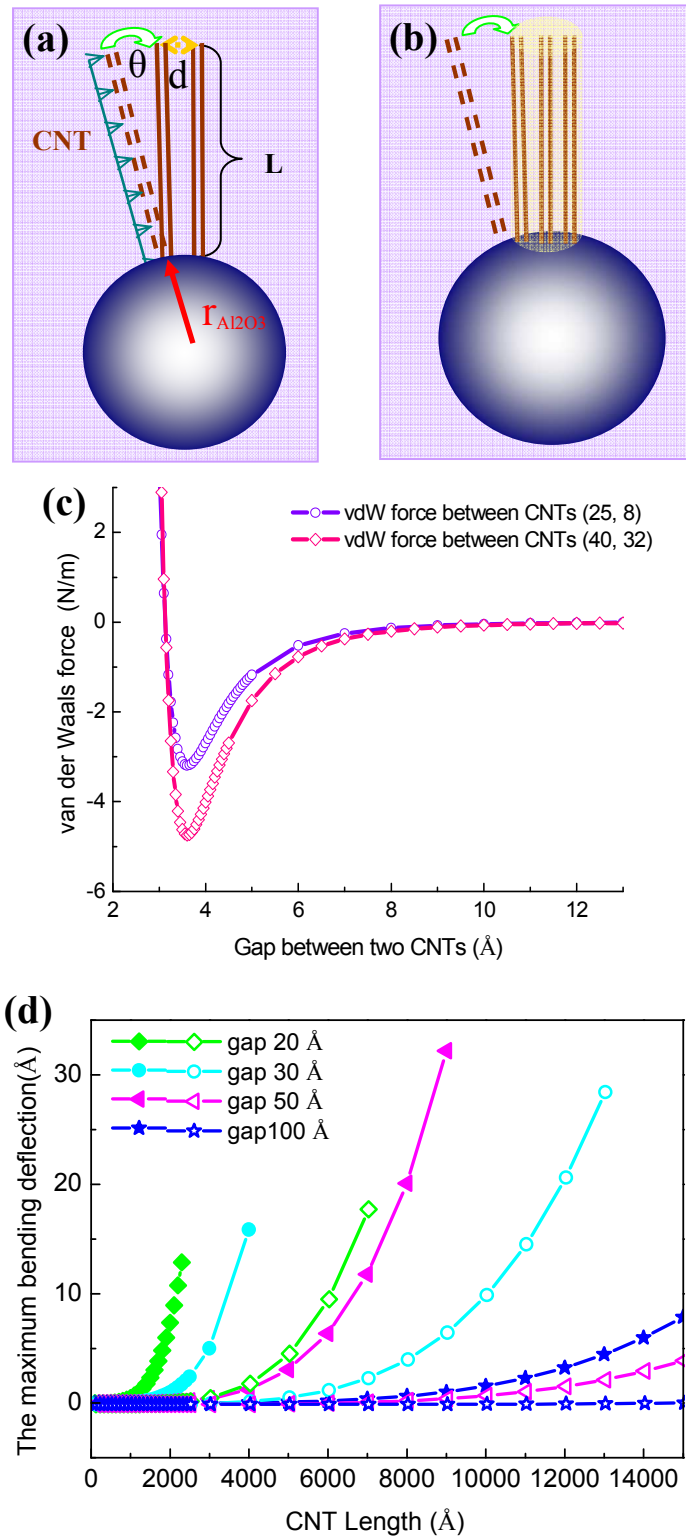


**Figure 88.** Weak VdW interactions between CNTs and nano-cantilever model to analyze the agglomeration of CNTs on  $\mu\text{Al}_2\text{O}_3$ . (a) Schematic of the interaction (uniform distribution loading) of two adjacent CNTs: perpendicularly grown CNTs ( $L$ , length) are seen as nano-cantilevers with one end fixed on the surface of  $\mu\text{Al}_2\text{O}_3$ , with a radius  $r_{\text{Al}_2\text{O}_3}$ . The gap between two roots of CNTs is noted with  $d$ .  $\theta$  corresponds to the angle resulting from the deflection of one CNT. (b) Schematic of the initial agglomeration of CNTs at one pole of alumina particle due to the weak VdW interactions; (c) Curves of VdW forces between one pair of parallel MWCNTs indicated by CNT(25,8)-(25,8) and CNT(40,32)-(40,32), according to the model proposed by

Girifalco<sup>[268]</sup> et al. and Sun et al.<sup>[274]</sup>; (d) Relationships between the maximum deflections of CNTs (25, 8)-(25,8) and (40, 32)-(40, 32), and their lengths, when CNT gaps are 20, 30, 50 and 100 Å, respectively. Solid and hollow symbols indicate CNT(25, 8) and CNT(40, 32), respectively.

It is noticed that the maximum bending deflection of one CNT depends on the VdW forces, the rigidity (EI) and the length of CNT. MWCNT rigidity is proportional to the second moment of its cross-section, which is a function of the outer and inner diameters (equation 9). The VdW forces are related to the distance between two CNTs. Therefore, the CNT deflection is controlled by its diameter, length and density on the surface of the alumina sphere.

To analyze the characteristics of CNT interaction in there different hybrids, two types of CNTs are chosen for detailed discussions. CNT (25, 8) corresponds to the CNT contained in the “short-dense-homogeneous” and the “six-branch” structures, and CNT (40, 32) represents the CNT in the “urchin-like” one. According to the obtained VdW forces (Fig. 88c), the bending deflection of two CNTs with the increase of length is calculated using different gaps between two CNTs (Fig. 88d).

First, it can be seen that the maximum blending deflections of both two groups of CNTs vary substantially with the distance between CNTs, or CNT density. Smaller is the distance between two CNTs, much easier is the deflection. Meanwhile, when the gap between two CNTs increases from 20 to 100 Å, the deflection falls down suddenly. This phenomenon becomes more and more evident with increasing the distance. Second, for a given gap distance, CNT(40, 32) exhibits much higher resistance to the blending deflection than CNT(25, 8). This could be first seen from the fact that small diameter CNT(25, 8) always losses the stability (deflection increases rapidly) earlier than CNT(40, 32), for the same gap distance. This phenomenon is more evident when the gap distance is smaller. The same relationship of the difference between two deflection augmentation rates and CNT gap distance has been found. The difference of the rigidities of CNTs is less important to the deflection, when the distance between two CNTs is big, as shown in Fig. 88d (gap =100 Å, L~1μm). A considerable difference between the deflections of CNT(25, 8) and CNT(40, 32) is only found when CNT is long.

CNT density is more than  $10^{15}$  m<sup>-2</sup> in the “short-dense-homogeneous” and “six-branch” structures. This means that the gap between CNTs with diameter of 10 nm is less than 100 Å. From the Fig. 88d, we find that the CNT under the VdW forces has an evident deflection when the CNT length is more than 1μm. However, the area number density is much lower

than  $10^{14} \text{ m}^{-2}$  for CNTs in the “urchin-like” hybrid structures. For instance, for CNTs with diameter of 50 nm, the gap between the CNTs will be about 5000 Å, therefore the deflection of the CNT is negligible and it will keep growing perpendicularly on the surface of alumina particles.

The analyses described above show that the weak VdW forces between CNTs of 10 nm in diameter are large enough to create bundles, when their length reach certain critical value. In our research, this value is around 1 μm for the  $\mu\text{Al}_2\text{O}_3$  spheres, which have the diameters ranging from 2 to 5 μm. However, we noticed that CNTs grown on ceramic spheres with diameters about 700 μm, would evidently crack into different bundles only when their length is more than 400 μm<sup>[222]</sup>. This is because the ceramic spheres have smaller curvature  $\sim 10^3$ . Whereas, the curvature of the alumina microparticles is nearly about  $10^6$  in our case.

In order to be parallel with the neighboring CNTs, the maximum deflection of one CNT on the spherical substrate can be estimated by  $u_0 \approx L \frac{d}{r_{sub}}$ , where L is the CNT length, d is the gap between two CNTs, and  $r_{sub}$  is the radius of the sphere. If we consider the CNT density and  $u_0$  as constant, a critical value of the ratio  $\frac{L}{r_{sub}}$  is required to obtain the bundle structures on spherical substrates. That corresponds to :  $\frac{L_{01}}{L_{02}} \approx \frac{r_{sub1}}{r_{sub2}}$ , where  $L_{01}, L_{02}$  are the critical lengths of the CNTs, and  $r_{sub1}, r_{sub2}$  are the radii of the spherical particles. We find that the in our materials, the CNT crack length is 1 μm on the alumina spheres of 2-5 μm in diameter, which is coherent with the 400 μm in length determined by Zhang et al. for  $\sim$ 700 μm on the ceramic spheres of  $\sim$ 700 μm in diameter.<sup>[222]</sup>

Therefore, when the length is smaller than 1μm (even for high area number density and small diameter  $\sim$ 10 nm), CNT stiffness is sufficient to resist to bending deflection. Thus, CNTs stand vertically on the spherical surface of  $\mu\text{Al}_2\text{O}_3$ , like in the “short-dense-homogenous” structures. Nevertheless, when the diameter remains about 10 nm, the increasing length greatly promotes the deflection. As a result, MWCNTs agglomerate into branches, like in the “six-branch” structures. MWCNTs with diameters beyond 20 nm have an enhanced rigidity, which prohibits the deflection of the elongated CNT. In this case, the most favorable hybrid structure is the “urchin-like” ones, which has lower CNT density on  $\mu\text{Al}_2\text{O}_3$ .

### 3.6 Conclusion

In this chapter, we have investigated in detail the influences of four key CVD parameters on CNT growth and organization on micrometer alumina particles. These parameters are catalyst precursor, carbon sources, temperature, and hydrogen ratio. The studies demonstrate that the CVD parameters have considerable influences on the growth and organization of CNTs on micrometer alumina particles. The coordination between the decomposition rates of catalyst and carbon precursors is greatly dependent on the interactions of these parameters.

The variation of ferrocene concentration and its feeding rate generates the variation of Fe/C ratios in CVD reactor. The small ferrocene concentration is unfavorable to the generation of well-organized hybrid structures, due to weak number density of catalyst particles and weak CNT growth rates. The increase of ferrocene concentration promotes the nucleation of catalyst particles, and in turn accelerates the CNT growth. High ferrocene concentrations favor the formation of large diameter catalyst particles at high temperatures. And the particle diameter varies in a wide range. The “urchin-like” hybrid structures form when the ferrocene concentration in xylene solution is more than 0.01 g ml<sup>-1</sup>, corresponding to 8.22E-4 in the iron/carbon molar ratio. At the low temperature (550 °C), high ferrocene-xylene solution injection rates promote the formation of the “six-branch” hybrid structures from the decomposition of acetylene.

The studies of the influence of carbon sources show that the decomposition of xylene requires a relatively high temperature in order to obtain the “urchin-like” hybrid structures. The addition of acetylene greatly increases CNT growth rate and number density at all the temperatures studied. More importantly, the distribution range of CNT diameter is homogenized by the strong interference of acetylene in the nucleation process of catalyst particles. A considerable reduction of the numbers of carbon-encapsulated and CNT-encapsulated iron particles indicates high utilization efficiency of catalyst particles when the mixture carbon source (xylene-acetylene) is used.

The temperature plays an essential role in the decomposition of catalyst precursor and carbon sources. The increase of temperature greatly improves CNT growth rate, and also CNT diameter and crystallinity. Meanwhile, the difference of hybrid structures along the CNT growth position in the reactor is generated, due to the increased concentration gradient of iron

and carbon species. This difference could be decreased by using acetylene/xylene mixture as carbon source at relatively low temperatures.

The presence of reductive hydrogen in CVD reactor prevents the formation of amorphous carbon particles during CNT growth on alumina microspheres, especially at relatively high temperatures. The high hydrogen ratios in carrier gases promote the decomposition of xylene to benzene, but reduce the dehydrogenation rates of the hydrocarbons. Therefore, a decreased CNT growth rate is found with increasing hydrogen ratio. Importantly, the high hydrogen ratios also favor to decrease the hybrid structure difference along the reactor length.

The alumina microparticles also play an essential role in the construction of multiform hybrids. The impact of the microparticle morphology on hybrid structures has been demonstrated. The symmetric CNT growth in six surface regions is discussed based on the multiphase structures of alumina particles. The growth of CNTs on the heat-treated particles reveals this heterogeneous CNT growth is not originated from the metastable  $\delta$ -Al<sub>2</sub>O<sub>3</sub> and  $\theta$ -Al<sub>2</sub>O<sub>3</sub>.

The initial CNT growth state and the connection between CNTs and microparticles are also demonstrated. It is found that the root of each CNT contains the catalyst particles which have different morphologies. Often, several particles get together around one nanotube. The detachment of CNTs from the microparticles is realized by the dissociation of the root catalyst particles from the substrate surface. The CNTs grow on the alumina microspheres in a linear way. The possible CNT elongation and deformation models are also proposed to explain various different CNT structures.

Finally, the self-organization mechanism of CNTs on  $\mu$ Al<sub>2</sub>O<sub>3</sub> is uncovered, which includes the heterogeneous growth and the self-assembly of CNTs. The heat-treated alumina spheres bring to light the specific microparticle surface structures. A huge number of crystal steps on the microparticle surface determine the potential numbers of CNT branches. Their specific arrangement consequently orients the CNT growth directions. The nano-cantilever model is proposed to explain the CNT self-organization mechanism due to weak Van der Waals interaction forces between neighboring CNTs. The calculation based on the model shows that CNT self-assembly is greatly dependent on their diameter, length and density on  $\mu$ Al<sub>2</sub>O<sub>3</sub>.

# Chapter IV

## Gas phase chemical reaction kinetics in CVD reactor

### 4.1 Introduction

In the previous chapter, we have demonstrated significant influences of the CVD parameters on the CNT growth on  $\mu\text{Al}_2\text{O}_3$ . A number of different CNTs- $\mu\text{Al}_2\text{O}_3$  hybrid structures have been obtained by varying the temperature, carbon source, hydrogen ratio, and catalyst precursor concentration. There are strong interactions among these parameters. For instance, the variation of CNTs- $\mu\text{Al}_2\text{O}_3$  hybrid structures produced by addition of acetylene is greatly dependent on the used temperature and hydrogen ratio. At the same time, chemical reaction kinetics in the CVD reactor also relies on physical mass and heat transport processes. The specific CVD reactor geometry creates intrinsic temperature and species concentration gradients, which generate the variation of non-uniform iron and carbon deposition on the substrate, and thus varied hybrid structures along the reactor length. However, reduction of these differences is required to large-scale production of the hybrid structures. Therefore, a comprehensive understanding of the coupling interactions of the physical and chemical phenomena in CVD reactor is desired to synthesize high-quality hybrids with desired structures in a controlled way.

In this chapter, the multi physical-chemical CVD processes are numerically analyzed by combining chemical reaction kinetics with physical transport phenomena. The simulation takes into account all influence factors such the reactor geometry, CVD parameters, chemical reactions, and mass and energy transports. It is helpful to understand the gas phase chemical reaction kinetics in the CVD reactor. This comprehensive study could guide us to improve the reactor and the synthesis method for the large-scale production of the desired hybrid structures in a controlled way.

## 4.2 CVD process analysis

### 4.2.1 CVD reactor geometry

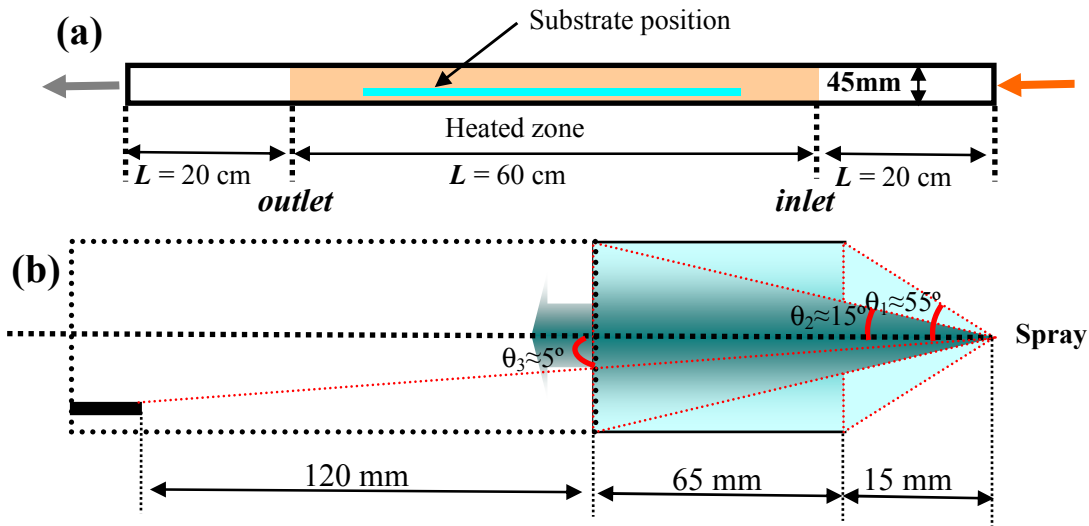


**Figure 89.** (a) Schematic of the quartz tube reactor having an inner diameter of 45 mm and a length of 1 m. A quartz plate ( $3 \times 50\text{ cm}^2$ ) is put in the middle of heated region (60 cm in length). (b) Schematic of the solution spray formed by  $\text{Ar}$  and  $\text{H}_2$  carrier gas with a flow rate of  $1\text{ l min}^{-1}$ . The angle ( $\theta_1 - \theta_2$ ) defines the quartz tube interior surface region where deposit a large amount of solution droplets. The angle  $\theta_3$  ( $\sim 5^\circ$ ) defines the front end of the quartz plate.

The used CVD reactor is schematically shown in Fig. 89a. It is a quartz tube with an inner diameter of 45 mm. The alumina microparticles are first homogeneously dispersed on the surface of a quartz plate which is then put in the middle of heated region of 60 cm in length. The two end parts about 20 cm in length are naturally cooled in air. The ferrocene/xylene solution is continuously injected from one end of the tube (as indicated by the arrow in Fig. 89a), then it is carried into the heated zone in spray form by carrier gases ( $\text{Ar} + \text{H}_2$ ). The distribution of the solution droplets are schematically shown in Fig. 89b. The largest spray angle is  $55^\circ$  when the gas and solution injection rates are 1 and  $0.2\text{ l min}^{-1}$ , respectively. A certain amount of droplets is directly deposited on the interior wall of the quartz tube. The deposition region corresponds to the zone defined by the angle ( $\theta_1 - \theta_2$ ). The angle between the front of substrate and the central line is very small,  $\sim 5^\circ$ . This measurement is conducted at room temperature with an ethanol solution. In contrast to large amounts of droplet deposition on the region defined by the angle ( $\theta_1 - \theta_2$ ), little deposition is found on the surface of the quartz plate. This means, the solution could be well atomized into droplets with

fine sizes even at the room temperatures. The small droplet sizes greatly promote the vaporization of the solution at the experimental temperatures. As little deposition of carbon is observed on the tube wall out of the heated region during CNT growth, in the latter analysis we only consider the physical and chemical phenomena occurred in the heated zone. And, it is assumed that the ferrocene/xylene solution has been completely vaporized in this zone. The inlet and outlet positions are marked in Fig. 89a.

#### **4.2.2 Chemistry and kinetics of chemical reactions**

The chemical reactions involved in the CVD process could be generally classified into the following two major categories: homogeneous gas-phase reactions and heterogeneous surface reactions. The former consists of all the chemical processes occurring in the gas phase, including the decomposition reactions of carbon sources and catalyst precursors. In this study, xylene, acetylene, and their mixture are used as carbon sources. The catalyst precursor is ferrocene. The heterogeneous reactions are the reactions which take place on the surface of catalyst particles and micrometer alumina. They are greatly related to the formation of iron catalyst particles and to the carbon deposition for CNT growth by dehydrogenation of the hydrocarbons. Due to the lack of surface reaction mechanisms and kinetics data, we consider only the gas phase homogeneous reactions in this study.

As it is well known, thermal decomposition of hydrocarbons is strong dependent on the reactor temperature. In different temperature ranges, the hydrocarbons have varied reaction mechanisms. It is worth noting that in our studies, the growth of CNTs on  $\mu\text{Al}_2\text{O}_3$  is mainly conducted at temperatures ranging from 500 to 800 °C. Therefore, the following discussion will be focused on the main gas-phase chemistry features in this temperature range. And, the reaction rate constant  $k$  is expressed using the modified Arrhenius equation,

$$k = AT^n \exp(E_a / R_g T), \quad (4-1)$$

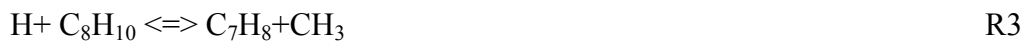
where  $A$  denotes the pre-exponential factor,  $T$  the temperature (K),  $n$  the exponent for temperature dependence of A;  $E_a$  activation energy ( $\text{J mol}^{-1}$ ), and  $R_g$  the gas constant,  $8.314 \text{ J mol}^{-1} \text{ K}^{-1}$ . The unit of pre-exponential factor is  $(\text{m}^3 \text{ mol}^{-1})^{a-1} \text{ s}^{-1}$ , where  $a$  is the order of the reaction.

#### 4.2.2.1 Decomposition of xylene

The mass spectrometry measurements have demonstrated the generation of toluene, benzene and methane from the xylene decomposition, especially at the temperatures higher than 700 °C. The direct transformations from xylene to toluene (R1), and from toluene to benzene (R2) were suggested to be neglected in the temperature range from 500 to 800 °C, due to the strong R-CH<sub>3</sub> bonds in toluene and xylene (434.7 kJ mol<sup>-1</sup>)<sup>[278]</sup>.



Instead, hydrogen (H) addition-exchange reactions are much easier than these direct bond cleavage reactions. As proposed by Benson and Shaw<sup>[279]</sup>, xylene and toluene could decompose to benzene by the following hydrogenolysis mechanism (R3-R4):



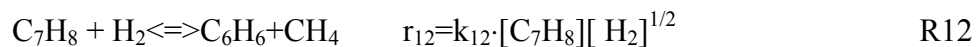
We notice that all the above three reactions are initiated by the substitution of methyl group (-CH<sub>3</sub>) with H. However, the direct production of H from molecular hydrogen is very slow. So the hydrogen equilibrium (R6),



is indirectly set up by the following mechanisms<sup>[280]</sup>:



The calculated reaction (R6) equilibrium constant is K<sub>6</sub>=4.0×10<sup>6</sup> exp (-436000/RT). The combination of R3 –R6 produces the following two global reactions (R11-R12):



where k<sub>11</sub>=K<sub>6</sub><sup>1/2</sup>k<sub>3</sub>=9.2×10<sup>9</sup>·exp(-220000/RT) and k<sub>12</sub>=K<sub>6</sub><sup>1/2</sup>k<sub>4</sub>=4×10<sup>9</sup>·exp(-224000/RT). The above global reactions (R11-R12) has been used to simulate the xylene pyrolysis and subsequent toluene pyrolysis in gas phase, by Endo et al.,<sup>[281]</sup> Kuwana et al.,<sup>[282]</sup> and Wasel et

al.<sup>[283]</sup> The global reactions showed excellent agreement with experiment results at temperatures below 1000 K. Kuwana et al.<sup>[284]</sup> conducted furthermore the simulation of the pyrolyses of xylene at different temperatures, using a detailed xylene oxidation reaction mechanism (160 species, 1175 reactions) constructed by Dagaut et al<sup>[285, 286]</sup>. This comprehensive mechanism includes the direct cleavage of R-CH<sub>3</sub> bonds, the generation of ethane, ethylene and acetylene, the decomposition of benzene, etc. The simulation results agreed well with the ones based on the global mechanism when the temperature was below 1073 K. Meanwhile, the simulation showed toluene, benzene and methane are three major pyrolysis products of xylene.

Considering that the CNT synthesis temperatures used in this study, the global mechanism (R11-R12) proposed by Bensow and Shaw<sup>[280]</sup> is used to describe the pyrolysis of xylene in our CVD reactor. Indeed, this model covers the three major species detected by mass spectrometry.

#### **4.2.2.2 Pyrolysis of acetylene**

Thermal pyrolysis of acetylene has been widely studied. Becker and Hüttinger<sup>[287]</sup> proposed a simplified model to predict the kinetics of carbon deposition from acetylene. They reported that the pyrolysis of acetylene at 1000 °C generated three main gaseous reaction products: ethylene, benzene and methane, as well as some more substituted benzenes and two-member ring compounds such as ethylbenzene (C<sub>6</sub>H<sub>5</sub>-CH<sub>2</sub>CH<sub>3</sub>), naphthalene (C<sub>6</sub>H<sub>4</sub>-C<sub>4</sub>H<sub>4</sub>), biphenyl (C<sub>6</sub>H<sub>5</sub>-C<sub>6</sub>H<sub>5</sub>), toluene, and diethyl benzene (C<sub>6</sub>H<sub>4</sub>(C<sub>2</sub>H<sub>5</sub>)<sub>2</sub>). Back et al<sup>[288]</sup> indicated that vinyl acetylene (C<sub>4</sub>H<sub>4</sub>) is one initial product from acetylene pyrolysis at temperatures below 1200 K. Kiefer et al.<sup>[289]</sup> also indicated that molecular polymerization is the main feature of the homogenous pyrolysis of acetylene at temperatures below 1100 K. Recently, Norinaga and Deutschmann<sup>[290]</sup> have modeled, based on a detailed reaction mechanism, the pyrolysis of acetylene under one condition relevant to the CVD of pyrolytic carbon at 900 °C. Their simulation predicted that acetylene was primarily transformed into vinylacetylene (86 %), diacetylene (17 %), and benzene (7 %). The sensitivity analysis indicated the following three acetylene-related reactions are most sensitive among hundreds of reactions:



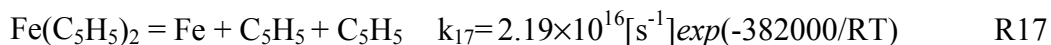
Given that the pyrolysis of acetylene takes place under hydrogen atmosphere, the following reaction between H<sub>2</sub> and C<sub>2</sub>H<sub>2</sub> should also be taken into account.



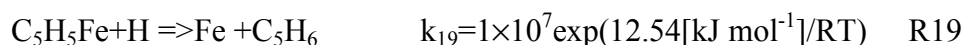
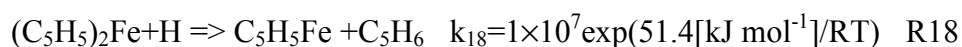
Based on the above discussion, the reactions R12-R16 are chosen to describe the principal features of the acetylene pyrolysis in our CVD system.

#### 4.2.2.3 Decomposition of ferrocene

Lewis and Smith<sup>[291]</sup> measured the thermal gas-phase decomposition of ferrocene using a very low pressure pyrolysis technique. A very high activation energy, ~382 kJ mol<sup>-1</sup>, has been obtained for the reaction R17:



No decomposition of ferrocene was observed when the temperature was below 1120 K. Dormans<sup>[292]</sup> reported the reduction of ferrocene at temperatures between 673 and 1173 K in hydrogen atmosphere, whereas no decomposition of ferrocene was observed until 1173 K under helium atmosphere. These measurements demonstrate the positive roles played by hydrogen in ferrocene decomposition. The interaction mechanism was proposed by Hirasawa et al<sup>[293]</sup> as follows,



Linteris<sup>[294]</sup> further proposed an one step decomposition model with an overall decomposition rate constant,  $k_{16} = 1.0 \times 10^{14} [\text{s}^{-1}] \exp(-209[\text{kJ mol}^{-1}]/RT)$ , in order to more realistically simulate the overall decomposition rate of ferrocene. They approximated the decomposition process with an one step process with an overall activation energy of 209 kJ mol<sup>-1</sup>. Based on the Hirasawa's model<sup>[293]</sup>, Kuwana and Saito<sup>[295]</sup> proposed a global reaction between ferrocene and hydrogen,



with an estimated reaction constant  $k_{20} = 1.6 \times 10^{11} (\text{m}^{3/2} \text{ mol}^{-1/2} \text{ s}^{-1}) \exp(-218000/RT)$ .

Here, we use the global reaction mechanism (R20) to describe the decomposition of ferrocene in our system.

In summary, table 7 gives the whole global mechanism used in this simulation.

**Table 7.** Global gas-phase reactions of xylene, acetylene and ferrocene in the CVD reactor

Index	Reaction	Rate constant expression	Reference
R11	C <sub>8</sub> H <sub>10</sub> +H <sub>2</sub> =>C <sub>7</sub> H <sub>8</sub> +CH <sub>4</sub>	$r_{11}=9.2\times10^9\cdot\exp(-220000/RT) [C_8H_{10}][H_2]^{1/2}$	Benson et al <sup>[280]</sup>
R12	C <sub>7</sub> H <sub>8</sub> + H <sub>2</sub> =>C <sub>6</sub> H <sub>6</sub> +CH <sub>4</sub>	$r_{12}=4\times10^9\cdot\exp(-224000/RT) [C_7H_8][H_2]^{1/2}$	Benson et al <sup>[280]</sup>
R13	2C <sub>2</sub> H <sub>2</sub> => C <sub>4</sub> H <sub>4</sub>	$k_{13}=5.5\times10^6\exp(-154650/RT) [m^3\ mole^{-1}\ s^{-1}]$ $k_{13}=8.65\times10^{13}\exp(-312850/RT) [s^{-1}]$	Norinaga et al <sup>[290]</sup>
R14	2C <sub>2</sub> H <sub>2</sub> => C <sub>4</sub> H <sub>2</sub> + H <sub>2</sub>	$k_{14}=1.5\times10^7\exp(-178670/RT) [m^3\ mole^{-1}\ s^{-1}]$	Norinaga et al <sup>[290]</sup>
R15	C <sub>2</sub> H <sub>2</sub> + C <sub>4</sub> H <sub>4</sub> => C <sub>6</sub> H <sub>6</sub>	$k_{15}=4.47\times10^5\exp(-126000/RT) [m^3\ mole^{-1}\ s^{-1}]$	Norinaga et al <sup>[290]</sup>
R16	C <sub>2</sub> H <sub>2</sub> + H <sub>2</sub> => C <sub>2</sub> H <sub>4</sub>	$k_{16}=1.41\times10^{35}T^{-9.06}\exp(-214000/RT) [m^3\ mole^{-1}\ s^{-1}]$	Norinaga et al <sup>[290]</sup>
R20	Fe(C <sub>5</sub> H <sub>5</sub> ) <sub>2</sub> +H <sub>2</sub> => Fe +2C <sub>5</sub> H <sub>6</sub>	$k_{20}=1.6\times10^{11}(m^{3/2}\ mol^{-1/2}\ s^{-1})\exp(-218000/RT)$	Kuwana et al <sup>[295]</sup>

#### 4.2.3 Thermodynamics and transport properties

##### 4.2.3.1 Fluid thermodynamic properties

The gas fluid in CVD system consists of a number of chemical species, including the injected catalyst and carbon precursors, and their decomposition products. In the fluid, the carrier gas argon takes an absolute molar percentage, ~ 85 %. For this reason, argon is treated as “solvent” of the gas mixture. Thus, the reaction fluid thermodynamic properties could be approximately evaluated by these of argon.

The molar enthalpy  $h$ , the molar entropy  $s$ , and the heat capacity  $C_p$ , could be expressed using the following polynomials,

$$h_i = R_g(a_1 T + \frac{a_2}{2} T^2 + \frac{a_3}{3} T^3 + \frac{a_4}{4} T^4 + \frac{a_5}{5} T^5 + a_6) \quad (4-2)$$

$$s_i = R_g(a_1 \ln T + a_2 T + \frac{a_3}{2} T^2 + \frac{a_4}{3} T^3 + \frac{a_5}{4} T^4 + a_7) \quad (4-3)$$

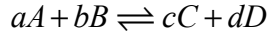
$$C_{p,i} = R_g(a_1 + a_2 T + a_3 T^2 + a_4 T^3 + a_5 T^4) \quad (4-4)$$

where  $T$  is the temperature (K), and  $R_g$  is the ideal gas constant, 8.314 (J mol<sup>-1</sup>K<sup>-1</sup>). Further,  $h_i$  is the species' molar enthalpy (J mol<sup>-1</sup>), and  $s_i$  represents its molar entropy (J mol<sup>-1</sup>K<sup>-1</sup>) at standard state. The coefficients a<sub>1</sub>-a<sub>7</sub> of argon are listed in table 8 (see the values of other species in Appendix 3). It is worth to point out that the coefficients of Fe(C<sub>5</sub>H<sub>5</sub>)<sub>2</sub> and Fe(C<sub>5</sub>H<sub>5</sub>) are obtained by the polynomial fitting of their specific heat values provided by the reference<sup>[293]</sup>.

**Table 8.** Thermal dynamic parameters of argon<sup>[290]</sup>

Polynomial coefficient, a	a <sub>1</sub>	a <sub>2</sub>	a <sub>3</sub>	a <sub>4</sub>	a <sub>5</sub>	a <sub>6</sub>	a <sub>7</sub>
a <sub>low,K</sub> (300 ≤ T ≤ 1000 K)	2.5	0	0	0	0	-7.45375×10 <sup>2</sup>	4.366
a <sub>high,K</sub> (1000 ≤ T ≤ 5000 K)	2.5	0	0	0	0	-7.45375×10 <sup>2</sup>	4.366

Chemical reactions have energy exchange with atmosphere by heat absorption or emission. For one reaction j,



the reaction rate  $r_j$  could be described by the formula

$$r_j = k_j^f \prod_{i \in reactant} c_i^{-v_{ij}} - k_j^r \prod_{i \in product} c_i^{v_{ij}} \quad (4-5)$$

where  $k_j^f$  and  $k_j^r$  denote the forward and reverse rate constants, respectively.  $c_i$  designates the concentration of species  $i$ , and  $v_{ij}$  denotes the stoichiometric coefficients (negative for reactants and positive for products). Therefore, the overall heat  $Q$  could be calculated from the sum of heat ( $Q_j$ ) generated by each chemical reaction:

$$Q = \sum_j Q_j = \sum_j (-H_j r_j) = -\sum_j \sum_i (v_{ij} h_i) \quad (4-6)$$

$$S_j = -\sum_i v_{ij} s_i \quad (4-7)$$

where  $H_j$  denotes the enthalpy of reaction  $r_j$ ,  $S_j$  the entropy of reaction  $r_j$ ,  $h_i$  and  $s_i$  are the species' molar enthalpy and entropy, respectively.

#### 4.2.3.2 Transport properties

##### 4.2.3.2.1 Dynamic viscosity

For gases, the dynamic viscosity could be expressed according to the kinetic gas theory<sup>[296]</sup> as

$$\eta_i = 2.669 \cdot 10^{-6} \frac{\sqrt{T(M_i \cdot 10^3)}}{\sigma_i^2 \Omega_v} \quad (4-8)$$

where  $\eta$  represents the dynamic viscosity (N s m<sup>-2</sup>), and  $\Omega_v$  is the collision integral, given by

$$\Omega_v = A(T^*)^{-B} + C[\exp(-DT^*)] + E[\exp(-FT^*)] + \frac{0.20\delta^2}{T^*} \quad (4-9)$$

$$\text{with } T^* = k \frac{T}{\varepsilon} \quad (4-10)$$

$$\text{and } \delta = \frac{1}{2} \frac{\mu^2}{\varepsilon \sigma^3} \quad (4-11)$$

where  $\mu$  is the species dipole moment (Debye).

The synthesis of CNTs is carried out under atmospheric pressure. In general, the used carrier gas flow rates range from 0.8 to 1.0 l min<sup>-1</sup>. In order to atomize xylene solution into fine spray, the gases have a flow rate as high as ~ 40 m s<sup>-1</sup>, at the entrance of the quartz tube. At the front of the heated zone (Fig. 89a), the flow rate is greatly reduced owing to the solution atomization interaction and the flow area expansion. The gas flow is in laminar regime, according to the Reynolds number (Re=40 < 2200), calculated following the formula:

$$Re = \frac{\rho V D}{\mu} = \frac{Q D}{\nu A} \quad (4-12)$$

where  $V$  is the mean flow velocity (m s<sup>-1</sup>),  $D$  is a characteristic diameter of the tube (m),  $\mu$  is the dynamic viscosity of the fluid (N s m<sup>-2</sup>);  $\nu$  is the kinetic viscosity ( $\nu = \mu / \rho$ ) (m<sup>2</sup> s<sup>-1</sup>),  $\rho$  is the density of the fluid (kg m<sup>-3</sup>),  $Q$  is the volumetric flow rate (m<sup>3</sup> s<sup>-1</sup>), and  $A$  is the cross-sectional area of the quartz tube (m<sup>2</sup>).

#### 4.2.3.2.2 Mass diffusivity

Besides mass convection, the diffusion is another kind of hydrocarbon transfer mechanism. Considering its absolute abundance in the CVD reactor, argon could be seen as the solvent of gas phase species. Correspondingly, other species would be solutes, which interact with argon molecules. Based on kinetic gas theory, the binary diffusion coefficient could be expressed as follows,

$$D_{AB} = 2.695 \cdot 10^{-3} \cdot \frac{\sqrt{T^3(M_A + M_B)(2 \cdot 10^3 M_A M_B)}}{p \sigma_A \sigma_B \Omega_D} \quad (4-13)$$

where  $D_{AB}$  is the binary diffusion coefficient (m<sup>2</sup> s<sup>-1</sup>),  $M$  is the molecular weight (kg mol<sup>-1</sup>),  $T$  represents the temperature (K),  $p$  is the pressure (Pa), and  $\sigma$  is the characteristic length (Å) of the Lennard-Jones (12-6) potential. In addition,  $\Omega_D$  is the collision integral, given by the following equation<sup>[296]</sup>:

$$\Omega_D = A(T^*)^{-B} + C[\exp(-DT^*)] + E[\exp(-FT^*)] + G[\exp(-HT^*)] + \frac{0.19\delta_{AB}^2}{T^*} \quad (4-14)$$

with  $T^* = k_b \frac{T}{(\epsilon_A \epsilon_B)^{1/2}}$ ,  $\delta_{AB} = (\delta_A \delta_B)^{1/2}$ ,  $\sigma_{AB} = (\sigma_A \sigma_B)^{1/2}$ , and  $\delta = \frac{1}{2} \frac{\mu^2}{\epsilon \sigma^3}$ .

where  $\epsilon$  is the maximum depth of the potential well,  $\sigma$  is the characteristic length, and  $\mu$  is the species dipole moment (Debye). These values are listed in table 9. As the solvent approximation is used for gases, the binary diffusivity is used to calculate the diffusivity of species  $A$  in a solvent  $B$ .

Due to the difficulty in finding the parameters  $\epsilon$  and  $\sigma$  of ferrocene, the following formula proposed by Wang et al<sup>[297]</sup> was used to approximately evaluate these parameters.

$$\sigma = 1.236 M_w^{1/3} \quad (4-15)$$

$$\epsilon/k = 37.15 M_w^{0.58} \quad (4-16)$$

These formulas indicate the strong correlations between the LJ parameters of PAHs (polycyclic aromatic hydrocarbons) and their molecular weight.

**Table 9.** The Lennard-Jones (12-6) potential parameters

Substance	Index <sup>a</sup>	Potential well depth	collision diameter Å	Dipole moment Debye	Molar mass (Kg mol <sup>-1</sup> )
Ar	0	136.500	3.330	0.000	$4 \times 10^{-2}$
H <sub>2</sub>	1	38.000	2.920	0.000	$2 \times 10^{-3}$
CH <sub>4</sub>	2	141.400	3.746	0.000	$1.6 \times 10^{-2}$
C <sub>2</sub> H <sub>2</sub>	1	265.300	3.721	0.000	$2.6 \times 10^{-2}$
C <sub>2</sub> H <sub>4</sub>	2	238.400	3.496	0.000	$2.8 \times 10^{-2}$
C <sub>4</sub> H <sub>2</sub>	1	357.000	4.720	0.000	$5 \times 10^{-2}$
CH <sub>2</sub> CHCCH	2	373.700	4.790	0.000	$5.2 \times 10^{-2}$
C <sub>5</sub> H <sub>6</sub>	1	408.000	5.200	0.000	$6.6 \times 10^{-2}$
C <sub>6</sub> H <sub>6</sub>	2	468.500	5.230	0.000	$7.8 \times 10^{-2}$
C <sub>7</sub> H <sub>8</sub>	2	523.600	6.182	0.43	$9.2 \times 10^{-2}$
C <sub>8</sub> H <sub>10</sub>	2	523.600	5.960	0.000	$1.06 \times 10^{-1}$
<sup>b</sup> Fe(C <sub>5</sub> H <sub>5</sub> ) <sub>2</sub>	-	769.72	7.056	-	$1.86 \times 10^{-1}$
Fe	-	3000	4.3	-	$5.6 \times 10^{-2}$

<sup>a</sup>: an index indicating whether the molecular has a monatomic(0), linear (1)or nonlinear(2) geometrical configuration. <http://maeweb.ucsd.edu/~combustion/cermech/sandiego20021001.trans>

<sup>b</sup>: Values evaluated using the formulas proposed by Wang et al<sup>[297]</sup>.

#### 4.2.3.2.3 Thermal conductivity

Besides thermal convection, thermal conduction is another energy transfer mechanism inside the reactor which contains the temperature gradient. According to the Stiel-Thodos equation<sup>[298]</sup>, the thermal conductivity of species is expressed as follows,

$$k = \frac{\eta}{M} (1.15C_p + 0.88R_g) \quad (4-17)$$

where  $k$  is the thermal conductivity ( $\text{W m}^{-1} \text{K}^{-1}$ ), and  $C_p$  denotes the heat capacity ( $\text{J mol}^{-1} \text{K}^{-1}$ ).

### 4.3 Modeling of gas phase reaction kinetics

#### 4.3.1 Governing equations

In order to develop a relatively robust model which can well describe the transport and kinetics of chemical species, one needs to solve the set of governing equations for transport of momentum and mass, and energy in a chemically reacting flow. Given the symmetry of the reactor and the continuous mass feeding, the reacting fluid is described by the 2d stationary momentum, mass and heat balance equations 4-18 to 4-21. The resolution of these equations is carried out using the commercial computational software COMSOL®.

First, the fluid flow is described by the weakly compressible Navier-Stokes equations:

$$\rho(\mathbf{u} \cdot \nabla)\mathbf{u} = \nabla \cdot [-p\mathbf{I} + \eta(\nabla\mathbf{u} + (\nabla\mathbf{u})^T) - (2\eta/3)(\nabla \cdot \mathbf{u})\mathbf{I}] \quad (4-18)$$

$$\nabla \cdot (\rho\mathbf{u}) = 0 \quad (4-19)$$

where  $\mathbf{u}$  is the velocity vector,  $\mathbf{u}=(u, v)$  ( $\text{m s}^{-1}$ ),  $\eta$  denotes the dynamic viscosity( $\text{N s m}^{-2}$ ),  $\rho$  is the density of the fluid ( $\text{kg m}^{-3}$ ), and  $p$  is the pressure(Pa).

The boundary conditions for the gas flow are :

$$\mathbf{u} \cdot \mathbf{n} = u_0 = 0.01 \text{ m/s} \quad \text{Inlet}$$

$$\mathbf{u} = \mathbf{0} \quad \text{Walls and quartz plate}$$

$$p = p_0 = 1.0 \times 10^5 \text{ Pa}$$

$$[\eta(\nabla\mathbf{u} + (\nabla\mathbf{u})^T) - (2\eta/3)(\nabla \cdot \mathbf{u})\mathbf{I}] \cdot \mathbf{n} = 0 \quad \text{Outlet (pressure, no viscous stress)}$$

Second, the mass transfer in the reactor is given by the convection-diffusion equation:

$$\nabla \cdot (-D\nabla c_i) = R_i - \mathbf{u} \cdot \nabla c_i \quad (c_i = \text{concentration}) \quad (4-20)$$

where  $D_i$  denotes the diffusion coefficient ( $\text{m}^2 \text{s}^{-1}$ ), and  $R_i$  is the reaction term ( $\text{mol m}^{-3} \text{s}^{-1}$ ).

The corresponding boundary conditions are as follows:

$$c_i = c_{i,0} \quad \text{inlet}$$

$$\mathbf{n} \cdot (-D_i \nabla c_i) = 0 \quad \text{outlet}$$

$$\mathbf{n} \cdot \mathbf{N}_i = c_i \mathbf{u} \cdot \mathbf{n}$$

here, the initial molar concentrations of the injected species are as follows:  $c_{\text{H}_2,0}=4.46 \text{ mol m}^{-3}$ ,  $c_{\text{C}_8\text{H}_{10},0}=1.62 \text{ mol m}^{-3}$ ,  $c_{\text{C}_2\text{H}_2,0}=0.446 \text{ mol m}^{-3}$ , and  $c_{\text{FeC}_10\text{H}_{10},0}=5.38 \times 10^{-2} \text{ mol m}^{-3}$ .

Third, the energy balance in the reactor is described by the convection and conduction equation:

$$\nabla \cdot (-k \nabla T) = Q - \rho C_p \mathbf{u} \cdot \nabla T \quad (\text{T=Temperature}) \quad (4-21)$$

where  $C_p$  denotes the specific capacity ( $\text{J kg}^{-1} \text{ K}^{-1}$ ),  $k$  is the thermal conductivity ( $\text{W m}^{-1} \text{ K}^{-1}$ ), and  $Q$  is the heat source term ( $\text{W m}^{-3}$ ). As the heat  $Q$  of the chemical reactions (R11-R20) is very weak, therefore it is neglected in this simulation.

The used boundary conditions are as follows:

$$T = T_0 \quad \text{inlet}$$

$$T = T_{\text{surf}} \quad \text{Tube surface}$$

$$\mathbf{q}_{\text{cond}} \cdot \mathbf{n} = -k \nabla T \cdot \mathbf{n} = 0 \quad \text{outlet}$$

$$\mathbf{q} \cdot \mathbf{n} = -\rho C_p T \mathbf{u} \cdot \mathbf{n} \quad \text{outlet (convection flux boundary condition)}$$

where  $T_{\text{surf}}$  is an interpolation function of the temperatures measured along the quartz tube wall (as shown in table 10).

**Table 10.** Temperature values measured along the length of the reactor wall at different given temperatures.

Distance(m)	Temperature distribution(°C)					
	780	700	650	600	550	450
0.57	736	658	601	554	480	375
0.52	761	681	631	580	518	414
0.47	774	693	641	591	538	434
0.42	780	699	647	597	545	444
0.37	786	703	653	602	552	452
0.32	789	705	657	605	557	459
0.27	787	704	657	604	557	460
0.22	780	697	651	596	551	455
0.17	770	690	645	587	543	449
0.12	749	672	628	569	521	422
0.07	718	631	592	536	476	383
0.02	650	572	509	459	402	317

### 4.3.2 Isothermal reaction kinetics

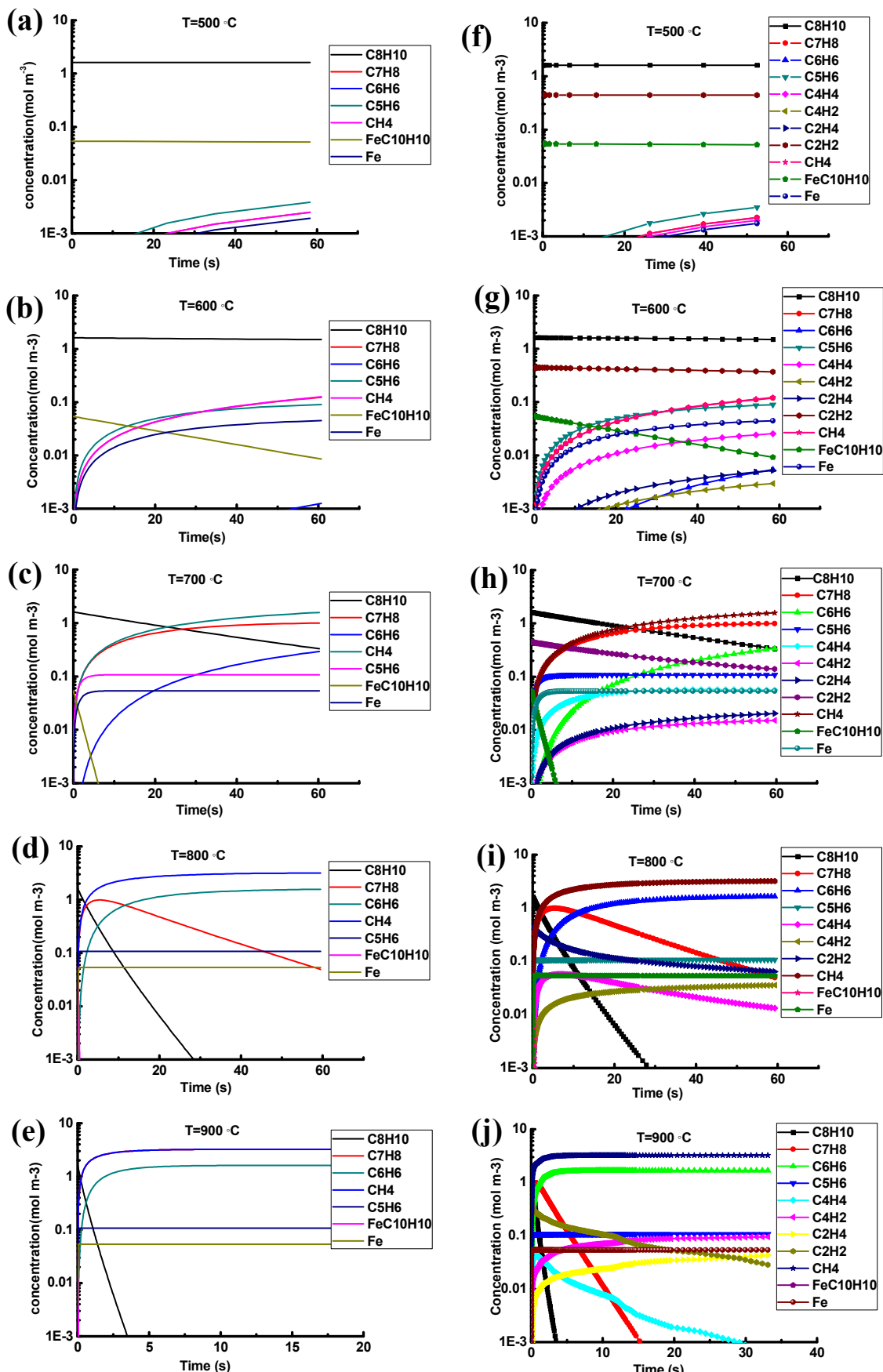


**Figure 91.** Isothermal decompositions of the ferrocene-xylene vapor without (a-e) and with (f-j) acetylene at the temperatures of 500, 600, 700, 800 and 900 °C.

Figures 91a-e show the isothermal decomposition kinetics of the ferrocene-xylene vapor in a perfectly mixed reactor at temperatures from 500 to 900 °C. The calculations are based on the global decomposition mechanisms given in table 7. The same initial concentrations of species are applied for the different temperatures, that is,  $1.62 \text{ mol m}^{-3}$  for xylene,  $5.38 \times 10^{-2} \text{ mol m}^{-3}$  for ferrocene,  $4.46 \text{ mol m}^{-3}$  for hydrogen, and  $40 \text{ mol m}^{-3}$  for argon. The species residence time is  $\sim 60 \text{ s}$  when the flow rate of carrier gas is equal to  $1 \text{ l min}^{-1}$ . It could be seen that temperature has considerable influences on the decomposition kinetics of xylene and ferrocene. This indirectly indicates that in real CVD reactors the temperature variation certainly results in the variation of the relative ratios of the species concentrations. The analysis on the reaction processes could help us to better understand the varied CNT growths at different temperatures.

At the temperatures lower than 600 °C (Fig. 91a-b), little xylene is decomposed during its residence in the reactor. The xylene decomposition ratio is less than 2 % at 500 °C, and < 8 % at 600 °C. Meanwhile, the ratio of decomposed ferrocene greatly increases from 3.5 % at 500 °C to 83 % at 600 °C. Xylene takes an important proportion in the gas atmosphere at these temperatures. The concentrations of methane and cyclopentadiene are greatly increased from 500 to 600 °C. At 700 °C, xylene has a large decomposition ratio,  $\sim 80 \text{ %}$  (Fig. 91c-d). At the same time, ferrocene is nearly completely decomposed in a short time. The major hydrocarbons in the gas phase are methane, toluene, benzene and residual xylene at this temperature. The major hydrocarbons become to methane and benzene generated from the decomposition of xylene and toluene. Methane and benzene are the absolutely-dominant species in the gas atmosphere at 900 °C (Fig. 91e), and ferrocene, xylene and toluene are completely decomposed in a very short time.

As a comparison, Fig. 91f-j show the corresponding reaction kinetics of the mixture of ferrocene-xylene vapor and acetylene at the same temperatures. The initial concentration of acetylene is  $0.045 \text{ mol m}^{-3}$ . A similar result is observed. Little amount of carbon sources (xylene and acetylene) are decomposed at 500 °C (Fig. 91f), and benzene and methane are two absolute dominant hydrocarbons in gas atmosphere at high temperatures, especially at 900 °C (Fig. 91j). However, within these two temperature limits, the decomposition of acetylene produces amounts of higher mass hydrocarbons such as diacetylene, vinylacetylene and benzene, as shown in Fig. 91g-i. The ratio of diacetylene gradually increases with temperature. Meanwhile, that of vinyl acetylene first increases and then decreases.

The comparison between the above analyses with the products obtained under the same conditions shows that CNT growth relies on the match between ferrocene decomposition rate and effective carbon source concentrations. High ferrocene decomposition rates at high temperatures makes it completely consumed in the front stage of furnace. This corresponds well with our experimental observation that the starting growth point of CNTs on the quartz plate draws back, and the length of the growth region shortens with the increase of temperature. The low CNT growth rates at 500 and 600 °C demonstrate that xylene was not a direct precursor for nanotube growth when it is used as carbon source. In contrast, acetylene could serve as a direct carbon precursor for CNT growth. This is indicated by the enhanced growth rates of CNTs when acetylene is added into the CVD system. This conclusion corresponds well with the results reported by Eres et al<sup>[299]</sup>.

### 4.3.3 Reaction kinetics in the CVD reactor

#### 4.3.3.1 Non-uniform mass transport

In fact, the decomposition of carbon and catalyst precursor is rarely uniform in real CVD reactors, especially in tube-like ones. The temperature gradient inside the reactor could generate varied chemical decomposition kinetics. In general, temperature distribution is greatly related to reactor geometry. Fig. 23 shows the variation of the tube wall temperatures along the reactor length. The non uniform temperature field will absolutely generate the variation of chemical reaction rates in the CVD system. This could result in the variation of relative ratios between the species. However, the coordination between the decomposition of carbon sources and ferrocene is of great significance to get the hybrid structures with homogeneous structures.

As we know, the CNT growth on  $\mu\text{Al}_2\text{O}_3$  follows the “bottom-up” mechanism. The carbon deposition mainly occurs on active catalyst particles located on the surface of alumina microparticles. Convection and diffusion are two mass transfer mechanisms involved in this process. They are responsible for the feeding of carbon and iron species for continuous CNT growth. Fig. 92a and b show the convective and diffusive fluxes of xylene and ferrocene at 700 °C, respectively. It is found that in the center region of the reactor the chemical species are principally transported forwards by gas convection. On the other hand, the species principally exchange through mass diffusion in radial directions, owing to concentration gradients. In particular, the diffusion dominates the mass transport in the layer near substrate surface, where the gas flow rate is very weak. These could be easily explained by the specific distributions of gas fluid velocity inside the CVD reactor, as well as the temperature field, as shown in Fig. 93a

and b. The fluid has the highest flow rate in the center region, but a weak one in regions near the tube inner wall and quartz plate due to viscosity interaction. The non-isothermal characteristic of the reactor displays the varied temperature gradients in the reactor, especially in the inlet and outlet regions. These differences would ultimately result in varied species concentration fields, which further influence nanotube formation and growth rate.

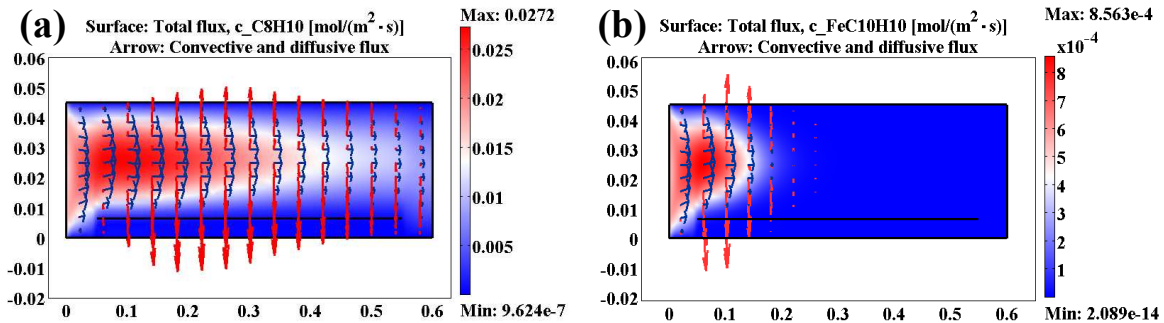


**Figure 92.** Convective and diffusive transport of xylene (a) and ferrocene (b) at 700 °C

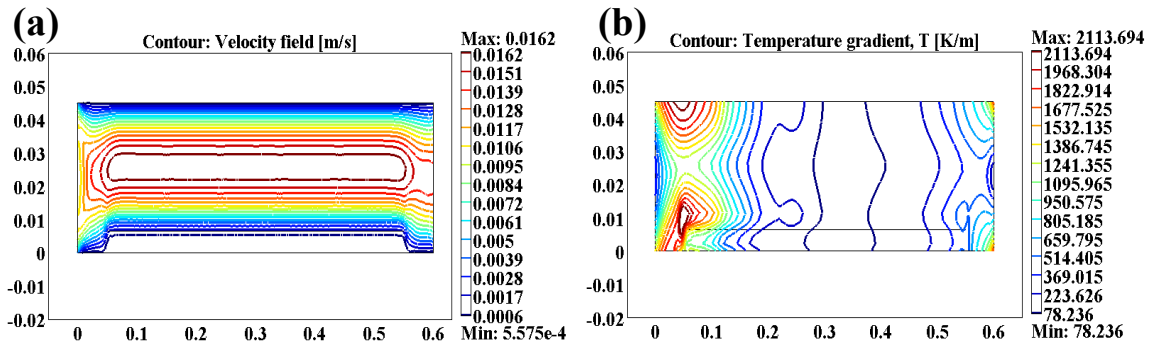


**Figure 93.** Velocity field (a) and temperature gradient (b) inside the CVD reactor heated at the given temperature of 700 °C.

#### 4.3.3.2 Chemical species concentration fields

##### 4.3.3.2.1 Comparisons between experimental measurement and simulation

Before discussion on the concentration distribution of the chemical species in the reactor space, we conduct a comparison between MS measurements and simulation results. Fig. 94a shows the concentration variations of xylene in the exhaust gas with temperature. The concentrations obtained from experiment and simulation have a similar variation tendency with the increase of temperature. A good agreement is obtained between the two results when the temperature is lower than 700 °C. The increasing differences at higher temperatures could be

due to the fact that this simulation does not take into account carbon decomposition reactions on the substrate surface. The intensified surface reactions at high temperatures result in the enlargement of the difference between the experiment and simulation results. Fig. 94b shows the variations of xylene and acetylene concentrations at the end of the reactor with temperature. Moreover, the experiment and simulation share a similar variation tendency of the xylene and acetylene concentrations.

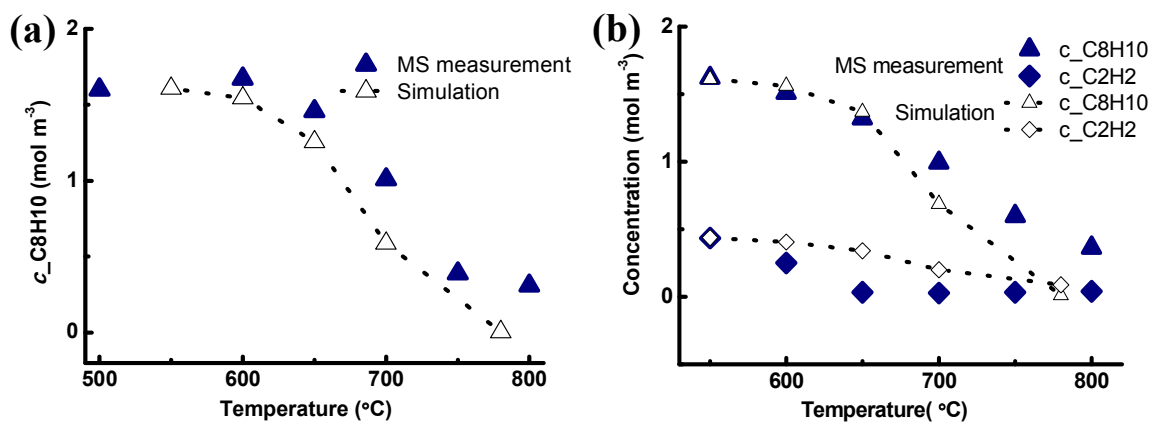


**Figure 94.** Comparisons of the carbon source concentrations obtained by MS measurements and simulations. (a) Decomposition of xylene at different temperatures, and (b) decomposition of xylene and acetylene.

The above analyses demonstrate that the simulation model could generally describe the consumptions of carbon and catalyst precursors under our experiment conditions. It could be used to predict the variation tendency of the chemical species.

#### 4.3.3.2.2 Xylene as carbon source

Figure 95 demonstrates the concentration distribution of the main chemical species involved in the decomposition of ferrocene-xylene solution at different temperatures. The reactor geometry is schematically shown in Fig. 95a. The concentration variations along the centerline are displayed in Fig. 95b. Both xylene and ferrocene have very low decomposition rates at 550 °C. Little xylene and ferrocene are decomposed in the first stage of the reactor. It is at the position of ~ 0.2 m where the concentrations of  $\text{C}_7\text{H}_8$ ,  $\text{C}_5\text{H}_6$ ,  $\text{CH}_4$  and  $\text{Fe}$  reach up to 0.001 mol m<sup>-3</sup>. From this point, these species concentrations gradually increase with the distance, and finally reach to the maximum value of ~ 0.01 mol m<sup>-3</sup> in the region near the outlet. This result corresponds very well with our experimental observations at 550 °C. That is, CNTs grow in a

very weak rate on  $\mu\text{Al}_2\text{O}_3$  (Fig. 27a), and the growth is only observed on the microparticles located in the zone farther than 0.2 m. At 600 °C, the decomposition ratio of ferrocene greatly increases, compared with the one of xylene. The position corresponding to the concentration of 0.001 mol m<sup>-3</sup> moves towards the inlet. Little benzene is produced at this temperature from the xylene decomposition. When the temperature is increased above 700 °C, the decomposition rate of ferrocene is so high that it is quickly decomposed in the first stage of the reactor. In the zone after ~ 0.23 m at 700 °C and ~ 0.12 m at 800 °C, the ferrocene concentration becomes very weak, lower than 0.001 mol m<sup>-3</sup>. In addition, the decomposition of xylene is greatly accelerated above 700 °C. The increased decomposition of toluene generates large amounts of benzene at the end of reactor. The dominant species in the exhaust gas are toluene and methane at 700 °C, whereas, they are benzene and methane at 800 °C. By comparison, the species concentration distributions along the line near quartz plate surface are given in Fig. 95c. The concentration variation tendency with temperature is found similar to the one along the centerline. However, due to the slow gas flow rates, higher decomposition rates of ferrocene and hydrocarbons are found in the region near the quartz plate surface, than that in the reactor center. In consequence, the product species such as methane, benzene, toluene and iron have relatively high concentrations.

Figure 95d shows the space-dependent concentration distribution of the main chemical species such as  $\text{C}_8\text{H}_{10}$ ,  $\text{C}_7\text{H}_8$ ,  $\text{C}_6\text{H}_6$ ,  $\text{CH}_4$ ,  $\text{FeC}_{10}\text{H}_{10}$ , and  $\text{Fe}$ . Obviously, each chemical species has a specific concentration distribution field. For a given temperature, the relative ratios of the species vary with the space position. Likewise, in the same space region, the variation of the temperature field also makes a considerable change of the species concentration ratios.

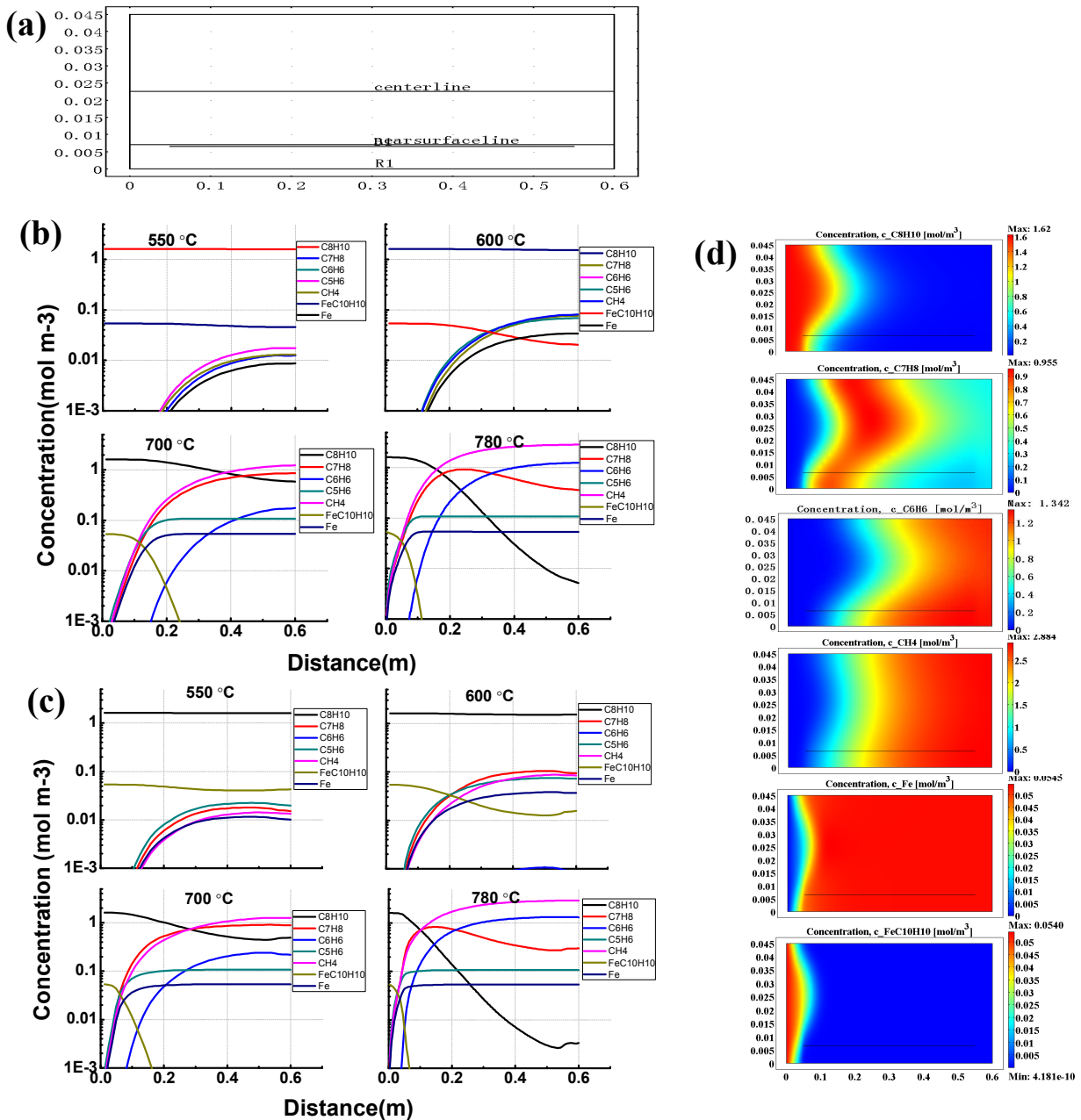


**Figure 95.** (a) CVD reactor geometry and the positions of the centerline and the line near quartz plate surface (5 mm above the plate surface). The length unit is m. Concentration distribution: (b) along the centerline and (c) along the line near quartz plate surface. (d) Surface graph of concentration distribution of the main chemical species at 780 °C.

#### 4.3.3.2.3 Xylene and acetylene as carbon sources

Figure 96a and b show the temperature-dependent species concentration distributions along the centerline and the near surface line, respectively. The addition of acetylene in the system shows little influence on the gas phase decompositions of ferrocene and xylene, which accelerate with the increase of temperature. In particular, ferrocene tends to be consumed in the beginning zone of the reactor at high temperatures. However, due to its high chemical activity, acetylene could efficiently contribute carbon to CNT growth. Therefore, its addition in the system provides more effective carbon sources. This effect is demonstrated by enhanced CNT growth at temperatures lower than 550 °C. Moreover, the addition of acetylene makes the CNT deposition region draw back about 10-15 cm on the quartz plate, compared with the CNT deposition without acetylene. This indicates a very small decomposition ratio of ferrocene could generate CNT growth in the presence of acetylene. As shown in Fig. 96a and b, the pyrolysis of acetylene produces low concentration C<sub>4</sub>H<sub>4</sub> in the end zone of reactor at 550 °C. Besides C<sub>4</sub>H<sub>4</sub>, other acetylene pyrolysis species such as C<sub>4</sub>H<sub>2</sub> and C<sub>6</sub>H<sub>6</sub> also exhibit an increase in their concentrations when the temperature is higher than 600 °C. Especially, their concentrations in the front of reactor considerably increase at the higher temperatures. The species concentration distributions in the reactor are displayed in Fig. 96c. As indicated previously, the chemical reactions are non-isothermal process in the reactor, and the concentration distribution of each species is space-dependent at a given temperature.

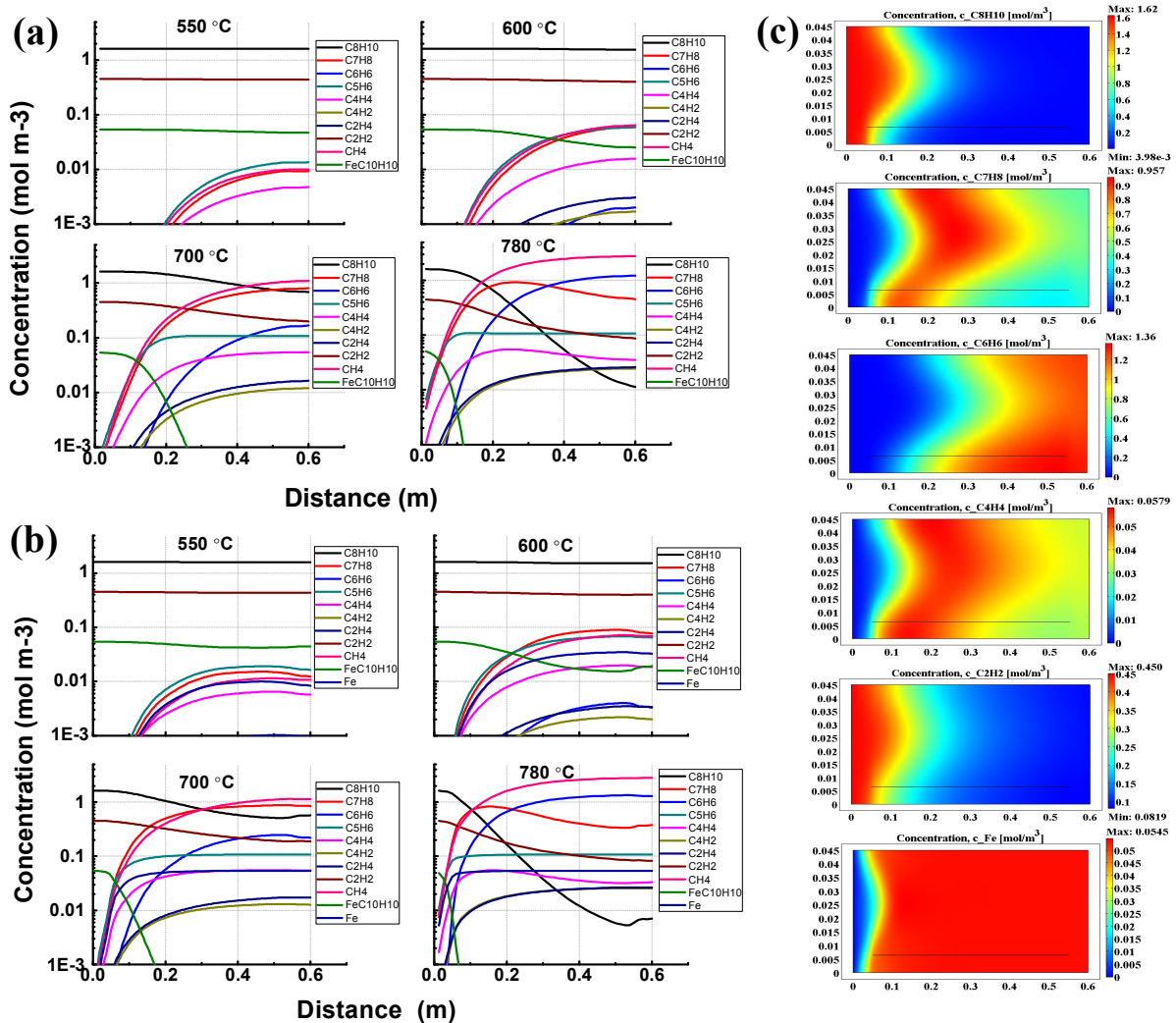


**Figure 96.** Chemical species concentration distributions along the centerline (a), and the near surface line (b) obtained by simulation of the decompositions of the mixture of xylene and acetylene at different temperatures. (c) Surface graph of concentration distribution of the main chemical species at 780 °C.

#### 4.3.3.3 Effective Iron and carbon species distribution

In the chapter III, we have demonstrated that ferrocene concentration has considerable impact on CNT growth and organization on  $\mu\text{Al}_2\text{O}_3$ . Different hybrid structures are obtained by varying Fe/C ratios in feedstock. However, all the carbon containing species are not effective carbon sources which efficiently contribute carbon atoms for CNT growth. In the formation of pyrocarbon, the light unsaturated species (e.g. C<sub>2</sub>H<sub>2</sub>) and methyl radicals were reported to be more efficient for the carbon deposition<sup>[300]</sup>. Moreover, different kinds of hydrocarbons have varied dehydrogenation properties on iron catalyst particles, and thus generate varied CNT growth rate. Therefore, it is desired to find out the dominant effective hydrocarbons in CNT growth process. At the same time, the iron in the reactor exists under

several forms, including decomposed iron atoms and non-decomposed iron compounds. Understanding of the role of these iron existences in CNT growth is of great significance to improve the yield of the hybrid materials with uniform structures.

The difference between the simulation concentration value and the MS measured one of each chemical species could give clues about the hydrocarbon efficiency for CNT growth. Because the carbon decomposition on the quartz tube wall and substrate surface is not taken into account of the simulation. Therefore, the chemical species having large concentration difference are extremely possible to contribute more carbon atoms during CNT growth. Figure 97a shows an increasing difference between the concentrations measured and simulated of each chemical species with increasing temperature, when xylene is used as carbon source. In particular, the measured concentrations of toluene and benzene are very weak, in contrast to evident simulation values. It indicates that the species from xylene decomposition are more efficient to CNT growth than xylene itself. The increased toluene, benzene and methane concentrations in the reactor correspond well the increased CNT growth rates at high temperatures. A similar phenomenon is also found when the mixture of acetylene and xylene is used as carbon source, as shown in Fig. 97b. The measured concentrations of acetylene are smaller than the simulated ones at different temperatures. This corresponds well to our observation that the addition of acetylene accelerates the CNT growth even at relatively low temperatures.

An incubation period is observed to accumulate sufficient amount of effective carbon sources which have concentrations high enough to promote CNT nucleation and growth, as shown in Fig. 91. The period duration is greatly dependent on the reaction temperature. Correspondingly, as shown in Fig. 95 and 96, there contains low concentrations of chemical species derived from the xylene decomposition in the first stage of the reactor. The concentrations greatly increase in the region far from the inlet. The increase of temperature results in the decrease of the shortest distances where the decomposition-generated species have a concentration of  $0.001 \text{ mol m}^{-3}$  (Fig. 95 and 96). This is one of the reasons why the deposition of CNTs occurs only on the microparticles located in the region far from the front of quartz plate. The increased temperatures generate the starting deposition point of CNTs moves toward the inlet of the reactor.

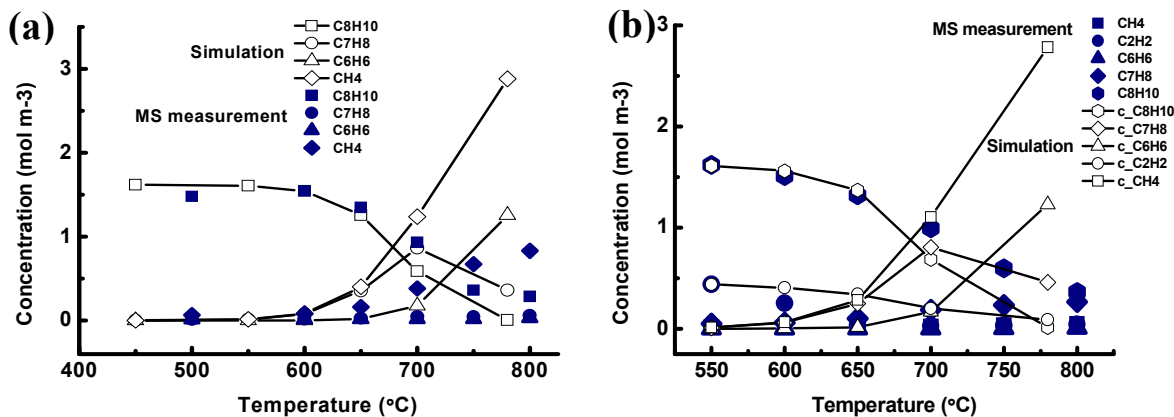


**Figure 97.** Comparisons of main chemical species concentrations obtained by MS measurements and simulation: (a) xylene as carbon source, and (b) xylene and acetylene as carbon sources.

On the other hand, the nucleation of iron catalyst particles is derived from the decomposition of ferrocene. Iron originates from iron atoms from the decomposition of ferrocene in gas phase, as well as the surface reaction of iron containing compounds. It is observed that CNT quantity is gradually decreased with the increase of the distance inside the reactor. Beyond certain distance, no CNT growth is found. The CNT decomposition region shrinks with increasing temperature. This phenomenon becomes more evident at high temperatures, as demonstrated in Fig. 53.

However, iron concentration inside the reactor increases along the tube length at the temperatures ranging from 450 to 800 °C. Figure 98a shows the concentration field of iron generated from the decomposition of ferrocene at different temperatures. The concentration variation tendency with temperature could be clearly seen. Iron concentration in the front part of the reactor increases with temperature. At a given temperatures, for example at 600 °C, the iron concentration is gradually augmented with the distance. Ferrocene has a high decomposition rate at temperatures higher than 700 °C. The decomposed iron could be quickly transferred forwards thanks to the convective gas flow. The distribution of the iron and ferrocene concentrations along the centerline of the reactor is demonstrated in Fig. 98b.

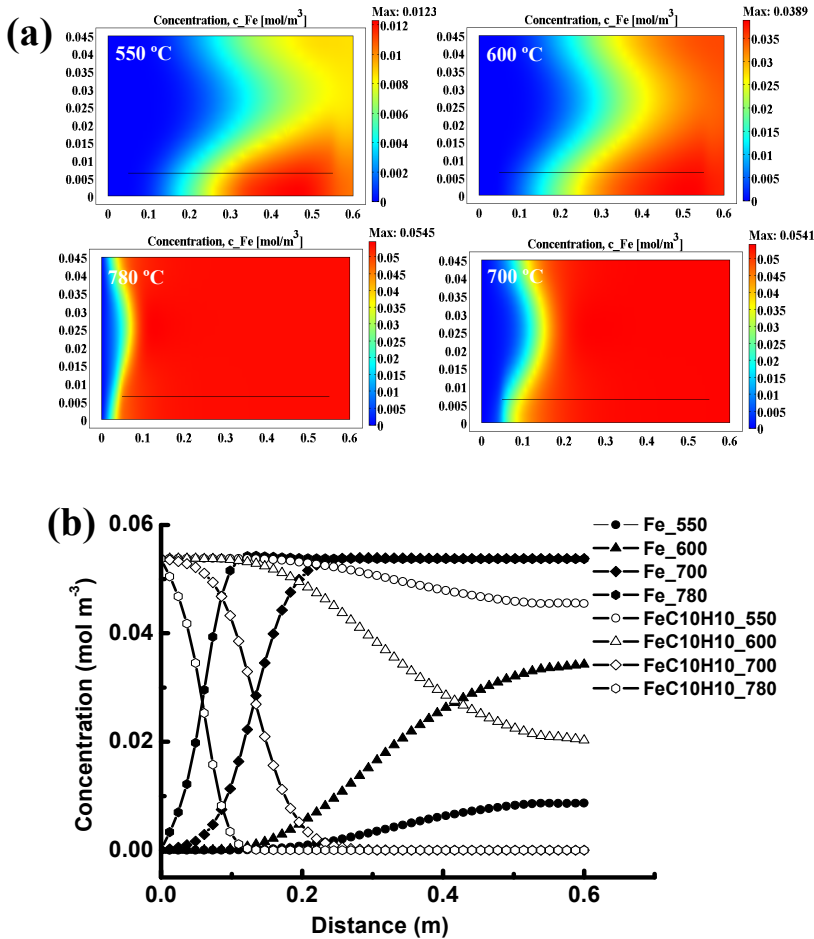


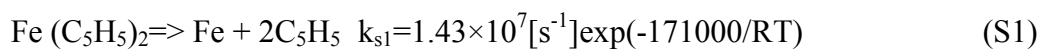
**Figure 98.** (a) Iron concentration fields at the temperatures from 450 to 780 °C. (b) Variation of iron and ferrocene concentrations along the axis of the quartz tube with the increase of temperature.

It is commonly believed that high iron concentrations in gas phase could promote the growth of CNTs with a high rate. However, our experiments demonstrate that after the starting growth point, CNT deposition decreases with the distance. That is, CNTs grown in the front part of the reactor have high number density and large length, whereas, CNTs have lower number density and small length in the latter part, accompanied with carbon encapsulated iron particles. In particular, no CNTs could be found at the last stage ( $l \geq 0.3$  m) at the high temperatures. X-ray fluorescence analysis (table 11) also shows the decreased quantity of iron deposited on the  $\mu\text{Al}_2\text{O}_3$  with the increase of the distance. A quantity of 0.2 g of ferrocene was vaporized at the entrance of quartz tube with a temperature around 250 °C. The reactor temperature was set to 600 °C. The flow rate of carrier gas is  $1\text{ l mn}^{-1}$ , including 90 % Ar and 10 % H<sub>2</sub>. Before the examination, the alumina microparticles collected at different positions are heated to 600 °C in air in order to burn out the decomposed carbon.

**Table 11.** Percentage of iron deposited on alumina microparticles located on different position

Position (m)	0.3	0.4	0.5
Fe percentage (No C <sub>2</sub> H <sub>2</sub> )	0.24%	0.14%	0.14%
Fe percentage (C <sub>2</sub> H <sub>2</sub> 10 ml min <sup>-1</sup> )	1.3%	1.3%	0.14%

The above results demonstrate the quantity of iron deposited on the microparticles is not proportional to the iron in gas phase. Indeed, the bottom-up CNT growth mechanism in floating CVD indicates the fact that catalyst particles are formed on substrate surface rather than in gas phase when the temperature is lower than 800 °C. The iron particles are preferentially nucleated at certain active sites on  $\mu\text{Al}_2\text{O}_3$ , by mass diffusion of the iron atoms generated from the decomposition of ferrocene. Once the catalyst particles are formed, they could serve as active sites for the further decomposition of iron and carbon, owing to their higher catalytic activity than substrate materials. Dyagileva et al<sup>[301]</sup> studied the thermal decomposition of iron metallocenes in vacuum. It was found that the metallocene pyrolysis in a closed system was a homogeneous-heterogeneous process occurring both in a volume and on a surface. The catalytic activity of solid decomposition products was observed at the temperature as low as 673 K. and a first-order decomposition of ferrocene was assumed at particle surface with the rate constant,  $k_{\text{surf}}=1.43\times10^7[\text{s}^{-1}]\exp(-171000/RT)$ . Kuwana and Saito<sup>[295]</sup> have used the above surface chemical reaction constant to simulate the iron nanoparticle formation from ferrocene in the CVD reactor.



It could be seen that the catalytic surface decomposition reactions have a much higher rate than the gas phase decomposition. Moreover, ferrocene has a decreasing concentration with the distance. For instance, the residual ferrocene is more than the decomposed one in the first 0.4 m of the reactor at 600 °C. Therefore, it is greatly reasonable to say that the ferrocene decomposes on the formed iron catalyst particles to release iron atom. The increased iron feeding rate accelerates the carbon deposition on substrate surface from gas-phase hydrocarbons, and thus promotes the CNT growth. On the other hand, ferrocene has low concentration in the last stage of the reactor. The feeding of iron to catalyst particles is mainly from the adsorption/absorption of iron generated in gas phase though mass diffusion. So slow renewability of iron catalyst greatly limits dehydrogenization of the hydrocarbons, and thus results in a weak CNT growth rate. Specially, the fast decomposition of ferrocene at high

temperatures could generate high iron concentrations, which promote the direct nucleation of iron particles in the gas phase. In consequence, the iron could easily nucleate as small particles during their transport process. These particles directly catalyze the decomposition of hydrocarbons on their surfaces. When the temperature is not favorable to CNT nucleation, these iron particles are covered by a thin carbon layer. In particular, the carbon encapsulated iron particles are largely observed when the ferrocene-xylene solution is decomposed at 900 °C.

Therefore, we could conclude that the decomposition of ferrocene on the catalyst particle surface is of great importance for acceleration of CNT growth.

The non-uniform hybrid structures are mainly resulted from the heterogeneous CNT growth in different stages of the reactor. The non-isothermal condition, along with the concentration gradient of each chemical species, generates varied CNT growth kinetics inside the reactor. The proposed numerical simulation could describe the general variation tendency of each chemical species concentration with temperature. This is a very helpful tool to get a better understanding of the chemical gas-phase reactions in CVD process.

#### ***4.3.4 Two end injections of the ferrocene-xylene solution***

The previous analyses demonstrate that more catalyst particles nucleate in the front of reactor than in the end part when the temperature is higher than 600 °C. However, a temperature higher than 700 °C is required to the formation of the “urchin-like” structures. But, these structures could only be obtained in a very short zone in the front of the reactor when the used temperature is more than 750 °C. So the hybrid structure yields are very low.

According to our simulation results, high CNT growth rates are due to the accelerated iron feeding by catalytic ferrocene decomposition on the surface of the formed catalyst particles. And, low ferrocene concentrations and increased gas phase iron nucleation at high temperatures do not favor the CNT formation in the back region of the reactor. In order to improve the yields of the hybrid structures, the ferrocene-xylene solution is injected from the two ends of the quartz tube, as schematically shown in Fig. 99. Ferrocene is dissolved in xylene with a concentration of 0.05 g ml<sup>-1</sup>. The solution feeding rate is ~0.2 ml min<sup>-1</sup>. Two carrier gas flows at an equal rate of 1 l min<sup>-1</sup> are also injected from two ends of the reactor in order to carry forwards the xylene solution. Here, each gas flow is constituted of Ar (90 %)

and H<sub>2</sub> (10 %). The decomposition of the catalyst and carbon precursors lasts for 10 min at 780 °C.

Figure 99b-c shows the CNTs- $\mu$ Al<sub>2</sub>O<sub>3</sub> hybrid structures obtained by injecting the ferrocene-xylene solution from two ends of the reactor. The atmosphere temperatures around the spray heads are ~ 250 °C. The CNTs have a length around 25 μm for 10 min growth. And, the CNT diameter varies in the range of 25-60 nm. It is found that the homogeneity of the hybrid structures on the quartz plate is improved compared with the previous “one-end injection” method. It is also observed that the hybrids have better structures in the regions near the two ends of quartz plate than those in the center region. This is because the low gas circulation in the reactor center results in the low catalyst and carbon precursor feeding rate.

Interestingly, another kind of hybrid structure is also obtained by the “two-end injection” method during our studies. The two carrier gas flows have a equal rate of 0.9 l min<sup>-1</sup>, and the atmosphere temperature around the spray heads is ~ 400 °C. Similarly, the hybrids collected in two end regions of quartz plate have homogenous structures. As shown in Fig. 99d-e, the CNT in this hybrid structure are capped by one catalyst particle at each end. One of them locates on the surface of  $\mu$ Al<sub>2</sub>O<sub>3</sub>, forming a connection between the CNT and microparticle. The other one freely suspends in atmosphere. High magnification SEM image (Inserted image in Fig. 99e) reveals that the particles possess regular crystal forms, rather than the spherical shape. As far as we know, it has not been reported in literature the large scale synthesis of CNTs with two ends capped by catalyst particles. This structure could provide an easy way to create novel CNTs-based hybrid structures. For instance, CNT-CNT joint could be largely created by CVD, which could be used in fields of electronics. In addition, 3D CNT network with strong connection could be easily developed based on these CNTs. This kind of materials has great application potential in the composites with multifunctional properties.

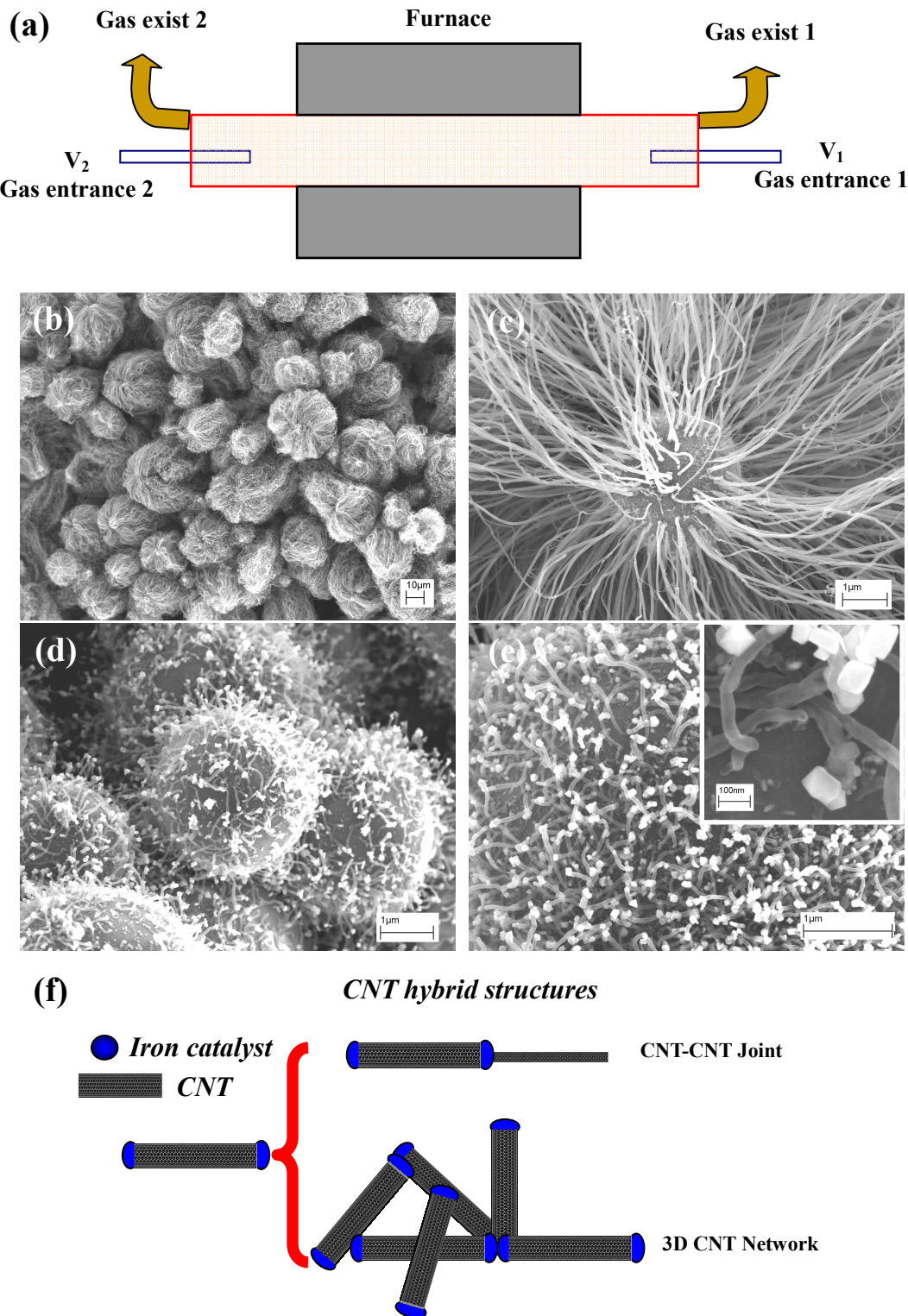


**Figure 99.** (a) Schematic of CVD equipment for the synthesis of CNTs- $\mu\text{Al}_2\text{O}_3$  hybrids by a “two end injection” method. SEM images of CNTs- $\mu\text{Al}_2\text{O}_3$  hybrid structures: (b-c) spray head temperature around 250 °C; (d-e) spray head temperature around 400 °C; (f) Schematic of two kinds of novel CNT hybrid structures (CNT-CNT Joint and 3D CNT network) based on CNTs with iron particles at two ends.

#### 4.4 Conclusion

In this chapter, gas phase chemical reaction kinetics in CVD reactor is numerically analyzed. The non-equilibrium CVD processes containing multi physical-chemical phenomena are simulated by combining chemical reaction kinetics with physical transport phenomena. The numerical model takes into account the influences of the reactor geometry, CVD parameters, chemical reactions, and mass and energy transports.

A global gas phase chemical reaction model is applied based on the MS measurements of the exhaust gases under various experiment conditions. This model could well describe the main decomposition characteristics of xylene, ferrocene and acetylene in the used temperature range. It is demonstrated that the temperature has considerable influences on kinetics of the isothermal decomposition of catalyst and carbon precursors in a perfectly mixed reactor. Due to the temperature gradient in the CVD reactor and the specific mass transfer mechanisms, the space-dependent concentration distribution of each species is revealed by simulating the reacting fluids. Moreover, the variations of concentration fields with temperature are separately discussed according to the presence or the absence of acetylene in the reactor system. It is found that low ferrocene and xylene decomposition ratios in the front of the reactor are not favorable to catalyst nucleation and CNT growth at low temperatures. On the other hand, high temperatures generate fast decomposition of the precursors. Especially, ferrocene could be quickly consumed in a short distance when the temperature is more than 700 °C. The addition of acetylene can enlarge the CNT growth region at the temperatures lower than 600 °C, because the high chemical activity makes acetylene an efficient carbon sources for CNT growth, rather than xylene. The comparison between the experimental results and simulation ones indicates that catalytic decomposition of ferrocene can greatly accelerate the feeding of iron atoms to catalyst particles, and thus results in the CNT growth in a high rate. This well explains the fact that the deposition quantity of CNTs decreases along the distance. The improved homogeneity of the hybrid structures by a “two end injection” method further confirms the prediction of the simulation. In surprise, a novel kind of CNTs- $\mu$ Al<sub>2</sub>O<sub>3</sub> hybrid structures is also obtained, in which the CNT is capped by an iron crystal at its each end.



# General conclusion and perspectives

## ***General conclusion***

The objectives of this thesis were to develop a multifunctional hybrid material containing well-organized CNTs and micrometer alumina particles by CVD, to study the formation mechanisms of the multiform structures, and to investigate the involved chemical reaction kinetics in CVD reactor for large scale production of the desired hybrid structures in a controlled way. The main results obtained during this research are summarized into the following three categories.

### **➤ Multiform hybrid structures and their exceptional thermal conductivities:**

The hybrid materials consisting of carbon nanotubes and micrometer alumina particles were produced by floating CVD, using a mixture of acetylene and xylene as carbon sources, and ferrocene as catalyst precursor. Three distinct hybrid architectures are “short-dense-homogeneous”, “six-branch” and “urchin-like”. When the “urchin-like” CNTs- $\mu\text{Al}_2\text{O}_3$  was added as fillers in Epoxy, the CNTs- $\mu\text{Al}_2\text{O}_3$ /Epoxy composites had a remarkably low percolation threshold (0.15 wt % CNTs) and high thermal conductivity (130 % enhancement). The well-organized hybrid structures and homogeneous dispersion of CNTs result in a significant reduction of the thermal contact resistance between CNTs in the composites.

### **➤ Mechanisms of the CNT organizations on $\mu\text{Al}_2\text{O}_3$ for the formation of multiform hybrid structures:**

The formation of the CNTs- $\mu\text{Al}_2\text{O}_3$  hybrid structures are greatly dependent on the coordination between carbon and iron depositing rates, which is a result of the competitive interactions of various CVD parameters such as catalyst precursor, carbon sources, temperature, and hydrogen ratios. Low CNT nucleation and growth rates are generated by the low iron deposition rates which could be resulted from the low ferrocene concentrations in xylene solution, the slow feeding rates of the ferrocene-xylene solution or the small decomposition rates at low temperatures. The increase of the ferrocene decomposition rates with temperature promotes the formation of the “urchin-like” hybrid structures which are constituted of CNTs

with big diameters varying in a wide range. The carbon feeding rates are strongly related to the decomposition rates of xylene in the gas phase. Due to the high chemical stability of xylene, it is only at temperatures higher than 700 °C that a high growth rate of CNTs could be achieved when xylene is used as carbon sources. The addition of acetylene in the system greatly increases the CNT growth rates and area number densities even at temperatures lower than 600 °C. Moreover, acetylene promotes the homogenization of the size of catalyst particles, and improves their catalytic efficiency for CNT growth by a considerable reduction of the quantity of carbon-encapsulated iron particles as well as CNT-encapsulated ones. The presence of hydrogen in the CVD system prevents the oxidation of catalyst particles, and decreases the quantities of amorphous carbon particles formed during CNT growth. The high hydrogen ratios inhibit the dehydrogenation of the hydrocarbons on the catalyst particles. In addition, CNTs grow on the alumina microspheres in a linear way when the mixture of acetylene and xylene is used as carbon source.

CNTs in the “six-branch” hybrid structures organize into six orthogonal bundles on  $\mu\text{Al}_2\text{O}_3$ . The observation of these hybrid structures obtained using the heat-treated  $\mu\text{Al}_2\text{O}_3$  reveals that the growth of CNTs principally occurs at crystal step sites, which largely exist on the surface of the particles. The CNT organization varies with the orientation of the crystal steps. The specific surface structures potentially determine the growth of CNTs in six orthogonal directions. The directions of six orthogonal CNT bundles are normal to {0002} or {1-100} planes, according to the analysis of TEM selected area diffraction.

Besides, the self assembly of CNTs takes place during their growth, due to weak Van der Waals interaction forces between neighboring CNTs. The calculation based on the proposed nano-cantilever model shows that the CNT self assembly is greatly dependent on the diameter, length and area number density of CNTs on  $\mu\text{Al}_2\text{O}_3$ .

#### ➤ **Chemical reaction kinetics in the CVD reactor:**

The CVD processes containing multi physical-chemical phenomena are simulated by combining chemical reaction kinetics with physical transport phenomena. A global chemical reaction model is used to describe the main characteristics of the decomposition of xylene, ferrocene and acetylene in gas phase. The reaction kinetics is firstly calculated in a perfectly mixed reactor. Then, the space-dependent concentration distributions at different temperatures were established in the cases, where xylene or its mixture with acetylene is used as carbon source. The comparison between experimental and simulation results indicates that acetylene, along with the species decomposed from xylene, is efficient carbon source for CNT growth.

The catalytic decomposition of ferrocene greatly accelerates the deposition of iron atoms on the catalyst particles, and thus results in the CNT growth at high rates.

### ***Perspectives***

The multifunctional nano/micrometer hybrid structures developed in this thesis have promising applications in the field of composites. The following aspects would be interesting for the future research:

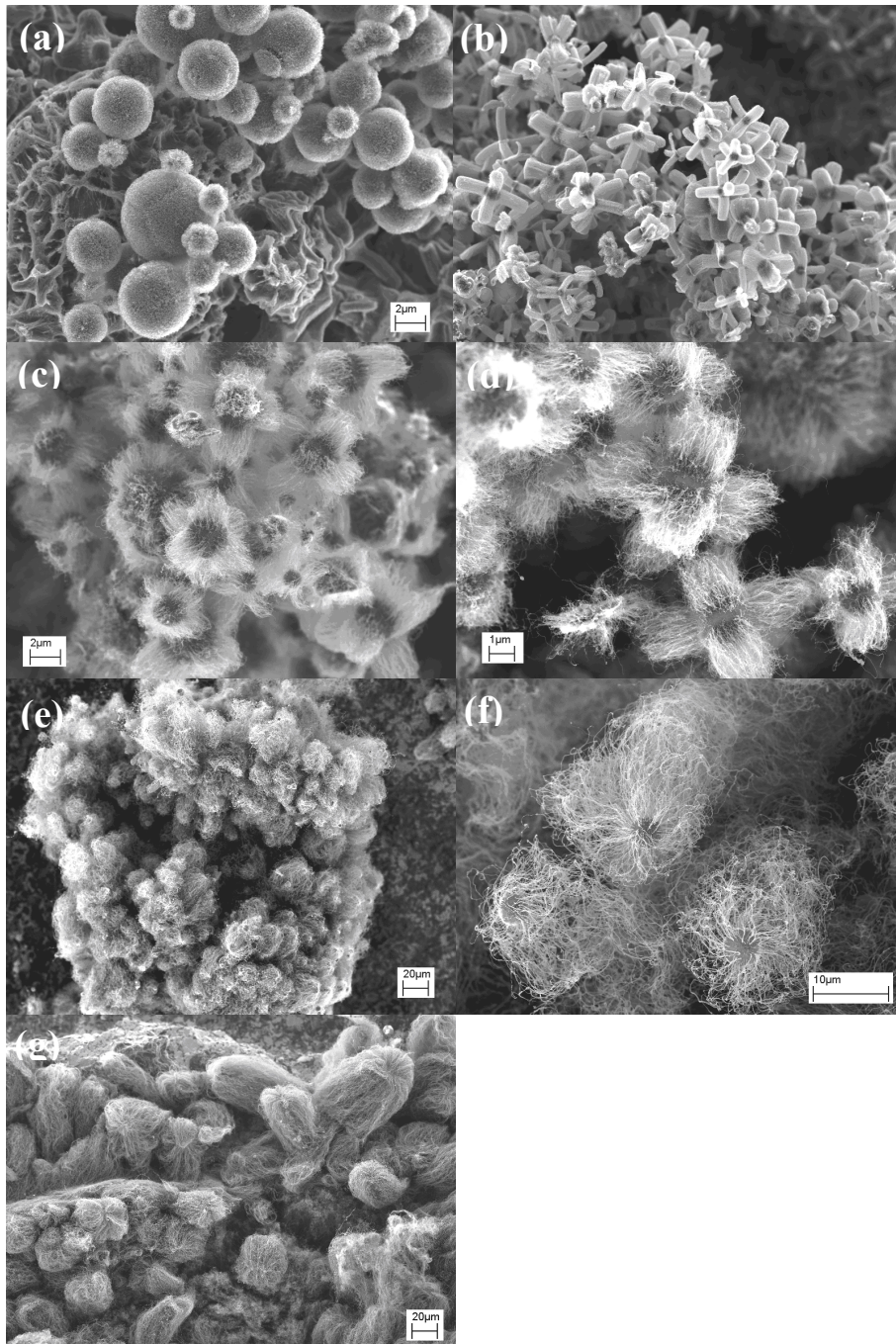
- Further characterizations of the crystal structures of micrometer substrates would be required to identify their influences on catalyst particles nucleation and orientation.
- One detailed chemical mechanism would be desired to better describe the gas phase decomposition of carbon and catalyst precursors, and the catalytic dehydrogenations of hydrocarbons for the deposition of carbon on catalyst particles.
- More efforts are encouraged to quantitatively determine the interfacial connection between single CNT and the microparticle by atomic force microscopy, and to study its evolution with CNT structures and geometries including the diameter and length.
- More investigations are proposed to study the thermal and mechanical reinforcements of different hybrid structures in polymer composites.
- It is promising to produce multifunctional ceramic materials with improved plasticity based on the nano-micro hybrid structures.



# Appendices

## Appendix 1

SEM images of three MWCNT- $\mu\text{Al}_2\text{O}_3$  hybrid structures



**“Short-dense-homogeneous” hybrid structures:** (a) carbon sources: xylene and acetylene, acetylene flow rate: 10 ml min<sup>-1</sup>, H<sub>2</sub> volumetric ratio: 40%, temperature: 550 °C.

**“Six-branch” hybrid structures:** (b) carbon sources: xylene and acetylene, acetylene flow rate: 10 ml min<sup>-1</sup>, H<sub>2</sub> volumetric ratio: 5 %, temperature: 550 °C; (c) carbon source: xylene, temperature: 600 °C; (d) carbon source: xylene, temperature: 650 °C.

**“urchin-like” hybrid structures:** (e) carbon source: xylene, temperature: 750 °C; (f) high magnification SEM of figure e; (g) carbon source: xylene, temperature: 800 °C.

## Appendix 2

Mass Spectrometry Data of several products related to this research (*from* Pfeiffer vacuum Spectra library)

Product names	Molecular formula	Number of peaks	m/z and relative intensity									
Acetylene	C <sub>2</sub> H <sub>2</sub>	8	26 999	25 201	13 56	24 56	27 28	12 25	14 2	28 2		
O-xylene	C <sub>8</sub> H <sub>10</sub>	10	91 999	106 576	105 241	39 174	51 161	77 127	27 110	78 84	92 75	107 48
Toluene	C <sub>7</sub> H <sub>8</sub>	11	91 999	92 784	50 709	39 206	65 138	51 107	63 101	90 91	27 60	38 57
Benzene	C <sub>6</sub> H <sub>6</sub>	9	78 999	52 194	51 186	50 157	77 144	39 142	79 64	76 60	38 58	
Air	-	9	28 999	32 160	14 72	16 18	40 14	29 8	20 1	18 1	34 1	
Argon	Ar	5		40 999		20 200		36 3		18 1		38 1
Water	H <sub>2</sub> O	5		18 999		17 230		16 11		20 3		19 1

## Appendix 3

Thermodynamic data<sup>[290]</sup>

<b>Ar</b> 120186Ar 1 G 0300.00 5000.00 1000.00	1
0.02500000E+02 0.00000000E+00 0.00000000E+00 0.00000000E+00 0.00000000E+00	2
-0.07453750E+04 0.04366000E+02 0.02500000E+02 0.00000000E+00 0.00000000E+00	3
0.00000000E+00 0.00000000E+00-0.07453750E+04 0.04366000E+02	4
<b>H2</b> 121286H 2 G 0300.00 5000.00 1000.00	1
0.02991423E+02 0.07000644E-02 -0.05633828E-06 -0.09231578E-10 0.15827519E-14	2
-0.08350340E+04-0.13551101E+01 0.03298124E+02 0.08249441E-02 -0.08143015E-05	3
-0.09475434E-09 0.04134872E-11 -0.10125209E+04 -0.03294094E+02	4
<b>C</b> 121086C 1 G 0300.00 5000.00 1000.00	1
0.02602087E+02-0.01787081E-02 0.09087041E-06-0.11499333E-10 0.03310844E-14	2
0.08542154E+06 0.04195177E+02 0.02498584E+02 0.08085776E-03-0.02697697E-05	3
0.03040729E-08-0.11066518E-12 0.08545878E+06 0.04753459E+02	4
<b>CH4</b> 121286C 1H 4 G 0300.00 5000.00 1000.00	1
0.01683478E+02 0.10237236E-01 -0.03875128E-04 0.06785585E-08 -0.04503423E-12	2

-0.10080787E+05	0.09623395E+02	0.07787415E+01	0.01747668E+00	-0.02783409E-03	3	
0.03049708E-06	-0.12239307E-10	-0.09825229E+05	0.13722195E+02		4	
<b>C2H4</b>	121286C	2H	4 G	0300.00	5000.00	
1000.00					1	
0.03528418E+02	0.11485185E-01	-0.04418385E-04	0.07844600E-08	-0.05266848E-12	2	
0.04428288E+05	0.02230389E+02	-0.08614880E+01	0.02796162E+00	-0.03388677E-03	3	
0.02785152E-06	-0.09737879E-10	0.05573046E+05	0.02421148E+03		4	
<b>C4H2</b>	121686C	4H	2 G	0300.00	5000.00	
1000.00					1	
0.09031407E+02	0.06047252E-01	-0.01948788E-04	0.02754863E-08	-0.13856080E-13	2	
0.05294735E+06	-0.02385067E+03	0.04005191E+02	0.01981000E+00	-0.09865877E-04	3	
-0.06635158E-07	0.06077413E-10	0.05424065E+06	0.01845736E+02		4	
<b>C6H6</b>	20387C	6H	6 G	0300.00	5000.00	
1000.00					1	
0.12910740E+02	0.01723296E+00	-0.05024210E-04	0.05893497E-08	-0.01947521E-12	2	
0.03664511E+05	-0.05002699E+03	-0.03138012E+02	0.04723103E+00	-0.02962207E-04	3	
-0.03262819E-06	0.01718691E-09	0.08890031E+05	0.03657573E+03		4	
<b>C5H6</b>	HR11/99BLYP00C	5H	6 0 G	300.000	5000.000	
1402.000	0				1	
1.26575005E+01	1.53301203E-02	-5.23821364E-06	8.12867095E-10	-4.71504821E-14	2	
1.03083446E+04	-4.75386061E+01	-4.78259036E+00	6.09873033E-02	-5.17363931E-05	3	
2.25173536E-08	-3.92621113E-12	1.58382836E+04	4.43226201E+01		4	
<b>C7H8</b>	BurcatL	6/87C	7H	800G	200.000	
6000.000	1000				1	
0.12940034E+02	0.26691287E-01	-0.96838505E-05	0.15738629E-08	-0.94663601E-13	2	
-0.69764908E+03	-0.46728785E+02	0.16152663E+01	0.21099438E-01	0.85366018E-04	3	
-0.13261066E-06	0.55956604E-10	0.40756300E+04	0.20282210E+02		4	
<b>C2H2</b>	121386C	2H	2 G	0300.00	5000.00	
1000.00					1	
0.04436770E+02	0.05376039E-01	-0.01912816E-04	0.03286379E-08	-0.02156709E-12	2	
0.02566766E+06	-0.02800338E+02	0.02013562E+02	0.15190446E-01	-0.16163189E-04	3	
0.09078992E-07	-0.01912746E-10	0.02612444E+06	0.08805378E+02		4	
<b>C8H10</b>	Burcat	T 9/96C	8H	1000G	200.000	
6000.000	1000				1	
0.15987319E+02	0.32676385E-01	-0.11890299E-04	0.19360904E-08	-0.11659656E-12	2	
-0.47073870E+04	-0.63675039E+02	0.24506692E+01	0.26239143E-01	0.99991348E-04	3	
-0.15573183E-06	0.65643572E-10	0.10189486E+04	0.16445176E+02		4	
<b>Fe(C5H5)2</b>	300	2000				
-11.72079	0.14038	-1.32E-04	6.08E-08	-1.07E-11	25760.247	70.6
<b>Fe(C5H5)</b>	300	2000				
-4.46195	0.06996	-6.82436E-5	3.24365E-8	-5.85716E-12	40745.087	43.024053
<b>Fe</b>	300	2000				
2.81253	0.00185	-4.09804E-6	2.7248E-9	-5.71774E-13	49035.474	5.2537387

Note: the coefficients of  $Fe(C_5H_5)_2$ ,  $Fe(C_5H_5)$  and  $Fe$  are obtained by the polynomial fitting of their specific heat values provided in ref<sup>[293]</sup>.



# References

- [1]. Henrich, F.; Chan, C.; Moore, V.; Rolandi, M.; O'Connell, M., The element carbon. In *Carbon Nanotubes: Properties and Applications*, O'Connell, M., Ed. CRC Press: FL, 2006; pp 1-18.
- [2]. Bundy, F. P.; Bassett, W. A.; Weathers, M. S.; Hemley, R. J.; Mao, H. U.; Goncharov, A. F., The pressure-temperature phase and transformation diagram for carbon; updated through 1994. *Carbon* **1996**, *34* (2), 141-153.
- [3]. Dresselhaus, M. S.; Dresselhaus, G.; Avouris, P., *Carbon Nanotubes : Synthesis, Structure, Properties and Applications (Topics in Applied Physics, vol. 80)* Springer-Verlag: Berlin, 2001.
- [4]. Wei, L.; Kuo, P. K.; Thomas, R. L.; Anthony, T. R.; Banholzer, W. F., Thermal conductivity of isotopically modified single crystal diamond. *Physical Review Letters* **1993**, *70* (24), 3764.
- [5]. Kroto, H. W.; Heath, J. R.; O'Brien, S. C.; Curl, R. F.; Smalley, R. E., C60: Buckminsterfullerene. *Nature* **1985**, *318* (6042), 162-163.
- [6]. Kratschmer, W.; Lamb, L. D.; Fostiropoulos, K.; Huffman, D. R., Solid C60: a new form of carbon. *Nature* **1990**, *347* (6291), 354-358.
- [7]. Hebard, A. F.; Rosseinsky, M. J.; Haddon, R. C.; Murphy, D. W.; Glarum, S. H.; Palstra, T. T. M.; Ramirez, A. P.; Kortan, A. R., Superconductivity at 18 K in potassium-doped C60. *Nature* **1991**, *350* (6319), 600-601.
- [8]. Tanigaki, K.; Ebbesen, T. W.; Saito, S.; Mizuki, J.; Tsai, J. S.; Kubo, Y.; Kuroshima, S., Superconductivity at 33 K in CsxCbyC60. *Nature* **1991**, *352* (6332), 222-223.
- [9]. Iijima, S., HELICAL MICROTUBULES OF GRAPHITIC CARBON. *Nature* **1991**, *354* (6348), 56-58.
- [10]. Radushkevich LV, L. V., O strukture ugleroda, obrazujucegosja pri termiceskom razlozenii okisi ugleroda na zeleznom kontakte. *Zurn Fisic Chim* **1952**, *26*, 88-95.
- [11]. Monthoux, M.; Kuznetsov, V. L., Who should be given the credit for the discovery of carbon nanotubes? *Carbon* **2006**, *44* (9), 1621-1623.
- [12]. Oberlin, A.; Endo, M.; Koyama, T., Filamentous growth of carbon through benzene decomposition. *Journal of Crystal Growth* **1976**, *32* (3), 335-349.
- [13]. Iijima, S.; Ichihashi, T., SINGLE-SHELL CARBON NANOTUBES OF 1-NM DIAMETER. *Nature* **1993**, *363* (6430), 603-605.
- [14]. Bethune, D. S.; Kiang, C. H.; Devries, M. S.; Gorman, G.; Savoy, R.; Vazquez, J.; Beyers, R., COBALT-CATALYZED GROWTH OF CARBON NANOTUBES WITH SINGLE-ATOMIC-LAYERWALLS. *Nature* **1993**, *363* (6430), 605-607.
- [15]. Novoselov, K. S.; Geim, A. K.; Morozov, S. V.; Jiang, D.; Zhang, Y.; Dubonos, S. V.; Grigorieva, I. V.; Firsov, A. A., Electric field effect in atomically thin carbon films. *Science* **2004**, *306* (5296), 666-669.
- [16]. Zheng, L. X.; O'Connell, M. J.; Doorn, S. K.; Liao, X. Z.; Zhao, Y. H.; Akhadov, E. A.; Hoffbauer, M. A.; Roop, B. J.; Jia, Q. X.; Dye, R. C.; Peterson, D. E.; Huang, S. M.; Liu, J.; Zhu, Y. T., Ultralong single-wall carbon nanotubes. *Nat. Mater.* **2004**, *3* (10), 673-676.
- [17]. Wilder, J. W. G.; Venema, L. C.; Rinzler, A. G.; Smalley, R. E.; Dekker, C., Electronic structure of atomically resolved carbon nanotubes. *Nature* **1998**, *391* (6662), 59-62.
- [18]. Baughman, R. H.; Zakhidov, A. A.; de Heer, W. A., Carbon Nanotubes--the Route Toward Applications. *Science* **2002**, *297* (5582), 787-792.
- [19]. Thess, A.; Lee, R.; Nikolaev, P.; Dai, H. J.; Petit, P.; Robert, J.; Xu, C. H.; Lee, Y. H.; Kim, S. G.; Rinzler, A. G.; Colbert, D. T.; Scuseria, G. E.; Tomanek, D.; Fischer, J. E.; Smalley, R. E., Crystalline ropes of metallic carbon nanotubes. *Science* **1996**, *273* (5274), 483-487.
- [20]. Delaney, P.; Choi, H. J.; Ihm, J.; Louie, S. G.; Cohen, M. L., Broken symmetry and pseudogaps in ropes of carbon nanotubes. *Nature* **1998**, *391* (6666), 466-468.
- [21]. Gao, G. H.; Cagin, T.; Goddard, W. A., Energetics, structure, mechanical and vibrational properties of single-walled carbon nanotubes. *Nanotechnology* **1998**, *9* (3), 184-191.
- [22]. Salvetat-Delmotte, J.-P.; Rubio, A., Mechanical properties of carbon nanotubes: a fiber digest for beginners. *Carbon* **2002**, *40* (10), 1729-1734.
- [23]. Ruoff, R. S.; Lorents, D. C., MECHANICAL AND THERMAL-PROPERTIES OF CARBON NANOTUBES. *Carbon* **1995**, *33* (7), 925-930.
- [24]. Salvetat, J. P.; Bonard, J. M.; Thomson, N. H.; Kulik, A. J.; Forro, L.; Benoit, W.; Zuppiroli, L., Mechanical properties of carbon nanotubes. *Appl. Phys. A-Mater. Sci. Process.* **1999**, *69* (3), 255-260.
- [25]. Treacy, M. M. J.; Ebbesen, T. W.; Gibson, J. M., Exceptionally high Young's modulus observed for

- individual carbon nanotubes. *Nature* **1996**, *381* (6584), 678-680.
- [26]. Krishnan, A.; Dujardin, E.; Ebbesen, T. W.; Yianilos, P. N.; Treacy, M. M. J., Young's modulus of single-walled nanotubes. *Physical Review B* **1998**, *58* (20), 14013.
- [27]. Wong, E. W.; Sheehan, P. E.; Lieber, C. M., Nanobeam mechanics: Elasticity, strength, and toughness of nanorods and nanotubes. *Science* **1997**, *277* (5334), 1971-1975.
- [28]. Yu, M.-F.; Files, B. S.; Arepalli, S.; Ruoff, R. S., Tensile Loading of Ropes of Single Wall Carbon Nanotubes and their Mechanical Properties. *Physical Review Letters* **2000**, *84* (24), 5552.
- [29]. Yu, M. F.; Lourie, O.; Dyer, M. J.; Moloni, K.; Kelly, T. F.; Ruoff, R. S., Strength and breaking mechanism of multiwalled carbon nanotubes under tensile load. *Science* **2000**, *287* (5453), 637-640.
- [30]. Ruoff, R. S.; Qian, D.; Liu, W. K., Mechanical properties of carbon nanotubes: theoretical predictions and experimental measurements. *C. R. Phys.* **2003**, *4* (9), 993-1008.
- [31]. Tibbetts, G. G., Why are carbon filaments tubular? *Journal of Crystal Growth* **1984**, *66* (3), 632-638.
- [32]. Lu, J. P., Elastic properties of carbon nanotubes and nanoropes. *Physical Review Letters* **1997**, *79* (7), 1297-1300.
- [33]. Nardelli, M. B.; Yakobson, B. I.; Bernholc, J., Brittle and ductile behavior in carbon nanotubes. *Physical Review Letters* **1998**, *81* (21), 4656-4659.
- [34]. Gogotsi, Y., *Advanced Materials Series*. CRC Press, Boca Rato: Boca Raton, Florida, **2006**.
- [35]. Popov, V. N., Carbon nanotubes: properties and application. *Materials Science and Engineering: R: Reports* **2004**, *43* (3), 61-102.
- [36]. Berber, S.; Kwon, Y. K.; Tomanek, D., Unusually high thermal conductivity of carbon nanotubes. *Phys. Rev. Lett.* **2000**, *84* (20), 4613-4616.
- [37]. Che, J. W.; Cagin, T.; Goddard, W. A., Thermal conductivity of carbon nanotubes. *Nanotechnology* **2000**, *11* (2), 65-69.
- [38]. Kim, P.; Shi, L.; Majumdar, A.; McEuen, P. L., Thermal Transport Measurements of Individual Multiwalled Nanotubes. *Physical Review Letters* **2001**, *87* (21), 215502.
- [39]. Pop, E.; Mann, D.; Wang, Q.; Goodson, K.; Dai, H., Thermal Conductance of an Individual Single-Wall Carbon Nanotube above Room Temperature. *Nano Letters* **2005**, *6* (1), 96-100.
- [40]. Yi, W.; Lu, L.; Zhang, D. L.; Pan, Z. W.; Xie, S. S., Linear specific heat of carbon nanotubes. *Physical Review B* **1999**, *59* (14), R9015-R9018.
- [41]. Dresselhaus, M. S.; Dresselhaus, G.; Saito, R., PHYSICS OF CARBON NANOTUBES. *Carbon* **1995**, *33* (7), 883-891.
- [42]. Ajayan, P. M., Nanotubes from Carbon. *Chemical Reviews* **1999**, *99* (7), 1787-1800.
- [43]. Ebbesen, T. W.; Lezec, H. J.; Hiura, H.; Bennett, J. W.; Ghaemi, H. F.; Thio, T., Electrical conductivity of individual carbon nanotubes. *Nature* **1996**, *382* (6586), 54-56.
- [44]. Frank, S.; Poncharal, P.; Wang, Z. L.; Heer, W. A.; de, Carbon Nanotube Quantum Resistors. *Science* **1998**, *280* (5370), 1744-1746.
- [45]. Bachtold, A.; Strunk, C.; Salvetat, J.-P.; Bonard, J.-M.; Forro, L.; Nussbaumer, T.; Schonenberger, C., Aharonov-Bohm oscillations in carbon nanotubes. *Nature* **1999**, *397* (6721), 673-675.
- [46]. Tans, S. J.; Devoret, M. H.; Dai, H.; Thess, A.; Smalley, R. E.; Geerligs, L. J.; Dekker, C., Individual single-wall carbon nanotubes as quantum wires. *Nature* **1997**, *386* (6624), 474-477.
- [47]. White, C. T.; Todorov, T. N., Carbon nanotubes as long ballistic conductors. *Nature* **1998**, *393* (6682), 240-242.
- [48]. Hong, S.; Myung, S., Nanotube Electronics: A flexible approach to mobility. *Nat Nano* **2007**, *2* (4), 207-208.
- [49]. Endo, M.; Strano, M. S.; Ajayan, P. M., Potential applications of carbon nanotubes. In *Carbon Nanotubes*, Springer-Verlag Berlin: Berlin, 2008; Vol. 111, pp 13-61.
- [50]. Ajayan, P. M.; Stephan, O.; Colliex, C.; Trauth, D., Aligned Carbon Nanotube Arrays Formed by Cutting a Polymer Resin--Nanotube Composite. *Science* **1994**, *265* (5176), 1212-1214.
- [51]. Du, J. H.; Bai, J.; Cheng, H. M., The present status and key problems of carbon nanotube based polymer composites. *Express Polym. Lett.* **2007**, *1* (5), 253-273.
- [52]. Moniruzzaman, M.; Winey, K. I., Polymer nanocomposites containing carbon nanotubes. *Macromolecules* **2006**, *39* (16), 5194-5205.
- [53]. Li, F.; Cheng, H. M.; Bai, S.; Su, G.; Dresselhaus, M. S., Tensile strength of single-walled carbon nanotubes directly measured from their macroscopic ropes. *Applied Physics Letters* **2000**, *77* (20), 3161-3163.
- [54]. Pichot, V.; Badaire, S.; Albouy, P. A.; Zakri, C.; Poulin, P.; Launois, P., Structural and mechanical properties of single-wall carbon nanotube fibers. *Physical Review B* **2006**, *74* (24), 245416.
- [55]. Dalton, A. B.; Collins, S.; Munoz, E.; Razal, J. M.; Ebron, V. H.; Ferraris, J. P.; Coleman, J. N.; Kim, B. G.; Baughman, R. H., Super-tough carbon-nanotube fibres. *Nature* **2003**, *423* (6941), 703-703.
- [56]. Vigolo, B.; Penicaud, A.; Coulon, C.; Sauder, C.; Pailler, R.; Journet, C.; Bernier, P.; Poulin, P., Macroscopic fibers and ribbons of oriented carbon nanotubes. *Science* **2000**, *290* (5495), 1331-1334.
- [57]. Miaudet, P.; Badaire, S.; Maugey, M.; Derr 茅, A.; Pichot, V.; Launois, P.; Poulin, P.; Zakri, C., Hot-Drawing of Single and Multiwall Carbon Nanotube Fibers for High Toughness and Alignment. *Nano Letters*

- 2005**, *5* (11), 2212-2215.
- [58]. Bryning, M. B.; Islam, M. F.; Kikkawa, J. M.; Yodh, A. G., Very low conductivity threshold in bulk isotropic single-walled carbon nanotube-epoxy composites. *Adv. Mater.* **2005**, *17* (9), 1186-+.
- [59]. Biercuk, M. J.; Llaguno, M. C.; Radosavljevic, M.; Hyun, J. K.; Johnson, A. T.; Fischer, J. E., Carbon nanotube composites for thermal management. *Applied Physics Letters* **2002**, *80* (15), 2767-2769.
- [60]. Choi, E. S.; Brooks, J. S.; Eaton, D. L.; Al-Haik, M. S.; Hussaini, M. Y.; Garmestani, H.; Li, D.; Dahmen, K., Enhancement of thermal and electrical properties of carbon nanotube polymer composites by magnetic field processing. *Journal of Applied Physics* **2003**, *94* (9), 6034-6039.
- [61]. Huang, H.; Liu, C. H.; Wu, Y.; Fan, S. S., Aligned carbon nanotube composite films for thermal management. *Adv. Mater.* **2005**, *17* (13), 1652-+.
- [62]. Huxtable, S. T.; Cahill, D. G.; Shenogin, S.; Xue, L. P.; Ozisik, R.; Barone, P.; Usrey, M.; Strano, M. S.; Siddons, G.; Shim, M.; Keblinski, P., Interfacial heat flow in carbon nanotube suspensions. *Nat. Mater.* **2003**, *2* (11), 731-734.
- [63]. Niu, C. M.; Sichel, E. K.; Hoch, R.; Moy, D.; Tennent, H., High power electrochemical capacitors based on carbon nanotube electrodes. *Applied Physics Letters* **1997**, *70* (11), 1480-1482.
- [64]. Baughman, R. H.; Cui, C.; Zakhidov, A. A.; Iqbal, Z.; Barisci, J. N.; Spinks, G. M.; Wallace, G. G.; Mazzoldi, A.; De Rossi, D.; Rinzler, A. G.; Jaschinski, O.; Roth, S.; Kertesz, M., Carbon Nanotube Actuators. *Science* **1999**, *284* (5418), 1340-1344.
- [65]. Endo, M.; Kim, C.; Nishimura, K.; Fujino, T.; Miyashita, K., Recent development of carbon materials for Li ion batteries. *Carbon* **2000**, *38* (2), 183-197.
- [66]. Gong, K.; Du, F.; Xia, Z.; Durstock, M.; Dai, L., Nitrogen-Doped Carbon Nanotube Arrays with High Electrocatalytic Activity for Oxygen Reduction. *Science* **2009**, *323* (5915), 760-764.
- [67]. Landi, B. J.; Castro, S. L.; Ruf, H. J.; Evans, C. M.; Bailey, S. G.; Raffaelle, R. P., CdSe quantum dot-single wall carbon nanotube complexes for polymeric solar cells. *Solar Energy Materials and Solar Cells* **2005**, *87* (1-4), 733-746.
- [68]. Hill, F. A.; Havel, T. F.; Livermore, C., Modeling mechanical energy storage in springs based on carbon nanotubes. *Nanotechnology* **2009**, *20* (25).
- [69]. Cao, A.; Dickrell, P. L.; Sawyer, W. G.; Ghasemi-Nejhad, M. N.; Ajayan, P. M., Super-Compressible Foamlike Carbon Nanotube Films. *Science* **2005**, *310* (5752), 1307-1310.
- [70]. Tans, S. J.; Verschueren, A. R. M.; Dekker, C., Room-temperature transistor based on a single carbon nanotube. *Nature* **1998**, *393* (6680), 49-52.
- [71]. Choi, W. B.; Chung, D. S.; Kang, J. H.; Kim, H. Y.; Jin, Y. W.; Han, I. T.; Lee, Y. H.; Jung, J. E.; Lee, N. S.; Park, G. S.; Kim, J. M., Fully sealed, high-brightness carbon-nanotube field-emission display. *Applied Physics Letters* **1999**, *75* (20), 3129-3131.
- [72]. Saito, Y.; Uemura, S., Field emission from carbon nanotubes and its application to electron sources. *Carbon* **2000**, *38* (2), 169-182.
- [73]. Rinzler, A. G.; Hafner, J. H.; Nikolaev, P.; Nordlander, P.; Colbert, D. T.; Smalley, R. E.; Lou, L.; Kim, S. G.; Tomanek, D., Unraveling Nanotubes: Field Emission from an Atomic Wire. *Science* **1995**, *269* (5230), 1550-1553.
- [74]. Deheer, W. A.; Chatelain, A.; Ugarte, D., A CARBON NANOTUBE FIELD-EMISSION ELECTRON SOURCE. *Science* **1995**, *270* (5239), 1179-1180.
- [75]. Ebbesen, T. W.; Ajayan, P. M., LARGE-SCALE SYNTHESIS OF CARBON NANOTUBES. *Nature* **1992**, *358* (6383), 220-222.
- [76]. He, D. L.; Zhao, T. K.; Liu, Y. N.; Zhu, J. W.; Yu, G.; Ge, L. L., The effect of electric current on the synthesis of single-walled carbon nanotubes by temperature controlled arc discharge. *Diamond and Related Materials* **2007**, *16*, 1722-1726.
- [77]. He, D. L.; Liu, Y. N.; Zhao, T. K.; Zhu, J. W.; Yu, G., Effect of metal oxide and oxygen on the growth of single-walled carbon nanotubes by electric arc discharge. *Journal of Nanoparticle Research* **2008**, *10* (3), 409-414.
- [78]. Joseyacaman, M.; Mikiyoshida, M.; Rendon, L.; Santiesteban, J. G., CATALYTIC GROWTH OF CARBON MICROTUBULES WITH FULLERENE STRUCTURE. *Applied Physics Letters* **1993**, *62* (2), 202-204.
- [79]. Dai, H. J., Carbon nanotubes: opportunities and challenges. *Surf. Sci.* **2002**, *500* (1-3), 218-241.
- [80]. Dai, H. J., Carbon nanotubes: Synthesis, integration, and properties. *Accounts Chem. Res.* **2002**, *35* (12), 1035-1044.
- [81]. Chen, Y.; Conway, M. J.; Fitz Gerald, J. D.; Williams, J. S.; Chadderton, L. T., The nucleation and growth of carbon nanotubes in a mechano-thermal process. *Carbon* **2004**, *42* (8-9), 1543-1548.
- [82]. Vander Wal, R. L.; Ticich, T. M.; Curtis, V. E., Diffusion flame synthesis of single-walled carbon nanotubes. *Chemical Physics Letters* **2000**, *323* (3-4), 217-223.
- [83]. Yuan, L.; Saito, K.; Pan, C.; Williams, F. A.; Gordon, A. S., Nanotubes from methane flames. *Chemical Physics Letters* **2001**, *340* (3-4), 237-241.
- [84]. Yuan, L. M.; Saito, K.; Hu, W. C.; Chen, Z., Ethylene flame synthesis of well-aligned multi-walled carbon

- nanotubes. *Chemical Physics Letters* **2001**, *346* (1-2), 23-28.
- [85]. Matveev, A. T.; Golberg, D.; Novikov, V. P.; Klimkovich, L. L.; Bando, Y., Synthesis of carbon nanotubes below room temperature. *Carbon* **2001**, *39* (1), 155-158.
- [86]. Hsu, W. K.; Terrones, M.; Hare, J. P.; Terrones, H.; Kroto, H. W.; Walton, D. R. M., Electrolytic formation of carbon nanostructures. *Chemical Physics Letters* **1996**, *262* (1-2), 161-166.
- [87]. Hsu, W. K.; Hare, J. P.; Terrones, M.; Kroto, H. W.; Walton, D. R. M.; Harris, P. J. F., CONDENSED-PHASE NANOTUBES. *Nature* **1995**, *377* (6551), 687-687.
- [88]. Bai, J. B.; Hamon, A. L.; Marraud, A.; Jouffrey, B.; Zymla, V., Synthesis of SWNTs and MWNTs by a molten salt (NaCl) method. *Chemical Physics Letters* **2002**, *365* (1-2), 184-188.
- [89]. Laplaze, D.; Bernier, P.; Maser, W. K.; Flamant, G.; Guillard, T.; Loiseau, A., Carbon nanotubes: The solar approach. *Carbon* **1998**, *36* (5-6), 685-688.
- [90]. Cho, W.-S.; Hamada, E.; Kondo, Y.; Takayanagi, K., Synthesis of carbon nanotubes from bulk polymer. *Applied Physics Letters* **1996**, *69* (2), 278-279.
- [91]. Li, Y. L.; Yu, Y. D.; Liang, Y., A novel method for synthesis of carbon nanotubes: Low temperature solid pyrolysis. *J. Mater. Res.* **1997**, *12* (7), 1678-1680.
- [92]. Journet, C.; Bernier, P., Production of carbon nanotubes. *Appl. Phys. A-Mater. Sci. Process.* **1998**, *67* (1), 1-9.
- [93]. Journet, C.; Maser, W. K.; Bernier, P.; Loiseau, A.; de la Chapelle, M. L.; Lefrant, S.; Deniard, P.; Lee, R.; Fischer, J. E., Large-scale production of single-walled carbon nanotubes by the electric-arc technique. *Nature* **1997**, *388* (6644), 756-758.
- [94]. Chiang, I. W.; Brinson, B. E.; Smalley, R. E.; Margrave, J. L.; Hauge, R. H., Purification and characterization of single-wall carbon nanotubes. *J. Phys. Chem. B* **2001**, *105* (6), 1157-1161.
- [95]. Guo, T.; Nikolaev, P.; Thess, A.; Colbert, D. T.; Smalley, R. E., CATALYTIC GROWTH OF SINGLE-WALLED NANOTUBES BY LASER VAPORIZATION. *Chemical Physics Letters* **1995**, *243* (1-2), 49-54.
- [96]. Hofmann, S.; Sharma, R.; Ducati, C.; Du, G.; Mattevi, C.; Cepek, C.; Cantoro, M.; Pisana, S.; Parvez, A.; Cervantes-Sodi, F.; Ferrari, A. C.; Dunin-Borkowski, R.; Lizzit, S.; Petaccia, L.; Goldoni, A.; Robertson, J., In situ Observations of Catalyst Dynamics during Surface-Bound Carbon Nanotube Nucleation. *Nano Letters* **2007**, *7* (3), 602-608.
- [97]. Choy, K. L., Chemical vapour deposition of coatings. *Progress in Materials Science* **2003**, *48* (2), 57-170.
- [98]. Walker, P. L.; Rakiszawski, J. F.; Imperial, G. R., Carbon Formation from Carbon Monoxide-Hydrogen Mixtures over Iron Catalysts.I. Properties of Carbon Formed. *The Journal of Physical Chemistry* **1959**, *63* (2), 133-140.
- [99]. Jose-Yacaman, M.; Miki-Yoshida, M.; Rendon, L.; Santiesteban, J. G., Catalytic growth of carbon microtubules with fullerene structure. *Applied Physics Letters* **1993**, *62* (6), 657-659.
- [100]. Endo, M.; Takeuchi, K.; Igarashi, S.; Kobori, K.; Shiraishi, M.; Kroto, H. W., The production and structure of pyrolytic carbon nanotubes (PCNTs). *Journal of Physics and Chemistry of Solids* **1993**, *54* (12), 1841-1848.
- [101]. Dai, H.; Rinzler, A. G.; Nikolaev, P.; Thess, A.; Colbert, D. T.; Smalley, R. E., Single-wall nanotubes produced by metal-catalyzed disproportionation of carbon monoxide. *Chemical Physics Letters* **1996**, *260* (3-4), 471-475.
- [102]. Karthikeyan, S.; Mahalingam, P.; Karthik, M., Large Scale Synthesis of Carbon Nanotubes. *E-J. Chem.* **2009**, *6* (1), 1-12.
- [103]. Teo, K. B. K. a. S., C. and Chhowalla, M. and Milne, W.I., Catalytic synthesis of carbon nanotubes and nanofibers. In *Encyclopedia of Nanoscience and Nanotechnology*, Nalwa, H. S., Ed. American Scientific Publishers: Stevenson Ranch, CA, 2003; pp 665-686.
- [104]. Takagi, D.; Homma, Y.; Hibino, H.; Suzuki, S.; Kobayashi, Y., Single-walled carbon nanotube growth from highly activated metal nanoparticles. *Nano Letters* **2006**, *6* (12), 2642-2645.
- [105]. Ren, Z. F.; Huang, Z. P.; Xu, J. W.; Wang, J. H.; Bush, P.; Siegal, M. P.; Provencio, P. N., Synthesis of Large Arrays of Well-Aligned Carbon Nanotubes on Glass. *Science* **1998**, *282* (5391), 1105-1107.
- [106]. Cheung, C. L.; Kurtz, A.; Park, H.; Lieber, C. M., Diameter-Controlled Synthesis of Carbon Nanotubes. *The Journal of Physical Chemistry B* **2002**, *106* (10), 2429-2433.
- [107]. Wei, Y. Y.; Eres, G.; Merkulov, V. I.; Lowndes, D. H., Effect of catalyst film thickness on carbon nanotube growth by selective area chemical vapor deposition. *Applied Physics Letters* **2001**, *78* (10), 1394-1396.
- [108]. Dupuis, A.-C., The catalyst in the CCVD of carbon nanotubes--a review. *Progress in Materials Science* **2005**, *50* (8), 929-961.
- [109]. Ivanov, V.; Nagy, J. B.; Lambin, P.; Lucas, A.; Zhang, X. B.; Zhang, X. F.; Bernaerts, D.; Van Tendeloo, G.; Amelinckx, S.; Van Landuyt, J., The study of carbon nanotubules produced by catalytic method. *Chemical Physics Letters* **1994**, *223* (4), 329-335.
- [110]. Kind, H.; Bonard, J.-M.; Emmenegger, C.; Nilsson, L.-O.; Hernadi, K.; Maillard-Schaller, E.; Schlappbach, L.; Forr?, L.; Kern, K., Patterned Films of Nanotubes Using Microcontact Printing of Catalysts. *Adv. Mater.* **1999**, *11* (15), 1285-1289.

- [111]. Baker, R. T. K.; Alonzo, J. R.; Dumesic, J. A.; Yates, D. J. C., Effect of the surface state of iron on filamentous carbon formation. *Journal of Catalysis* **1982**, 77 (1), 74-84.
- [112]. Merkulov, V. I.; Lowndes, D. H.; Wei, Y. Y.; Eres, G.; Voelkl, E., Patterned growth of individual and multiple vertically aligned carbon nanofibers. *Applied Physics Letters* **2000**, 76 (24), 3555-3557.
- [113]. Bower, C.; Zhou, O.; Zhu, W.; Werder, D. J.; Jin, S., Nucleation and growth of carbon nanotubes by microwave plasma chemical vapor deposition. *Applied Physics Letters* **2000**, 77 (17), 2767-2769.
- [114]. Su, M.; Zheng, B.; Liu, J., A scalable CVD method for the synthesis of single-walled carbon nanotubes with high catalyst productivity. *Chemical Physics Letters* **2000**, 322 (5), 321-326.
- [115]. Kukovecz, A.; Konya, Z.; Nagaraju, N.; Willems, I.; Tamasi, A.; Fonseca, A.; Nagy, J. B.; Kiricsi, I., Catalytic synthesis of carbon nanotubes over Co, Fe and Ni containing conventional and sol-gel silica-aluminas. *PCCP Phys. Chem. Chem. Phys.* **2000**, 2 (13), 3071-3076.
- [116]. Satishkumar, B. C.; Govindaraj, A.; Rao, C. N. R., Bundles of aligned carbon nanotubes obtained by the pyrolysis of ferrocene-hydrocarbon mixtures: role of the metal nanoparticles produced in situ. *Chemical Physics Letters* **1999**, 307 (3-4), 158-162.
- [117]. Lee, Y. T.; Kim, N. S.; Park, J.; Han, J. B.; Choi, Y. S.; Ryu, H.; Lee, H. J., Temperature-dependent growth of carbon nanotubes by pyrolysis of ferrocene and acetylene in the range between 700 and 1000 degrees C. *Chemical Physics Letters* **2003**, 372 (5-6), 853-859.
- [118]. Ci, L.; Li, Y.; Wei, B.; Liang, J.; Xu, C.; Wu, D., Preparation of carbon nanofibers by the floating catalyst method. *Carbon* **2000**, 38 (14), 1933-1937.
- [119]. Cheng, H. M.; Li, F.; Su, G.; Pan, H. Y.; He, L. L.; Sun, X.; Dresselhaus, M. S., Large-scale and low-cost synthesis of single-walled carbon nanotubes by the catalytic pyrolysis of hydrocarbons. *Applied Physics Letters* **1998**, 72 (25), 3282-3284.
- [120]. Smith, D. K.; Lee, D. C.; Korgel, B. A., High yield multiwall carbon nanotube synthesis in supercritical fluids. *Chem. Mat.* **2006**, 18 (14), 3356-3364.
- [121]. Xiang, R.; Luo, G.; Yang, Z.; Zhang, Q.; Qian, W.; Wei, F., Large area growth of aligned CNT arrays on spheres: Cost performance and product control. *Materials Letters* **2009**, 63 (1), 84-87.
- [122]. Huang, S. M.; Dai, L. M.; Mau, A. W. H., Patterned growth and contact transfer of well-aligned carbon nanotube films. *J. Phys. Chem. B* **1999**, 103 (21), 4223-4227.
- [123]. Nikolaev, P.; Bronikowski, M. J.; Bradley, R. K.; Rohmund, F.; Colbert, D. T.; Smith, K. A.; Smalley, R. E., Gas-phase catalytic growth of single-walled carbon nanotubes from carbon monoxide. *Chemical Physics Letters* **1999**, 313 (1-2), 91-97.
- [124]. Duesberg, G. S.; Graham, A. P.; Liebau, M.; Seidel, R.; Unger, E.; Kreupl, F.; Hoenlein, W., Growth of Isolated Carbon Nanotubes with Lithographically Defined Diameter and Location. *Nano Letters* **2003**, 3 (2), 257-259.
- [125]. Li, Y.; Kim, W.; Zhang, Y.; Rolandi, M.; Wang, D.; Dai, H., Growth of Single-Walled Carbon Nanotubes from Discrete Catalytic Nanoparticles of Various Sizes. *The Journal of Physical Chemistry B* **2001**, 105 (46), 11424-11431.
- [126]. Joon Yoon, Y.; Cheol Bae, J.; Koo Baik, H.; Cho, S.; Lee, S.-J.; Moon Song, K.; Seung Myung, N., Growth control of single and multi-walled carbon nanotubes by thin film catalyst. *Chemical Physics Letters* **2002**, 366 (1-2), 109-114.
- [127]. Zhang, Y.; Li, Y.; Kim, W.; Wang, D.; Dai, H., Imaging as-grown single-walled carbon nanotubes originated from isolated catalytic nanoparticles. *Appl. Phys. A-Mater. Sci. Process.* **2002**, 74 (3), 325-328.
- [128]. Zhang, W. D.; Wen, Y.; Tjiu, W. C.; Xu, G. Q.; Gan, L. M., Growth of vertically aligned carbon-nanotube array on large area of quartz plates by chemical vapor deposition. *Appl. Phys. A-Mater. Sci. Process.* **2002**, 74 (3), 419-422.
- [129]. Lan, A.; Iqbal, Z.; Aitouchen, A.; Libera, M.; Grebel, H., Growth of single-wall carbon nanotubes within an ordered array of nanosize silica spheres. *Applied Physics Letters* **2002**, 81 (3), 433-435.
- [130]. Alvarez, W. E.; Kitiyanan, B.; Borgna, A.; Resasco, D. E., Synergism of Co and Mo in the catalytic production of single-wall carbon nanotubes by decomposition of CO. *Carbon* **2001**, 39 (4), 547-558.
- [131]. Cassell, A. M.; Raymakers, J. A.; Kong, J.; Dai, H., Large Scale CVD Synthesis of Single-Walled Carbon Nanotubes. *The Journal of Physical Chemistry B* **1999**, 103 (31), 6484-6492.
- [132]. Schaper, A. K.; Hou, H.; Greiner, A.; Philipp, F., The role of iron carbide in multiwalled carbon nanotube growth. *Journal of Catalysis* **2004**, 222 (1), 250-254.
- [133]. Nishimura, K.; Okazaki, N.; Pan, L. J.; Nakayama, Y., In situ study of iron catalysts for carbon nanotube growth using X-ray diffraction analysis. *Jpn. J. Appl. Phys. Part 2 - Lett. Express Lett.* **2004**, 43 (4A), L471-L474.
- [134]. Hernadi, K.; Fonseca, A.; Nagy, J. B.; Fudala, A.; Bernaerts, D.; Kiricsi, I., Catalytic production of carbon nanofibers over iron carbide doped with Sn<sup>2+</sup>. *Applied Catalysis A: General* **2002**, 228 (1-2), 103-113.
- [135]. Herreyre, S.; Gadelle, P.; Moral, P.; Millet, J. M. M., Study by Mössbauer spectroscopy and magnetization measurement of the evolution of iron catalysts used in the disproportionation of CO. *Journal of Physics and Chemistry of Solids* **1997**, 58 (10), 1539-1545.
- [136]. Li, W. Z.; Xie, S. S.; Qian, L. X.; Chang, B. H.; Zou, B. S.; Zhou, W. Y.; Zhao, R. A.; Wang, G.,

- Large-Scale Synthesis of Aligned Carbon Nanotubes. *Science* **1996**, *274* (5293), 1701-1703.
- [137]. Wei, B. Q.; Vajtai, R.; Jung, Y.; Ward, J.; Zhang, R.; Ramanath, G.; Ajayan, P. M., Microfabrication technology: Organized assembly of carbon nanotubes. *Nature* **2002**, *416* (6880), 495-496.
- [138]. Li, Q. W.; Yan, H.; Cheng, Y.; Zhang, J.; Liu, Z. F., A scalable CVD synthesis of high-purity single-walled carbon nanotubes with porous MgO as support material. *J. Mater. Chem.* **2002**, *12* (4), 1179-1183.
- [139]. Couteau, E.; Hernadi, K.; Seo, J. W.; Thien-Nga, L.; Miko, C.; Gaal, R.; Forro, L., CVD synthesis of high-purity multiwalled carbon nanotubes using CaCO<sub>3</sub> catalyst support for large-scale production. *Chemical Physics Letters* **2003**, *378* (1-2), 9-17.
- [140]. Hayashi, T.; Kim, Y. A.; Matoba, T.; Esaka, M.; Nishimura, K.; Tsukada, T.; Endo, M.; Dresselhaus, M. S., Smallest Freestanding Single-Walled Carbon Nanotube. *Nano Letters* **2003**, *3* (7), 887-889.
- [141]. Jeong, S. H.; Hwang, H. Y.; Lee, K. H.; Jeong, Y., Template-based carbon nanotubes and their application to a field emitter. *Applied Physics Letters* **2001**, *78* (14), 2052-2054.
- [142]. Iwasaki, T.; Motoi, T.; Den, T., Multiwalled carbon nanotubes growth in anodic alumina nanoholes. *Applied Physics Letters* **1999**, *75* (14), 2044-2046.
- [143]. Kathayayini, H.; Nagaraju, N.; Fonseca, A.; Nagy, J. B., Catalytic activity of Fe, Co and Fe/Co supported on Ca and Mg oxides, hydroxides and carbonates in the synthesis of carbon nanotubes. *J. Mol. Catal. A-Chem.* **2004**, *223* (1-2), 129-136.
- [144]. Baker, R. T. K., Catalytic growth of carbon filaments. *Carbon* **1989**, *27* (3), 315-323.
- [145]. Sinnott, S. B.; Andrews, R.; Qian, D.; Rao, A. M.; Mao, Z.; Dickey, E. C.; Derbyshire, F., Model of carbon nanotube growth through chemical vapor deposition. *Chemical Physics Letters* **1999**, *315* (1-2), 25-30.
- [146]. Ward, J. W.; Wei, B. Q.; Ajayan, P. M., Substrate effects on the growth of carbon nanotubes by thermal decomposition of methane. *Chemical Physics Letters* **2003**, *376* (5-6), 717-725.
- [147]. Su, M.; Li, Y.; Maynor, B.; Buldum, A.; Lu, J. P.; Liu, J., Lattice-Oriented Growth of Single-Walled Carbon Nanotubes. *The Journal of Physical Chemistry B* **2000**, *104* (28), 6505-6508.
- [148]. Han, S.; Liu, X.; Zhou, C., Template-Free Directional Growth of Single-Walled Carbon Nanotubes on a- and r-Plane Sapphire. *J. Am. Chem. Soc.* **2005**, *127* (15), 5294-5295.
- [149]. Maret, M.; Hostache, K.; Schouler, M.-C.; Marcus, B.; Roussel-Dherbey, F.; Albrecht, M.; Gadelle, P., Oriented growth of single-walled carbon nanotubes on a MgO(0??) surface. *Carbon* **2007**, *45* (1), 180-187.
- [150]. Hafner, J. H.; Bronikowski, M. J.; Azamian, B. R.; Nikolaev, P.; Rinzler, A. G.; Colbert, D. T.; Smith, K. A.; Smalley, R. E., Catalytic growth of single-wall carbon nanotubes from metal particles. *Chemical Physics Letters* **1998**, *296* (1-2), 195-202.
- [151]. Flahaut, E.; Govindaraj, A.; Peigney, A.; Laurent, C.; Rousset, A.; Rao, C. N. R., Synthesis of single-walled carbon nanotubes using binary (Fe, Co, Ni) alloy nanoparticles prepared in situ by the reduction of oxide solid solutions. *Chemical Physics Letters* **1999**, *300* (1-2), 236-242.
- [152]. Kong, J.; Cassell, A. M.; Dai, H. J., Chemical vapor deposition of methane for single-walled carbon nanotubes. *Chemical Physics Letters* **1998**, *292* (4-6), 567-574.
- [153]. Colomer, J. F.; Stephan, C.; Lefrant, S.; Van Tendeloo, G.; Willem, I.; Kónya, Z.; Fonseca, A.; Laurent, C.; Nagy, B.J., Large-scale synthesis of single-wall carbon nanotubes by catalytic chemical vapor deposition (CCVD) method. *Chemical Physics Letters* **2000**, *317* (1-2), 83-89.
- [154]. Che, G.; Lakshmi, B. B.; Martin, C. R.; Fisher, E. R.; Ruoff, R. S., Chemical vapor deposition based synthesis of carbon nanotubes and nanofibers using a template method. *Chem. Mat.* **1998**, *10* (1), 260-267.
- [155]. Andrews, R.; Jacques, D.; Rao, A. M.; Derbyshire, F.; Qian, D.; Fan, X.; Dickey, E. C.; Chen, J., Continuous production of aligned carbon nanotubes: a step closer to commercial realization. *Chemical Physics Letters* **1999**, *303* (5-6), 467-474.
- [156]. Pichot, V.; Launois, P.; Pinault, M.; Mayne-L'Hermite, M.; Reynaud, C., Evidence of strong nanotube alignment and for iron preferential growth axis in multiwalled carbon nanotube carpets. *Applied Physics Letters* **2004**, *85* (3), 473-475.
- [157]. Hou, H. Q.; Schaper, A. K.; Weller, F.; Greiner, A., Carbon nanotubes and spheres produced by modified ferrocene pyrolysis. *Chem. Mat.* **2002**, *14* (9), 3990-3994.
- [158]. Yaws, C. L., *Chemical properties handbook: physical thermodynamic, environmental, transport, safety and health related properties for organic and inorganic chemicals* McGraw-hill Professional Publishing 1998.
- [159]. Hernadi, K.; Fonseca, A.; Nagy, J. B.; Siska, A.; Kiricsi, I., Production of nanotubes by the catalytic decomposition of different carbon-containing compounds. *Appl. Catal. A-Gen.* **2000**, *199* (2), 245-255.
- [160]. Zhou, Z. P.; Ci, L. J.; Chen, X. H.; Tang, D. S.; Yan, X. Q.; Liu, D. F.; Liang, Y. X.; Yuan, H. J.; Zhou, W. Y.; Wang, G.; Xie, S. S., Controllable growth of double wall carbon nanotubes in a floating catalytic system. *Carbon* **2003**, *41* (2), 337-342.
- [161]. Suekane, O.; Nagasaka, T.; Kiyotaki, K.; Nosaka, T.; Nakayama, Y., Rapid growth of vertically aligned carbon nanotubes. *Jpn. J. Appl. Phys. Part 2 - Lett. Express Lett.* **2004**, *43* (9A-B), L1214-L1216.
- [162]. Porro, S.; Musso, S.; Giorcelli, M.; Chiodoni, A.; Tagliaferro, A., Optimization of a thermal-CVD system for carbon nanotube growth. *Physica E* **2007**, *37* (1-2), 16-20.
- [163]. Lin, C. H.; Chang, H. L.; Hsu, C. M.; Lo, A. Y.; Kuo, C. T., The role of nitrogen in carbon nanotube

- formation. *Diamond and Related Materials* **12** (10-11), 1851-1857.
- [164]. Ren, W. C.; Cheng, H. M., Aligned double-walled carbon nanotube long ropes with a narrow diameter distribution. *J. Phys. Chem. B* **2005**, *109* (15), 7169-7173.
- [165]. Wasel, W.; Kuwana, K.; Reilly, P. T. A.; Saito, K., Experimental characterization of the role of hydrogen in CVD synthesis of MWCNTs. *Carbon* **2007**, *45* (4), 833-838.
- [166]. Singh, C.; Shaffer, M. S. P.; Windle, A. H., Production of controlled architectures of aligned carbon nanotubes by an injection chemical vapour deposition method. *Carbon* **2003**, *41* (2), 359-368.
- [167]. Juang, Z. Y.; Chien, I. P.; Lai, J. F.; Lai, T. S.; Tsai, C. H., The effects of ammonia on the growth of large-scale patterned aligned carbon nanotubes using thermal chemical vapor deposition method. *Diamond and Related Materials* **13** (4-8), 1203-1209.
- [168]. Hata, K.; Futaba, D. N.; Mizuno, K.; Namai, T.; Yumura, M.; Iijima, S., Water-assisted highly efficient synthesis of impurity-free single-walled carbon nanotubes. *Science* **2004**, *306* (5700), 1362-1364.
- [169]. Zhang, G. Y.; Mann, D.; Zhang, L.; Javey, A.; Li, Y. M.; Yenilmez, E.; Wang, Q.; McVittie, J. P.; Nishi, Y.; Gibbons, J.; Dai, H. J., Ultra-high-yield growth of vertical single-walled carbon nanotubes: Hidden roles of hydrogen and oxygen. *Proc. Natl. Acad. Sci. U. S. A.* **2005**, *102* (45), 16141-16145.
- [170]. Cao, A.; Zhang, X. F.; Xu, C. L.; Liang, J.; Wu, D. H.; Wei, B. Q., Aligned carbon nanotube growth under oxidative ambient. *J. Mater. Res.* **2001**, *16* (11), 3107-3110.
- [171]. Futaba, D. N.; Hata, K.; Yamada, T.; Mizuno, K.; Yumura, M.; Iijima, S., Kinetics of water-assisted single-walled carbon nanotube synthesis revealed by a time-evolution analysis. *Physical Review Letters* **2005**, *95* (5), 4.
- [172]. Murakami, Y.; Chiashi, S.; Miyauchi, Y.; Hu, M. H.; Ogura, M.; Okubo, T.; Maruyama, S., Growth of vertically aligned single-walled carbon nanotube films on quartz substrates and their optical anisotropy. *Chemical Physics Letters* **2004**, *385* (3-4), 298-303.
- [173]. Valles, C.; Perez-Mendoza, M.; Castell, P.; Martinez, M. T.; Maser, W. K.; Benito, A. M., Towards helical and Y-shaped carbon nanotubes: the role of sulfur in CVD processes. *Nanotechnology* **2006**, *17* (17), 4292-4299.
- [174]. Rao, C. N. R.; Govindaraj, A., Carbon nanotubes from organometallic precursors. *Accounts Chem. Res.* **2002**, *35* (12), 998-1007.
- [175]. Xu, Z.; Lu, W. G.; Wang, W. L.; Gu, C. Z.; Liu, K. H.; Bai, X. D.; Wang, E. G.; Dai, H. J., Converting Metallic Single-Walled Carbon Nanotubes into Semiconductors by Boron/Nitrogen Co-Doping. *Adv. Mater.* **2008**, *20* (19), 3615-+.
- [176]. Wang, W. L.; Bai, X. D.; Liu, K. H.; Xu, Z.; Golberg, D.; Bando, Y.; Wang, E. G., Direct synthesis of B-C-N single-walled nanotubes by bias-assisted hot filament chemical vapor deposition. *J. Am. Chem. Soc.* **2006**, *128* (20), 6530-6531.
- [177]. Ducati, C.; Alexandrou, I.; Chhowalla, M.; Amaratunga, G. A. J.; Robertson, J., Temperature selective growth of carbon nanotubes by chemical vapor deposition. *Journal of Applied Physics* **2002**, *92* (6), 3299-3303.
- [178]. Kong, J.; Soh, H. T.; Cassell, A. M.; Quate, C. F.; Dai, H., Synthesis of individual single-walled carbon nanotubes on patterned silicon wafers. *Nature* **1998**, *395* (6705), 878-881.
- [179]. Kukovitsky, E. F.; L'Vov, S. G.; Sainov, N. A., VLS-growth of carbon nanotubes from the vapor. *Chemical Physics Letters* **2000**, *317* (1-2), 65-70.
- [180]. Wagner, R. S.; Ellis, W. C., VAPOR-LIQUID-SOLID MECHANISM OF SINGLE CRYSTAL GROWTH. *Applied Physics Letters* **1964**, *4* (5), 89-90.
- [181]. Dai, H., Nanotube Growth and Characterization. In *Carbon Nanotubes : Synthesis, Structure, Properties and Applications (Topics in Applied Physics, vol. 80)* Dresselhaus, M. S.; Dresselhaus, G.; Avouris, P., Eds. Springer-Verlag: Berlin, 2001; pp 29 – 53.
- [182]. Nasibulin, A. G.; Queipo, P.; Shandakov, S. D.; Brown, D. P.; Jiang, H.; Pikhtsa, P. V.; Tolochko, O. V.; Kauppinen, E. I., Studies on mechanism of single-walled carbon nanotube formation. *J. Nanosci. Nanotechnol.* **2006**, *6* (5), 1233-1246.
- [183]. Homma, Y.; Kobayashi, Y.; Ogino, T.; Takagi, D.; Ito, R.; Jung, Y. J.; Ajayan, P. M., Role of transition metal catalysts in single-walled carbon nanotube growth in chemical vapor deposition. *J. Phys. Chem. B* **2003**, *107* (44), 12161-12164.
- [184]. Shibuta, Y.; Maruyama, S., A molecular dynamics study of the effect of a substrate on catalytic metal clusters in nucleation process of single-walled carbon nanotubes. *Chemical Physics Letters* **2007**, *437* (4-6), 218-223.
- [185]. Gohier, A.; Ewels, C. P.; Minea, T. M.; Djouadi, M. A., Carbon nanotube growth mechanism switches from tip- to base-growth with decreasing catalyst particle size. *Carbon* **2008**, *46* (10), 1331-1338.
- [186]. Vinciguerra, V.; Buonocore, F.; Panzera, G.; Occhipinti, L., Growth mechanisms in chemical vapour deposited carbon nanotubes. *Nanotechnology* **2003**, *14* (6), 655-660.
- [187]. Ajayan, P. M., Nanotechnology: How does a nanofibre grow? *Nature* **2004**, *427* (6973), 402-403.
- [188]. Helveg, S.; Lopez-Cartes, C.; Sehested, J.; Hansen, P. L.; Clausen, B. S.; Rostrup-Nielsen, J. R.; Abild-Pedersen, F.; Norskov, J. K., Atomic-scale imaging of carbon nanofibre growth. *Nature* **2004**, *427* (6973), 426-429.

- [189]. Lin, M.; Ying Tan, J. P.; Boothroyd, C.; Loh, K. P.; Tok, E. S.; Foo, Y.-L., Direct Observation of Single-Walled Carbon Nanotube Growth at the Atomistic Scale. *Nano Letters* **2006**, *6* (3), 449-452.
- [190]. Wako, I.; Chokan, T.; Takagi, D.; Chiashi, S.; Homma, Y., Direct observation of single-walled carbon nanotube growth processes on SiO<sub>2</sub> substrate by in situ scanning electron microscopy. *Chemical Physics Letters* **2007**, *449* (4-6), 309-313.
- [191]. Rodriguez-Manzo, J. A.; Janowska, I.; Pham-Huu, C.; Tolvanen, A.; Krasheninnikov, A. V.; Nordlund, K.; Banhart, F., Growth of Single-Walled Carbon Nanotubes from Sharp Metal Tips. *Small* **2009**, *5* (23), 2710-2715.
- [192]. Rodriguez-Manzo, J. A.; Banhart, F.; Terrones, M.; Terrones, H.; Grobert, N.; Ajayan, P. M.; Sumpter, B. G.; Meunier, V.; Wang, M.; Bando, Y.; Golberg, D., Heterojunctions between metals and carbon nanotubes as ultimate nanocontacts. *Proc. Natl. Acad. Sci. U. S. A.* **2009**, *106* (12), 4591-4595.
- [193]. Mayne, M.; Grobert, N.; Terrones, M.; Kamalakaran, R.; Ruhle, M.; Kroto, H. W.; Walton, D. R. M., Pyrolytic production of aligned carbon nanotubes from homogeneously dispersed benzene-based aerosols. *Chemical Physics Letters* **2001**, *338* (2-3), 101-107.
- [194]. Kamalakaran, R.; Terrones, M.; Seeger, T.; Kohler-Redlich, P.; Ruhle, M.; Kim, Y. A.; Hayashi, T.; Endo, M., Synthesis of thick and crystalline nanotube arrays by spray pyrolysis. *Applied Physics Letters* **2000**, *77* (21), 3385-3387.
- [195]. Pinault, M.; Mayne-L'Hermite, M.; Reynaud, C.; Pichot, V.; Launois, P.; Balltaud, D., Growth of multiwalled carbon nanotubes during the initial stages of aerosol-assisted CCVD. *Carbon* **2005**, *43* (14), 2968-2976.
- [196]. Zhang, X. F.; Cao, A. Y.; Wei, B. Q.; Li, Y. H.; Wei, J. Q.; Xu, C. L.; Wu, D. H., Rapid growth of well-aligned carbon nanotube arrays. *Chemical Physics Letters* **2002**, *362* (3-4), 285-290.
- [197]. Li, X. S.; Cao, A. Y.; Jung, Y. J.; Vajtai, R.; Ajayan, P. M., Bottom-up growth of carbon nanotube multilayers: Unprecedented growth. *Nano Letters* **2005**, *5* (10), 1997-2000.
- [198]. Pinault, M.; Pichot, V.; Khodja, H.; Launois, P.; Reynaud, C.; Mayne-L'Hermite, M., Evidence of sequential lift in growth of aligned multiwalled carbon nanotube multilayers. *Nano Letters* **2005**, *5* (12), 2394-2398.
- [199]. Heresanu, V.; Castro, C.; Cambedouzou, J.; Pinault, M.; Stephan, O.; Reynaud, C.; Mayne-L'Hermite, M.; Launois, P., Nature of the catalyst particles in CCVD synthesis of multiwalled carbon nanotubes revealed by the cooling step study. *J. Phys. Chem. C* **2008**, *112* (19), 7371-7378.
- [200]. Kim, H.; Sigmund, W., Iron nanoparticles in carbon nanotubes at various temperatures. *Journal of Crystal Growth* **2005**, *276* (3-4), 594-605.
- [201]. Tasis, D.; Tagmatarchis, N.; Bianco, A.; Prato, M., Chemistry of carbon nanotubes. *Chemical Reviews* **2006**, *106* (3), 1105-1136.
- [202]. Georgakilas, V.; Gournis, D.; Tzitzios, V.; Pasquato, L.; Guldi, D. M.; Prato, M., Decorating carbon nanotubes with metal or semiconductor nanoparticles. *J. Mater. Chem.* **2007**, *17* (26), 2679-2694.
- [203]. Banerjee, S.; Wong, S. S., Synthesis and characterization of carbon nanotube-nanocrystal heterostructures. *Nano Letters* **2002**, *2* (3), 195-200.
- [204]. Kim, B.; Sigmund, W. M., Functionalized multiwall carbon nanotube/gold nanoparticle composites. *Langmuir* **2004**, *20* (19), 8239-8242.
- [205]. Tzitzios, V.; Georgakilas, V.; Oikonomou, E.; Karakassides, M.; Petridis, D., Synthesis and characterization of carbon nanotube/metal nanoparticle composites well dispersed in organic media. *Carbon* **2006**, *44* (5), 848-853.
- [206]. Li, X. L.; Liu, Y. Q.; Fu, L.; Cao, L. C.; Wei, D. C.; Wang, Y., Efficient synthesis of carbon nanotube-nanoparticle hybrids. *Adv. Funct. Mater.* **2006**, *16* (18), 2431-2437.
- [207]. Martin, C. R.; Kohli, P., The emerging field of nanotube biotechnology. *Nat. Rev. Drug Discov.* **2003**, *2* (1), 29-37.
- [208]. Chen, R. J.; Zhang, Y. G.; Wang, D. W.; Dai, H. J., Noncovalent sidewall functionalization of single-walled carbon nanotubes for protein immobilization. *J. Am. Chem. Soc.* **2001**, *123* (16), 3838-3839.
- [209]. Huang, W. J.; Taylor, S.; Fu, K. F.; Lin, Y.; Zhang, D. H.; Hanks, T. W.; Rao, A. M.; Sun, Y. P., Attaching proteins to carbon nanotubes via diimide-activated amidation. *Nano Letters* **2002**, *2* (4), 311-314.
- [210]. Monthioux, M., Filling single-wall carbon nanotubes. *Carbon* **2002**, *40* (10), 1809-1823.
- [211]. Foygel, M.; Morris, R. D.; Anez, D.; French, S.; Sobolev, V. L., -Theoretical and computational studies of carbon nanotube composites and suspensions: Electrical and thermal conductivity. *PHYSICAL REVIEW B* **2005**, *71* (10), 104201(1-8).
- [212]. Ci, L.; Suhr, J.; Pushparaj, V.; Zhang, X.; Ajayan, P. M., Continuous Carbon Nanotube Reinforced Composites. *Nano Letters* **2008**, *8* (9), 2762-2766.
- [213]. Cadek, M.; Coleman, J. N.; Ryan, K. P.; Nicolosi, V.; Bister, G.; Fonseca, A.; Nagy, J. B.; Szostak, K.; Beguin, F.; Blau, W. J., Reinforcement of Polymers with Carbon Nanotubes:&nbsp; The Role of Nanotube Surface Area. *Nano Letters* **2004**, *4* (2), 353-356.
- [214]. Ajayan, P. M.; Tour, J. M., Materials Science: Nanotube composites. *Nature* **2007**, *447* (7148), 1066-1068.

- [215]. Ajayan, P. M.; Zhou, O. Z., Applications of carbon nanotubes. In *Carbon Nanotubes*, Springer-Verlag Berlin: Berlin, 2001; Vol. 80, pp 391-425.
- [216]. Zhu, J.; Kim, J.; Peng, H.; Margrave, J. L.; Khabashesku, V. N.; Barrera, E. V., Improving the Dispersion and Integration of Single-Walled Carbon Nanotubes in Epoxy Composites through Functionalization. *Nano Letters* **2003**, 3 (8), 1107-1113.
- [217]. Thostenson, E. T.; Li, W. Z.; Wang, D. Z.; Ren, Z. F.; Chou, T. W., Carbon nanotube/carbon fiber hybrid multiscale composites. *Journal of Applied Physics* **2002**, 91 (9), 6034-6037.
- [218]. Ci, L.; Bai, J., Novel Micro/Nanoscale Hybrid Reinforcement: Multiwalled Carbon Nanotubes on SiC Particles. *Advanced Materials* **2004**, 16 (22), 2021-2024.
- [219]. Thostenson, E. T.; Li, C.; Chou, T.-W., Nanocomposites in context. *Composites Science and Technology* **2005**, 65 (3-4), 491-516.
- [220]. Gournis, D.; Karakassides, M. A.; Bakas, T.; Boukos, N.; Petridis, D., Catalytic synthesis of carbon nanotubes on clay minerals. *Carbon* **2002**, 40 (14), 2641-2646.
- [221]. Huang, S., Growing carbon nanotubes on patterned submicron-size SiO<sub>2</sub> spheres. *Carbon* **2003**, 41 (12), 2347-2352.
- [222]. Zhang, Q.; Huang, J.-Q.; Zhao, M.-Q.; Qian, W.-Z.; Wang, Y.; Wei, F., Radial growth of vertically aligned carbon nanotube arrays from ethylene on ceramic spheres. *Carbon* **2008**, 46 (8), 1152-1158.
- [223]. Zhang, Q.; Huang, J. Q.; Wei, F.; Xu, G. H.; Wang, Y.; Qian, W. Z.; Wang, D. Z., Large scale production of carbon nanotube arrays on the sphere surface from liquefied petroleum gas at low cost. *Chin. Sci. Bull.* **2007**, 52 (21), 2896-2902.
- [224]. Xiang, R.; Luo, G.; Qian, W.; Wang, Y.; Wei, F.; Li, Q., Large area growth of aligned CNT Arrays on spheres: towards large scale and continuous production. *Chem. Vapor Depos.* **2007**, 13 (10), 533-536.
- [225]. Philippe, R.; Caussat, B.; Falqui, A.; Kihn, Y.; Kalck, P.; Bordere, S.; Plee, D.; Gaillard, P.; Bernard, D.; Serp, P., An original growth mode of MWCNTs on alumina supported iron catalysts. *Journal of Catalysis* **2009**, 263 (2), 345-358.
- [226]. Yamamoto, N.; John Hart, A.; Garcia, E. J.; Wicks, S. S.; Duong, H. M.; Slocum, A. H.; Wardle, B. L., High-yield growth and morphology control of aligned carbon nanotubes on ceramic fibers for multifunctional enhancement of structural composites. *Carbon* **2009**, 47 (3), 551-560.
- [227]. Ci, L. J.; Zhao, Z. G.; Bai, J. B., Direct growth of carbon nanotubes on the surface of ceramic fibers. *Carbon* **2005**, 43 (4), 883-886.
- [228]. Zhao, Z. G.; Ci, L. J.; Cheng, H. M.; Bai, J. B., The growth of multi-walled carbon nanotubes with different morphologies on carbon fibers. *Carbon* **2005**, 43 (3), 663-665.
- [229]. Wei, B. Q.; Vajtai, R.; Jung, Y.; Ward, J.; Zhang, R.; Ramanath, G.; Ajayan, P. M., Assembly of Highly Organized Carbon Nanotube Architectures by Chemical Vapor Deposition. *Chem. Mat.* **2003**, 15 (8), 1598-1606.
- [230]. E.J. Bae; W.B. Choi; K.S. Jeong; J.U. Chu; G.-S. Park; S. Song; I.K. Yoo, Selective Growth of Carbon Nanotubes on Pre-patterned Porous Anodic Aluminum Oxide. *Advanced Materials* **2002**, 14 (4), 277-279.
- [231]. Hata, K.; Futaba, D. N.; Mizuno, K.; Namai, T.; Yumura, M.; Iijima, S., Water-Assisted Highly Efficient Synthesis of Impurity-Free Single-Walled Carbon Nanotubes. *Science* **2004**, 306 (5700), 1362-1364.
- [232]. Sohn, J. I.; Lee, S.; Song, Y.-H.; Choi, S.-Y.; Cho, K.-I.; Nam, K.-S., Patterned selective growth of carbon nanotubes and large field emission from vertically well-aligned carbon nanotube field emitter arrays. *Applied Physics Letters* **2001**, 78 (7), 901-903.
- [233]. Han, Z. H.; Yang, B.; Kim, S. H.; Zachariah, M. R., Application of hybrid sphere/carbon nanotube particles in nanofluids. *Nanotechnology* **2007**, 18 (10), 105701-4.
- [234]. Hart, A. J.; Slocum, A. H., Rapid Growth and Flow-Mediated Nucleation of Millimeter-Scale Aligned Carbon Nanotube Structures from a Thin-Film Catalyst. *Journal of Physical Chemistry B* **2006**, 110 (16), 8250-8257.
- [235]. Han, Z. H.; Yang, B.; Kim, S. H.; Zachariah, M. R., Application of hybrid sphere/carbon nanotube particles in nanofluids. *Nanotechnology* **2007**, 18 (10), 4.
- [236]. Naito, K.; Yang, J.-M.; Xu, Y.; Kagawa, Y., Enhancing the thermal conductivity of polyacrylonitrile- and pitch-based carbon fibers by grafting carbon nanotubes on them. *Carbon* **48** (6), 1849-1857.
- [237]. Jorio, A.; Dresselhaus, M. S.; Dresselhaus, G., *Carbon Nanotubes: Advanced Topics in the Synthesis, Structure, Properties and Applications (Topics in Applied Physics 111)*. Springer- Verlag Berlin Heidelberg: New York, 2008.
- [238]. Endo, M.; Kim, Y. A.; Hayashi, T.; Fukai, Y.; Oshida, K.; Terrones, M.; Yanagisawa, T.; Higaki, S.; Dresselhaus, M. S., Structural characterization of cup-stacked-type nanofibers with an entirely hollow core. *Applied Physics Letters* **2002**, 80 (7), 1267-1269.
- [239]. Kim, P.; Shi, L.; Majumdar, A.; McEuen, P. L., Thermal transport measurements of individual multiwalled nanotubes. *Phys. Rev. Lett.* **2001**, 8721 (21), 4.
- [240]. Kim, T. H.; Choi, W. M.; Kim, D. H.; Meitl, M. A.; Menard, E.; Jiang, H. Q.; Carlisle, J. A.; Rogers, J. A., Printable, flexible, and stretchable forms of ultrananocrystalline diamond with applications in thermal management. *Adv. Mater.* **2008**, 20 (11), 2171-+.
- [241]. Graebner, J. E.; Jin, S.; Kammlott, G. W.; Herb, J. A.; Gardiner, C. F., LARGE ANISOTROPIC

- THERMAL-CONDUCTIVITY IN SYNTHETIC DIAMOND FILMS. *Nature* **1992**, *359* (6394), 401-403.
- [242]. Duong, H. M.; Papavassiliou, D. V.; Mullen, K. J.; Maruyama, S., Computational modeling of the thermal conductivity of single-walled carbon nanotube - polymer composites. *Nanotechnology* **2008**, *19* (6), 8.
- [243]. Yu, C.; Kim, Y. S.; Kim, D.; Grunlan, J. C., Thermoelectric Behavior of Segregated-Network Polymer Nanocomposites. *Nano Lett.* **2008**, *8* (12), 4428-4432.
- [244]. Yu, A. P.; Ramesh, P.; Sun, X. B.; Bekyarova, E.; Itkis, M. E.; Haddon, R. C., Enhanced Thermal Conductivity in a Hybrid Graphite Nanoplatelet - Carbon Nanotube Filler for Epoxy Composites. *Adv. Mater.* **2008**, *20* (24), 4740-+.
- [245]. Wei Lin, K.-S. M. C. P. W., A Combined Process of In Situ Functionalization and Microwave Treatment to Achieve Ultrasmall Thermal Expansion of Aligned Carbon Nanotube-Polymer Nanocomposites: Toward Applications as Thermal Interface Materials. *Adv. Mater.* **2009**, *9999* (9999), NA.
- [246]. Rao, A. M.; Eklund, P. C.; Bandow, S.; Thess, A.; Smalley, R. E., Evidence for charge transfer in doped carbon nanotube bundles from Raman scattering. *Nature* **1997**, *388* (6639), 257-259.
- [247]. Azuhata, T.; Sota, T.; Suzuki, K.; Nakamura, S., POLARIZED RAMAN-SPECTRA IN GAN. *J. Phys.-Condens. Matter* **1995**, *7* (10), L129-L133.
- [248]. Ajayan, P. M.; Tour, J. M., Materials science - Nanotube composites. *Nature* **2007**, *447* (7148), 1066-1068.
- [249]. Zhu, J.; Kim, J. D.; Peng, H. Q.; Margrave, J. L.; Khabashesku, V. N.; Barrera, E. V., Improving the dispersion and integration of single-walled carbon nanotubes in epoxy composites through functionalization. *Nano Lett.* **2003**, *3* (8), 1107-1113.
- [250]. Peng, X. H.; Wong, S. S., Functional Covalent Chemistry of Carbon Nanotube Surfaces. *Adv. Mater.* **2009**, *21* (6), 625-642.
- [251]. Bozlar, M.; Miomandre, F.; Bai, J. B., Electrochemical synthesis and characterization of carbon nanotube/modified polypyrrole hybrids using a cavity microelectrode. *Carbon* **2009**, *47* (1), 80-84.
- [252]. Thostenson, E. T.; Chou, T. W., Processing-structure-multi-functional property relationship in carbon nanotube/epoxy composites. *Carbon* **2006**, *44* (14), 3022-3029.
- [253]. Shaikh, S.; Li, L.; Lafdi, K.; Huie, J., Thermal conductivity of an aligned carbon nanotube array. *Carbon* **2007**, *45* (13), 2608-2613.
- [254]. Cai, D. Y.; Song, M., Latex technology as a simple route to improve the thermal conductivity of a carbon nanotube/polymer composite. *Carbon* **2008**, *46* (15), 2107-2112.
- [255]. Kharchenko, S. B.; Douglas, J. F.; Obrzut, J.; Grulke, E. A.; Migler, K. B., Flow-induced properties of nanotube-filled polymer materials. *Nat. Mater.* **2004**, *3* (8), 564-568.
- [256]. Cai, D.; Song, M., Latex technology as a simple route to improve the thermal conductivity of a carbon nanotube/polymer composite. *Carbon* **2008**, *46* (15), 2107-2112.
- [257]. Putz, K. W.; Palmeri, M. J.; Cohn, R. B.; Andrews, R.; Brinson, L. C., Effect of cross-link density on interphase creation in polymer nanocomposites. *Macromolecules* **2008**, *41* (18), 6752-6756.
- [258]. Cahill, D. G.; Lee, S. M.; Selinder, T. I., Thermal conductivity of kappa-Al<sub>2</sub>O<sub>3</sub> and alpha-Al<sub>2</sub>O<sub>3</sub> wear-resistant coatings. *J. Appl. Phys.* **1998**, *83* (11), 5783-5786.
- [259]. Benveniste, Y., EFFECTIVE THERMAL-CONDUCTIVITY OF COMPOSITES WITH A THERMAL CONTACT RESISTANCE BETWEEN THE CONSTITUENTS - NONDILUTE CASE. *J. Appl. Phys.* **1987**, *61* (8), 2840-2843.
- [260]. Prasher, R. S.; Hu, X. J.; Chalopin, Y.; Mingo, N.; Lofgreen, K.; Volz, S.; Cleri, F.; Keblinski, P., Turning Carbon Nanotubes from Exceptional Heat Conductors into Insulators. *Physical Review Letters* **2009**, *102* (10), 4.
- [261]. Dunitz, J. D.; Orgel, L. E.; Rich, A., THE CRYSTAL STRUCTURE OF FERROCENE. *Acta Crystallographica* **1956**, *9* (4), 373-375.
- [262]. Liu, Q.; Chen, Z.-G.; Liu, B.; Ren, W.; Li, F.; Cong, H.; Cheng, H.-M., Synthesis of different magnetic carbon nanostructures by the pyrolysis of ferrocene at different sublimation temperatures. *Carbon* **2008**, *46* (14), 1892-1902.
- [263]. Eres, G.; Puretzky, A. A.; Geohegan, D. B.; Cui, H., In situ control of the catalyst efficiency in chemical vapor deposition of vertically aligned carbon nanotubes on predeposited metal catalyst films. *Applied Physics Letters* **2004**, *84* (10), 1759-1761.
- [264]. Chráska, P.; Dubsky, J.; Neufuss, K.; Písacka, J., Alumina-base plasma-sprayed materials part I: Phase stability of alumina and alumina-chromia. *Journal of Thermal Spray Technology* **1997**, *6* (3), 320-326.
- [265]. Kittaka, S.; Morimoto, T., Spherical particles and their surface properties. III. Formation of spherical particles of metal oxides by O<sub>2</sub>-H<sub>2</sub> flame fusion. *Bulletin of the Chemical Society of Japan* **1981**, *54* (10), 2882-2885.
- [266]. Porto, S. P. S.; Krishnan, R. S., Raman Effect of Corundum. *The Journal of Chemical Physics* **1967**, *47* (3), 1009-1012.
- [267]. Lodzianna, Z.; Noskov, J. K., Interaction of Pd with steps on [alpha]-Al<sub>2</sub>O<sub>3</sub>(0 0 1). *Surface Science* **2002**, *518* (1-2), L577-L582.
- [268]. Girifalco, L. A.; Hodak, M.; Lee, R. S., Carbon nanotubes, buckyballs, ropes, and a universal graphitic

- potential. *Physical Review B* **2000**, *62* (19), 13104.
- [269]. Henrard, L.; Hernandez, E.; Bernier, P.; Rubio, A., van der Waals interaction in nanotube bundles: Consequences on vibrational modes. *Physical Review B* **1999**, *60* (12), R8521-R8524.
- [270]. Kis, A.; Csanyi, G.; Salvietat, J. P.; Lee, T.-N.; Couteau, E.; Kulik, A. J.; Benoit, W.; Brugger, J.; Forro, L., Reinforcement of single-walled carbon nanotube bundles by intertube bridging. *Nat Mater* **2004**, *3* (3), 153-157.
- [271]. Buehler, M. J., Mesoscale modeling of mechanics of carbon nanotubes: Self-assembly, self-folding, and fracture. *J. Mater. Res.* **2006**, *21* (11), 2855-2869.
- [272]. Fan, S. S.; Chapline, M. G.; Franklin, N. R.; Tombler, T. W.; Cassell, A. M.; Dai, H. J., Self-oriented regular arrays of carbon nanotubes and their field emission properties. *Science* **1999**, *283* (5401), 512-514.
- [273]. Baughman, R. H.; Zakhidov, A. A.; de Heer, W. A., Carbon Nanotubes--the Route Toward Applications *Science* **2002**, *297* (5582), 787 - 792.
- [274]. Sun, C.-H.; Yin, L.-C.; Li, F.; Lu, G.-Q.; Cheng, H.-M., Van der Waals interactions between two parallel infinitely long single-walled nanotubes. *Chemical Physics Letters* **2005**, *403* (4-6), 343-346.
- [275]. Sun, C.-H.; Lu, G.-Q.; Cheng, H.-M., Simple approach to estimating the van der Waals interaction between carbon nanotubes. *Physical Review B (Condensed Matter and Materials Physics)* **2006**, *73* (19), 195414-5.
- [276]. Wong, E. W.; Sheehan, P. E.; Lieber, C. M., Nanobeam Mechanics: Elasticity, Strength, and Toughness of Nanorods and Nanotubes *Science* **1997**, *277* (5334), 1971-1975.
- [277]. Gere, J. M.; Timoshenko, S. P., *Mechanics of materials* PWS-Kent: Boston, 1984; p 762.
- [278]. Rodgers, A. S.; Golden, D. M.; Benson, S. W., KINETICS OF REACTION OF IODOBENZENE AND HYDROGEN IODIDE . HEAT OF FORMATION OF PHENYL RADICAL AND ITS IMPLICATIONS ON REACTIVITY OF BENZENE. *Journal of the American Chemical Society* **1967**, *89* (18), 4578-&.
- [279]. Benson, S. W.; Shaw, R., Kinetics and Mechanism of Hydrogenolyses. The Addition of Hydrogen Atoms to Propylene, Toluene, and Xylene. *The Journal of Chemical Physics* **1967**, *47* (10), 4052-4055.
- [280]. Benson, S. W.; Shaw, R., KINETICS AND MECHANISM OF HYDROGENOLYSES . ADDITION OF HYDROGEN ATOMS TO PROPYLENE TOLUENE AND XYLENE. *Journal of Chemical Physics* **1967**, *47* (10), 4052-&.
- [281]. Endo, H.; Kuwana, K.; Saito, K.; Qian, D.; Andrews, R.; Grulke, E. A., CFD prediction of carbon nanotube production rate in a CVD reactor. *Chemical Physics Letters* **2004**, *387* (4-6), 307-311.
- [282]. Kuwana, K.; Endo, H.; Saito, K.; Qian, D.; Andrews, R.; Grulke, E. A., Catalyst deactivation in CVD synthesis of carbon nanotubes. *Carbon* **2005**, *43* (2), 253-260.
- [283]. Wasel, W.; Kuwana, K.; Saito, K., Chemical and thermal structures of a xylene-based CVD reactor to synthesize carbon nanotubes. *Chemical Physics Letters* **2006**, *422* (4-6), 470-474.
- [284]. Kuwana, K.; Li, T.; Saito, K., Gas-phase reactions during CVD synthesis of carbon nanotubes: Insights via numerical experiments. *Chemical Engineering Science* **2006**, *61* (20), 6718-6726.
- [285]. Dagaut, P.; Pengloan, G.; Ristori, A., Oxidation, ignition and combustion of toluene: Experimental and detailed chemical kinetic modeling. *PCCP Phys. Chem. Chem. Phys.* **2002**, *4* (10), 1846-1854.
- [286]. Gail, S.; Dagaut, P., Experimental kinetic study of the oxidation of p-xylene in a JSR and comprehensive detailed chemical kinetic modeling. *Combustion and Flame* **2005**, *141* (3), 281-297.
- [287]. Becker, A.; Huttinger, K. J., Chemistry and kinetics of chemical vapor deposition of pyrocarbon - II - Pyrocarbon deposition from ethylene, acetylene and 1,3-butadiene in the low temperature regime. *Carbon* **1998**, *36* (3), 177-199.
- [288]. Back, M. H., MECHANISM OF PYROLYSIS OF ACETYLENE. *Canadian Journal of Chemistry* **1971**, *49* (13), 2199-&.
- [289]. Kiefer, J. H.; Vondrasek, W. A., THE MECHANISM OF THE HOMOGENEOUS PYROLYSIS OF ACETYLENE. *Int. J. Chem. Kinet.* **1990**, *22* (7), 747-786.
- [290]. Norinaga, K.; Deutschmann, O., Detailed Kinetic Modeling of Gas-Phase Reactions in the Chemical Vapor Deposition of Carbon from Light Hydrocarbons. *Industrial & Engineering Chemistry Research* **2007**, *46* (11), 3547-3557.
- [291]. Lewis, K. E.; Smith, G. P., Bond dissociation energies in ferrocene. *Journal of the American Chemical Society* **1984**, *106* (16), 4650-4651.
- [292]. Dormans, G. J. M., OMVCD of transition metals and their silicides using metallocenes and (di) silane or silicon tetra-bromide. *Journal of Crystal Growth* **1991**, *108* (3-4), 806-816.
- [293]. Hirasawa, T.; Sung, C.-J.; Yang, Z.; Joshi, A.; Wang, H., Effect of ferrocene addition on sooting limits in laminar premixed ethylene-oxygen-argon flames. *Combustion and Flame* **2004**, *139* (4), 288-299.
- [294]. Linteris, G. T.; Rumminger, M. D.; Babushok, V.; Tsang, W., Flame inhibition by ferrocene and blends of inert and catalytic agents. *Symposium (International) on Combustion* **2000**, *28* (2), 2965-2972.
- [295]. Kuwana, K.; Saito, K., Modeling ferrocene reactions and iron nanoparticle formation: Application to CVD synthesis of carbon nanotubes. *Proceedings of the Combustion Institute* **2007**, *31* (2), 1857-1864.
- [296]. Neufeld, P. D.; Janzen, A. R.; Aziz, R. A., Empirical Equations to Calculate 16 of the Transport Collision Integrals Omega [sup (l,s)\*] for the Lennard-Jones (12-6) Potential. *The Journal of Chemical Physics*

1972, 57 (3), 1100-1102.

- [297]. Wang, H.; Frenklach, M., Transport properties of polycyclic aromatic hydrocarbons for flame modeling. *Combustion and Flame* **1994**, 96 (1-2), 163-170.
- [298]. Stiel, L. I.; Thodos, G., THE THERMAL CONDUCTIVITY OF NONPOLAR SUBSTANCES IN THE DENSE GASEOUS AND LIQUID REGIONS. *Aiche Journal* **1964**, 10 (1), 26-30.
- [299]. Eres, G.; Kinkhabwala, A. A.; Cui, H.; Geohegan, D. B.; Puretzky, A. A.; Lowndes, D. H., Molecular Beam-Controlled Nucleation and Growth of Vertically Aligned Single-Wall Carbon Nanotube Arrays. *The Journal of Physical Chemistry B* **2005**, 109 (35), 16684-16694.
- [300]. Lacroix, R.; Fournet, R.; Ziegler-Devin, I.; Marquaire, P. M., Kinetic modeling of surface reactions involved in CVI of pyrocarbon obtained by propane pyrolysis. *Carbon* **48** (1), 132-144.
- [301]. Dyagileva, L. M.; Mar'in, V. P.; Tsyanova, E. I.; Razuvayev, G. A., Reactivity of the first transition row metallocenes in thermal decomposition reaction. *Journal of Organometallic Chemistry* **1979**, 175 (1), 63-72.

# Résumé

Les nanotubes de carbone (CNTs), intégrant à la fois la structure parfaite, la géométrie unique, et des propriétés exceptionnelles, sont d'une grande importance dans le domaine des nanotechnologies. Leur association avec d'autres matériaux produit de nouvelles propriétés remarquables, et étend par conséquent leurs domaines d'applications comme charges multifonctionnelles. Cette thèse vise à développer un nouveau matériau hybride avec une structure multi-échelle à base de CNTs et de particules micrométriques d'alumine ( $\mu\text{Al}_2\text{O}_3$ ) par une méthode de dépôt chimique en phase vapeur (CVD). Nos études démontrent que les structures CNTs- $\mu\text{Al}_2\text{O}_3$  ont une propriété exceptionnelle en matière de transport thermique dans les composites polymères. Celle-ci nous a amenée à explorer plus en profondeur les mécanismes de l'organisation des CNTs sur  $\mu\text{Al}_2\text{O}_3$ , et d'étudier la cinétique de réactions chimiques dans l'espace gazeux du réacteur CVD.

Dans le premier chapitre, nous faisons une revue de l'état de l'art sur la structure, les propriétés et les applications des CNTs, ainsi que les mécanismes de croissance de CNTs par CVD. Une attention particulière est également accordée aux structures hybrides nano-micrométriques qui sont synthétisées par greffage in-situ des CNTs sur des substrats micrométriques.

Dans le deuxième chapitre, nous présentons trois types de structures hybrides, qui sont classifiées selon différents modes d'organisation des CNTs sur les microsphères d'alumine. L'évolution des structures hybrides est démontrée en faisant varier le diamètre, la longueur et la densité numérique des CNTs sur  $\mu\text{Al}_2\text{O}_3$ . L'organisation spécifique et la dispersion homogène des CNTs permettent de diminuer considérablement leurs résistances de contacts thermiques lorsque les matériaux hybrides CNTs- $\mu\text{Al}_2\text{O}_3$  sont utilisés comme charges dans les composites polymères. Une amélioration importante de la conductivité thermique des composites Epoxy/CNTs- $\mu\text{Al}_2\text{O}_3$ , par rapport à celle des composites constitués de CNTs et de résine époxy, est obtenue à une fraction massique ultra-faible en CNTs.

Dans le troisième chapitre, nous avons étudié en détail les rôles joués par les paramètres CVD et les microparticules sphériques d'alumine dans la construction de structures hybrides multiformes. En particulier, les fortes corrélations entre la température, les sources de carbone et les ratios d'hydrogène ont été discutées. Le lien entre les CNTs et les microparticules est mis en évidence, ainsi que la dynamique de croissance des CNTs. L'auto-organisation des CNTs sur  $\mu\text{Al}_2\text{O}_3$  est expliquée par les deux mécanismes suivants. Dans un premier temps, la structure hétérogène de la surface des particules entraîne une distribution différente des particules du catalyseur, et leur arrangement cristallin spécifique détermine potentiellement l'orientation des CNTs. Dans un deuxième temps, l'auto-assemblage des CNTs est dû à l'interaction des forces faibles de Van der Waals entre CNTs voisins. Le calcul basé sur le modèle du nano-cantilever montre que l'auto-assemblage des CNTs dépend fortement de leur diamètre, de leur longueur et de leur densité numérique sur  $\mu\text{Al}_2\text{O}_3$ .

Dans le quatrième chapitre, la cinétique chimique des réactions dans l'espace gazeux du réacteur CVD est numériquement analysée. Le processus non-équilibré de CVD qui contient plusieurs phénomènes physico-chimiques est simulé avec succès en combinant la cinétique des réactions chimiques avec les phénomènes de transport physique. Les champs des concentrations de chaque espèce est révélée aux températures utilisées par simulation des réactions chimiques. Les sources effectives de carbone et de fer pour la croissance des CNTs ont été éclaircies en comparant les résultats de simulation avec les observations expérimentales, y compris les mesures de spectrométrie de masse. Ces analyses sont nécessaires pour améliorer la production des hybrides avec des structures homogènes.

# Abstract

Carbon nanotubes (CNTs), integrating perfect structure, unique geometry, and exceptional properties, are of great significance in nanotechnology. Their hybridization with a variety of other materials generates huge amounts of attractive properties, and thus expands largely their application fields as multifunctional fillers. This thesis aims to develop a novel multi-scale hybrid material based on carbon nanotubes and micrometer alumina particles ( $\mu\text{Al}_2\text{O}_3$ ) by an in-situ floating chemical vapor deposition (CVD) method. Our studies demonstrate that the CNTs- $\mu\text{Al}_2\text{O}_3$  structures have outstanding thermal transport properties in polymer composites. This greatly motivates us to further explore the organization mechanisms of CNTs on microparticles, and to investigate gas phase chemical reaction kinetics in CVD reactor.

In the first chapter, we review the state of the art of research in CNT structure, properties and applications, as well as CNT growth mechanisms in CVD. Special attention is also paid to the nano-micro hybrid structures which are synthesized by in-situ grafting CNTs on micrometer substrates.

In the second chapter, we present three types of hybrid structures which are classified according to distinct CNT organization patterns on alumina microspheres. The evolution of the hybrid structures is demonstrated by varying CNT diameter, length and number density on  $\mu\text{Al}_2\text{O}_3$ . The specific organization and homogeneous dispersion of CNTs could significantly reduce their thermal contact resistances when the CNTs- $\mu\text{Al}_2\text{O}_3$  hybrid materials are used as fillers in polymer composites. Enhanced thermal conductivities of the Epoxy/CNTs- $\mu\text{Al}_2\text{O}_3$  composites are obtained at ultra-low CNT weight fractions compared with that of the composites constituted of pristine CNTs and epoxy.

In the third chapter, we investigate in detail the roles played by CVD parameters and alumina spherical microparticles in the construction of multiform hybrid structures. In particular, the strong correlations among the temperature, carbon sources and hydrogen ratios are discussed. The connection between the CNTs and the microparticles are demonstrated, along with the CNT growth dynamics on  $\mu\text{Al}_2\text{O}_3$ . The self-organization behavior of CNTs on  $\mu\text{Al}_2\text{O}_3$  is explained by the following two mechanisms: first, heterogeneous surface structures of  $\mu\text{Al}_2\text{O}_3$  generate varied nucleation of catalyst particles, and their specific crystal arrangement potentially determines CNT growth orientations; second, the self assembly of CNTs is due to weak Van der Waals interaction forces between neighboring nanotubes. The calculation based on the nano-cantilever model shows that the CNT self assembly is greatly dependent on their diameter, length and number density on  $\mu\text{Al}_2\text{O}_3$ .

In the forth chapter, gas phase chemical reaction kinetics in CVD reactor is numerically analyzed. The non-equilibrium CVD processes which involve multi physical-chemical phenomena are successfully simulated by combining the chemical reaction kinetics with the physical transport phenomena. The space-dependent concentration distribution of each species is revealed by simulating the reacting fluid at the used temperatures. The effective carbon and iron precursors for CNT growth are illuminated by comparing simulation results with experimental observations including mass spectrometry measurements. These analyses of chemical reactions in CVD system are helpful to improve the production of the hybrids with homogeneous structures.